

CERN 94-07  
25 October 1994

ORGANISATION EUROPÉENNE POUR LA RECHERCHE NUCLÉAIRE  
**CERN** EUROPEAN ORGANIZATION FOR NUCLEAR RESEARCH

International Workshop  
on  
Advanced Materials  
for  
High Precision Detectors

Archamps, Haute-Savoie, France  
28–30 September 1994

Proceedings

Editors: B. Nicquevert  
C. Hauviller

GENEVA  
1994

© Copyright CERN, Genève, 1994

Propriété littéraire et scientifique réservée pour tous les pays du monde. Ce document ne peut être reproduit ou traduit en tout ou en partie sans l'autorisation écrite du Directeur général du CERN, titulaire du droit d'auteur. Dans les cas appropriés, et s'il s'agit d'utiliser le document à des fins non commerciales, cette autorisation sera volontiers accordée.

Le CERN ne revendique pas la propriété des inventions brevetables et dessins ou modèles susceptibles de dépôt qui pourraient être décrits dans le présent document; ceux-ci peuvent être librement utilisés par les instituts de recherche, les industriels et autres intéressés. Cependant, le CERN se réserve le droit de s'opposer à toute revendication qu'un usager pourrait faire de la propriété scientifique ou industrielle de toute invention et tout dessin ou modèle décrits dans le présent document.

Literary and scientific copyrights reserved in all countries of the world. This report, or any part of it, may not be reprinted or translated without written permission of the copyright holder, the Director-General of CERN. However, permission will be freely granted for appropriate non-commercial use.

If any patentable invention or registrable design is described in the report, CERN makes no claim to property rights in it but offers it for the free use of research institutions, manufacturers and others. CERN, however, may oppose any attempt by a user to claim any proprietary or patent rights in such inventions or designs as may be described in the present document.

ISSN 0007-8328

ISBN 92-9083-066-2

ORGANISATION EUROPÉENNE POUR LA RECHERCHE NUCLÉAIRE  
**CERN** EUROPEAN ORGANIZATION FOR NUCLEAR RESEARCH

International Workshop  
on  
Advanced Materials  
for  
High Precision Detectors

Archamps, Haute-Savoie, France  
28–30 September 1994

# Proceedings

Editors: B. Nicquevert  
C. Hauviller

GENEVA  
1994





## Abstract

These *Proceedings* gather together the contributions to the *Workshop on Advanced Materials for High Precision Detectors*, which was held from 28-30 September 1994 in Archamps, Haute-Savoie, France.

This meeting brought together international experts (researchers, physicists and engineers) in the field of advanced materials and their use in high energy physics detectors or spacecraft applications. Its purpose was to discuss the status of the different *materials* currently in use in the *structures* of detectors and spacecraft, together with their actual performances, technological implications and future prospects. Environmental effects, such as those of moisture and radiation, were discussed, as were design and *manufacturing* technologies. Some case studies were presented.



# Welcome

The Haute-Savoie local authorities have been particularly pleased and honoured to welcome this Workshop in Archamps, an international location where synergies between research and industry are currently being developed.

Here, at the heart of the French Alps, the fields of electronics, particle physics, biotechnology and micromechanics have found a nice homeland. Leading industrial groups are present, such as Salomon, Eaton, Digital, Parker Hannifin, Dassault, Alcatel, Evian, Roche or Tefal. They benefit from one of the world's most digitized telecommunications network and realize why international exchange is so easy in Haute-Savoie.

Training and research are of a quality to meet the standards of the industrial tissue. For example, the Archamps French Geneva Campus provides further training in international management and post-graduate studies, while the Annecy Laboratory of Particle Physics works in tight cooperation with CERN in Geneva and participates in the development of the microelectronics sector.

If your preference lies more outdoors on hiking circuits or on the ski slopes, the Mont-Blanc mountain range, complete with the most impressive of glaciers, will certainly guarantee you endless hours of fresh Alpine air and enjoyment. All the polls that have been conducted show that Haute-Savoie is sought out by all those who wish to reconcile their professional life with their social, cultural and leisure activities.

Here, we know that science and research have constantly been a vast field for innovation and that innovation has changed our life. Come and join those who strongly believe that nothing could exist without the faith of researchers who are constantly committed to improve scientific research and innovation.

Roland PASCAL

General manager Haute-Savoie Administration  
President International Business Park





## Foreword

The Workshop on Advanced Material for High Precision Detectors, which has been held in Archamps, Haute-Savoie, France, from 28-30 September 1994, was the first one on this highly technological subject. Its success was above expectation: more than one hundred registration forms have been received, but unfortunately, it was technically impossible to accept all of them. There was 86 participants, coming not only from CERN member states, but also Russia, the USA and Canada.

The design goal of the central parts of the High Energy Particle Physics detectors, the so-called *trackers*, is to achieve a measurement accuracy at the micron level over a large detection volume of many cubic metres.

The principal sources of errors are caused by the structures: material creates unwanted background and a lack of stability impinges on the positioning of the detecting elements. Optimisation leads to a choice mainly governed by a high specific modulus (similar to aerospace): composites (non-metallic and metallic matrices); or advanced light materials (beryllium and its alloys, foamed ceramics, ...).

The hostile environment leads to major concerns about the micron level stability of the structures: ionizing radiations up to  $10^6$  gray, temperature gradients, humidity transients,... together with inherent mechanical behaviour: internal stresses, creep, etc...

The Workshop was divided into three main parts.

- *structures* used for detectors or spacecraft applications;
- *materials* and their behaviour in the detectors' environment;
- *design*, optimization and *manufacturing* technologies.

The aim of the workshop was to gather engineers, researchers and scientists to sum up the state-of-the-art, and to determine ways for future development.

The Workshop has been locally organized by the Technical Assistance Group 1 of the Particle Physics Experiments Division at CERN. It received help from the Conseil Général de la Haute-Savoie and especially from the team of the International Business Park, and we would like to thank them for their support.

The efficient help and advice from the members of the Organizing Committee should also be warmly acknowledged.

Claude HAUVILLER  
Chairman of the Organizing Committee



# Workshop Organization

## Organizing Committee

A. Fallou	CNRS (CPPM), Marseille
C. Girard	CNRS (LAPP), Annecy
C. Hauviller	CERN (Chairman)
B. Nicquevert	CERN (Secretary)
E. Perrin	Université de Genève
M. J. Price	CERN
H. Schönbacher	CERN
G. Tappern	Rutherford Appleton Lab.
T. Thompson	Los Alamos National Lab.

## Workshop Secretariat

Sue Cousins  
Sandrine Sciarrino

## at the International Business Park

Stéphane Bérard  
Valérie Guichet

## Edition of the Proceedings

with the help of  
the CERN Desktop Publishing Centre

## CONTENTS

### Foreword

<i>C. Hauviller (CERN)</i> .....	vii
----------------------------------	-----

### PART I. Generalities ..... 1

#### Advanced Materials for High Precision Detectors

<i>C. Hauviller (CERN)</i> .....	3
----------------------------------	---

#### The Use of High Stiffness Material and Dimensionally Stable Materials in Spacecraft Applications

<i>D. Bashford (ERA Technology Ltd, Leatherhead, UK), D. Eaton, A. Pradier (ESA/ESTEC, Noordwijk, The Netherlands)</i> .....	9
--	---

#### Recent Developments in Low Cost Stable Structures for Space

<i>T. C. Thompson, C. Grastataro, B. G. Smith (Los Alamos Nat. Lab., USA)</i> .....	21
---	----

### PART II. Structures ..... 31

#### Highly Dimensional Stable Composite Structures

<i>G. Helwig (DASA-Dornier GmbH, Germany)</i> .....	33
---	----

#### High Stability Supporting Platforms for Optical Communications

<i>F. Arévalo, E. Ozores, A. Bonet, J.-M. Andrés, J.-M. Larrauri (CASA, Space Division, Spain)</i> .....	39
--	----

#### The CMS Inner Tracker Barrel Mechanical Structure

<i>M. Price, B. Nicquevert, C. Hauviller (CERN)</i> .....	49
---	----

#### The Mechanical Structure of the Inner Tracker for ATLAS

<i>A. Fallou (CPPM, CNRS, France), E. Perrin (Univ. Genève, Switzerland), G. Tappern (Rutherford Appleton Lab., UK)</i> .....	59
---	----

#### Detailed Design and Manufacture of the Support Frames for a Transition Radiation Tracker Detector for the LHC

<i>J. Enz, G. Lippmann (DASA-Dornier GmbH, Germany)</i> .....	69
---	----

#### Inner Tracking System for ALICE: Conceptual Design of Mechanics, Cooling and Alignment

<i>G. A. Feofilov (St Petersburg State Univ., Russia), P. Giubellino, L. Riccati (INFN, Italy), J. Schukraft (CERN), V. M. Dobulevitch, V. M. Fedorov, O. N. Godisov, S. N Igolkin, M. I. Yudkin (Meson, St Petersburg, Russia), S. F. Gerasimov, I. A. Novikov, L. F. Vitushkin (Mendeleev Institute for Metrology, St Petersburg, Russia)</i> .....	77
---	----



<b>PART III. Materials .....</b>	<b>87</b>
High Specific Stiffness Beryllium and Beryllium Alloys N. F. Levoy, K. R. Raftery, R. L. White ( <i>Nuclear Metals Inc., USA</i> ) .....	89
High Dimensional Stability Structure: Continuous Fibre Metal Matrix Composites J.-F. Peltier, J. Pernon ( <i>Aerospatiale Espace et Défense, France</i> ) M. Rabinovitch ( <i>ONERA, France</i> ).....	97
High Performance Polyarylates under radioactive, cryogenic and high temperature conditions P. R. Fialla ( <i>ISONOVA, Austria</i> ) .....	105
Advanced Composite Stable Structures, Appropriate Materials for High Precision Detectors S. Robitaille, G. Patz, S. Johnson ( <i>YLA Inc., USA</i> ) .....	115
<b>PART IV. Materials and Environment .....</b>	<b>121</b>
The dimensional stability of composite laminates: sensitivity to gradients in fibre content and misalignment P. Kim, R. Phillips, S. Toll, J.-A. E. Månson ( <i>Lab. Tech. Composites, EPF Lausanne, Switzerland</i> ) .....	123
Interfacial Moisture Transport in Composite Materials W. Benhamida, H. Dumontet ( <i>Lab. de Modélisation et Mécanique des Structures, CNRS - Univ. Paris VI - ENSAM - ENS Cachan, France</i> ) A. Lekhder ( <i>CNRS Paris/Lab. de Mécanique et des Matériaux, Fac. Sciences, Rabat, Morocco</i> )	133
Radiation Effects on Structural Materials for High-Energy Particle Accelerators and Detectors H. Schönbacher, M. Tavlet ( <i>CERN</i> ) .....	139
Radiation resistant Epoxy Glass fibre Laminates W. Eichberger ( <i>ISOVOLTA, Austria</i> ) .....	147
Radiation resistance and other safety aspects of high-performance plastics by ERTA M. Tavlet ( <i>CERN</i> ), H. van der Burgt ( <i>ERTA-EPEC, Belgium</i> ) .....	157
<b>PART V. Manufacturing .....</b>	<b>169</b>
Influence of Processing Parameters on the Dimensional Stability of Polymer Composites R. Phillips, P. Kim, P. Sunderland, J.-A. E. Månson ( <i>Lab. Tech. Composites, EPF Lausanne, Switzerland</i> ) .....	171
Design and manufacture of an accurate composite piece M. Raymond, L. Martin, L. Lopez ( <i>CPPM - CNRS, France</i> ), F. Navarro, C. Esnault ( <i>B+, France</i> ) .....	179
A High Dimensional Stability Structures Verification Facility I. Cabeza, G. Galipienso ( <i>CASA, Space Division, Spain</i> ) .....	189
<b>PART VI. Index of Authors – List of Participants.....</b>	<b>195</b>



CERN 94-07  
25 October 1994

ORGANISATION EUROPÉENNE POUR LA RECHERCHE NUCLÉAIRE  
**CERN** EUROPEAN ORGANIZATION FOR NUCLEAR RESEARCH

International Workshop  
on  
Advanced Materials  
for  
High Precision Detectors

Archamps, Haute-Savoie, France  
28–30 September 1994

Proceedings

Editors: B. Nicquevert  
C. Hauviller

GENEVA  
1994



© Copyright CERN, Genève, 1994

Propriété littéraire et scientifique réservée pour tous les pays du monde. Ce document ne peut être reproduit ou traduit en tout ou en partie sans l'autorisation écrite du Directeur général du CERN, titulaire du droit d'auteur. Dans les cas appropriés, et s'il s'agit d'utiliser le document à des fins non commerciales, cette autorisation sera volontiers accordée.

Le CERN ne revendique pas la propriété des inventions brevetables et dessins ou modèles susceptibles de dépôt qui pourraient être décrits dans le présent document; ceux-ci peuvent être librement utilisés par les instituts de recherche, les industriels et autres intéressés. Cependant, le CERN se réserve le droit de s'opposer à toute revendication qu'un usager pourrait faire de la propriété scientifique ou industrielle de toute invention et tout dessin ou modèle décrits dans le présent document.

Literary and scientific copyrights reserved in all countries of the world. This report, or any part of it, may not be reprinted or translated without written permission of the copyright holder, the Director-General of CERN. However, permission will be freely granted for appropriate non-commercial use.

If any patentable invention or registrable design is described in the report, CERN makes no claim to property rights in it but offers it for the free use of research institutions, manufacturers and others. CERN, however, may oppose any attempt by a user to claim any proprietary or patent rights in such inventions or designs as may be described in the present document.

ISSN 0007-8328

ISBN 92-9083-066-2



ORGANISATION EUROPÉENNE POUR LA RECHERCHE NUCLÉAIRE  
**CERN** EUROPEAN ORGANIZATION FOR NUCLEAR RESEARCH

International Workshop  
on  
Advanced Materials  
for  
High Precision Detectors

Archamps, Haute-Savoie, France  
28–30 September 1994

# Proceedings

Editors: B. Nicquevert  
C. Hauviller

GENEVA  
1994



## Abstract

These *Proceedings* gather together the contributions to the *Workshop on Advanced Materials for High Precision Detectors*, which was held from 28-30 September 1994 in Archamps, Haute-Savoie, France.

This meeting brought together international experts (researchers, physicists and engineers) in the field of advanced materials and their use in high energy physics detectors or spacecraft applications. Its purpose was to discuss the status of the different *materials* currently in use in the *structures* of detectors and spacecraft, together with their actual performances, technological implications and future prospects. Environmental effects, such as those of moisture and radiation, were discussed, as were design and *manufacturing* technologies. Some case studies were presented.



# Welcome

The Haute-Savoie local authorities have been particularly pleased and honoured to welcome this Workshop in Archamps, an international location where synergies between research and industry are currently being developed.

Here, at the heart of the French Alps, the fields of electronics, particle physics, biotechnology and micromechanics have found a nice homeland. Leading industrial groups are present, such as Salomon, Eaton, Digital, Parker Hannifin, Dassault, Alcatel, Evian, Roche or Tefal. They benefit from one of the world's most digitized telecommunications network and realize why international exchange is so easy in Haute-Savoie.

Training and research are of a quality to meet the standards of the industrial tissue. For example, the Archamps French Geneva Campus provides further training in international management and post-graduate studies, while the Annecy Laboratory of Particle Physics works in tight cooperation with CERN in Geneva and participates in the development of the microelectronics sector.

If your preference lies more outdoors on hiking circuits or on the ski slopes, the Mont-Blanc mountain range, complete with the most impressive of glaciers, will certainly guarantee you endless hours of fresh Alpine air and enjoyment. All the polls that have been conducted show that Haute-Savoie is sought out by all those who wish to reconcile their professional life with their social, cultural and leisure activities.

Here, we know that science and research have constantly been a vast field for innovation and that innovation has changed our life. Come and join those who strongly believe that nothing could exist without the faith of researchers who are constantly committed to improve scientific research and innovation.

Roland PASCAL

General manager Haute-Savoie Administration  
President International Business Park





## Foreword

The Workshop on Advanced Material for High Precision Detectors, which has been held in Archamps, Haute-Savoie, France, from 28-30 September 1994, was the first one on this highly technological subject. Its success was above expectation: more than one hundred registration forms have been received, but unfortunately, it was technically impossible to accept all of them. There was 86 participants, coming not only from CERN member states, but also Russia, the USA and Canada.

The design goal of the central parts of the High Energy Particle Physics detectors, the so-called *trackers*, is to achieve a measurement accuracy at the micron level over a large detection volume of many cubic metres.

The principal sources of errors are caused by the structures: material creates unwanted background and a lack of stability impinges on the positioning of the detecting elements. Optimisation leads to a choice mainly governed by a high specific modulus (similar to aerospace): composites (non-metallic and metallic matrices); or advanced light materials (beryllium and its alloys, foamed ceramics, ...).

The hostile environment leads to major concerns about the micron level stability of the structures: ionizing radiations up to  $10^6$  gray, temperature gradients, humidity transients,... together with inherent mechanical behaviour: internal stresses, creep, etc...

The Workshop was divided into three main parts.

- *structures* used for detectors or spacecraft applications;
- *materials* and their behaviour in the detectors' environment;
- *design*, optimization and *manufacturing* technologies.

The aim of the workshop was to gather engineers, researchers and scientists to sum up the state-of-the-art, and to determine ways for future development.

The Workshop has been locally organized by the Technical Assistance Group 1 of the Particle Physics Experiments Division at CERN. It received help from the Conseil Général de la Haute-Savoie and especially from the team of the International Business Park, and we would like to thank them for their support.

The efficient help and advice from the members of the Organizing Committee should also be warmly acknowledged.

Claude HAUVILLER  
Chairman of the Organizing Committee



# Workshop Organization

## Organizing Committee

A. Fallou	CNRS (CPPM), Marseille
C. Girard	CNRS (LAPP), Annecy
C. Hauviller	CERN (Chairman)
B. Nicquevert	CERN (Secretary)
E. Perrin	Université de Genève
M. J. Price	CERN
H. Schönbacher	CERN
G. Tappern	Rutherford Appleton Lab.
T. Thompson	Los Alamos National Lab.

## Workshop Secretariat

Sue Cousins  
Sandrine Sciarrino

## at the International Business Park

Stéphane Bérard  
Valérie Guichet

## Edition of the Proceedings

with the help of  
the CERN Desktop Publishing Centre

## CONTENTS

### Foreword

<i>C. Hauviller (CERN)</i> .....	vii
----------------------------------	-----

### PART I. Generalities ..... 1

#### Advanced Materials for High Precision Detectors

<i>C. Hauviller (CERN)</i> .....	3
----------------------------------	---

#### The Use of High Stiffness Material and Dimensionally Stable Materials in Spacecraft Applications

<i>D. Bashford (ERA Technology Ltd, Leatherhead, UK), D. Eaton, A. Pradier (ESA/ESTEC, Noordwijk, The Netherlands)</i> .....	9
--	---

#### Recent Developments in Low Cost Stable Structures for Space

<i>T. C. Thompson, C. Grastataro, B. G. Smith (Los Alamos Nat. Lab., USA)</i> .....	21
---	----

### PART II. Structures ..... 31

#### Highly Dimensional Stable Composite Structures

<i>G. Helwig (DASA-Dornier GmbH, Germany)</i> .....	33
---	----

#### High Stability Supporting Platforms for Optical Communications

<i>F. Arévalo, E. Ozores, A. Bonet, J.-M. Andrés, J.-M. Larrauri (CASA, Space Division, Spain)</i> .....	39
--	----

#### The CMS Inner Tracker Barrel Mechanical Structure

<i>M. Price, B. Nicquevert, C. Hauviller (CERN)</i> .....	49
---	----

#### The Mechanical Structure of the Inner Tracker for ATLAS

<i>A. Fallou (CPPM, CNRS, France), E. Perrin (Univ. Genève, Switzerland), G. Tappern (Rutherford Appleton Lab., UK)</i> .....	59
---	----

#### Detailed Design and Manufacture of the Support Frames for a Transition Radiation Tracker Detector for the LHC

<i>J. Enz, G. Lippmann (DASA-Dornier GmbH, Germany)</i> .....	69
---	----

#### Inner Tracking System for ALICE: Conceptual Design of Mechanics, Cooling and Alignment

<i>G. A. Feofilov (St Petersburg State Univ., Russia), P. Giubellino, L. Riccati (INFN, Italy), J. Schukraft (CERN), V. M. Dobulevitch, V. M. Fedorov, O. N. Godisov, S. N. Igolkin, M. I. Yudkin (Meson, St Petersburg, Russia), S. F. Gerasimov, I. A. Novikov, L. F. Vitushkin (Mendeleev Institute for Metrology, St Petersburg, Russia)</i> .....	77
--	----

<b>PART III. Materials .....</b>	<b>87</b>
High Specific Stiffness Beryllium and Beryllium Alloys N. F. Levoy, K. R. Raftery, R. L. White ( <i>Nuclear Metals Inc., USA</i> ) .....	89
High Dimensional Stability Structure: Continuous Fibre Metal Matrix Composites J.-F. Peltier, J. Pernon ( <i>Aerospatiale Espace et Défense, France</i> ) M. Rabinovitch ( <i>ONERA, France</i> ).....	97
High Performance Polyarylates under radioactive, cryogenic and high temperature conditions P. R. Fialla ( <i>ISONOVA, Austria</i> ) .....	105
Advanced Composite Stable Structures, Appropriate Materials for High Precision Detectors S. Robitaille, G. Patz, S. Johnson ( <i>YLA Inc., USA</i> ) .....	115
<b>PART IV. Materials and Environment .....</b>	<b>121</b>
The dimensional stability of composite laminates: sensitivity to gradients in fibre content and misalignment P. Kim, R. Phillips, S. Toll, J.-A. E. Månson ( <i>Lab. Tech. Composites, EPF Lausanne, Switzerland</i> ) .....	123
Interfacial Moisture Transport in Composite Materials W. Benhamida, H. Dumontet ( <i>Lab. de Modélisation et Mécanique des Structures, CNRS - Univ. Paris VI - ENSAM - ENS Cachan, France</i> ) A. Lekhder ( <i>CNRS Paris/Lab. de Mécanique et des Matériaux, Fac. Sciences, Rabat, Morocco</i> ) .....	133
Radiation Effects on Structural Materials for High-Energy Particle Accelerators and Detectors H. Schönbacher, M. Tavlet ( <i>CERN</i> ) .....	139
Radiation resistant Epoxy Glass fibre Laminates W. Eichberger ( <i>ISOVOLTA, Austria</i> ) .....	147
Radiation resistance and other safety aspects of high-performance plastics by ERTA M. Tavlet ( <i>CERN</i> ), H. van der Burgt ( <i>ERTA-EPEC, Belgium</i> ) .....	157
<b>PART V. Manufacturing .....</b>	<b>169</b>
Influence of Processing Parameters on the Dimensional Stability of Polymer Composites R. Phillips, P. Kim, P. Sunderland, J.-A. E. Månson ( <i>Lab. Tech. Composites, EPF Lausanne, Switzerland</i> ) .....	171
Design and manufacture of an accurate composite piece M. Raymond, L. Martin, L. Lopez ( <i>CPPM - CNRS, France</i> ), F. Navarro, C. Esnault ( <i>B+, France</i> ) .....	179
A High Dimensional Stability Structures Verification Facility I. Cabeza, G. Galipienso ( <i>CASA, Space Division, Spain</i> ) .....	189
<b>PART VI. Index of Authors – List of Participants.....</b>	<b>195</b>





# Advanced Materials for High Precision Detectors

C. Hauviller  
CERN - PPE  
CH 1211 Geneva 23 - Switzerland

## Abstract

After some background on High Energy Physics (HEP) and the future accelerator and its detectors, tracking detectors principle are described. Sources of errors which impinge the resolution of these so-called trackers is then analysed. It is shown that to achieve a measurement accuracy at the micron level over a huge detection volume of many cubic meters, it is of a prime importance that the structures are as light as possible while providing a very high stability.

Optimisation leads to a choice mainly governed by a high specific modulus, similar to aerospace. But an hostile environment leads to major concerns on the micron level stability of these structures: ionizing radiations, temperature gradients, humidity transients, ... together with inherent mechanical behaviour: internal stresses, creep, ...

Therefore, can we achieve what is proposed for the future trackers?

This workshop is the occasion to share the existing information but it should be also a forum to get hints how to proceed for the future.

## 1. High energy physics and accelerators

To satisfy the constant quest of the physics community to look deeper into matter, more powerful accelerators are always requested.

Now, with the LEP machine, the latest and largest of CERN's accelerators, with a collision energy in the range of 200 GeV, we can probe the structure of matter down to the level of  $10^{-18}$  meter.

But new fundamental questions arose: yet undetected particle families leading to a better understanding of the dark matter in the Universe, why W and Z particles have such a high mass whereas photon is massless, ... and many ideas and scenarios for a better understanding of our so complex world. To get answers or at least clues,

we need to achieve one order of magnitude in resolution down to  $10^{-19}$  meter and that implies collision energies in the TeV range at the constituents level.

The LHC (Large Hadron Collider) is designed for that purpose [1]. This 27 km long proton-proton collider of 14 TeV centre-of-mass energy will recreate the conditions prevailing in the Universe just  $10^{-12}$  second after the "Big Bang" when the temperature was  $10^{16}$  degrees. But a high luminosity is also required to benefit from this increase of energy. The  $10^{34} \text{ cm}^{-2} \text{ s}^{-1}$  design luminosity of LHC leads to events generated by the collisions with a huge number of particles to be analysed in some nanoseconds and an unusual high radiation level.

To analyse in fine details such complex interactions, detectors will have millions of

measuring channels which should give accurate information on the mass, the charge, the momentum and the trajectory of each of the generated particles.

## 2. Detector

A typical detector for LHC, installed around one of the interaction points has an overall cylindrical shape with both a diameter and a length up to 20 meters. Weighting up to 15,000 tons, it consists basically of three subsystems embedded one inside the other like russian dolls: an inner detector or tracker, the calorimeters and completely enclosing the others the muon system. In addition, a magnetic field deflecting particles to measure charge and momentum, is generated by one (or more) powerful electromagnet.

If the precision is a major concern for all the elements of the detector, the more stringent specifications are found in the innermost part, the tracker.

## 3. Tracker

As most of all the present detectors, the measuring techniques of the tracking detectors are based on the ionization and excitation phenomena in gases and solids. Presently used detectors and candidates for future experiments will be subsequently presented.

### 3.1. *MultiWire Proportional and Drift Chambers*

The most common ones, the MultiWire Proportional Chamber (MPWC) and the Drift Chamber (DC) measure the ionization produced by a charged particle in a gas. Generated electrons produce a signal measured on precisely positioned wires.

The accuracy currently achieved with a MPWC is 600 microns and reaches 150 microns in the best cases. Performances of large DC ( $100\text{ m}^3$ ) are in the same range but could be improved to 30 microns for small volumes ( $1\text{ m}^3$ ).

However, the too high density of tracks at LHC leads to separation difficulties and the too slow drift time (occupancy around 100 ns) is incompatible with the LHC repetitivity rate of 25 ns.

### 3.2. *Strip detectors*

Momentum measurements and particle identification require now to be able to locate the particle trajectories in some cases at better than

the ten microns level. The more precise devices are the silicon or gallium arsenide or diamond strip detectors, the first ones being the most common ones. They are made of high resistivity doped silicon wafers, 300 microns thick. The two other types are based on the same principle with a different substrate, with the advantage of a better radiation resistance.

Narrow strips are ion implanted with a pitch of 50 microns or better. The electrical signal is measured at the strip end in less than 20 ns and the measurement precision is around 10 microns and even could go down to 3 microns. It is also possible to measure two coordinates with a double-sided detector or with an other type of device, the pixel detector where the electrodes are in the form of pads.

In the detectors presently taking data, this strip technology is only applied in rather small volumes, some cubic decimetres.

### 3.3. *Microstrip Gas Chambers*

Microstrip Gas Chambers (MSGC) are devices less accurate than silicon strips, used further away from the interaction point at radii usually greater than 50 cm. In this technology, the strips are implanted on thin glass plates with a pitch of 200 microns covered by a gas drift volume 2 to 5 mm thick. Accuracy achieved here is around 50 microns.

### 3.4. *Straw tubes*

An other evolution of the drift chambers is the straw tubes where the gas is contained in individual thin tubes of a diameter of some millimetres equipped with an axial measuring wire. Accuracy achieved here is presently of the order of 150 microns for a single straw and 50 microns for an array.

### 3.5. *Scintillating fibres*

Finally, to be complete, scintillating fibres should be mentioned. Fibres of a small diameter or even of hexagonal shape give also the possibility to reach an accuracy of the order of 50 microns.

## 4. Detection accuracy

If it has been possible to work at a resolution better than 10 microns in small detecting volumes, now the aim for the near future is to achieve almost the same precision inside huge volumes of tens of cubic meters. This step in the technology is obviously a major challenge.

#### 4.1. Sources of errors

To fully use the very high intrinsic resolution of the detecting elements, it is of the utmost importance not to spoil it in the fully assembled detector. Main sources of errors on the measurement of a particle trajectory can be summarized as the intrinsic resolution of the detecting element and its electronics, the multiple scattering created by all the materials used in the construction of the detector and the mechanical positioning and stability in the 3-dimensional space. The total resulting error is the r. m. s. of all these errors.

#### 4.2. Multiple scattering

Multiple scattering is caused by electromagnetic interactions with electrons and nuclei when traversing a medium. Loss of energy is small but large scattering is creating major errors in the momentum definition.

The r. m. s. scattering angle  $\theta_p$  is given by

$$\theta_p = \frac{0.014}{\beta p} \sqrt{\frac{L}{X_0}}$$

where

- $\beta = v/c$
- $p$  is the momentum, in GeV/c

•  $L$  is the length of material traversed by the particle

•  $X_0$ , radiation length, is a physical property of the material. Its approximate value, expressed in meters, is

$$X_0 = 7.16 \frac{A}{\rho Z(Z+1) \ln(287/\sqrt{Z})}$$

where

- $\rho$  is the density,
- $A$  is the atomic mass,
- $Z$  is the atomic number.

In first approximation,  $X_0$  is roughly inversely proportional to  $\rho Z$ .

#### 4.3. Positioning stability

The mechanical design of the structures is based on deflection and, usually, not on stress. To avoid any permanent deformations, the material should behave in its elastic range. A lot of vibration sources (pumps, motors, ventilation, ...) exist in an experimental hall and will undoubtedly generate displacements in the microns range. Therefore, it is necessary to maximize the rigidity which could be expressed in general terms as the product of the Young's modulus  $E$  by a length  $L$ .

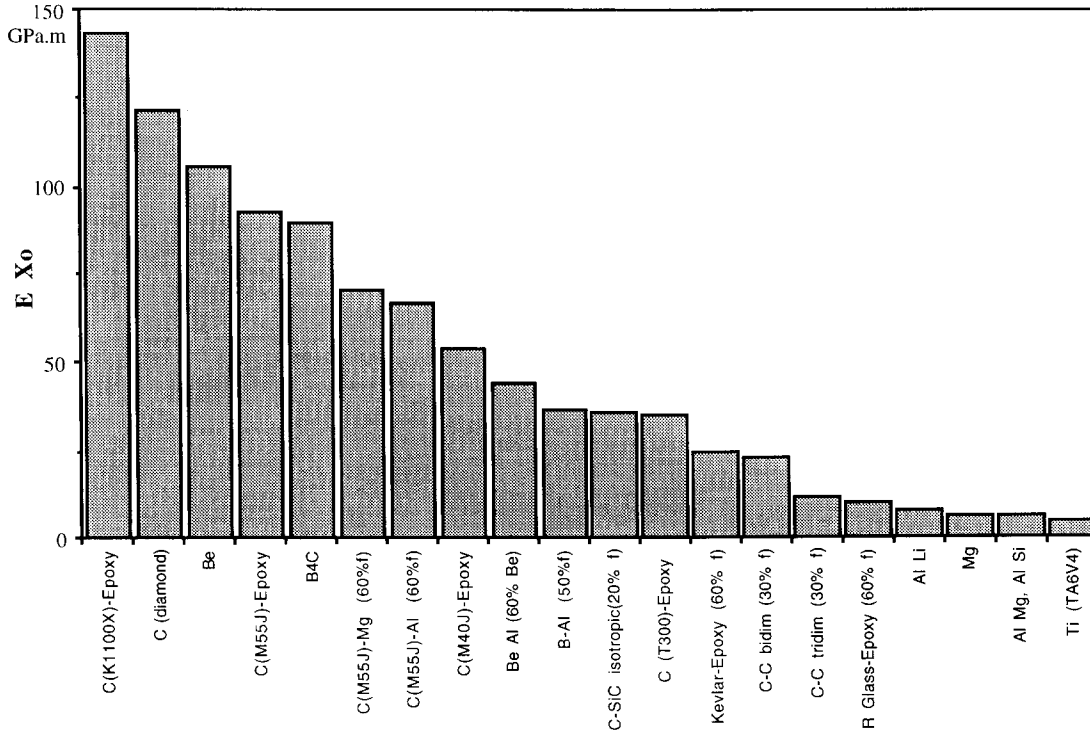


Figure 1.  $EX_0$  product for some materials

Taking into account the necessary minimisation of the multiple scattering, the previous product can be written as  $EX_0$ , an expression depending only upon the material. As a consequence, this product  $EX_0$  can be used as figure of merit for all the structural materials of the detectors and both the Young's modulus and the radiation length should be as high as possible. Figure 1 shows most of the best representatives of material families available on the market (unidirectional properties).

All these materials are also known for their high specific stiffness  $E/\rho$  and it is therefore obvious that the selection criterion  $EX_0$  will lead to a choice very similar to the one for aeronautics and aerospace.

## 5. Environment

A stiff structure will not necessary be stable, especially if the environmental conditions are too harsh. For the trackers, one should take into account the radiations, the temperature, the humidity and the macroscopic phenomena related to time, and possible coupling effects between them.

### 5.1. Radiations

The very high luminosity of the LHC will generate a high radiative environment inside the detectors, largely above the present level. The expected fluences inside the tracker volume are, for an integrated luminosity of  $10^{42} \text{cm}^{-2}$  (ten years of LHC running at nominal conditions),

$$\Phi_{\text{charged}} = \frac{1.3 \times 10^{17}}{r^2} \text{cm}^{-2}$$

$r$  in centimetres giving an integrated dose up to the megagray range,

and

$$\Phi_{\text{neutron}} = 3 \times 10^{13} \text{cm}^{-2},$$

constant inside the volume.

This large radiation doses can be easily withstood by metals but may become prohibitive for most of the standard plastics in the innermost layers of the detectors. Behaviour of composites in these conditions is neither so well understood and, if it is generally admitted that common resins withstand higher doses, it has not been demonstrated that micron level movements will not spoil the dimensional tolerances and moreover that the other environment conditions will not even be coupled, worsening the situation.

### 5.2. Temperature

The temperature range inside a tracker is quite limited: room temperature around  $20^\circ\text{C}$  except for the central region where a temperature around  $0^\circ\text{C}$  is foreseen to minimise radiation effects on silicon strip detectors. But temperature stabilisation on such large volumes cannot be achieved better than at the degree range; these even small temperature variations will generate displacements larger than tens of microns on metallic structures due to their large values of the coefficient of thermal expansion (CTE). On the other hand, carbon fibres with an almost zero CTE could be a better basis to solve this problem.

### 5.3. Humidity

Up to now, humidity is only partially controlled: the dew point is always kept high enough to avoid condensation on the coldest parts of the detectors. But in-situ measurements have shown humidity variations between 20% and 80%, close to the atmospheric conditions. Metals are insensible to these transients but is there a way to get an acceptable stability of a composite structure, avoiding fibres sensitive to humidity and using hydrophobic resins or putting leak-tight protective layers? Or is it necessary to specify a better (and expensive) humidity control inside the experimental cavern?

### 5.4. Macroscopic phenomena

Materials properties could also change with time: creep occurs even at a low load level, internal stresses built-in during the manufacturing process relax more or less quickly, micro-cracks propagate slowly, ... Moreover, in the case of a gaseous detector, a very limited outgassing is compulsory to avoid any pollution of the highly purified detecting gases.

## 6. Which material?

In résumé, an acceptable material for a tracker should be:

- light (high  $X_0$ ),
- stiff (high  $E$ ) (structural material),
- radiation resistant (radiation index  $> 6$ ),
- insensitive to temperature variations (low CTE),
- insensitive to humidity variations (low coefficient of moisture expansion CME, and moisture absorption),
- stable with time.

It is not very surprising to find again that all these requirements are more or less present in the materials selection criteria for aerospace structures [2]. But a unique solution has not been found yet. Each material family has his own defenders.

The best compromise depends more on the relative priority set between the different criteria. But this material choice should also be directed largely by other major factors :

- the way to tackle the safety problems,
- the availability of the material in rather small quantities,
- the ability of the industry to process it,
- and last but not least, the final cost of the manufactured parts.

## 7. Conclusion: going ahead

An approach of cost-effective design has led to acceptable solutions for space, but can we fulfil the specifications set for the future trackers? This workshop should at least give clues to answer this question.

The first step is to understand what has been done and what is going on in this field. The presentations are intended to answer most of the major points:

- stable structures for spacecrafts and detectors,
- materials available and the environmental effects,
- design and manufacturing.

But the second step is to obtain a cross-fertilisation of the ideas from all the participants, engineers, researchers, scientists coming from industries, universities and research centres.

We have similar problems and therefore a common interest. We should share existing information and, why not, define and proceed to common development work.

- Do we know all the available materials?
- Do we know enough about their behaviour?
- Is it possible to transform our dreams into real parts?
- What sort of surprises could we expect? ...

This is now time to understand that, even with our scarcer resources, we could succeed to build reliable structures at the uppermost limit of the technologies.

HEP community has definitively one more common interest with the Space community, the Lightweight Structures; and one could expect that, in the near future, the loop will be closed when sophisticated particle trackers will be sent into space to study matter far from all the perturbations of our Earth.

## References

- [1]. LHC, *the Large Hadron Collider Accelerator Project*, CERN/AC/93-03, Nov. 1993.
- [2]. *International Workshop on Advanced Materials for Lightweight Structures '94* - 22-25 March, 1994 - ESA-ESTEC, Noordwijk, The Netherlands

# The Use of High Stiffness Material and Dimensionally Stable Materials in Spacecraft Applications

David Bashford  
ERA Technology Ltd, Leatherhead, UK  
&  
David Eaton, Alain Pradier  
ESA/ESTEC, Noordwijk, The Netherlands

## Abstract

This paper looks at the historical use of high stiffness materials in spacecraft constructions and the benefits they provide. The space industry remains reluctant to change from proven materials of construction but is gradually being forced to as mission specifications become more ambitious and exacting with respect to dimensional stability. The motivation to adopt new material technologies is also being driven by increases in design-life requirements from the accepted 5 - 7 years to those approaching 30 years in orbit. Carbon fibre reinforced epoxy composites are now accepted as the baseline materials for dimensionally stable structures. To these we now need to add: cyanate ester composites, sandwich panels with carbon or aramid composite cores and the emerging metal or ceramic matrix composites. Typical potential applications include antennas, reflectors, mirrors, optics, cameras and telescopes.

## 1. Introduction

Dimensionally stable structures are those which are required to retain their physical shape and dimensions under the thermal cyclic conditions experienced in orbit, typically  $-150^{\circ}\text{C}$  to  $+100^{\circ}\text{C}$ . The requirement to hold dimensional tolerances is becoming more exacting for the following reasons:

- ♦ Structures are becoming larger
- ♦ Signal frequencies are becoming higher
- ♦ Optical devices demand tighter tolerances

Each mission and structure has its own requirements, which is why no single material can meet all requirements. The material options are discussed with respect to the intended applications.

Where appropriate, examples are given of ESA/ESTEC funded support to the development of dimensionally materials and structures.

## 2. Basic Requirements of Materials

All the materials discussed have a structural, load bearing function to perform sometime during the mission [1,2]. The desired characteristics are:

- ♦ High stiffness to weight ratio
- ♦ Low, stable CTE
- ♦ Inert to space environments

Application specific needs may include:

- ♦ High thermal conductivity
- ♦ Non-electrical conductance (signal transparent)

## 3. Material Options

Low CTE is a primary driver to materials selection. In this respect, carbon fibres, and to a lesser extent aramids, become the accepted starting point as the reinforcing phases for composites. These composites



are used in laminate form, either by themselves or as faceskins for sandwich panel constructions. These fibres are principally used with epoxy thermosetting resins but other thermosets, and thermoplastics, can be realistically used if the commercial motivation exists. Carbon fibres can also confer low CTE on metal and ceramic matrix composites. The options available [1] can therefore be listed as:

UHM Carbon Fibres: eg Toray M55J/M60J, Mitsubishi Dialed K135/K137/K139, Nippon Granoc XN-50/XN-70.

Aramid Fibres: eg Kevlar 49/149, Twaron HM.

Sandwich core materials: eg Al, CFRP, ARP.

Metal Matrix Composites (MMC): eg C/Al, C/Mg.

Glass and Glass-Ceramic Matrix Composites.

Ceramic Matrix Composites: C/SiC.

The continued commercial availability of materials and process technologies is of keen concern to the space industry due to the low volumes of material consumed.

## 4. Composite Anisotropy

Carbon fibres possess zero, or slightly negative, CTE in the axial ( $0^\circ$ ) direction. In the transverse ( $90^\circ$ ) direction, the CTE is positive and large. All matrices of whatever type have positive CTEs to some degree. Composites will exhibit CTE anisotropy in that the fibres cannot be placed in all orientations. The CTE can therefore be controlled in preferred orientations but not in others. The through-thickness CTE of cross-ply laminates will be highly positive.

For antennas and reflectors, minimum gauge sections are required, often defining a need to use thin CFRP unidirectional (UD) or fabric prepregs.  $0^\circ/90^\circ$ , 4-ply UD laminates are popular with an overall thickness of  $250\mu\text{m}$ , or equivalent thickness in fabric.

To control through thickness CTE the use of 3-D fibre preforms, eg for MMC and CMC, is feasible if the application demands it and can allow sufficient depth of section, as in mirrors.

## 5. Sandwich Constructions

A sandwich construction offers the ability to produce very rigid structures with the minimum amount of

mass [1]. Minimum gauge facesheets are permissible, typically of the  $0^\circ/90^\circ$  construction noted above. The available choice of core material has increased in recent years. For brevity, the following broad classifications are given, with their attendant features:

### 5.1 Aluminium Honeycomb

This is the most popular, largely because it is readily available in many sizes (cell shape, cell size and thickness) and offers good shear/compressive properties. Aluminium possesses good thermal conductivity which assists when there is a difference in temperature between sandwich faces.

Detraction: High positive CTE, which in turn is conferred on the through thickness direction of the sandwich panel.

### 5.2 CFRP Honeycomb

This is now more frequently used when the through thickness CTE of the sandwich must be kept low and controlled.

Detractions: It is costly and available in few forms unless specifically fabricated. Less robust than aluminium and difficult to machine.

### 5.3 ARP Honeycomb

Aramid fibre composite cores are occasionally used where electrical insulation requirements (signal transparency) negate the use of aluminium or CFRP.

Detractions: Poor compressive/shear strength. Prone to moisture absorption. Very difficult to machine. Limited availability and costly.

## 6. Space Environments

The missions for dimensionally stable structures vary depending on whether they orbit the earth or are interplanetary (deep space). There are various earth orbits each with their own environments:

Low Earth Orbit (LEO), circa 500 km altitude - (Space Shuttle/Space Station regime): Acute thermal cycling; atomic oxygen (AO) erosion; Vacuum Ultra-Violet (VUV); Micrometeoroid and debris impact.

Geo-Stationary Orbit, circa 36000 km altitude - High vacuum; wide temperature spectrum; reduced number of thermal cycles; radiation degradation possible.

The principal concerns for composites used in dimensionally stable structures are [1]:

### 6.1 Outgassing

All materials used in space have to pass ESA PSS-01-702 on minimum outgassing requirements with respect to total mass loss and condensable volatile material. All materials identified in this paper will achieve this. However, the consequences of outgassing for highly dimensionally stable structures goes beyond this requirement. In this respect the following comments are most pertinent to polymer composites.

The moisture content of epoxy CFRP materials is fairly low, circa 1% fully saturated. Satellite constructions are manufactured and stored under controlled humidity conditions to keep moisture absorption as low as possible. Problems can arise when antennas and reflectors are calibrated in these stored conditions prior to being launched. In orbit, the absorbed moisture is outgassed and a small change in the dimensions of the structure occurs. Often, such changes could be ignored, however this may no longer be the case in the future. There is therefore a motivation to specify CFRP and ARP materials where the matrix phase is less prone to moisture absorption. The Coefficient of Moisture Expansion (CME) is increasingly deemed an important parameter in defining the acceptance of a composite material. Newer generation epoxies and the more recent cyanate esters have come to prominence in offering low CME values.

MMC and CMC materials do not have constituents that will outgas.

### 6.2 Thermal Cycling

Severe and repetitive thermal cycling is a significant mechanism for inducing microscopic cracking in polymer composites. The occurrence of microcracking results from residual stresses in the matrix exceeding the strength of the matrix or matrix/fibre interface. Microcracking principally occurs on the cooling part of the cycle, and is driven by the high positive CTE of the matrix, in comparison with the low/negative axial CTE of the fibre. The choice of matrix is usually influenced by the maximum anticipated operating temperature, which defines the minimum acceptable matrix glass transition temperature ( $T_g$ ) and in turn the cure temperature. The temperature at which residual stresses are retained in the matrix is directly linked to the cured resin  $T_g$ . The minimum temperature on the

thermal cycle is the primary reason for microcracking, ie  $-180^\circ\text{C}$  is more severe than  $-150^\circ\text{C}$ . Therefore high cure temperatures and extreme low temperature in service represent the conditions most conducive to microcracking. It has been established that wherever possible the following should be implemented to reduce the occurrence of microcracking:

- ♦  $130^\circ\text{C}$  curing, as opposed to  $170^\circ\text{C}$ , is preferable.
- ♦ Use toughened, high strain matrices, eg cyanate esters.
- ♦ Avoid acute angle fibre crossovers, eg  $0^\circ/90^\circ$ ,  $\pm 45^\circ$ . Where possible  $\pm 30^\circ$  and  $\pm 60^\circ$  are preferable.

This said, it is not always possible to achieve these criteria. It is also in the nature of composites, that the fibre/matrix interface plays an important role in determining the susceptibility of a composite to microcracking. Some fibre/matrix combinations offer better interfacial adhesion than others which is translated into higher transverse ( $90^\circ$ ) ply strengths.

When microcracking occurs, the majority are intralaminar, ie within a single UD ply. Microcracking is deemed more serious when crack densities (population) are high or when cracks join up. Interlaminar cracking (between plies) and cracks which traverse two plies are deemed more serious. A commonly used criteria for comparing materials is the number of cracks per unit length of conditioned composites, ie post thermal cycling. Those with 0 to 5 cracks/cm are deemed more desirable than those with higher populations, eg 15 to 20+ cracks/cm.

In some applications, the entire structure is thermally cycled prior to launch to deliberately induce microcracking prior to calibration. The effectiveness of this is based on the assumption that the majority of microcracking occurs in the first few (up to 10) cycles that a structure encounters. This does make sense for some applications, however, structures experiencing 30000, or even 150000+ cycles, may never reach an equilibrium condition after the initial cycles. For very highly dimensionally stable structures, a non-equilibrium state may be very significant. Microcracking behaviour is very dependent on laminate lay-up and thickness.

### 6.3 Radiation Damage

Orbiting composite structures experience radiation dosages from various sources [1]. Unreinforced polymers are modified by radiation which results in

embrittlement after prolonged exposures. Composites on the other hand experience immediate surface degradation in the matrix phase. The surface reinforcing fibres do however screen the radiation to inhibit bulk degradation to the composite. It is therefore reported that modifications to the mechanical properties of CFRP are very small, ~5%, and difficult to discern. Measurement of CTE values also show little change. There is however some evidence to suggest that very high dosages, >1000 MRad, of penetrative radiation may significantly change mechanical properties and CTE. This is not a well studied area, but may have significance as missions become longer, approaching 30 years.

MMC and CMC materials do not have constituents that are degraded by radiation.

#### **6.4 Low Earth Orbit**

Examination of composite specimens flown on the Long Duration Exposure Facility (LDEF) from 1985 to 1990 revealed that CFRP will erode significantly under AO flux. It is therefore accepted that CFRP will need to be coated for protection on those surfaces experiencing the highest flux. The erosion of material has a direct effect on both mechanical properties and CTE as surface material is physically lost. In addition, accumulated damage from debris and micrometeoroid impacts should not be underestimated, to the point where selective protective shielding may need to be specified.

MMC and CMC have matrix phases that are more capable of resisting long-term LEO exposure.

#### **6.5 Surface Coatings**

The application of coatings to polymer composites should be undertaken as a last resort because of difficulties in obtaining reliable adhesion. The following circumstances may dictate a need to apply protective or surface modifying coating:

- ♦ to inhibit moisture absorption, eg metallic barrier.
- ♦ to inhibit AO erosion, eg silicon containing polymer coating.
- ♦ to provide thermal control, eg paints.
- ♦ to provide a reflective coating, eg sputtered metal.
- ♦ to provide continuity of electrical conductivity.

### **7. Adhesive Bonding and Joints**

The issue of jointing techniques is an important one for dimensionally stable structures, as a connection between components can be a significant source of expansion [3,4]. Adhesively bonded metallic end connections are attractive for tubular structures, because they can be made very strong and mass efficient. If however the high CTE of metals, such as aluminium and titanium alloys cannot be tolerated, then joint connections can be made with CFRP clam-shell designs for instance.

Adhesive bonding has an important role to play in satellite and spacecraft assemblies [3]. The selection of an acceptable adhesive is driven not only by mechanical performance requirements of the joint but also on compatibility with space environments.

### **8. UHM CFRP Prepregs**

For satellites, the requirement for high stiffness/low mass drives material selection towards ultra-high modulus (UHM) carbon fibre composites. The space industry does not consume much of these materials, so commercial availability can become a problem. In 1993, an industry accepted standard fibre, Celanese GY70, was withdrawn from the market. GY70 had poor strength and low strain to failure which could be improved on by newer generation Japanese fibres. This promoted a search for replacements, which at the same time was coupled with a wish to replace first generation epoxy prepregs for resins with lower moisture absorption and reduced susceptibility to microcracking. In an ESTEC supported study (1993/94) on microcracking behaviour [5], those companies participating showed a preference to use the following prepreg materials:

- ♦ Vicotex M18/Toray M55J
- ♦ Cycom 950-1/M55J
- ♦ Fiberite 934/M55J
- ♦ RS3 (Cyanate Ester)/XN-50A or M55J

The exercise confirmed a residual preference amongst many to retain epoxy prepregs for immediate requirements. However, the cyanate ester systems, including Fiberite 954-3, will continue to be developed and as such will be noted later. European space hardware is already being made with cyanate ester composites. The study revealed that microcracking behaviour was very dependent on how individual contractors processed the respective prepregs. The issue of processing techniques was so strong as to camouflage any individual merits on

which material offered the best resistance to microcracking.

The pitch based UHM fibres, eg XN-50/XN-70 and K137/K139, offer very high thermal conductivities which may be deemed essential in some applications. Toray M55J, a PAN-based fibre, has a much lower thermal conductivity but superior strength and wide commercial availability, making it suitable for structural configurations.

## 9. MMC and CMC Materials

Metal and ceramic matrix composites have not as yet been applied in significant quantities in space programmes. In some respects, these materials were originally developed for purely structural functions, sometimes at high temperatures [1]. Their use in dimensionally stable applications is now proposed largely as a means of avoiding the instabilities already discussed for the well used polymer composites. Present MMC and CMC technology is characterised by the following :

- ♦ They are very costly.
- ♦ Expertise in manufacture is limited.
- ♦ They are difficult to machine and fabricate.
- ♦ Their microstructures are very complex, as are the failure mechanisms.
- ♦ Mechanical and physical property data is lacking.

The rest of the paper will seek to concentrate on their attributes.

### 9.1 Metal Matrix Composites

For dimensionally stable applications, carbon fibre reinforcement is essential, either with magnesium or aluminium alloys. The use of a metal matrix removes any concerns relating to CTE changes by outgassing, moisture absorption and radiation damage. For carbon fibre MMC material the emphasis of controlled CTE behaviour centres on enhancing fibre/matrix interface strength and reducing residual stresses caused by high process temperatures. The anisotropy of the composite means that CTE in transverse and through thickness directions are still matrix dominated. There are attendant problems associated with matrix creep and microcracking at fibre/matrix interfaces.

Some credence can be given to particulate reinforced aluminium alloys where very low CTE is not essential. The particles will suppress the high CTE of

aluminium whilst the composites retains good thermal conductivity.

## 9.2 Ceramic/Inorganic Matrix Composites

The attraction of these stiff materials, is the relatively low, positive CTE of the matrices ( $3$  to  $10 \times 10^{-6} \text{ }^\circ\text{C}^{-1}$ ) coupled with their complete environmental stability under space orbit conditions. Again, carbon fibres are essential if zero CTE constructions are to be made. The immediate realistic options for commercial development lie with glass (eg borosilicate), silicon carbide or carbon matrix composites. This judgement is largely made on the availability of commercial materials expertise within Europe.

## 10. Application Requirements

Each application will have its own individual requirements. These can be highlighted so as to indicate which materials may be suitable for their construction.

### 10.1 Antennas and Reflectors

These need to be :

- 1) Lightweight; storable for launch; and sustain launch loadings/acoustic environment.
- 2) Deployable in space to their full dimensions and sustain the orbit environment for the design life required.

The performance of antenna reflectors is dependent upon their dimensional stability, as in Figure 1.

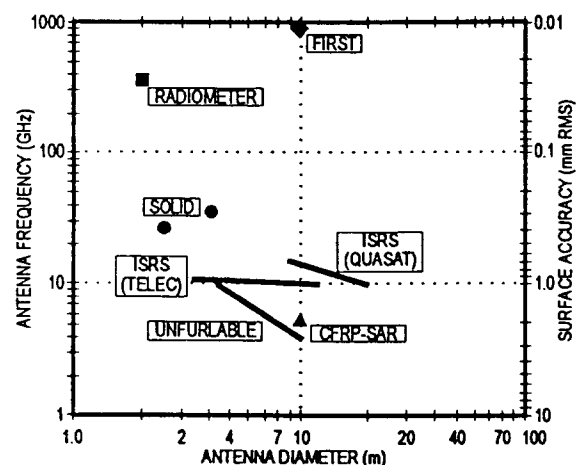


Figure 1. Antenna Surface Precision and Usable Frequency versus Size [1].

The composites used in lightweight antenna constructions can be differentiated as:

- ♦ Sandwich structures : for high accuracy and high natural frequencies.
- ♦ Monolithic structures : for highly loaded, compact parts.
- ♦ Framework structures : for voluminous, high stiffness structures, typically with jointed tubes.

To highlight recent structures, the following examples are given of European projects, some with details of the structure [1]:

#### DEPLOYABLE REFLECTORS

- *Contraves Inflatable Space Rigidised Reflector*

- Concept: Inflatable space rigidised.
- Construction: Thermally cured resin with Kevlar fabric and metallised Kapton.
- Application: From 5 to 20m diameter, and from 20 GHz to 800 MHz.
- Precision: 1 mm RMS.
- Reflector density: 0.4 kg/m<sup>2</sup>.

#### SOLID DEPLOYABLE REFLECTORS

- *Dornier Daisy*

- Concept: Deployable rigid-panel reflector.
- Construction: Sandwich panels with CFRP skin and 40 mm Kevlar core.
- Application: 8 m diameter at 3000 GHz.
- Precision: 8  $\mu$ m RMS.
- Reflector density: 6 kg/m<sup>2</sup>.

- *SELENIA Hinged Tip Reflector*

#### SOLID REFLECTORS

- *CASA 11/14 GHz Reflector*

- Concept: Largest one-piece reflector within ARIANE IV shroud.
- Construction: Sandwich rib-stiffened structure with CFRP skin and 8 mm Al honeycomb.
- Application: 3.1m x 2.3 m dimension and 11/14 GHz frequency.
- Precision: 0.4 mm RMS.
- Reflector density: 2.8 kg/m<sup>2</sup>.

- *MBB Polarisation Sensitive Reflector*
- *ERA Dichroic Sub-reflector*
- *CSELT/SELENIA Dichroic Sub-Reflector*

- *CASA Radiometer*

#### PLANAR ARRAYS

- *Dornier CFRP SAR Reflector*

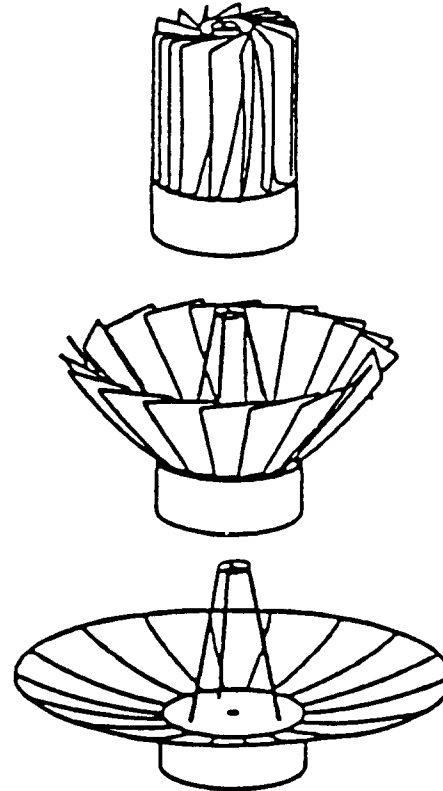


**Figure 2 : Dornier Daisy**

### **10.2 Mirrors and Optics**

Mirrors by necessity have to be very stiff and have reflective surfaces. Traditionally, monolithic materials such as low expansion glasses have been used, eg ZERODUR. These materials however have modest specific stiffness resulting in heavy designs. Some MMC and CMC materials can improve on this by giving lightweight constructions [6]. The materials studied include particulate MMCs, Mg/C, Al/C, borosilicate/C, C/SiC and C/C.

### **10.3 Cameras and Telescopes**

These contain the mirrors and optics arranged in the desired configuration. Around these items there is a support structure and enclosure. As with antennas, the support structure has to survive launch and provide the necessary thermal and dimensional control when on orbit. Recent examples of launched structures include:

- ♦ Hubble Space Telescope
- ♦ Mars Observer Camera

The support structure and enclosure is typically in CFRP material. Sometimes a mixture of UHM and HS CFRP is used to balance the structural and CTE requirements.

## 11. European Programmes

The following are recent or incomplete European projects demonstrating the use of advanced material technologies:

### 11.1 MBB Unfurlable Mesh Antenna Reflector (UMA)

This was developed in the late 1980s by MBB to meet Canadian M-SAT requirements. The basic construction is that of a 'double-hinged umbrella' and was as follows:

- ♦ The reflector surface consisted of a knitted gold-plated Mo-wire mesh tensioned by 8 foldable CFRP main ribs and 8 intermediate ribs.
- ♦ The main ribs were hinged to a central hub made of CFRP sandwich, which carried a deployment and retraction actuator in its centre.
- ♦ In the deployed position the straight main ribs were locked and inner- and outer ribs adjusted to each other under certain angles. Mesh adjustment to the required parabolic surface was then achieved by stand-offs along the rib parts.
- ♦ The parabolic contour between the main ribs was achieved by the intermediate ribs (CFRP ribbons) which were tensioned during deployment by means of cables leading to the main ribs.

The reflector was designed for high stiffness providing for eigen frequencies of 4 Hz deployed and > 35 Hz stowed for launch. The aperture diameter was 5 m, with a focal length of 3.125 m. Precision was from 0.2 to 0.7 mm RMS.

### 11.2 High Stability Telescope Structures

A study by CASA was completed in 1992 to address the requirements for telescope support structures [7]. These are characterised by:

- ♦ A requirement for very accurate pointing

- ♦ Large physical dimensions
- ♦ Attached telescope and components are of greater mass than the supporting structure itself.

Previous structures such as the Large Space Telescope (L.S.T) and Grazing Incidence Solar Telescope (GRIST) were evaluated. This resulted in a basic specification for the study of:

- ♦ Geometry: 3 m diameter, 6 m high truss structure, built-up of a 4m high cylinder section and a 2 m high conical section and upper diameter of 1.5 meters, as given in Figure 3.
- ♦ Stiffness: Minimum frequencies 35 Hz (axial) and 15 Hz (lateral)
- ♦ Temperature range: +123°C to -100°C
- ♦ Global CTE:  $0.2 \times 10^{-6} \text{ }^{\circ}\text{C}^{-1}$ , ideally with a zero CTE structure ( $< 10^{-8} \text{ }^{\circ}\text{C}^{-1}$ )
- ♦ Material requirements: high microyield strength and low microcreep

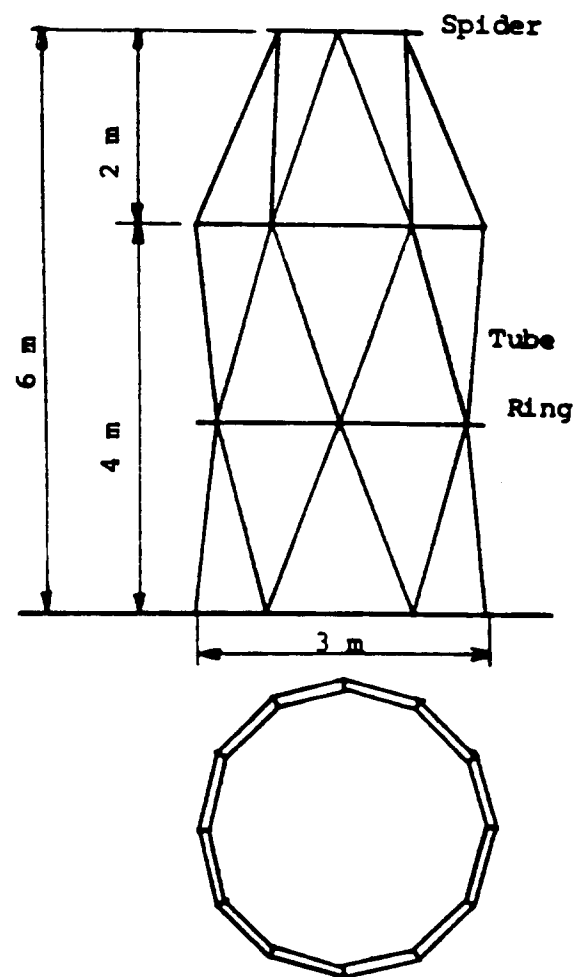


Figure 3. HSTS Demonstrator [7].



The requirements dictated that the structure had to be made of CFRP. A truss-structure configuration was developed with CFRP material tailored for each component including: rings, tubes, panels and joints. The latter either being slotted tubes, rigid connecting plates (gusset) or bonded clips (tube and ring clips). Two typical joint configurations are shown in Figures 4 and 5.

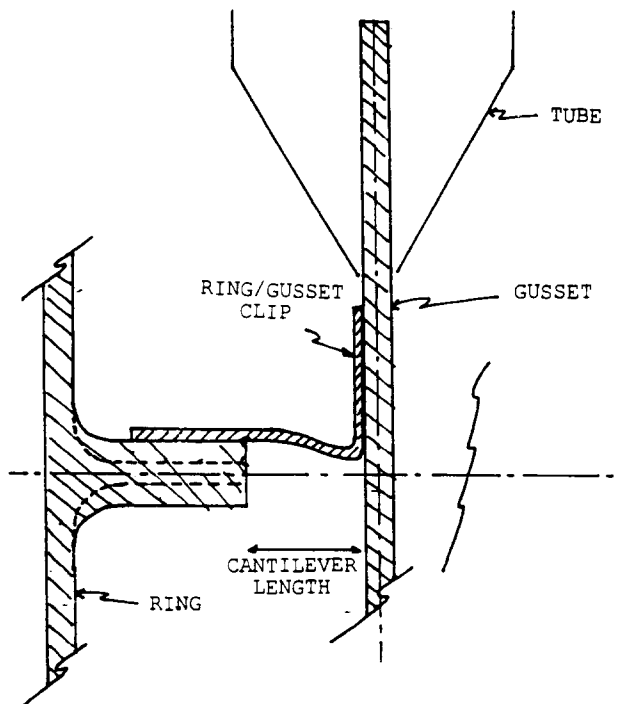


Figure 4. HSTS Gusset and Tube Clips [7].

### 11.3 SILEX and Isostatic Mounts

The Semiconductor Laser Inter-satellite Link Experiment (SILEX) is a revolutionary laser data-relay payload [8]. This will be part of the technology demonstrator to the fore-runner of commercial satellite phone networks. The laser systems requires optics for transmissions between satellites and hence very stable structures, assemblies and platforms are required.

A study was carried out by CASA to define the construction of a demonstrator Isostatic Mounting

Platform (Optical Head Bench). The OHB attachment was required to absorb distortions caused in the carrier structure by thermal cycling. The study concluded that the structural and dimensional stability requirements could only be met by using a sandwich concept with CFRP skins and a CFRP core, as shown in Figure 6. A compromise was reached to find the optimum skin thickness and core depth.

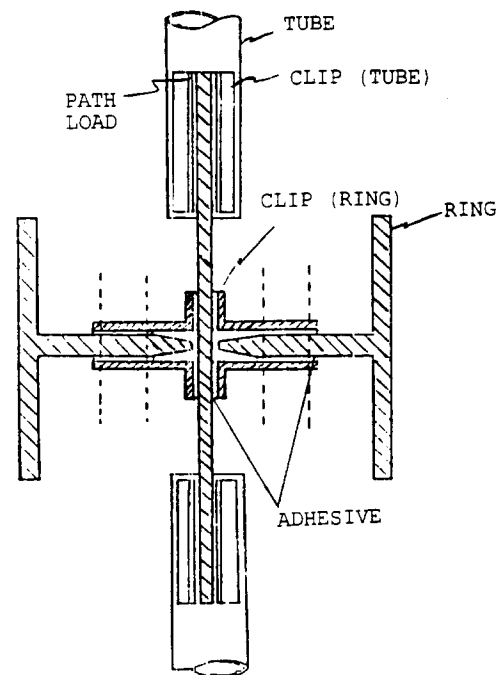


Figure 5. HSTS Joint Configuration [7].

The OHB consisted of a bench plate and isostatic attachment device. The basic constituents can be summarised as:

Baseplate: Skins and core of GY70/Code 87 in  $(0^\circ, \pm 60^\circ)_s$  construction bonded with Hysol EA 9394.

Inserts: Invar.

Attachment devices from baseplate to carrier structure: Titanium Ti 6Al 4V.

Optical unit isostatic attachment devices from optical units to optical bench: GY70/Code 87  $(0^\circ, \pm 60^\circ, \pm 45^\circ)_s$  plates.

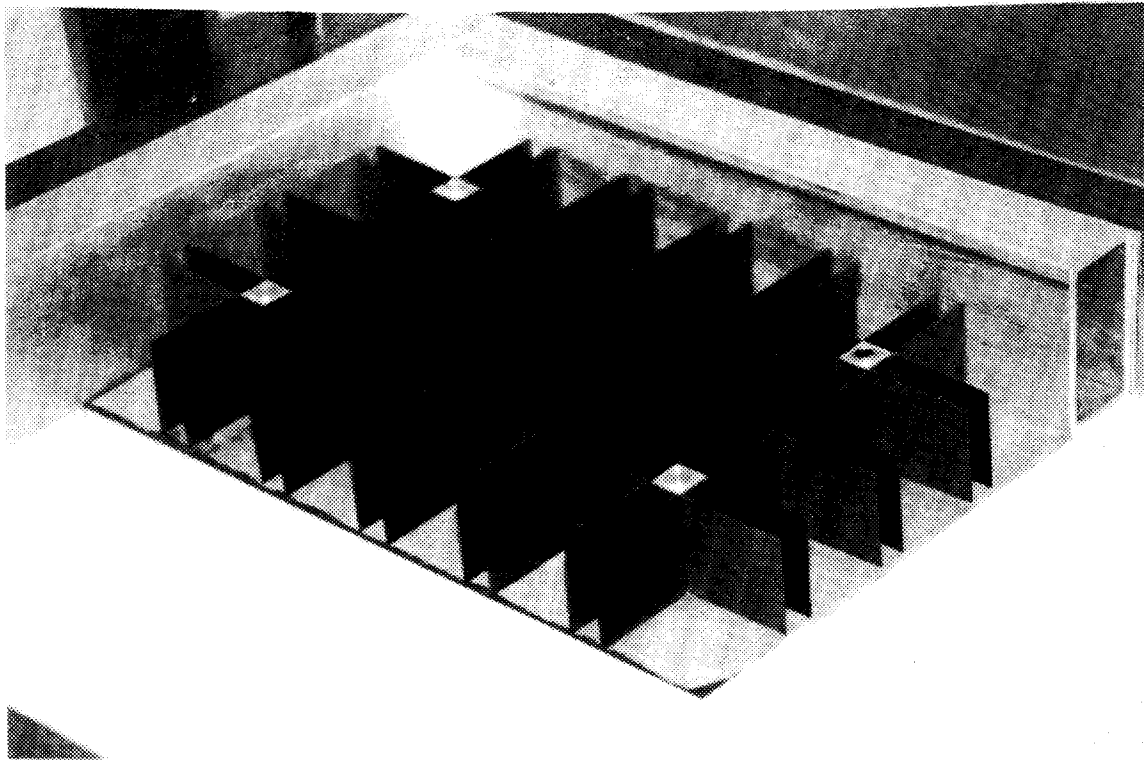


Figure 6. Isostatic Mount CFRP Core

SILEX will be carried aboard ARTEMIS and is due for launch in 1997.

#### 11.4 ARTEMIS LLM and SKDR Antenna Reflectors

ARTEMIS will use satellite-to-satellite communications between its SILEX laser data-relay payload and lower orbiting craft. ARTEMIS will be a dual-purpose craft operating in geostationary orbit at 36000 km altitude. It will also advance satellite telecommunications for cellular mobile telephones. In this respect, it will carry two payloads:

LLM (L-Band Land Mobile) and Radio data-relay payload SKDR (S/Ka-band Data Relay). Each requires a parabolic reflector which is presently being developed and tested by CASA.

Concept: 3.3 x 2.8 m parabolic reflectors  
Precision: less than 100  $\mu$ m RMS

The precision requirements have driven the design towards combining newer materials, all with low CTE/CME and resistance to microcracking:

Dish skin material: Cyanate ester prepreps  
RS3/XN50A and RS3/Kevlar 49.  
Core material: Kevlar HRH 49-1/4-2.1.

Backing structure ribs: RS3/XN50A and RS3/T300 combined with HRH 49-1/4-2.1 core.

#### 11.5 Far Infrared and Submillimetre Space Telescope (FIRST)

Both CASA [9,10] and Dornier [11,12] have participated in establishing technologies for this telescope. This has involved various concepts of using CFRP honeycombs with CFRP face-sheets as the basis for a large reflector. An initial design study centred on a small version antenna, as shown in Figure 7. The specification requires 7  $\mu$ m overall RSS.

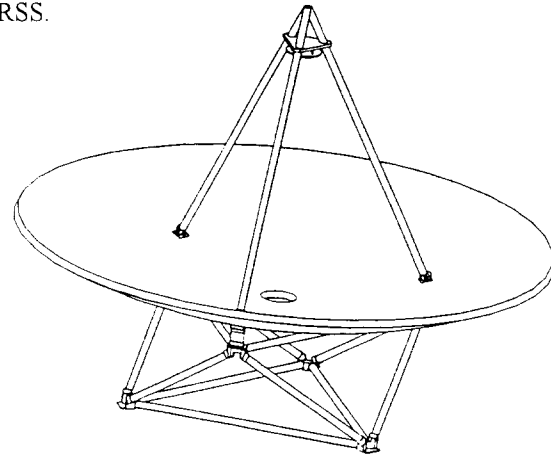


Figure 7. 4.5m FIRST Reflector [11].

The CFRP core concepts studied produced different cell shapes and were:

- ♦ a rigid core (similar to Figure 6)
- ♦ a flexible core (similar to conventional honeycomb but with different cell shapes)
- ♦ 60° CFRP segments (triangles with rounded corners)

All concepts had to be manufactured specifically for the project.

The 60° segments used by Dornier are made individually by wrapping around mandrels. These are then placed on a mould cavity and co-cured. Once the mandrels are released, the core is machined and then bonded to pre-manufactured CFRP face-skins. The CFRP material is UHM M60J/950-1.

### 11.6 Scan Mirror

ESTEC is supporting the development of an ultra-lightweight scan mirror substrate by DASA - Ottobrunn/SGL Carbon/IABG. The foreseen application is a Meteosat second generation SEVIRI (Spinning Enhanced Visible/IR Imager) instrument. The substrate is shown in Figure 8, and is 800 x 600 mm with a mass of 5.45 kg. The material is chopped carbon fibre reinforced silicon carbide (C/SiC). It is foreseen that C/SiC will be extremely stable in the working environment, so allowing full retention of dimensions.

## 12. Smart Technologies

Dimensionally stable materials cannot meet all the requirements that might be stipulated on future space projects. ESA/ESTEC has therefore made a policy decision to invest in active techniques. These may be needed to resolve inadequacies found in structural configurations which materials selection alone cannot resolve [1]. For the purpose of this paper, these structural configuration requirements fall into two categories:

### 12.1 Active Compensation

Where in-orbit distortions of a reflector occurs, there is the opportunity to use piezoelectric actuators to restore the shape. ERA Technology and Dornier GmbH are presently undertaking an ESTEC supported study to define the actuator and control requirements. Such systems will only be viable if the additional mass and power consumption produce an acceptable contribution to the stability of the structure.

### 12.2 Microvibration damping

On both the Hubble Space Telescope and Olympus satellite microvibrations were induced in orbit. The former due to 'thermal ratcheting', the latter due to inertia wheel misalignment. Such vibrations are undesirable. Active systems, again based on

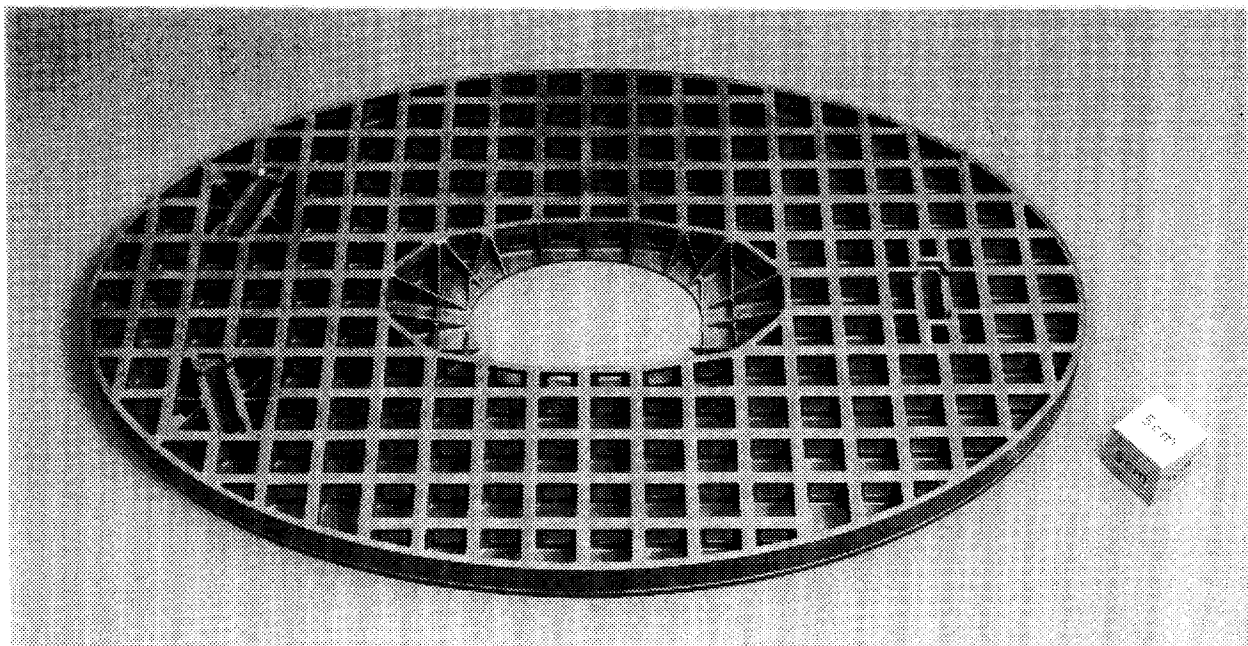


Figure 8. C/SiC Scan Mirror Substrate Development Model.

piezoelectric actuators, could reduce the amplitude of vibrations by introducing anti-phase vibration energy.

### 13. Conclusions

The European space sector is presently undergoing a contraction reflecting reduced government funding. There are many interesting areas which could be studied, however priorities have to be set based on funding levels available and work supported by ESA/ESTEC reflects this. In the immediate future, the development of materials and structural solutions for dimensionally stable applications will concentrate on:

- 1) Low moisture absorption (low CME), toughened CFRP materials, such as cyanate esters.
- 2) Evaluation of space inert materials, notably carbon fibre reinforced CMC (eg C/SiC) and to a lesser extent MMC, for optical applications.
- 3) The use of active Smart techniques to suppress microvibrations or achieve compensation of shape through the use of piezoelectric transducers.

### 14. Acknowledgements

The authors wish to thank all contractors, and members of ASMIEG, who supplied information and illustrations for this paper, plus contributions included in the ESA Structural Materials Handbook which is referenced [1].

### 15. References

- [1] Structural Materials Handbook  
ESA PSS-03-203, June 1994  
Volume 1 : Polymer Composites  
Volume 2 : New Advanced Materials (metallics and ceramics)
- [2] Proceedings of the International Symposium on Advanced Materials for Lightweight Structures '94, ESTEC, Noordwijk, March 1994, ESA WPP-070 to be published.
- [3] Adhesive Bonding Handbook for advanced structural materials.  
ESA PSS-03-210, February 1990.
- [4] Insert Design Handbook  
PSS-03-1202, June 1987.
- [5] D P Bashford  
"Microcracking Behaviour of Epoxy and Cyanate Ester UHM CFRP Composites".  
ERA Technology Report 76-05-0624, Work Order No. 34, ESTEC Contract 7090/87/NL/PP, April 1994.
- [6] SPIE Proceedings : Advances in Optical Structure Systems, 16-19 April 1990, Volume 1303, ISBN 08194-0354-7.
- [7] High Stability Telescope Structures  
CASA Space Division Final Report, ESTEC Contract No 56/83/NL/PB, November 1992.
- [8] B.Gergonne et al  
"SILEX Optimal Terminal Structure: Overview of the Design and Performances".  
To be published in [2]
- [9] A.Alonso et al  
"An Approach to High Precision Antenna Structures by a CFRP Core Sandwich Concept".  
An International Symposium on Advanced Materials for Lightweight Structures, ESTEC, Noordwijk, March 1992, ESA SP-336, p39-44
- [10] E.Ozores et al  
"Development Tests for a High-Stability Optical Bench"  
An International Symposium on Advanced Materials for Lightweight Structures, ESTEC, Noordwijk, March 1992, ESA SP-336, p271-276.
- [11] G.Helwig et al  
"Low Cost and Thermally Stable Sandwich Design for FIRST"  
An International Symposium on Advanced Materials for Lightweight Structures, ESTEC, Noordwijk, March 1992, ESA SP-336, p45-50.
- [12] D.Ehmann & G.Helwig  
"Material Tailoring and Design Optimisation for the FIRST Reflector"  
To be published in [2]
- [13] M.Deyerler et al  
"C-SiC - An Ultra-lightweight Structural Material for Optical Components and further Space Application"  
To be published in [2]

## Recent Developments in Low Cost Stable Structures for Space

Timothy C. Thompson, Cathleen Grastataro, Brian G. Smith  
Los Alamos National Laboratory, Los Alamos, NM

### Abstract

The Los Alamos National Laboratory (LANL) in partnership with Composite Optics Incorporated (COI) is advancing the development of low cost, lightweight, composite technology for use in spacecraft and stable structures. The use of advanced composites is well developed, but the application of an all-composite tracker structure has never been achieved. This paper investigates the application of composite technology to the design and fabrication of an all-composite spacecraft bus for small satellites, using technology directly applicable to central tracking in a high luminosity environment.

The satellite program Fast On-Orbit Recording of Transient Events (FORTÉ) is the second in a series of satellites to be launched into orbit for the US Department of Energy (DOE). This paper will discuss recent developments in the area of low cost composites, used for either spacecraft or ultra stable applications in high energy physics (HEP) detectors. The use of advanced composites is a relatively new development in the area of HEP. The Superconducting Super Collider (SSC) spawned a new generation of Trackers which made extensive use of graphite fiber reinforced plastic (GFRP) composite systems. LANL has designed a structure employing new fabrication technology. This concept will lower the cost of composite structures to a point that they may now compete with conventional materials. This paper will discuss the design, analysis and proposed fabrication of a small satellite structure. Central tracking structures using advanced materials capable of operating in an adverse environment typical of that found in a high luminosity collider could use identical concepts. LANL designed and analyzed the proposed technology for use on the gamma, electron, and muon (GEM) detector.

This paper will discuss the issues of design, analysis, testing, and fabrication required to deliver the FORTÉ spacecraft applications, and its associated components within a two-year period. Due to the extremely tight time constraints, a novel low-cost solution using GFRP composites was required to achieve the performance goals of the mission. The paper will give the details of material selection, characterization of design allowables, and the approach used in determining the structural geometry that will provide the optimum performance for this mission are presented.

## 1. Introduction

### 1.1. Overview

There is currently considerable interest in the use of low cost, small satellites to increase the ratio of payload-to-structure performance for space missions. This technology can be used to significantly reduce the cost of structures proposed for large stable detectors used for Large Hadron Collider (LHC).

A common practice for constructing small spacecraft structures is to use an all-aluminum spacecraft bus. This reduces the payload capacity significantly, however the cost of the aluminum structure has historically been lower than using advanced composites. LANL mission requirements dictate the need for a long term solution which substantially increased the ratio of payload to structural mass while maintaining a low-risk low cost approach. LANL intends to use the concept developed for FORTÉ on future HEP central tracking structures.

### 1.2. Aluminum vs. Composites

LANL and its industrial partner (COI) have built an all-graphite composite spacecraft structure. Incorporating advanced materials and unique manufacturing techniques, this structure will enable higher fractions of useful payload (as a percentage of total launch weight) to be placed in orbit. The FORTÉ experiment will provide the test bed and space validation for this structure and for other key aspects of these technologies that can be used in other HEP programs. This major technology development will make a significant contribution to the nation's many industrial pursuits that involve advanced performance structures.

Staying close to known designs and well-known materials can go a long way in reducing risk and cost of stable structures as in this case of a spacecraft. The original proposed design was an all-aluminum bolted structure that did not meet the weight target. Composites have a clear advantage in performance over aluminum and are required to meet the mission weight objectives.

## 2. Spacecraft Configuration

### 2.1. Design Approach

Several factors influenced the FORTÉ design. The approach used by LANL was to do a sufficient amount of analysis to validate the design concept and to thoroughly test the concept through rigorous testing of the spacecraft. The schedule permitted two design iterations that allowed the Engineering Model (EM) to be thoroughly tested and subsequent changes to be fed back into the final flight hardware that will be constructed in the fall of 1994. The geometry is simple and modular for low cost and improved maintainability and repairability. The configuration selected allowed us to efficiently use the solar array substrate (SAS) panels for shear panels and as a load-bearing member. Finally, materials that are critical to the project's success have already been proven in space.

### 2.2. Design Considerations

The resulting design drivers for the spacecraft bus are weight, strength, stiffness, and launch vehicle volume. The overall cost, schedule and associated risks with performance, cost, and schedule also have a significant influence on the design.

### 2.3. Description of Spacecraft and Payload

The FORTÉ spacecraft primary structure consists of 6 major structural components, 3 structural trusses, 3 instrument decks, and 24 SAS panels. The fundamental principles behind this unique spacecraft design are simplicity, modularity and interchangeability, as shown in Figure 1.

The three frame structural trusses are termed the lower, mid and upper cages. The lower and mid cages are identical to each other. Rectangular frame subassemblies comprise the lower and mid cages. The upper cage assembly is constructed using trapezoidal frame subassemblies. Eight frame subassemblies are bonded together to form each of the three octagonal cages, as shown in Figure 2.

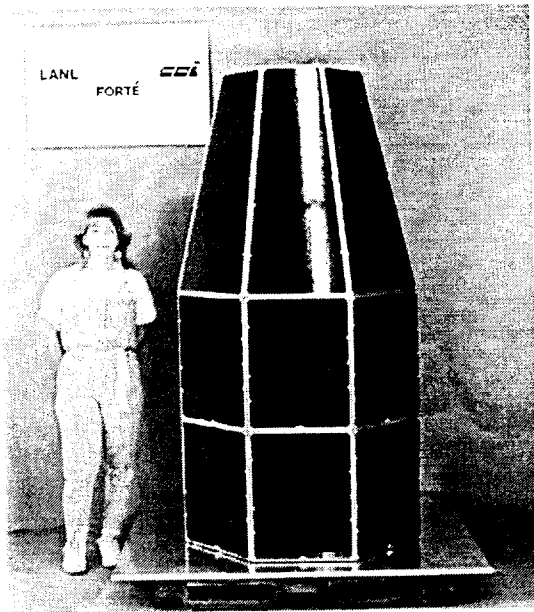


Figure 1. Fully assembled spacecraft structure with SAS panels installed

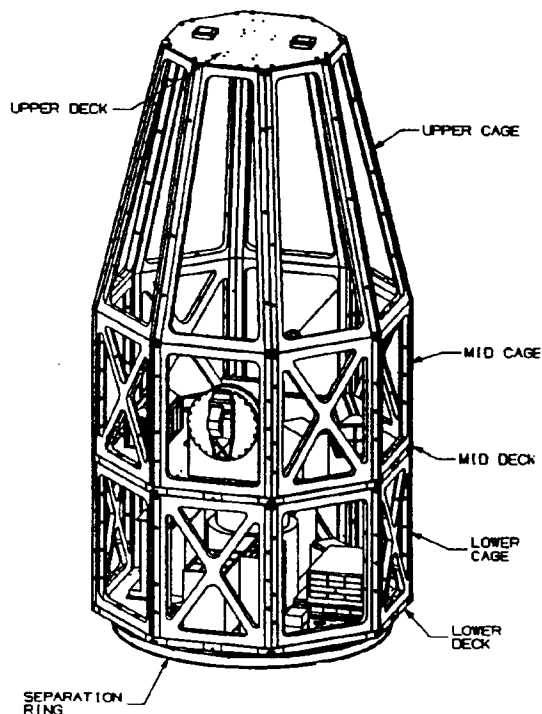


Figure 2. Structural components of the FORTÉ spacecraft

The three decks are termed the lower, mid and upper decks. The lower and mid decks are structurally identical to each other. Aluminum honeycomb core is sandwich-bonded between graphite/epoxy (Gr/E) skins. The upper deck closes out the structure and is fabricated from

aluminum honeycomb sandwich-bonded between Gr/E skins.

The SAS panels are fabricated from the same materials as the upper deck. Aluminum inserts in the panels mate up against threaded block-type inserts in the cages. The substrates are then bolted into place.

The decks and cages are mechanically fastened to each other via aluminum corner fittings that are bonded into the cages and decks as shown in Figure 3. This arrangement ensures that the highly loaded structure has excellent load transfer in the corners of the cage.

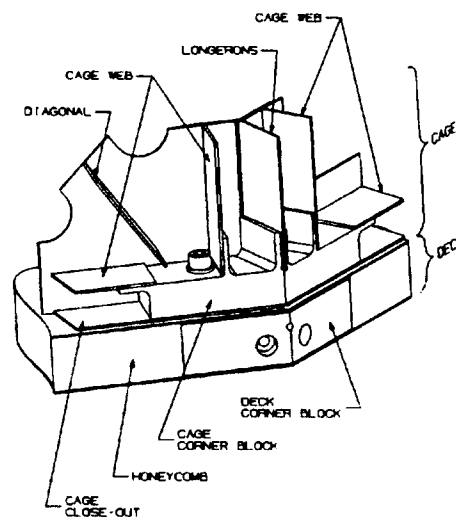


Figure 3. Spacecraft cage structure and deck joint detail with outer skin removed for clarity

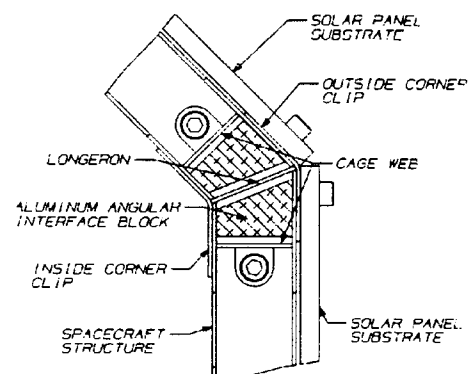


Figure 4. Cage structure joint detail

The cross-sectional view of the cage corner is shown in Figure 4. This view shows how the outer clip and inner clip are used to join the cage subassemblies together for a robust structural joint.

### 3. Design/Analysis Summary

The design of the FORTÉ spacecraft composite structure and solar panel substrates can best be discussed by addressing the following areas:

- structural design heritage
- design-to-cost considerations
- dynamic loads analysis
- structural analysis summary.

#### 3.1. Structural Design Heritage

The premise for the FORTÉ design concept originated from earlier work LANL had done for the SSC. LANL designed an ultra stable support structure for the SSC GEM Silicon Tracker as shown in Figure 5. FORTÉ is using this concept again, keeping as many of the structural components similar to the original design to further reduce the cost of the structure. A corner detail can be seen in figure 6.

The original structural support consisted of an octagonal spaceframe made from advanced metal matrix composites (MMC). This network of tubes and joints proved to be highly stable and quite costly. The structure shown in Figure 5 was costed at one-tenth the comparable MMC frame cost, with only small degradation in stability. This large reduction in cost simply could not be overlooked in today's ever tightening budget scenario.

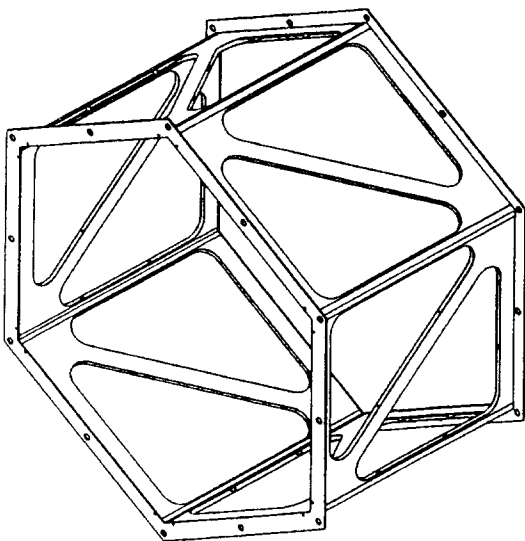


Figure 5. GEM tracker structure

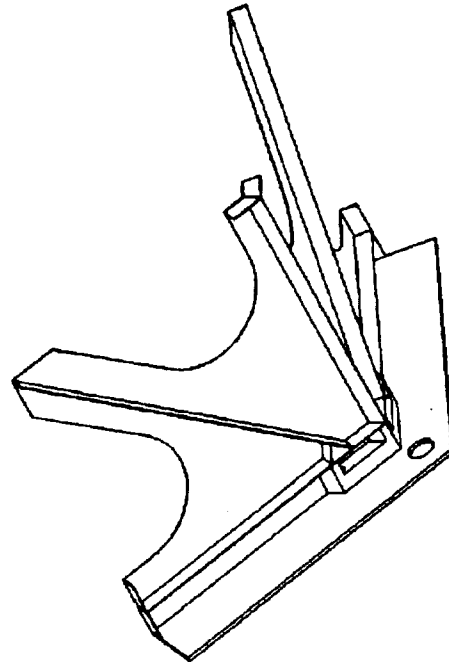


Figure 6. GEM tracker structure corner detail

Because of the apparent economic and structural benefits of this basic design approach for composite structures, engineers at LANL thought it prudent to replace the heavier aluminum design being considered for FORTÉ. LANL's subsequent structural analysis effort for FORTÉ was supported by an extensive material database that substantiated the suitability of this type of composite structural design concept. This will be evident in the following sections.

#### 3.2. Design-to-Cost Considerations

A concept associated with composite structures is that they are much more expensive than aluminum structures. Technological advancements in the design and manufacturing of composite structures have disproved this idea. The cost of the FORTÉ spacecraft structure is very near that of the aluminum spacecraft structure it replaced. This was accomplished by using advanced design and manufacturing technology. For FORTÉ, the following design features were established to minimize manufacturing cost.

1. Design to maximize use of flat composite laminates to:
  - eliminate large production molds
  - increase the rate (pounds of prepreg per hour) at which composites can be laid up
  - minimize inspection time



- facilitate use of programmable routers/waterjet machining
  - reduce schedule by using existing composite stock material.
2. Design in commonality between parts to:
    - minimize tooling
    - improve the learning curve (details and assembly)
    - allow laminate stacking for waterjet machining.
  3. Design in self-fixturing techniques to:
    - minimize tooling
    - minimize subassembly time
    - minimize inspection time.

Along with these specific features that reduce the manufacturing cost comes a reduction in time needed to fabricate a unit. Time factors have a significant effect on the overall FORTÉ spacecraft program costs.

### 3.3. Dynamic Loads Analysis

Using the drop transient shock response spectrum for a Pegasus launch as a guide, the goal was to design the spacecraft structure so that the primary modal response would be at about 35 Hz. Preliminary analysis showed primary modes in the 20 Hz range with excessive deformation at the corners of the lower deck. Stiffeners added at the eight deck corners of the lower deck brought the primary modes up to the 50 Hz range. This is in the region of maximum response, which is not ideal, but is adequate. If the modal frequencies shift, any changes in frequency will lower these responses, which would be desirable.

A frequency analysis showed the first 19 modes to be between 35 Hz and 74 Hz. Several of the key vibrational modes are illustrated in Figures 7a and 7b.

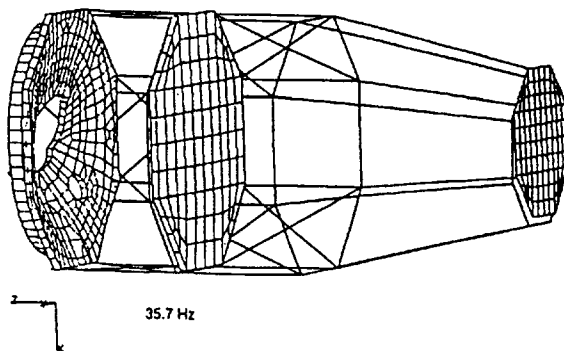


Figure 7a. First mode lower deck

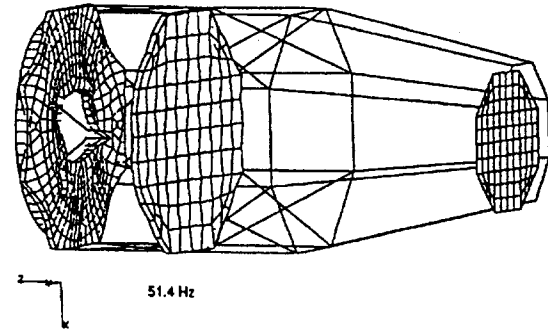


Figure 7b. First bending body mode Y-direction

### 3.4. Structural Analysis Summary

The analysis effort of the FORTÉ primary spacecraft structure focused on evaluating its performance and optimizing its design for the drop portion of the launch. The structure was also analyzed during the third stage acceleration but as noted earlier this was not the critical loading condition.

A finite element model (FEM) of the structure was constructed using the COSMOS\M finite element package. The structure was modeled using three-dimensional beam elements for the longerons that would make the backbone of the structure once the cages and decks were assembled. The decks were modeled using isotropic plate elements. The mechanical properties for the aluminum honeycomb graphite skin combination was calculated and used as input. To simulate the mass of the components on the decks, the mass was distributed uniformly over the surface. The SAS panels were modeled in an identical fashion. They were attached to the rest of the structure with short beam elements so that an estimate of the in-plane shear forces could be identified. The model was fixed at its base with spring elements to simulate the shock attenuating flexures.

The most severe acceleration that developed during the drop launch was a linearly varying lateral X-component acceleration of 8.5 g at the base and 18.5 g at the structure top deck. A constant lateral acceleration 2.5 g orthogonal to the linearly varying acceleration and a longitudinal acceleration of 4.5 g compressed the structure.

The initial design had no cross bracing in the cage structure and relied solely on the SAS panels to carrying the shear from the drop transient

accelerations. Analysis showed this arrangement was not feasible and studies were undertaken to determine the minimum number and location (acceptable to access requirements) of necessary cross bracing additions. In addition to the cross bracing, the number of fasteners in the substrates had to be increased from 6 per panel to 10 to meet the design allowable of 666 lbs shear-out for in-plane failure of the substrate. Figure 8 shows the component forces acting on a typical SAS panel while Table 1 shows the resultant loads.

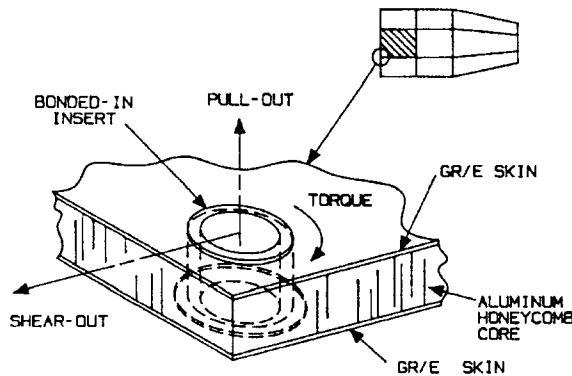


Figure 8. SAS panel showing maximum loads

Table 1: SAS Panel Resultant Loads

Load	Maximum Calculated	Allowable
Pull-Out	5 psi	516 psi
Shear-Out	265 lbs	666 lbs
Torque-Out	5 in-lbs	72.6 in-lbs

Forces from the beam elements were calculated and put into detailed model of the cage corner interface. A detailed FEM was made of the joint area to predict adhesive stresses. The results are summarized in Table 2 and Figure 9 illustrates the joint FEM.

Table 2: Joint Results

Longeron-Aluminum Block Max in Plane Shear Stresses	324 psi
Longeron-Aluminum Block Maximum Peel Stresses	517 psi
Maximum Outer Skin Von Mises Stress	2500 psi

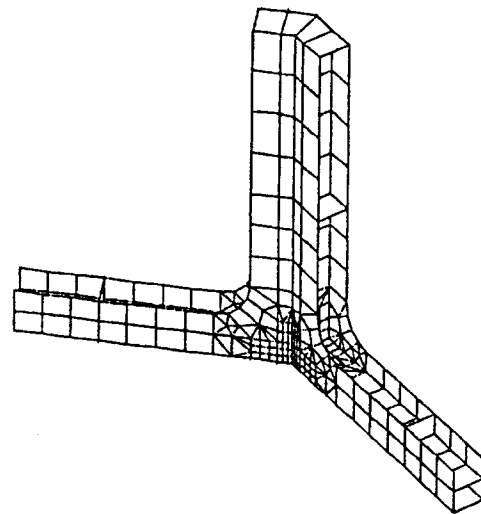


Figure 9. FEM of the structural joint

The shear results in the SAS panels were then used to determine the buckling characteristics. The panel was analyzed using finite element and conventional composite techniques. To help gain confidence in the analytical results, modal testing was performed on the substrate panels. The first five natural frequencies were calculated using finite elements and then the panels actual first five frequencies were found. Table 3 shows the analytical modes compared to the measured values. Figure 10 shows the experimental mode shape for a Type A panel. The natural frequencies were found by subjecting the panels to sine sweep on the function and looking for peaks on the frequency response function (FRF). The panels were excited at frequencies close to the resonance and sand was used to identify the nodal points of the mode shape.

Table 3: Analytical and Measured Results for Fundamental Mode Shapes of Type A SAS Panel

Mode #	FEM	FRF	% Difference
1	164.8	165	0.1%
2	203.3	214	5.0%
3	349.1	373	6.4%
4	375.5	389	3.5%
5	456.2	483	5.5%

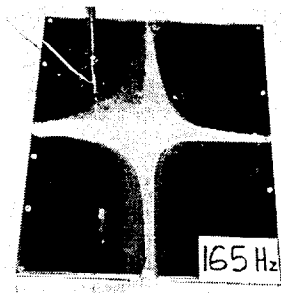


Figure 10. Measured fundamental frequency of a Type A SAS panel

## 4. Fabrication

When bolted together the 3 frame structures, 3 equipment decks, and 24 SAS panels constitute the complete primary structure for the FORTÉ spacecraft, as shown previously in Figure 1. The following discussion addresses tooling and the various FORTÉ spacecraft structure components and illustrates the simple manufacturing approach afforded by this low cost structure.

### 4.1. SAS Panels

The 24 SAS panels for the upper, mid, and lower cages were fabricated and machined from 8 large panels that could produce 16 lower or mid panels and eight upper panels. The large panels were 0.020" thick precured panel assemblies of Gr/E T-50/ERL1962, [0/45/90/135]<sub>s</sub> with either co-cured 0.2 mil copper on one side or co-cured 2.0 mil Kapton®. Figure 11 shows a typical cross-section of an SAS panel.

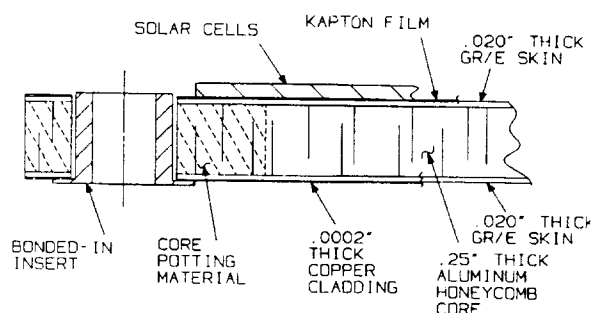


Figure 11. Typical cross section of an SAS panel

These precured skins were then bonded using FM-300-2U film adhesive to .25" aluminum honeycomb core (1/8" cell; 3.1 lbs/ft<sup>3</sup>). All aluminum inserts were post potted in Corefil 615 and bonded using room temperature epoxy adhesive, Hysol EA9394.

Insert locations were machined into the various panels at the time the sandwich subassemblies were cut from the larger panels. Then, using master bond plates that are common to those used for the corresponding frame subassemblies, all inserts were located into the SAS panel.

### 4.2. Spacecraft Structure

The space frame assemblies and equipment decks that make up the spacecraft structure differ in construction. The decks are manufactured similarly to the SAS panels, except that copper was co-cured on both sides of each deck. The space frame is made from flat laminates. The upper deck is the same thickness as the SAS panels but the mid and lower decks have a one inch thick aluminum core (1/8" cell, 4.3 lbs/ft<sup>3</sup>). Figure 12 shows a lower deck bonded and machined. The skin thickness on all decks is 0.030" with an orientation of [0/60/120]<sub>s</sub>.

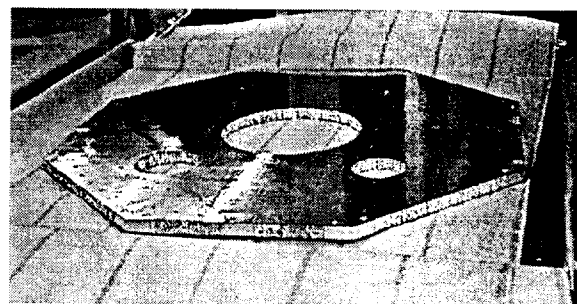


Figure 12. Lower deck

The frame subassemblies are made from flat 0.048" thick laminates of T50/ERL1962 with a [0/45/90/135]<sub>s</sub> orientation. As is typical of flat laminate construction, all details can be "nested" tightly on larger cured laminates and machined out with a waterjet machining head mounted to a programmable router. Four laminates of one configuration and two laminates of the other configuration were machined.

Utilizing COI's concept for a self-fixturing fabrication process (the Short Notice Accelerated Production Satellite or SNAPSAT™\*), all details are removed from a completely processed panel (prepped for bonding) and "snapped" together. The snapping together feature is mortise and tenon joints that are precision machined into the details.

\* SNAPSAT™ is a patent-pending trademark of COI.

Figure 13 shows a portion of the frame assembly. Note that blade longerons and inner and outer angle clips are not bonded at this time. The deck angular interface fittings are what initially ties the structure together. These are visible in Figure 14. Corner splicing angles are later installed which cover up the blade longeron. The upper and lower decks are used to assemble and jig the frame. Angular interface fittings accept the mid frame subassemblies. The frame assembly can then be bonded together on the decks.

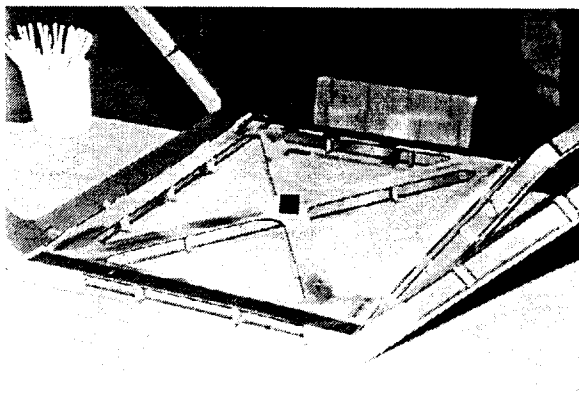


Figure 13. Cage panel frame subassembly showing the interface fittings

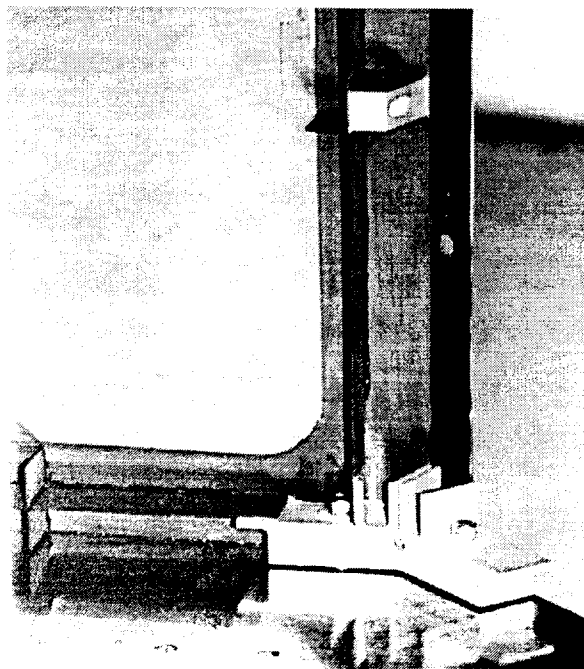


Figure 14. Cage corner detail

#### 4.3. Final Assembly

By repeating the above process for all decks and frames, the final assembly shown in Figure 15 is achieved. The SAS panels have not yet been installed. Note that the mid and upper frame assemblies are unplated for this first unit. The lower frame assembly is copper electroplated on the outer surface of the outside panels only. This was done in order to evaluate the RF shielding effectiveness of unplated vs. plated Gr/E. Pending the electromagnetic interference (EMI) test results on the EM, the flight unit will be configured for EMI protection. The copper on the back of the SAS panels provides the EMI protection for the spacecraft equipment and also serves to electrically shield the spacecraft from its antenna system.

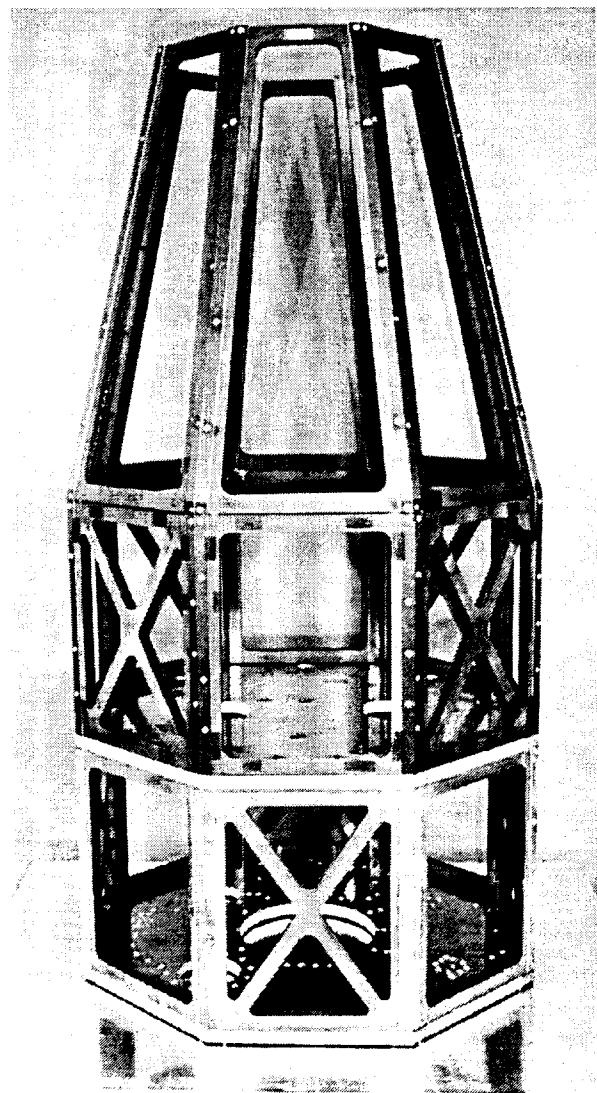


Figure 15. Final spacecraft assembly

## 5. Testing

### 5.1. Material Testing

The uniqueness of the FORTÉ primary spacecraft structure meant that some of the detailed design information was lacking. Parts of other spacecraft devices were similar but not exactly the same. A testing effort was initiated to define design allowables in critical areas. The primary concerns were the high shear stress areas of the SAS panels, the shear stress between the graphite and the aluminum angular interface block corner joints, and the deck component insert pullout allowables.

The SAS panels were viewed as the most critical area of the structure and no design data existed for them. Edge coupons were fabricated by COI, and tested at LANL. The coupons were designed to carry a maximum shear load through the corner of the coupon since analysis showed the maximum shear force was along this direction. Along with determining the absolute design allowables there was also an interest to know the effects of thermal cycling on the bonded joints.

The spacecraft would be maintained near room temperature during the launch phase, but it would be cycled from  $-65^{\circ}\text{C}$  to  $80^{\circ}\text{C}$  five times prior to launch as part of its qualification testing. Therefore it would be imperative to know the effects of thermal cycling on the shear-out design allowable. Ten coupons were tested with thermal cycling and ten coupons were tested without thermal cycling. The cycle commenced at room temperature with the cooling to  $-65^{\circ}\text{C}$  at a rate of  $10^{\circ}\text{C}/\text{min}$ . This extreme was held for 10 minutes and then the part was heated to  $80^{\circ}\text{C}$  at  $10^{\circ}\text{C}/\text{min}$  and held at that extreme for 10 minutes. Then the part was returned to room temperature. This cycle was repeated five times. All coupons were then tested at room temperature.

The results of the two tests are summarized in Table 4. The average ultimate shear-out load for the thermal cycled coupons degraded by 13% and the design allowable was decreased by 24%.

Ten additional coupons were tested after a modified thermal cycle. The extreme temperatures were held for one hour. The increased soak times at the extreme temperatures only decreased the mean ultimate shear-out load an additional 9% and the design allowable an additional 17%.

Table 4: Corner Static Load Test

	Mean Ultimate Shear-Out	Allowable Shear-Out
All Coupons Combined	940 lbs	750 lbs
Non Thermal Cycled Coupons	1003 lbs	881 lbs
Thermal Cycled Coupons	877 lbs	666 lbs

Another critical area for which little design data existed is the cage structure corners where aluminum angular interface blocks are bonded to the graphite skins. Initially the published shear strength for the adhesive was used to determine the design allowable. Fifteen single lap shear coupons were fabricated and tested at COI. Of the 15, 5 were not thermally cycled and 10 were subjected to the same thermal cycle as the corner coupons. The mean ultimate shear load showed no dependence on thermal cycling. The design allowables varied substantially, ranging from 507 psi for all 15, 473 psi for only the thermally cycled set, to 231 psi the non-thermal-cycled set. The very low value for the non-thermal-cycled set is a reflection of the small sample set size, given that the mean and standard deviation are almost identical to those of the other cases (Table 5).

Table 5: Shear Coupon Load Test

	Measured Bulk Area Mean Ultimate Shear Stress	Calculated Bulk Area Allowable Shear Stress
All Coupons Combined (15 Coupons)	895 psi	507 psi
Non-Thermal-Cycled (5 Coupons)	888 psi	231 psi
Thermal-Cycled (10 Coupons)	900 psi	438 psi

Analytical solutions and FEM's of the coupons were created to determine the stress distribution at failure. The analytical solution suggested by Ojalvo and Eidinoff, 1977 show a bulk shear stress of approximately 660 psi and a peak at the edge of the bond area of more than 5000 psi. Their results indicate a peak peel stress at the bond edge of 3550 psi. A plane two-dimensional model showed the same stress distributions as suggested by the analytical solutions but a bulk area shear stress of about 125 psi and a corresponding peak of 8600 psi. In this case the stresses are plotted from the bonded joint center to the edge because of symmetry. The bulk area peel stress is initially close to zero, then becomes compressive near the edge and peaks at the very edge at almost 13,500 psi when the peel stress is plotted against the bonded joint length.

The actual joint in the FORTÉ structure unfortunately does not resemble the lap shear coupons. In the structure a relatively thin graphite skin is bonded to a relatively massive aluminum block (Figure 3). Therefore, further study of the lap shear finite element model was done to determine the effect of considerably increasing the thickness of one adherent on the stress distribution. The results showed a dramatic change in both the shear and peel stresses. The bulk area shear stress was reduced slightly to 580 psi. The shear stress then peaks at the bond edge at slightly over 3800 psi. The bulk area peel stress is initially 170 psi and increases to 435 psi. The peel stress then peaks at the bond edge at 2227 psi. These results indicate that the peel stress is reduced significantly when one adherent is much thicker than the adhesive and the other adherent.

The results also show that the bulk area shear stresses are lower than those determined from the lap shear coupons tests (indicated in Table 5). To determine those values the ultimate load was divided by the bond area. From the FEM shown in Figure 9, the maximum shear stress calculated was 324 psi and the peak peel stress was 517 psi, far below the analytical results or the finite element predictions. These are slightly larger than the allowables determined by testing, but when compared to the analytical results or the FEMs the peak stresses may be considered acceptable.

## 6. Conclusions

LANL has designed, analyzed, and demonstrated a simplified, cost-effective method for the production of small satellite spacecraft structures, which can be readily applied to stable structure design. This process produces an all-composite spacecraft structure that is lightweight and very strong, providing substantial improvement over aluminum designs in its payload-to-weight ratio. The fabrication technology that has been developed produces savings in production time and expense over previous composite processes. It is competitive with aluminum structure processes in expense and speed of production and is applicable to a wide variety of stable structures. The simple but robust spacecraft structure provides a platform that will be useful for a wide variety of scientific applications.

## 7. References

- "GEM Silicon Tracker Mechanical Subsystem Final Design Report", Los Alamos National Laboratory, June 1994.
- Goland, M. and E. Reissner, "The Stresses in Cemented Joints", *Journal of Applied Mechanics*, March 1994, Vol. 11, pp. A17-A27.
- Griiffin, M. D. and J. R. French, *Space Vehicle Design*, AIAA Publishing, 1991, pp. 345, 351, 356.
- "Mechanical Properties of Hexcel Honeycomb Materials", Hexcel TSB 120, Hexcel Corporation, 1987.
- "Guidelines for the Presentation of Data", MIL-HDBK-5D, June 1, 1983.
- Kilpatrick, M., J. Girard, K. Dodson, "Design of a Precise and Stable Telescope Structure for the Ultraviolet Chronograph Spectrometer (UVCS)", SPIE, Volume 1690, Design of Optical Instruments, 1962.
- Ojalvo, I.U., and H. L. Eidinoff, "Bond Thickness Effects Upon Stresses in Single-Lap Adhesive Joints", *AIAA Journal*, Vol.16, No.3, 1977.
- Pegasus Air Force Small Launch Vehicle Interface Design Document, Release 1.00, August 31, 1993.

# Highly Dimensional Stable Composite Structures

G. Helwig, Dornier GmbH  
D- 88039 Friedrichshafen

## Abstract

The still increasing requirements for highly accurate space structures like optical benches, telescopes and reflectors make it necessary to use advanced materials, mainly composites. They offer high specific stiffness and strength and low thermal expansion, especially when CFRP (Carbon Fiber Reinforced Plastic) is applied. By optimization of the laminate lay-up highly desirable properties e.g. zero thermal expansion can be adjusted. The partly hostile environment in space for polymer composites has to be regarded carefully not to lose their advantages. Restpolymerization, microcracking due to thermal cycling, outgassing in vacuum, shrinkage due to moisture release, radiation, creep etc. have to be considered for longer operation. Based on the experience of different space projects, today, there are solutions to the mentioned problems, which even can be transferred to earth bound environments.

## 1. Introduction

Dimensional stability describes the behaviour of highly accurate structures to maintain their dimensions under all kinds of conditions like mechanical loads, temperature, humidity, vacuum, irradiation and chemical environment. Dimensional changes should usually be in the order of a few microns ( $<10\mu\text{m}$ ) for 1 m length. For space application the structures should be very light. It seems that especially carbon fiber reinforced materials are very promising for that application.

## 2. Candidate Materials

### 2.1 Carbon Fibers

Developed over the last twenty years there are numerous different kinds of carbon fibers known as HT (high tensile, e.g. T300, T800), HM- (high modulus, e.g. M40) or UHM- (ultra high modulus, e.g. GY-70, P-120) fibers (Fig. 1). For mechanical structures their excellent strength and stiffness, very low thermal expansion and good thermal conductivity are very advantageous.

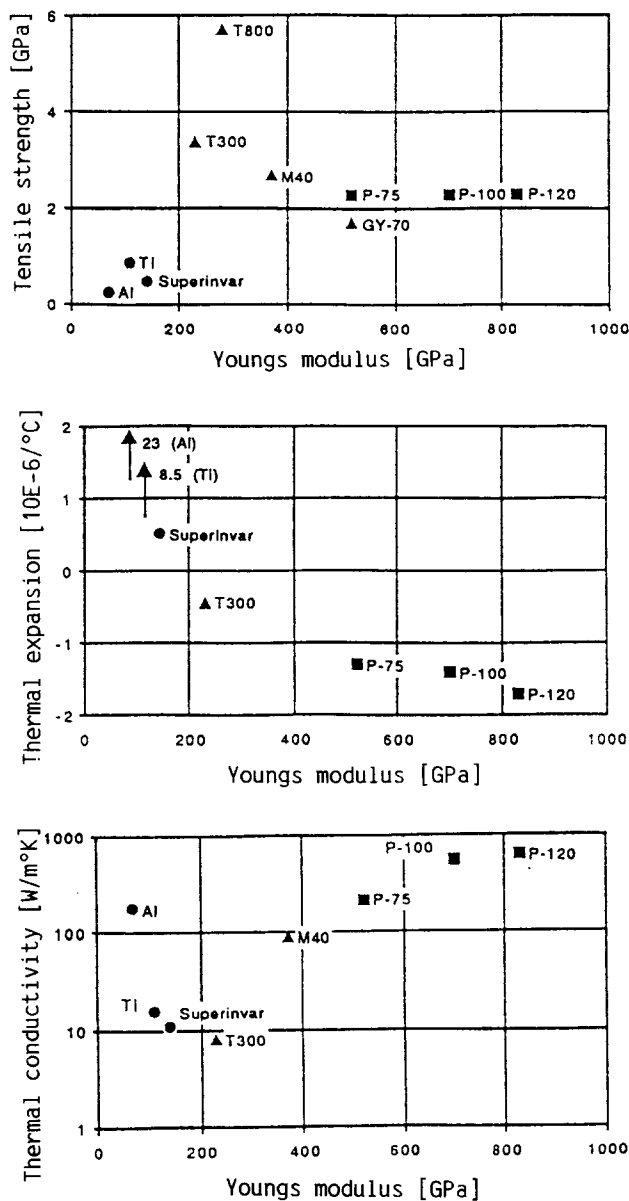


Fig. 1: Properties of different carbon fibers (some metals for comparison)

## 2.2 Matrix Materials

The carbon fibers are most commonly inbedded in polymer matrices (resins) to make a composite. The low temperature resistance and the moisture sensitivity of most polymers have to be considered thoroughly. The swelling or shrinkage due to moisture (for instance outgassing in vacuum) results

in undesired dimensional changes. The moisture absorption of neat resins (Fig. 2) ranges from almost none to roughly 5% weight gain.

Even the curing of the resins causes shrinkage in the range of 0.05 to 0.1 % which is directly correlated to the degree of polymerisation. After curing most polymers are polymerized to slightly over 90%. The last few percents cure more or less with time and therefore give dimensional changes (restpolymerisation).

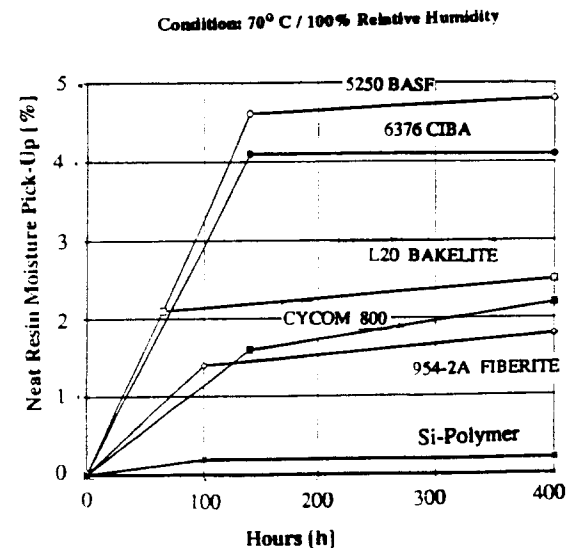


Fig. 2: Moisture pick-up of different resins

Other matrix materials can be ceramic (SiC), carbon (C) or even metal (Al, Mg). They have no moisture problems, but they all have high processing temperatures and together with carbon fibers will have high internal stresses.

## 2.3 Carbon Fiber Reinforced Material Systems

The correct combination of carbon fiber type and matrix material is essential for dimensionally stable composite structures. Promising candidate



composite materials are listed in Fig. 3. The C/SiC and C/C materials are carbon fiber reinforced ceramics respectively carbons while CFRPs are reinforced polymers. The chopped fiber C/SiC has excellent stiffness, relatively high thermal expansion and good thermal conductivity. This material is very suitable for optical mirrors. The long fiber C/SiC has moderate stiffness and thermal conductivity but very low thermal expansion. C/C is between the two C/SiC's regarding thermal expansion but is weak in stiffness. The LOMO (low moisture) CFRP is very similar to the long fiber CSiC but absorbs/desorbs some moisture and is much easier to process.

	Specific Weight [g/cm <sup>3</sup> ]	Tensile Strength [N/mm <sup>2</sup> ]	Tensile Modulus [N/mm <sup>2</sup> ]	Thermal Expansion [10 <sup>-6</sup> K <sup>-1</sup> ]	Moisture Expansion [10 <sup>-6</sup> % <sup>-1</sup> ]	Thermal Conduct. [W/mK]
chopped fibres C/SiC *	2.4	160	230.000	2.3	0	125
long fibres C/SiC	1.6	200	110.000	0.1	0	60
C/C	1.7	200	50.000	1	0	60
LOMO CFRP	1.6	400	110.000	0.1	80	50
NOMO CFRP	1.6	400	110.000	0.1	0	50

\* DASA-Munich

Fig. 3: Dimensional stable composite materials (quasi isotropic)

The NOMO (no moisture) CFRP is very new and needs further investigations. It is the first polymer composite material with almost no moisture pick-up. If it proves that most probably the moisture expansion is very low (to be verified) it would be the ideal material for dimensional stable structures.

### 3. Designing of Composite Materials

#### 3.1 Tailoring of Composites

With an optimized stacking sequence (ply angles, ply thicknesses) certain properties of a composite can be tailored to the requirements. The high orthotropy of

composites allows the adaption of properties usually in one direction, only. The tailoring for zero thermal expansion is a well known example. Zero moisture expansion is possible, too, and is illustrated in Fig. 4. Under moisture changes this laminate would not expand.

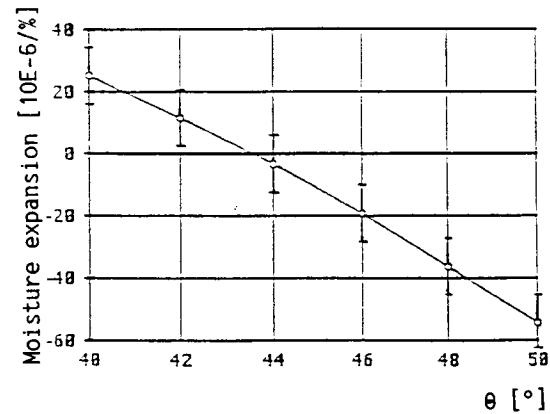


Fig. 4: Coefficient of moisture expansion for a  $(90^\circ \pm \Theta, 90^\circ)_s$  laminate

To achieve isotropic zero thermal expansion is more difficult and is only possible by a combination of two CFRPs having different fibers. Mixing the HM- with UHM-fibers (hybride) at a certain ratio yields isotropic zero thermal expansion at room temperature (Fig. 5). For zero expansion at different temperatures other ratios have to be used.

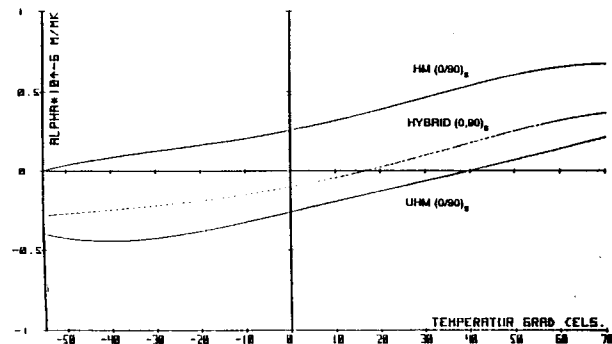


Fig. 5: Tailoring for zero isotropic thermal expansion

### 3.2 Long Term Behaviour of Composites

Properties of polymer matrix composites cannot only depend on temperature or moisture but even change their behaviour over time. Fig. 6 shows creep curves (creep modulus over  $\log t$ ) of a  $\pm 45^\circ$  CFRP laminate under permanent load and different temperatures. Additionally the specimens were thermally cycled between  $100^\circ\text{C}$  and  $-160^\circ\text{C}$  in vacuum 1500 times. Under these conditions microcracking occurs which changes Young's modulus and all other properties depending on it (for instance thermal expansion). If Young's modulus is known, even predictions become possible using viscoelastic analyses and classical lamination theory.

Deterioration by irradiation can be calculated the same way, so far data are available.

Ceramic matrix composites have the advantages, especially the long fiber C/SiC of very low thermal expansion, of no moisture pick-up, no outgassing, no irradiation problems but are difficult to process because of high temperature treatment ( $> 1000^\circ\text{C}$ ).

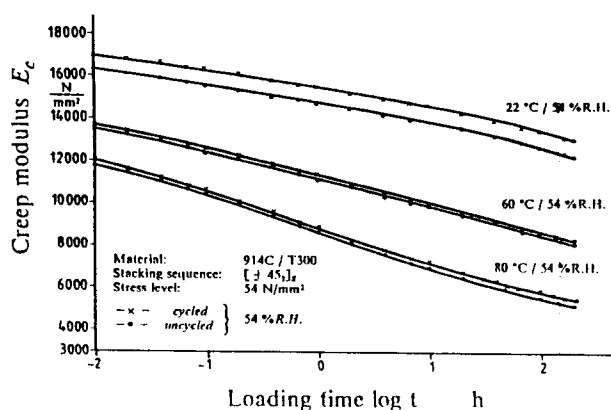


Fig. 6: Creep curves of  $\pm 45$  CFRP laminates  
 (tests by DLR-Braunschweig)

## 4. Dimensional Stable Structures

The following 3 structures stand for their extraordinary dimensional stability so far achieved.

### 4.1 Triangulation Optical Bench

A five metre CFRP tube as an optical bench for a triangulation measurement facility was manufactured with an overall thermal coefficient of expansion of lower  $1.10^{-7}/^\circ\text{C}$ . Additional special preventions to avoid any moisture pick-up have been taken by covering the tube with diffusion tight aluminium foil (roughly  $20\ \mu\text{m}$  thick).

### 4.2 XMM-X-Ray Multi Mirror Telescope

The XMM is a X-ray telescope planned by ESA (European Space Agency). It contains 3 mirror modules, each consisting of 58 highly nested, thinwalled ( $\sim 1\ \text{mm}$ ) 600 mm long parabolic/hyperbolic mirror shells ranging from 300 to 700 mm in diameter. Main requirements for the mirror shells are absolute radius  $\leq 5\ \mu\text{m}$ , circumferential slope  $\leq 1\ \text{arcmin}$  and a surface microroughness  $< 1\ \text{nm RMS}$  (root mean square). These accuracies were achieved by high precision filament wound CFRP carriers which in a further step were replicated from high precision superpolished gold coated glass mandrels transferring the gold/epoxy to the carrier making the mirror surface (Fig. 7).

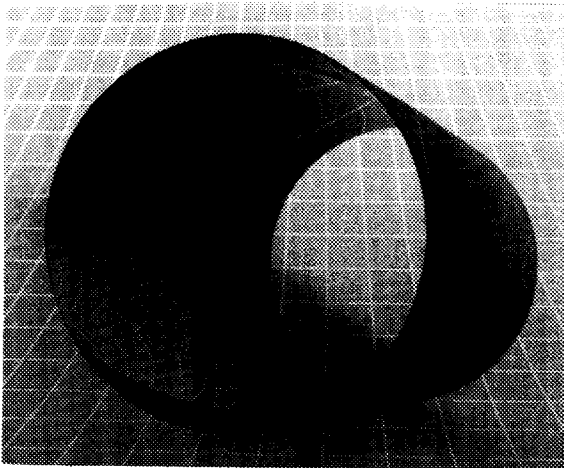


Fig. 7: XMM-CFRP-carrier

After enhanced analyses (moisture expansion in circumferential direction equal zero), laminate quality improvements and dry replication (the CFRP carrier were dried before replication) the specification for long term stability in vacuum was demonstrated (Fig. 8). Even irradiation with doses of 10 years in orbit did not degrade the CFRP mirrors.

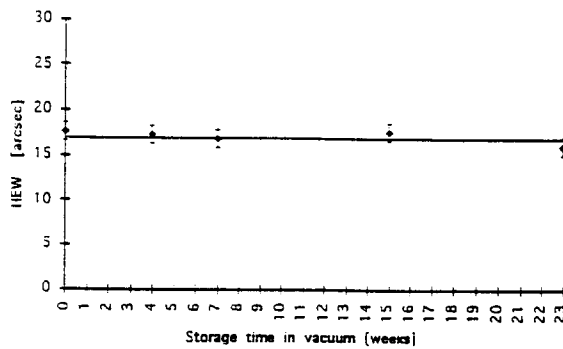


Fig. 8: Long term stability of XMM mirror

#### 4.3 FIRST-Far Infrared and Sub millimeter Space Telescope

The FIRST reflector (Fig. 9) has a diameter of 3 m and will be a sandwich with skins and core out of CFRP to meet the thermal stability requirement of  $\leq 4 \mu\text{m RMS}$  surface change under a cool down from room to operational temperature in space ( $\Delta T = -140^\circ\text{C}$ ). Manufacturing accuracy has to be within another  $4 \mu\text{m RMS}$ .

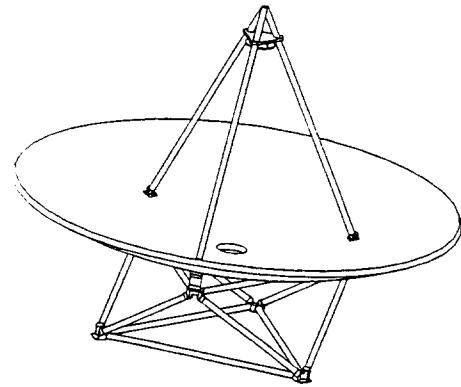


Fig. 9: 3 m FIRST telescope

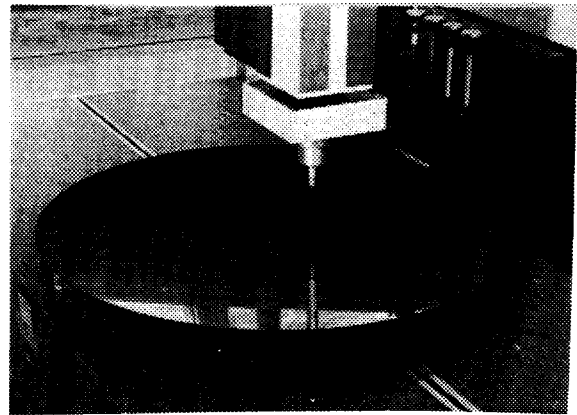


Fig. 10: FIRST 1.1 m all CFRP-reflector

In a feasibility study for ESA a 1.1 m all CFRP reflector as a demonstrator was built and thermally tested. Achieved manufacturing accuracy was close to  $4 \mu\text{m RMS}$ , while the thermal distortions resulted in  $2 \mu\text{m RMS}$ , only. These results were only possible by the use of a low temperature curing resin system (L20/SL) to avoid microcracking in combination with ultra high modulus carbon fibers (M60J). The low process temperature and very precision placement of the carbon fibers with an automated machine guarantee almost no warpage. The verified coefficient of thermal expansion of all parts of  $0 \pm 0.2 \times 10^{-6}/^\circ\text{C}$  over the total temperature range explains the extrem thermal stability of the 1.1 m reflector.

# High Stability Supporting Platforms for Optical Communications

F. Arévalo, E. Ozores, A. Bonet, J.-M. Andrés, J.-M. Larrauri  
C. A. S. A. - Space Division  
28022 Madrid - Spain

## Abstract

During the last five years, CASA has been working at designing, manufacturing and testing innovative supporting platforms able to fulfil the stringent stability requirements imposed to these systems under severe environments. They were the consolidation of previous works on high stability structures.

The various tasks started with the Isostatic mounting platforms project, under ESA contract, and the latest design has been implemented in the SILEX experiment. The SILEX (Semiconductor Laser Intersatellite Link EXperiment) is the main core of the European Space Agency development activities for bringing the required intersatellite connections technologies to flight standards. The optical technologies are the most appropriate solution to support such links.

The experiment requires an optical head enclosure consisting of various optical head equipment fixed to an optical head bench and aligned with fine tolerances which are to be maintained throughout the space mission.

This paper presents briefly the several approaches for the optical head bench design and emphasises the work performed and the results obtained during the development test campaigns and the qualifications tests.

Main objective of the Development test campaigns were: the characterization of the dimensional stability of each component of the global design upon the most important instability contributors (thermal loads, thermal cycling, moisture desorption, creep, ...) and verification of the influence of the main manufacturing parameters on the design performances. The Test Campaign demonstrated that the complete unit exhibits good performance.

## 1. Introduction

Nowadays the space to space optical links represent one of the latest developments in satellite communication technology. These developments are aimed to design the optical terminals required for these intersatellite/inter orbit communication links. Such optical terminal typically includes an optical Head Enclosure in which there are located several

critical equipments (transmitting laser diodes, fine pointing mechanisms, tracking sensor...) mounted onto an optical Head Bench which, in consequence, shall show challenging performances and features such as:

- Stringent alignment tolerances and high stability among the different equipments.
- High flexibility in the arrangement of the units.

- High stiffness to mass ratio.
- Good thermal decoupling with respect to its interface attachment point.

In this frame CASA has been working in the design, manufacturing and testing of several supporting baseplate concepts able to fulfil the above related performances and features.

These activities started with the Isostatic Mounting Platform Project (ESA Development Program) and they had an specific application on the design and development of an Optical Head Bench for the SILEX project.

In both cases the Optical Bench consists of two parts:

- The Optical Head Bench Baseplate: It supports the optical equipments and ensures highly stable long and short terms alignments for those units.
- The Optical Head Bench Attachment Devices: They give isostatic fixation between the baseplate and carrier structure, allowing differential expansion between them.

Figure 1 shows an overview of the Optical Head Bench.

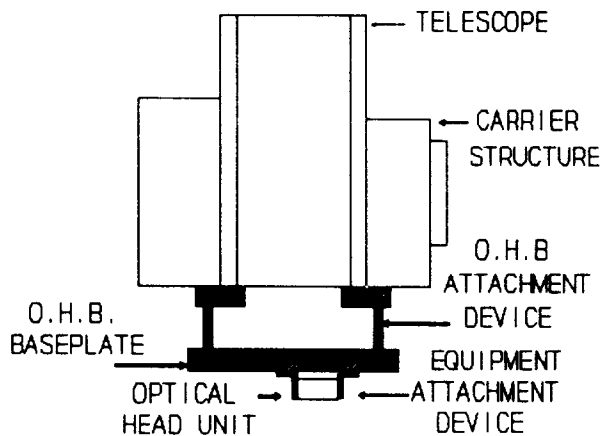


Fig. 1. Optical Bench Lay-out

## 2. Design drivers

Table 1 shows the SILEX OHB main requirements.

ITEM	REQUIREMENT
Stiffness	> 130 Hz
Mass	< 4 Kg
Strength upon 38 g quasistatic load x, y, z axis	Safety margin > 0
Long term stability upon <ul style="list-style-type: none"> <li>- moisture desorption</li> <li>- gravity release</li> <li>- ground testing effects</li> <li>- quasistatic loads</li> <li>- L.T. thermal variations</li> <li>- materials ageing</li> </ul>	Maximum optical paths: <ul style="list-style-type: none"> <li>• misalignments 0.5 mr/500 mm</li> <li>• displacements 5 <math>\mu</math>m/100 mm</li> </ul>
Short term stability upon short term thermal environment	TSDU/LDT units misalignment < 0.004 mrad

Table 1. SILEX OHB Main Requirements

This table gives an idea about the structure design criticality and it allows to establish the main design drivers:

- **HIGH DIMENSIONAL STABILITY:**  
This point leads the material and processes selection and also demands the necessity of an adequate test facility to verify with a great accuracy its fulfilment.
- **HIGH STIFFNESS TO MASS RATIO:**  
This point affects the material selection and leads the dimensioning of the elements.
- **LOCAL AREAS:**  
Local areas (i.e. isostatic devices, insert, ...) demand local solutions which take into account all affected aspects: materials, design, processes.

Each OHB entity was then looked at from different aspects as to derive, based on the previously mentioned key design points, the particular design drivers (Table 2) and, according to these drivers, generic design solutions were taken as to configure the preliminary baseline.

OHB ENTITY	DESIGN ASPECT	DESIGN DRIVER
O.H.B. BASEPLATE	Materials	- High Specific Stiffness - Low sensitivity to instability contributors
	Design	- High Inertia to mass ratio - Plane Isotropic behaviour
O.H.B. ATTACHMENT DEVICES	Materials	- High Specific Stiffness and Strength
	Design	- Two rigid degrees of freedom - Four ideally free d.o.f. - Good compromise between isostaticity and buckling - Thermal decoupling
FIXATION ELEMENTS	Materials	- Low density - Machinability - Good dimensional stability
	Design	- Dismountability

Table 2. Design Drivers

### 3. CASA development/design

After technical requirements were analyzed in depth, a trade-off study of several innovative concepts for the OHB was carried out, at the first stages of the IMP programme, to select the most appropriate design. The finally selected baseline consists of the following parts (Fig. 2):

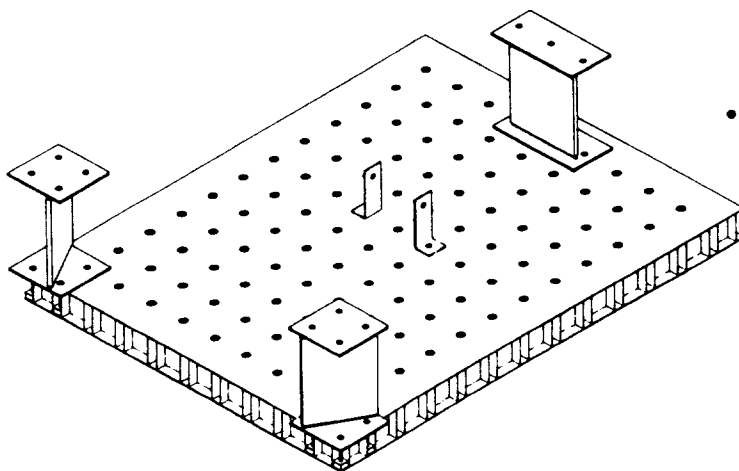


Figure 2. Optical Bench Components

- Baseplate: It is a sandwich of CFRP (GY70/Code 87: (60,0,-60),) skins and CFRP/Invar core. The sandwich core is manufactured by assembling CFRP strips in a structure of biparallel laminate. Adequately distributed slots are machined to interlock the strips in a whole core. Attachment nodes (Fig. 3), made of invar, are located in the vertices of the biparallel mesh and they will be bonded to all around strips, giving a regular grid of fixation points (212) in both sandwich sides, with a perfect symmetry with respect to the three coordinate planes.
- Optical Bench attachment Devices made of titanium in order to obtain a good thermal decoupling.

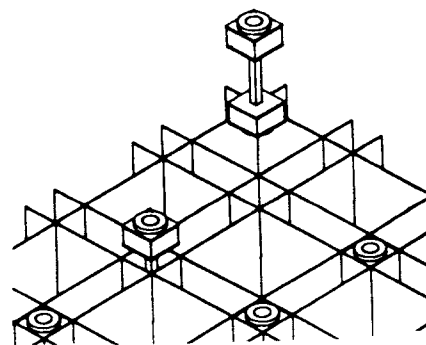


Figure 3. Core Assembly

As a back-up solution, a very promising baseplate concept was selected for the IMP. This alternative design was called triple sandwich. It consists on two outer standard CFRP sandwich separated by means of an intermediate CFRP structure (Fig. 4 ).

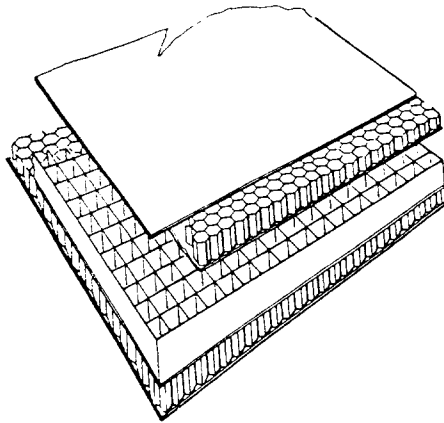


Figure 4. Triple sandwich

When the IMP OHB was not totally characterized, CASA was involved in the SILEX project, with the necessity of selecting a design that had to fulfil similar requirements to IMP ones.

A trade-off was carried out considering three alternative concepts for the baseplate:

- A. IMP baseline design: sandwich core by assembling biparallel CFRP strips.
- B. IMP back-up design: triple sandwich.
- C. Standard sandwich with aluminium honeycomb core.

Main aspects of this trade-off are shown in Table 3.

Trade-off criteria	Baseplate concept		
	A	B	C
Mechanical performances	1	2	3
Associated mass	1	2	3
Flexibility	3	2	1
Experience/associated risk	3	2	1
Cost	3	2	1

Table 3. Trade-off evaluation

The high weighting factor considered for aspects like the experience, associated risk and concept flexibility, derived in the C option selection.

For the O.H.B.A.D. the same philosophy as in the IMP was considered: single titanium piece with reduced thickness area.

The fixation points in the baseplate were made also in Invar.

Figure 5 shows an overview of the OHB generic design.

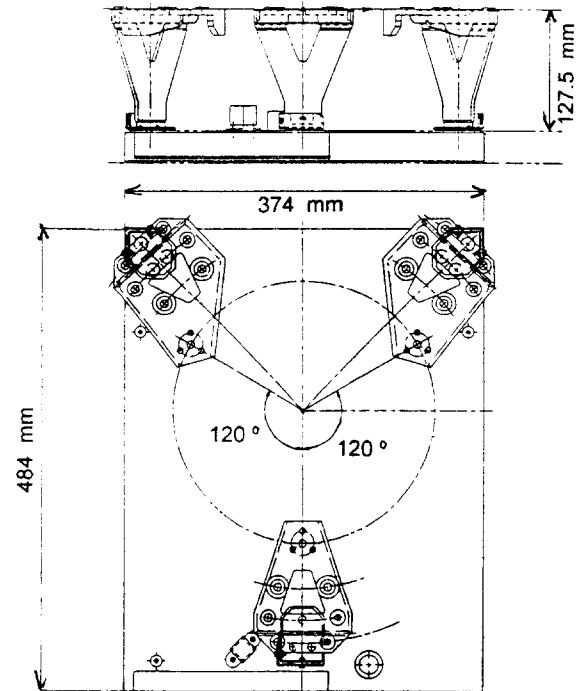


Figure 5. SILEX OHB design overview

## 4. Material characterization

### 4.1. Material selection

As a general idea, all materials involved in this kind of structures must provide stability, both dimensional and mechanical. Dimensional stability refers to the geometry of a component which, once established, remains fixed during handling and use. The successful performance of space baseplates greatly depends on the properties of materials used in their construction. The requirements imposed on them are derived from this, besides those applied to materials for space structures. The entities can be classified under the material type point of view:

- A) CFRP material parts: - Baseplate
- B) Non-CFRP material parts: - Attachment devices  
- Attachment points

A) CFRP materials: An ultra-high modulus fiber is needed to provide enough specific stiffness. The dimensional stability of resins depends on how much it is affected by the moisture, the temperature, and the thermomechanical cycling. Commercial low moisture absorption space qualified resins processed with ultra-high modulus fibers were very few.

The final choice of the system CODE 87/GY-70, was taken after considering CASA's past experience with this material, and the high degree of knowledge available of it. With this material, the selected design provides high stiffness to mass ratio and good dimensional stability behaviour.

During the development of the SILEX project, cyanate resins processed with ultra-high modulus fibers appear in the market. Actually they would be an advantage candidate for this kind of applications, mainly due to their great stability under thermal cycling and the actual CASA experience with these materials.

B) Non-CFRP materials: The low thermal conductivity of the Titanium (17 w/m °K) and the design of the O.H.B.A.D. provide the required decoupling.

The attachment points were considered as a critical area due to the strict requirements imposed to the material to be made of: very low density, very low thermal expansion coefficient, good mechanical properties, and easy mechanicability.

The low thermal expansion coefficient of the Invar ( $6 \cdot 10^{-7} \text{ }^{\circ}\text{C}^{-1}$ ) makes it a good candidate for

precision applications, but its high density advices against its use in space structures where weight is a major factor. With the aim of finding a more suitable material, a research was done considering different types of materials (Table 4).

- Light metals, like Aluminium (2.5 gr/cc) or Berilium (1.85 gr/cc) were disregarded because of their high CTE ( $25 \cdot 10^{-6} \text{ }^{\circ}\text{C}^{-1}$  and  $12.5 \cdot 10^{-6} \text{ }^{\circ}\text{C}^{-1}$  respectively).
- Glass ceramics, in spite of their low CTE, are not considered because the procurement in small quantities is difficult and the machinability is complicated.
- Graphite presents low density and low CTE, but is not a structural material.
- Metal matrix composites (Al) can be designed to obtain the required properties by means of the location and orientation of the reinforcement in sufficient quantity and with the proper direction. In regard to that, Aluminium matrix composites were considered as the baseline for the manufacturing of the attachment nodes. Unfortunately, a further step of manufacturing carbon fiber reinforced aluminium nodes did not provide the expected results. The state of the art of this technology lacks of repeatability and the material obtained was anisotropic in terms of CTE. At this point, it turns out that Invar remains the best material for the manufacturing of the nodes.

MATERIAL	DENSITY	C.T.E.	MACHINABILITY
Graphite	1.6	2.4	Easy
Zerodur	2.53	0.1	Very difficult
U.L.E.	2.2	0.1	Very difficult
Zirconium	3.44	2.2	Difficult
Silicon nitride	3.28	2.9	Difficult
Silica	2.2	0.4	Difficult
Silica composite	2.2	0.5	Difficult
C.F./Al composite	2.5	2.	Easy

Table 4. Material Properties



## 4.2. Material testing

In order to verify that the thermomechanical properties of the selected materials really show a behaviour according to the theoretically predicted values a complete material characterization test campaign was carried out. An additional objective of this test campaign was to determine the degradation of the most important properties when the material is cycled. As a summary, Figure 6 shows the testing activities flow logic.

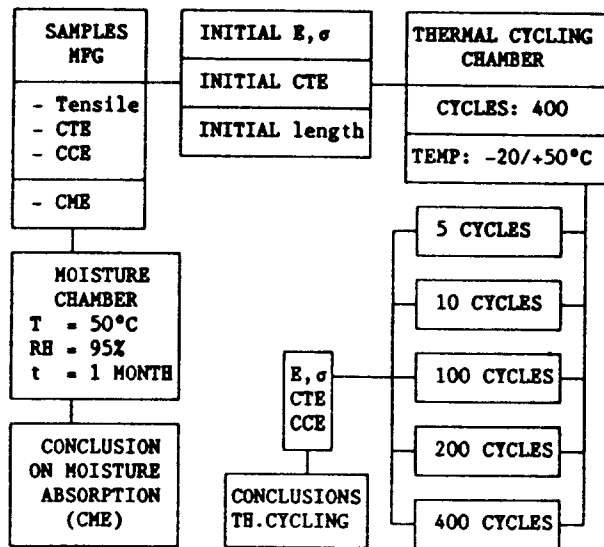


Figure 6. Material Testing Flow Logic

From the test campaign results the following conclusions could be derived:

- The thermomechanical properties of the different materials show test values in the range of the assumed data (Table 5).
- Young Modulus of the CFRP laminates is not significantly affected by the thermal cycling.
- The coefficient of thermal expansion of the CFRP laminates seems to become more negative when the material is cycled, due to the increasing dominance of the carbon fibre.
- The water absorption and the length variation induced by the swelling of the resin show test measurements in the range of the predicted for the performed test (Accelerated process: RH = 95%, T = 50 °C).
- The length variations induced in the CFRP laminates by the thermal cycling is an effect of relative importance:  $\Delta l/l = 20 \times 10^{-6}$  (stabilized after 50 cycles).
- It can be concluded that the distortions induced by the pointed phenomena (moisture, thermal expansion, cycling...) remain in the allowed range.

	TEST	EXPECTED VALUES	TEST VALUES
CFRP Laminate  (GY70/Code 87: (60,0,-60) <sub>s</sub>	VF	$60 \pm 3\%$	58.8%
	$\rho$	$1.7 \text{ g/cm}^3$	$1.65 \text{ g/cm}^3$
	E	102 GPa	112 GPa
	$\Delta E/\text{cycl.}$	---	+ 2 GPa
	CTE	$-8 \times 10^{-7} \text{ }^\circ\text{C}^{-1}$	$-7.0 \times 10^{-7} \text{ }^\circ\text{C}^{-1}$
	$\Delta \text{CTE}/\text{cycl.}$	---	$-5.0 \times 10^{-7} \text{ }^\circ\text{C}^{-1}$
	CME	0.017	0.0168
	CCE	---	$18.3 \times 10^{-6}$
Invar	CTE	$5.0 \times 10^{-7} \text{ }^\circ\text{C}^{-1}$	$3.5 \times 10^{-7} \text{ }^\circ\text{C}^{-1}$
	$\rho$	$8.1 \text{ g/cm}^3$	$7.95 \text{ g/cm}^3$

Table 5. Material Tests Results

## 5. Component tests

These tests presented evaluate the component performances calculated theoretically in preliminary analysis phase and, in this way, confirm the design configuration by means of the results obtained in this test campaign.

The baseplate was subjected to the following tests:

- Modal survey (free-free conditions): to characterize the stiffness behaviour of the baseplate.
- Thermal test: to determine the thermal conductivity in the different directions.
- CTE, CME Tests: to verify the dimensional stability of the baseplate.

The isostatic devices were subjected to dynamic tests (modal survey) in order to determine the stiffness behaviour of the referred components.

### Component Test Results

The tests performed in the different components

showed that the mechanical characteristics were, in both cases (SILEX and IMP), within the range of the theoretically predicted values (table 6 and 7), with some small deviations discussed hereunder.

- The baseplate frequency study showed a good correlation between predictions and tests, with low deviations in the three early eigenmodes, in both cases.
- The thermal test gave longitudinal conductivity results better than the specification ones, whereas the transversal conductivity was worse than required.
- The CTE and CME test data were very close to the predicted ones.
- The isostatic devices modal survey tests showed that the mathematical models used in the structural analysis were very representative.

The global result for both test campaigns (for IMP and SILEX) clearly indicates that the selected materials are appropriate for the required applications and also that the selected designs seem to be able to meet all the specified requirements.

Component	Test	Expected Values	Test Results
Baseplate	f1	634 Hz	640 Hz
	Modal f2	1040 Hz	984 Hz
	Survey f3	1322 Hz	1298 Hz
	Ther. $\lambda_l$	28 W/m °C	33.5 W/m °C
	Cond. $\lambda_t$	40 W/m <sup>2</sup> °C	30 W/m <sup>2</sup> °C
	CTE <sub>x,y</sub>	-1.1 x 10 <sup>-6</sup> °C <sup>-1</sup>	-.8 x 10 <sup>-6</sup> °C <sup>-1</sup>
OHBAD	Dim. CTE <sub>z</sub>	.6 x 10 <sup>-6</sup> °C <sup>-1</sup>	.9 x 10 <sup>-6</sup> °C <sup>-1</sup>
	Stab. CME	0.025	0.02
	f1	8. Hz	8.6 Hz
OHBAD	Modal f2	35.6 Hz	37.9 Hz
	Survey f3	39.7 Hz	40.7 Hz

Table 6. IMP Component Test Results

Component	Test	Expected Values	Test Results
Baseplate	f1	811 Hz	797 Hz
	Modal f2	1165 Hz	1042 Hz
	Survey f3	1584 Hz	1514 Hz
	Ther. $\lambda_1$	58.5 W/m °C	73.7 W/m °C
	Cond. $\lambda_1$	80.0 W/m <sup>2</sup> °C	74.6 W/m <sup>2</sup> °C
	CTE <sub>x,y</sub>	4.5 x 10 <sup>-7</sup> °C <sup>-1</sup>	6.0 x 10 <sup>-7</sup> °C <sup>-1</sup>
	Dim. CTE <sub>z</sub>	3.2 x 10 <sup>-5</sup> °C <sup>-1</sup>	3.4 x 10 <sup>-5</sup> °C <sup>-1</sup>
	Stab. CME	170 x 10 <sup>-6</sup>	125 x 10 <sup>-6</sup>
OHBAD	f1	8.91 Hz	9.76 Hz
	Modal f2	22.45 Hz	14.44 Hz
	Survey f3	40.59 Hz	39.91 Hz

Table 7. SILEX Component Test Results

## 6. Prototype manufacturing

In both, IMP and SILEX Projects, after a complete design confirmation by the different development steps (analysis, material tests, component characterization), the manufacturing of a prototype, fully representative, was undertaken. The aim of these final stages of the programmes was to produce a complete first model which could determine the feasibility of the whole assembly and, in a later phase, could be used to test, at assembly level, their mechanical and dimensional stability performances.

The experience acquired during the feasibility tests was used to adequately modify the manufacturing tooling and processes and, in this way, to correct the detected deviations.

The final prototypes corrected the previous manufacturing deviations and their demonstrated that, from a manufacturing point of view, the proposed baselines were suitable designs.

Figure 7 shows the IMP OHB prototype and Figure 8 shows the SILEX OHB Engineering Qualification Model.

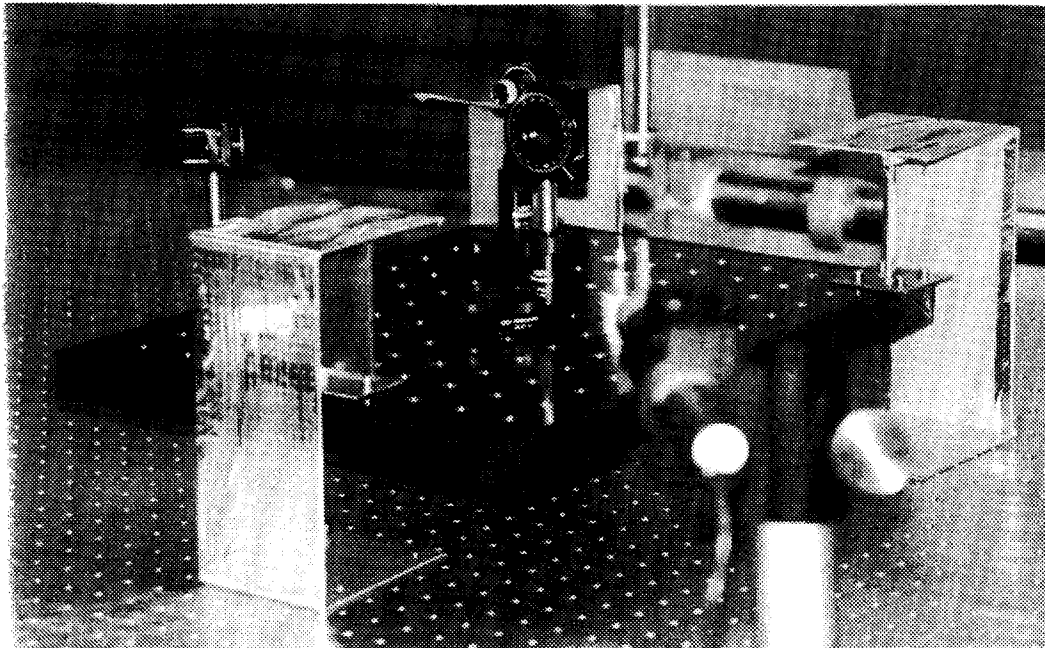
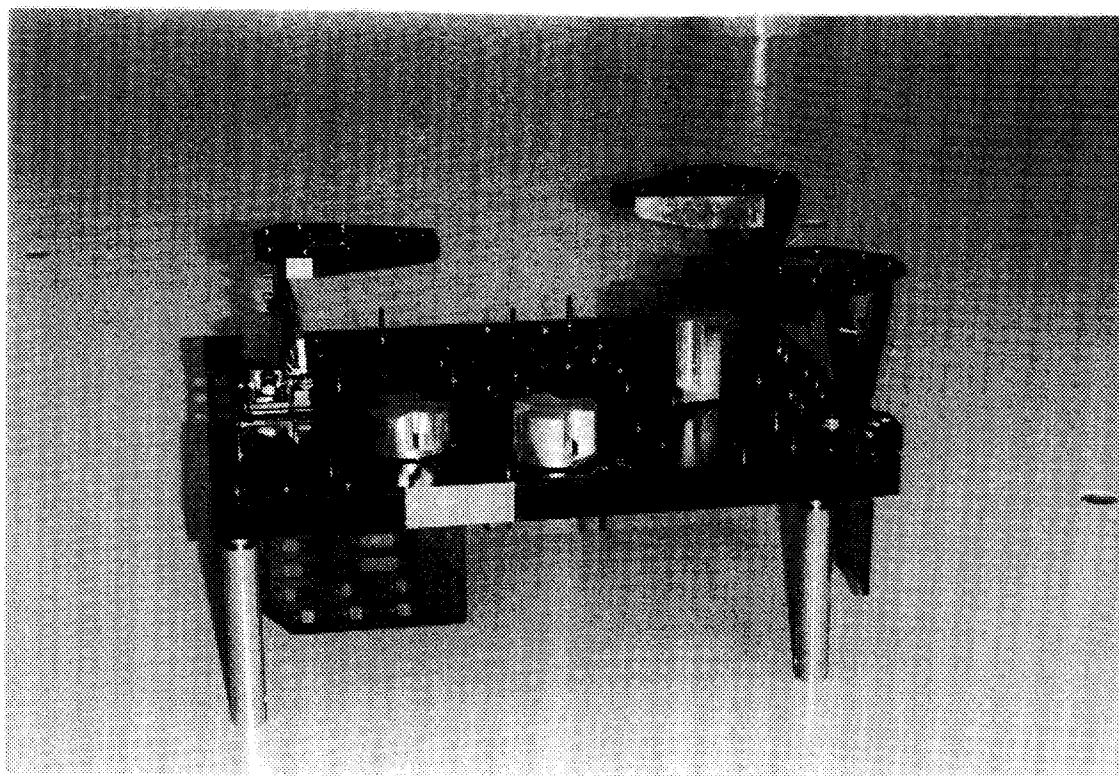


Figure 7. IMP Prototype



**Figure 8. SILEX OHB Engineering Model**

A IMP Verification program has been initiated with the objective of determining by test the OHB dimensional stability performances.

## 7. Conclusions

With the SILEX project, CASA consolidates its experience on high stability space structures with this design, based on previous works in the same field:

Isostatic mounting platform and high stability telescope structures. The designed, manufactured and tested OHB exhibits: optimize stiffness to mass ratio and alignment stability in the short and long term.

After engineering qualification model validation, CASA has manufactured, tested and delivered to MATRA Space the first and second flight models, for satellite integration.

# The CMS Inner Tracker Barrel Mechanical Structure

M. Price, B. Nicquevert, C. Hauviller  
CERN - PPE/TA1  
CH 1211 Geneva 23 - Switzerland

## Abstract

The design philosophy of the proposed support structure of the barrel part of the CMS inner tracker is described. Finite element calculations of the behaviour of two different implementations of this structure are presented, together with the first ideas on the manufacturing process. After a technical description of the detecting elements, the general layout is discussed, taking into account the demands on precision.

## 1. Introduction

The CMS (Compact Muon Solenoid) detector is a general purpose apparatus intended to run at the highest luminosity of the LHC. Although especially optimised to search for the SM Higgs boson over the mass range 90 GeV to 1 TeV it is also capable of detecting a wide range of signatures from alternative electro-weak symmetry breaking mechanisms and of studying beauty, top and tau physics at lower luminosities. The detector is designed to identify and measure muons, photons and electrons with high precision. The core of the detector (including the inner tracker) is situated in a 4 T magnetic field generated in a superconducting solenoid. This leads to a compact design of the muon spectrometer without compromising the momentum resolution... The inner tracker is intended to measure all high  $p_t$  charged tracks with a momentum resolution of  $\Delta p/p \approx 0.1 p_t$  ( $p_t$  in TeV) in the range  $|\eta| < 2.5$ .

The central tracker measures the momentum of charged tracks by measuring the radius of curvature of their helical trajectories in the strong magnetic field. For particles with very high transverse momentum (i.e. the component of momentum perpendicular to the field direction) this is equivalent to measuring the sagitta of the particle's

path. The coordinates in  $r, \phi$  are measured using high precision detectors and it is clear that, in order to have a sagitta measurement which is as precise as possible, the detector elements should be very fine grained and positioned with an accuracy at least equivalent to the detector grain.

The Central Tracker of the CMS experiment has a diameter of 2.6 m and a length of 7 m. A high momentum particle emerging from the interaction region passes initially through four silicon micro-strip detectors and then through 8 Micro-strip Gas Chambers (MSGCs). Both of these detector types have strips as detector elements; in the case of the silicon detectors the strip spacing is 50  $\mu\text{m}$  and in the case of the MSGCs the spacing is 200  $\mu\text{m}$ . In the central region of the tracker (i.e. for small values of  $z$  and for particles with polar angles approaching  $\pi/2$ ) the detector strips lie parallel to the beam axis and in the "forward" region (corresponding to small values of the polar angle) the strips are perpendicular to the beam axis. A layout of the device is shown in Figure 1.

Considerable work has been carried out on the design of both the barrel and forward region. Since the authors have been much more involved in the design of the barrel region, we shall concentrate on this.

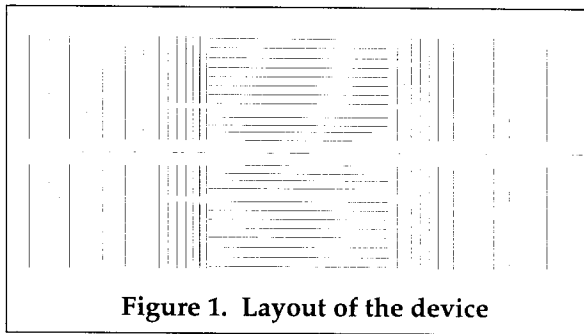


Figure 1. Layout of the device

## 2. Detectors

### 2.1. Silicon micro-strip detectors.

These devices are fabricated from thin (typically 300  $\mu\text{m}$  thick) silicon wafers. The size of the wafer is essentially determined by the maximum size which can be industrially processed (4 inch wafers are an industrial standard). Other important factors in determining the maximum size of these detectors are:

1. the fact that the noise generated in the front end electronics is governed by the capacitance of the strips, the higher this capacitance the more noise is generated;
2. especially in the regions closest to the interaction point, the rate of particles passing through the device is very large and there is every interest in reducing the area of the strips.

For these reasons the maximum practical strip length is about 6 cm. The signals are read out by fast electronics. One of these front end read-out chip reads 128 channels. To prevent an excessive amount of data transfer the data is already treated on the read-out chip and only the addresses of those channels within the strip which read a signal are transmitted to the control room. This data is converted to a light pulse by an opto-coupler and this pulse is sent to the control room along a 0.25 mm diameter optical fibre. In the present design one complete silicon micro-strip detector will have eight such chips and thus eight output optical fibres. In addition each detector element will have three power leads ( $\pm 2$  V and ground), a high voltage connection, several control optical fibres and a cooling water pipe. In fact, the services will make up a substantial part of the whole detector mass.

### 2.2. Micro-Strip Gas Chamber

Figure 2 shows a cross-sectional view of a MSGC. It can be seen that there are anode strips (with widths between 5 and 10  $\mu\text{m}$ ) and 50  $\mu\text{m}$  wide

cathode strips, mounted on a glass substrate. At some 3 mm from these strips there is a cathode plane. By applying suitable voltages to the cathode plane and to the two sets of strips, electrons produced during the passage of charged particles are attracted to the anode strips and, by the process of gas amplification, produce a measurable signal of some  $10^4$  electrons at the entrance to the amplifier. The front end electronics is the same as that used in the Silicon detectors but, due to the difference in pitch, the density is four times less. The services will be essentially the same as for the Silicon detectors with the exception of two extra high voltage connections.

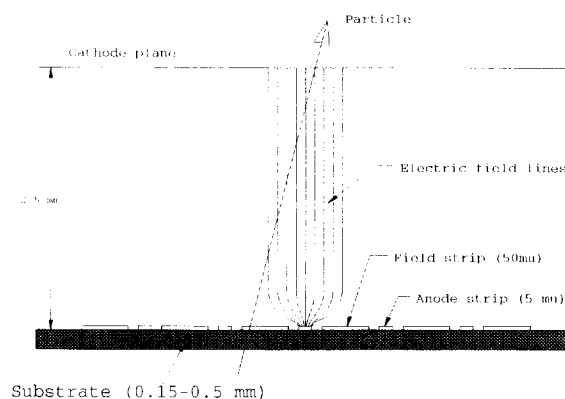


Figure 2. Cross-sectional view of a MSGC

In the barrel region the magnetic field is parallel to the read-out strips in both the silicon detectors and the MSGCs, i.e. the magnetic and electric drift fields are at right angles. As a result of this the electrons are subject to an additional force described in direction and in magnitude by the vector product  $\mathbf{E} \wedge \mathbf{B}$  making them drift with an angle to the electric field. To compensate for this effect, the MSGCs must be tilted at an angle of some  $16^\circ$  compared to their position with no magnetic field. This value is about  $8^\circ$  for the silicon detectors. Note that this effect does not exist in the forward region where the electric and magnetic fields are zero.

## 3. Layout

### 3.1. Geometry

In the CMS Letter of Intent [2], it was envisaged to arrange the 12 detector layers in the barrel region (four layers of silicon detectors and eight layers of MSGCs) in the form of three "super-layers" where each super-layer was made up from four layers of closely spaced detectors. The principal disadvantage of this scheme is that the cables are "trapped" by the super layers; the only reasonable solution for cable routing is to direct

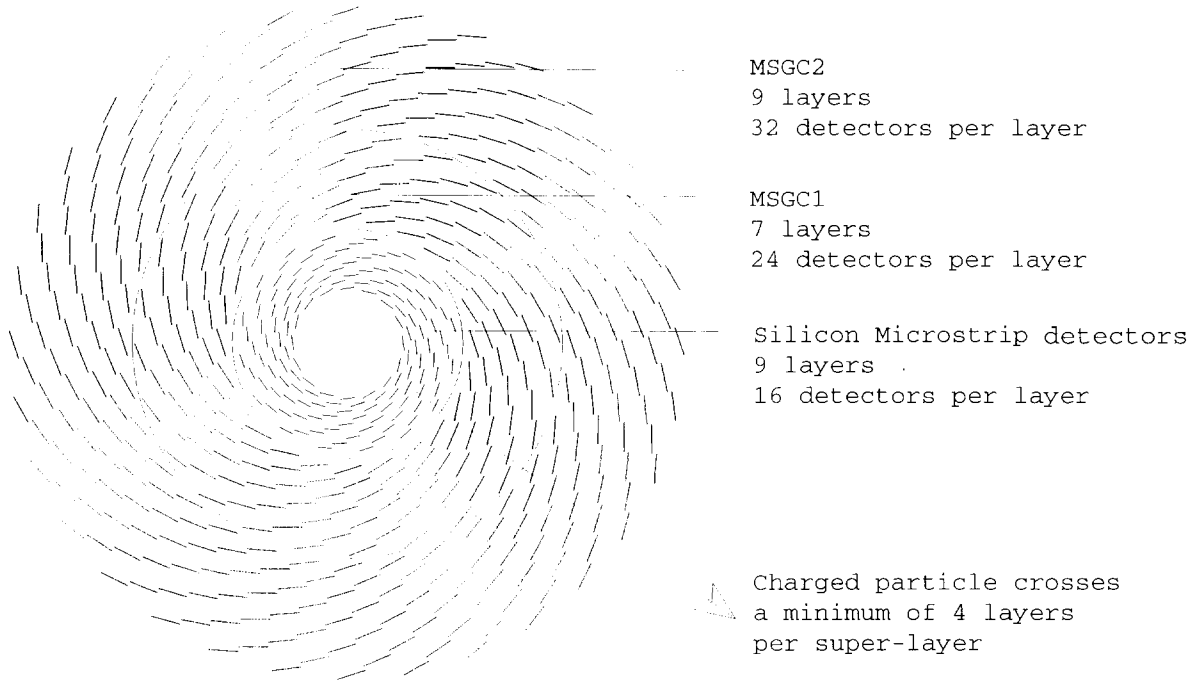


**Figure 3. The spiral layout**

them parallel to the beam axis and to bring them out radially at the region between the barrel and forward parts. This has the unfortunate consequence of adding to the quantity of material at certain critical polar angles. It was realised that the condition of having four crossing points per super layer could also be met by having more than four layers per super-layer and by having the appropriate spacing between detectors at a given radius. The result of this is the “spiral structure” in which there are 25 layers of detectors (9 Silicon, 7 MSGC layer 1 and 9 MSGC layer 2). As can be seen in Figure 3, the condition of having at least four crossing points per super-layer is still maintained. This layout, combined with the necessary tilt of the detectors because of the  $E \wedge B$  effect, leads naturally to channels through which the cables and services can be led out.

In the present design, the detectors are arranged in wheels. This arrangement is natural in the forward region but is a departure from conventional designs in the barrel region. The motivation behind this design was that it was considered wasteful in material to have longitudinal members (as in ladders supporting detector elements). The logic of this is that there has to be some form of support structure normal to the beam direction (the radial support structure) which takes the gravitational load and transmits this to the outside support structure. For a given maximum

deformation then, whatever the design of the total structure, the radial support structure will need the same quantity of material since this is governed by the total weight of the structure. Following this argument it was concluded that to have a device in which there was only radial support structures should produce a structure with a minimum of weight since unnecessary longitudinal support members could be dispensed with. It should be realised, however, that this reasoning is only valid if the radial support structure in the wheel concept can have the same configuration as in a space frame construction.

### 3.2. Demands on precision

As mentioned above, the silicon micro-strip detectors have a strip spacing of  $50\text{ }\mu\text{m}$  and the MSGCs of  $200\text{ }\mu\text{m}$ . It can be shown that, in fact, the associated measurement errors will be  $50/\sqrt{12}\text{ }\mu\text{m}$  and  $200/\sqrt{12}\text{ }\mu\text{m}$  respectively. To profit from this accuracy, the silicon detectors should ideally be positioned to within about  $10\text{ }\mu\text{m}$  with respect to each other while the corresponding figure for the MSGC detectors should be about  $40\text{ }\mu\text{m}$ . In most high precision trackers however, the actual positions of the detector elements are found using high momentum particle tracks. In this case the theoretical positions are used as starting points for the alignment procedure so that the absolute positioning accuracy of the detectors is still important. It is more important, however, that the

position of the detectors should not move with time. Clearly a structure which has small inherent distortions under load will have a higher resonant frequency (and thus will be less susceptible to vibrations). It is also to be expected that a stiff structure will have less deformation due to the other perturbing factors such as radiation damage and changing values of physical parameters due to humidity. For these reasons, it has been considered important that the deformations of the structure under load should be consistent with the 10  $\mu\text{m}$  and 40  $\mu\text{m}$  figures quoted above.

### 3.3. Working environment

The silicon detectors are subject to a very large radiation dose due to the crossing charged particles. This effect is exacerbated by the strong magnetic field which causes the tracks to curl and possibly pass through the same detector more than once. In addition there is a very large neutron background. This bombardment of particles damages the silicon and leads to a strong increase in leakage current. The effect can, to a certain extent, be reduced by running the silicon detectors at low temperature. At the current state of knowledge it is assumed that this temperature will be in the neighbourhood of 5°C. On the other hand, there appears to be great problems in operating the MSGCs at these low temperatures. It thus appears necessary to thermally split the wheels into two regions with the central region at around 5°C and the outside part at 20°C. This will be done by having an active heat shield between the two regions.

As well as affecting the silicon detectors the radiation will obviously also cause damage to the material of the support structure.

### 3.4. Proposed solution

Figure 4 illustrates the basic barrel detector layout surrounded by a strut structure. This configuration was the first to be studied. As a result of the shortcomings of this configuration a modified structure with substantial cross bracing was proposed (see Figure 9). Finite element calculations have been performed on both structures using a variety of calculation methods. A discussion of these calculations will be the subject of the next section.

The choice of construction material is very important. One of the very stringent physics demands made on this detector is that the quantity of material, measured in terms of "radiation length<sup>(1)</sup>", should be as small as possible in order to avoid spurious production of gamma rays and

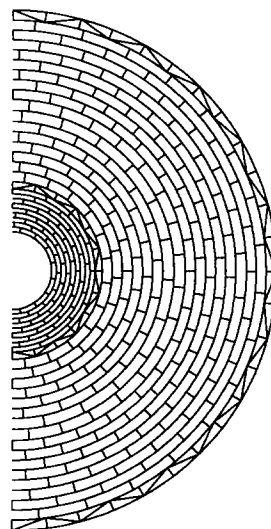


Figure 4. Basic barrel detector layout

unwanted deflections of the charged particles. The radiation length decreases with increasing atomic number so that materials with low  $Z$  are favoured. However, the radiation length is not the only important property of a construction material. Clearly the material's Young's modulus determines the distortions under load and, in fact, the product of radiation length and Young's modulus ( $EX_0$ ) is a convenient measure of the suitability of a given material. On account of its low atomic weight beryllium is often cited as an interesting material for the construction of trackers and its  $EX_0$  of 106 GPa.m is one of the highest for any material. In the present context, beryllium's comparatively large coefficient of thermal expansion is a disadvantage and there are severe doubts about the safety aspects of using this material. A good candidate, from the point of view of temperature stability, would be carbon-fibre resin composite. This has an added advantage in the proposed strut structure since the fibres could be laid in a quasi-longitudinal direction thus increasing the effective Young's modulus in the needed direction. All calculations have been carried out assuming a carbon fibre type M40J, embedded in an epoxy resin. This material has  $EX_0$  of 54 (worse than Beryllium). On the other hand, it is highly probable that the final construction material will have superior properties.

1. The radiation length of a given material is the distance that a high energy electron travels through the material before, on average, being deviated by a nucleus in the material to produce a gamma ray.



## 4. Finite element calculations on the structure

The first results of the finite elements calculations, done on the structure from the static and dynamical point of view, are briefly summarized.

### 4.1. Geometrical layout

As it has been specified above, we have studied a wheel which has to support the detectors following a spiral layout. The wheel consists of two plane structures, detectors being hung between (see Figure 5). Each plane disc has rings and radial straight elements (see Figure 4). In a second step, cross-bracing struts are included for the outer most region of MSGCs.

The inner and outer diameters of the plane discs are respectively 0.85 and 2.55 m. The distance between the plane discs is 180 mm (see Figure 7).

### 4.2. Modelling and mesh

The software *Mechanica*<sup>®</sup> release 6, from Rasna Corporation, which is doing a *p*-analysis (increasing the degree of the interpolating polynomial) has been used for these calculations. They are done on a 3D-model. The most important results

have been checked with *Ansys* 5<sup>®</sup> software, and are similar within a 1% accuracy.

Two kinds of structures have been considered. The first one is made of rectangular cells for the three different regions (Silicon, inner MSGC and outer MSGC). For the second one, it has been decided to reinforce the outer MSGC region by replacing radial struts by inclined ones, so that to create triangular cells (see Figure 9).

For both options, the mesh, loads, boundary conditions, materials and size of the cross-sections are the same. This is detailed in the following subsections.

The mesh was automatically generated by *Mechanica*, and is made of the so-called beam elements. Beams are two to nine nodes, following the degree of the interpolating polynomial.

### 4.3. Loads and boundary conditions

The loads on the structure are of two kinds:

- weight of the detectors, applied as forces on certain nodes; the mass has been determined following the values used for the materials budget calculation ([5]), and is between 24 and 35 g each. The total number of detectors is exactly 600, for a total mass of around 16.1 kg.

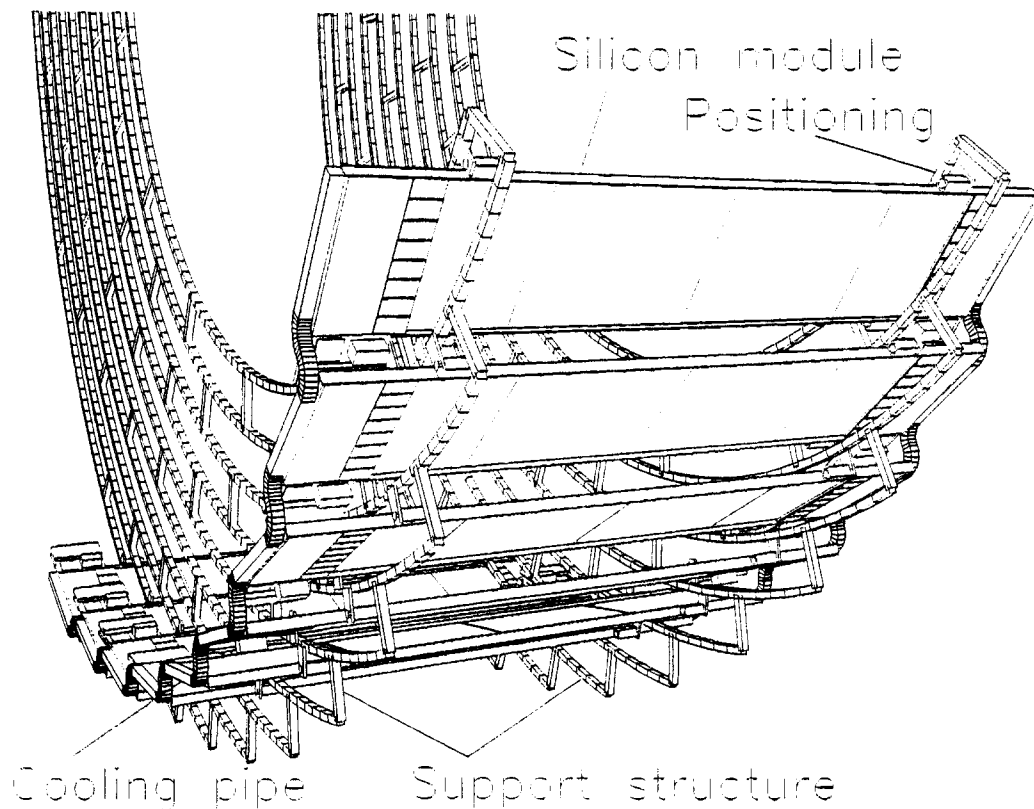


Figure 5. Perspective view

On each plane disc, half the mass is applied, i. e. 8 kg.

- gravitational load on the skeleton of the structure itself.

The weight of the cables and other services (cooling tubes...) is not taken in account for the first step.

The first calculations are done with a vertical structure, but the real structure will be put in the LEP/LHC tunnel in a place inclined at 1.39 % with respect to the horizontal plane. This inclination is taken into account in a second step.

For faster computing, it was decided, when possible, to cut the structure into two parts, despite the fact that it is not strictly symmetrical. Actually, the spiral layout was obtained by rotating one eighth of the structure, for the number 8 is the lowest common factor of 16, 24 and 32, which are respectively the number of cells per ring in each region (see Figure 3).

The boundary conditions in the symmetrical plane are: blocked in the  $y$  translation and  $z$  rotation, free otherwise. The support point is in the  $y=0$  plan, with  $x$  translation and  $z$  rotation free, other degrees of freedom blocked. For a whole wheel, the other support point is blocked in addition in the  $x$  translation.

#### 4.4. Materials and size of the cross-sections

As specified above, the material used is a carbon fibre reinforced composite, with M40J type (High Modulus) and epoxy resin. The equivalent mechanical properties are the following, the material being considered (wrong assumption, of course) as isotropic:

**Table 1 : Equivalent properties**

Young's Modulus (GPa)	Poisson's coefficient	Shear modulus (GPa)	Specific weight (kg/m <sup>3</sup> )
180	0.3	4.8	1680

All the struts, including the rings, have a rectangular cross-section, the size of which is one of the parameters of the studies. The thickness of 4 mm has been fixed constant all over the structure. The other dimension is different, depending on each region (Si, MSGC1, MSGC2). Due to the necessary space for the assembly of the detectors, the maximum values for the other dimension of the cross-

section of the radial or inclined struts are the ones given in the following table:

**Table 2 : Maximum size of cross-sections**

Si region	MSGC1 region	MSGC2 region
4x8	4x12	4x14

#### 4.5. Static analysis of the rectangular cells solution

##### 4.5.1. Skeleton of the structure

A first study [7] has been done on a 2D model. The parameter of the study was the transverse dimension of the struts. The criterion used is the weight of the structure, and a balance between the maximum displacement in the structure and the increase of this weight with the transverse dimension of the struts had to be found.

The first calculations have been made **without** the detectors. For the skeleton alone, and for various combinations of the transverse dimensions in the three different regions, the following cluster of points has been obtained:

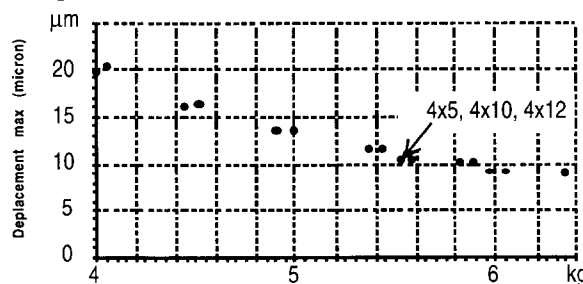


**Figure 6. Maximum displacement versus the weight of a plane disc**

It can be noticed that the optimised choice of transverse dimension could be 5 mm in the Si-region, 10 mm in the MSGC1-region and 12 mm in the MSGC2-region.

The stresses have never reached high levels: the highest one is a Von Mises stress of about 2 MPa, in the regions of the support points.

##### 4.5.2. Horizontal plane disc with detectors

The "optimised" structure will now be further studied, by putting on the weight of the detectors. A maximum displacement in the vertical direction of 24  $\mu\text{m}$  is obtained, the location being in the inner upper part, in the vertical mid plane. It appears that more than 50 % of this displacement is due to the weight of the detectors, half of this displacement is due to the silicon central detectors, which are heavier than the MSGCs.

#### 4.5.3. Influence of the inclination

When the plane disc is inclined of 1.39 % ( $0.8^\circ$ ), the  $y$  displacement keeps approximately the same. But the  $z$  displacement, normal to the structure, becomes very high: with no outer reinforcement (as the one showed on the Figure 4), it can reach up to 4 mm! With these reinforcements, it decreases to 2 mm, but it still stays too much.

#### 4.5.4. The double-structure with external skin

To have a correct apprehension of the behaviour of the structure, it should not be forgotten that the plane disc studied before is not alone, and the second plane disc of the complete wheel detector has to be taken in consideration. The benefit of the so-called sandwich-effect is added. To maximize this effect, an external skin has been added around the two plane discs, as shown in Figure 7:

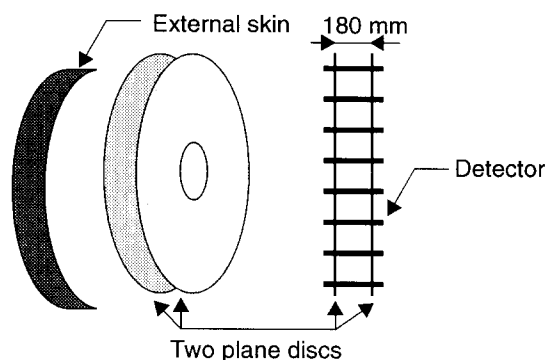


Figure 7. External skin

An external skin of 1 mm thick let the maximal normal displacement fall from 2500 to 400  $\mu\text{m}$ . A 2 mm thick skin gives a displacement of 370  $\mu\text{m}$ . The influence of intermediate struts is noticeable (more than 10 % of improvement).

#### 4.5.5. Radiation length

The definition of the radiation length is given above, page 4. The calculation of the relative radiation length has been made [6]. It appears that the structure with reinforcements and the relatively large cross-sections of  $4 \times 5$ ,  $4 \times 10$  and  $4 \times 12 \text{ mm}^2$  has a radiation length of about 5 % in the most thick regions. The radiation length seems not to be a critical problem. But the cables have not been taken into account...

### 4.6. Towards a more optimised structure: cross-bracing

#### 4.6.1. Theoretical considerations

Let's consider two different beams, of the same height, one being made of two rows of rectangular cells and the other being made of one row of triangular cells, two times higher. The cross-sections of the struts, the boundary conditions (clamped/free) and the loads are the same for both cases.

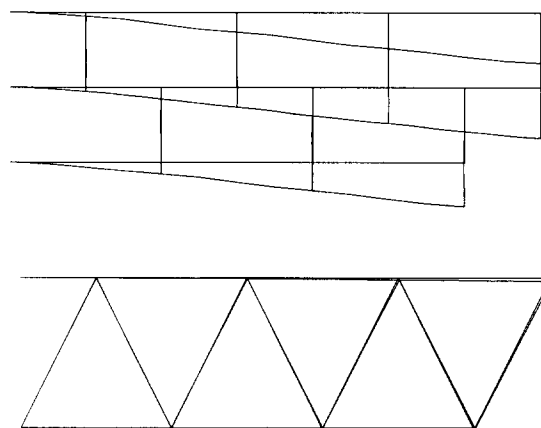


Figure 8. Two different layouts of struts

On Figure 8, the non deformed and the deformed shape are superimposed, and the amplification factor of deformation is the same for the two pictures. It can be seen that the second one is much less deformed (about 14 times less) than the first one. This is one of the reasons why it was decided to replace the eight outer layers of MSGCs by four double layers with cross-bracing struts.

#### 4.6.2. Static analysis results

New calculations [8] have proved a substantial improvement of the displacement. For a vertical plane disc, the maximum displacement is now less than 14  $\mu\text{m}$  (compared to the previous results of 24  $\mu\text{m}$ ) in the vertical direction.

As can be seen on Figure 9 (please note that the deformation amplification factor is 6000), the outer region is much less deformed than before. The central Silicon region, which the heaviest, weighs on the intermediate region, where the deformations are the highest. The typical local deformation of the rectangular cells in the upper part (stretched) and in the lower part (compressed) can be noticed.

Displacement Y  
Deformed Original Model  
Max +1.3377E-02  
Scale 7.0000E+03  
Load: load1

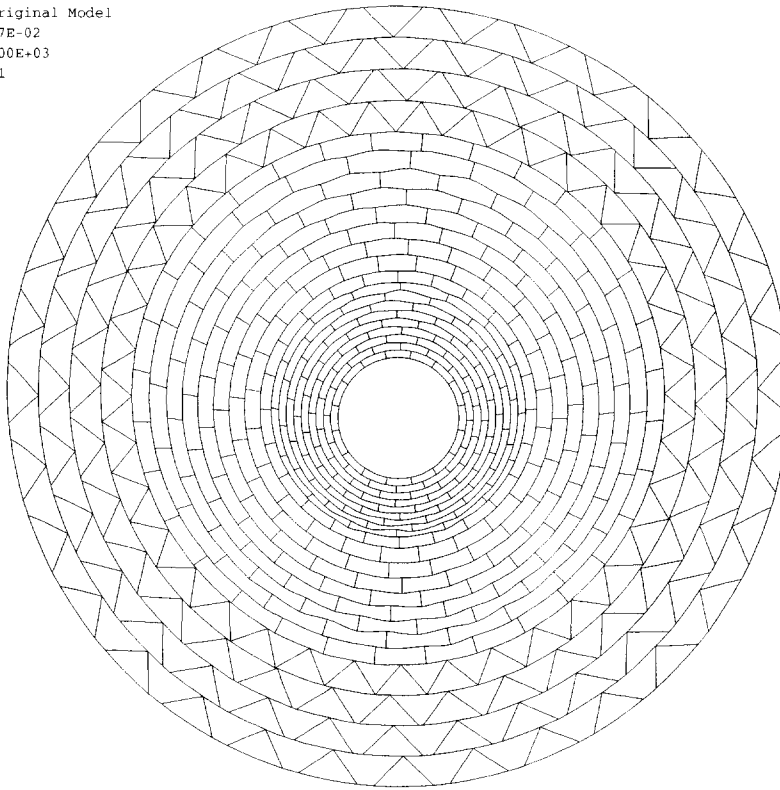


Figure 9. Structure with cross bracing (deformed)

#### 4.7. Dynamic analysis: first results

First calculations have been done on the eigenfrequencies and natural mode shapes of the disc structure (only skeleton). The first five frequencies are given in the following table:

Table 3 : Eigenfrequencies

N°	1	2	3	4	5
Freq (Hz)	1.67	2.40	6.81	7.32	7.33

The first mode is a global rotation around the horizontal axis, with high deformation in the region of the support points. The second mode is a pseudo-two-nodes mode, the whole plane of the structure passing through the median vertical plane. The third mode is a twist mode around the vertical axis, the horizontal one staying undeformed. The fourth mode is a full membrane mode; it is strongly coupled with the fifth one, a pseudo-three-nodes mode. These first five natural modes are given in Figure 10 and Figure 11.

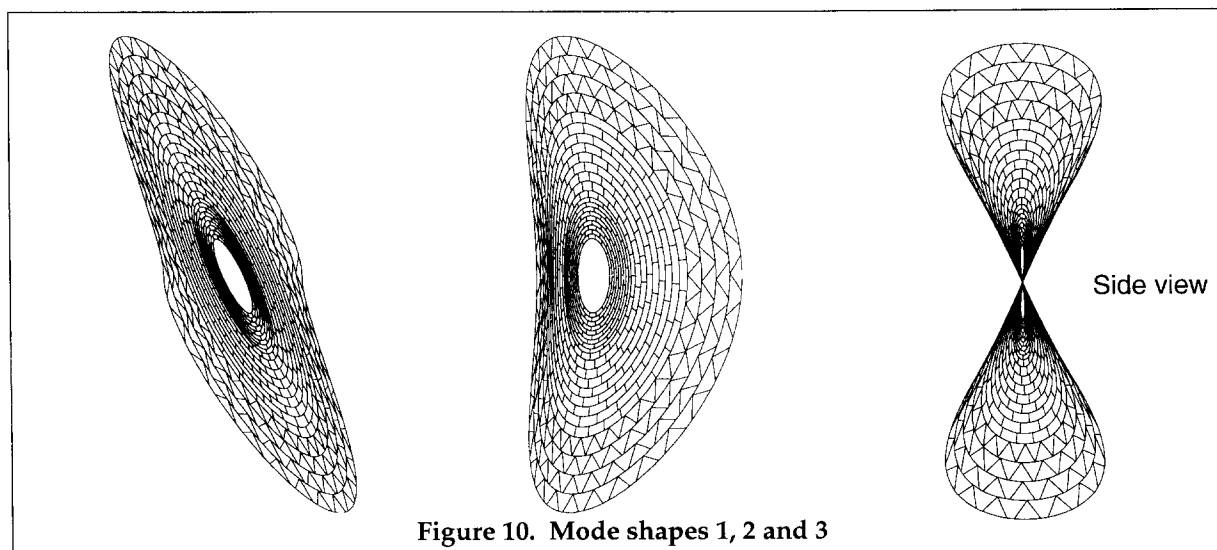


Figure 10. Mode shapes 1, 2 and 3

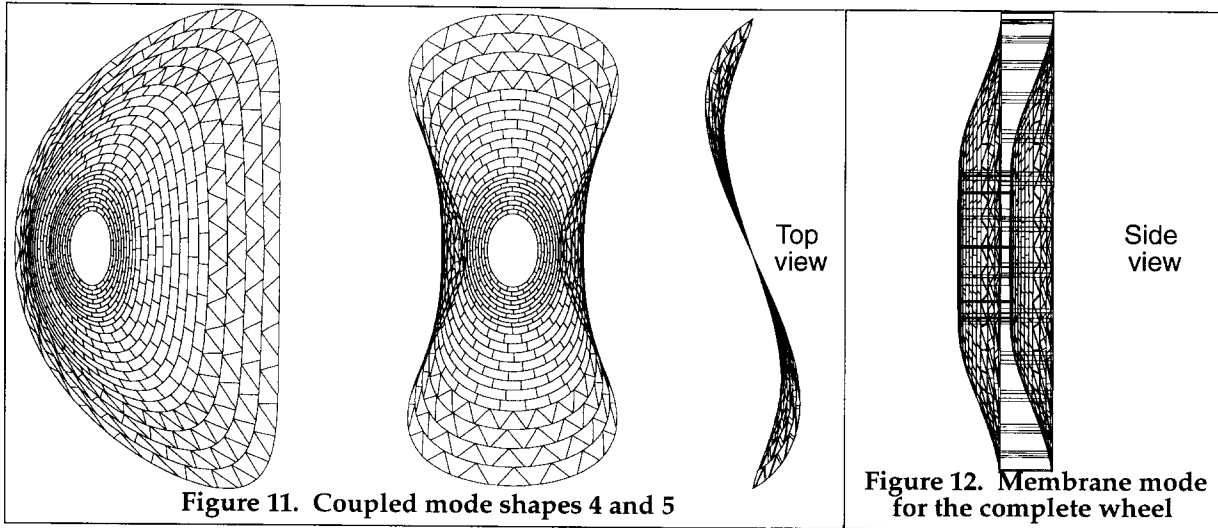


Figure 11. Coupled mode shapes 4 and 5

Figure 12. Membrane mode for the complete wheel

In the global structure of the barrel, plane discs are attached together along the axial direction. Most of these modes vanish, to the exception of the mode 4 (the membrane mode, see Figure 12), whose frequency goes up to 7.7 Hz. The second one (similar to the previous fifth one) has a natural frequency of 26.3 Hz. Nevertheless, it will be of great importance to control the excitation in the range of 5 to 60 Hz, to avoid too big displacements due to resonances in the structure.

#### 4.8. Deformation due to thermal constraints

Another source of deformations is due to the difference of temperature between the Silicon and the MSGCs regions. It has been decided to separate the two regions by a thermal shield in the intermediate region. First results are briefly summarized [9].

##### 4.8.1. Geometry and material properties

The global wheel with two parallel plane discs is considered. The discs are linked together with two cylinders. The inner cylinder (the thermal insulating shield) is joined with discs along the outermost layer of the Si region. The outer cylinder is joined along the outer edges of the discs, like the previous external skin. They both are 1 mm thick. Because of the symmetry, the 3D-model is a half wheel model.

The mechanical properties of the materials used are the same as previous. The cylinders are made of the same materials as the discs, and anisotropy is not considered. The coefficient of thermal expansion of the carbon fibre reinforced plastic is  $10^{-6} \text{ m.m}^{-1}.\text{K}^{-1}$  in a first approach.

##### 4.8.2. Boundary conditions and loading

As previous, the disc is supported on the edge in the horizontal mid plane. The left node is constrained in  $x$  and  $y$  directions, the right node is only constrained in the  $y$  (vertical) direction. The nodes along the symmetry boundaries are constrained in the  $z$ -translation and  $x$  and  $y$  rotations.

In addition to the gravitational loads, the nodes in the MSGC and Silicon regions are respectively constrained to  $20^\circ\text{C}$  and  $0^\circ\text{C}$ , the reference temperature being  $20^\circ\text{C}$ . Heat flows are not calculated, the structure being considered as thermally steady state (infinitely insulating shield).

##### 4.8.3. Results

Different cases have been studied, with or without thermal effects, and with or without the  $0.8^\circ$  inclination. Results are given in the Table 4.

Table 4 : Thermal influence

Inclination	$0^\circ$	$0^\circ$	$0.8^\circ$	$0.8^\circ$
Thermal expansion	0	1	0	1
$x$ max displ ( $\mu\text{m}$ )	2	10	2	10
$y$ max displ ( $\mu\text{m}$ )	13	20	13	20
$z$ max displ ( $\mu\text{m}$ )	2	9	31	38
Max stress (MPa)	3	10	3	10

Data are the maximum absolute values in the disc region, the cylinder region being excluded.

The thermal influence has to be taken into account:  $y$ -displacement are much bigger than without, and stresses are considerably increased, even if they stay in a compatible level with the materials.

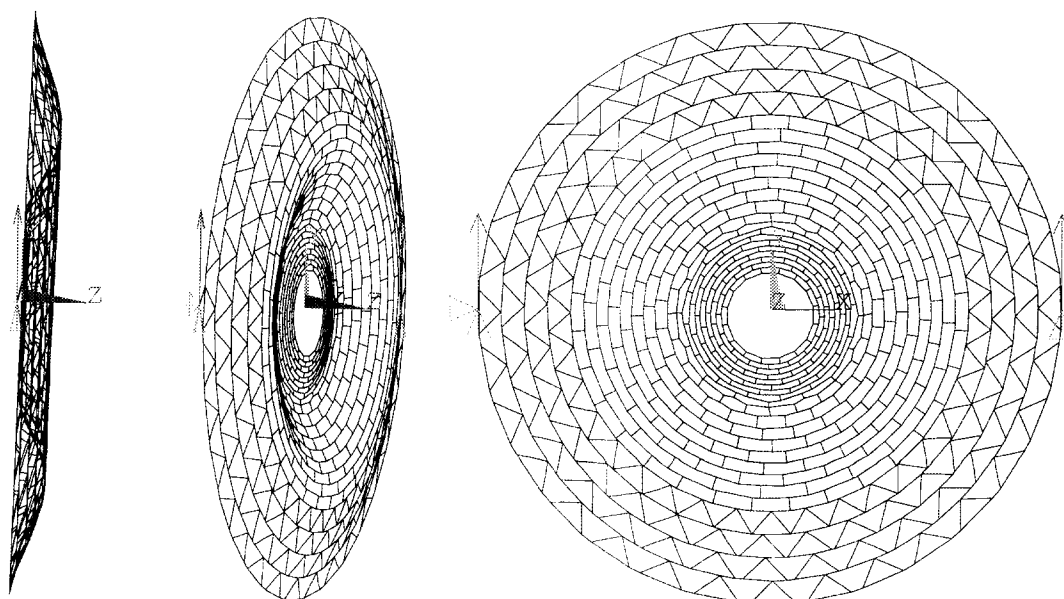


Figure 13. Deformed shape of the half wheel (the cylinders are not represented)

The  $z$ -displacement stays under  $50\text{ }\mu\text{m}$  with the two cylinders solution. For the reconstruction of the particles' track, this deflection could be considered as compatible, but the shape of the deformed wheel (see Figure 13) shows a relative weakness of the inner MSGC region (where cells are still rectangular). This weakness could be strengthened by local reinforcements.

## 5. Manufacturing

If the mechanical properties used in the design of the wheel are quite conservative, there is no doubt that a better material like M55J, M60J or even stiffer could be used to improve the performances.

On the other hand, many manufacturing options have been envisaged. The most straightforward is to use an assembly of struts and tubes, glued together through connection pieces, specially designed to minimize the thermal expansion. But a more sophisticated approach would be to filament wind a complex plane disc, either in a wet or dry approach. An other idea would be to simply machine large slots in a thick composite plate, but to the expense of an increase in the material budget.

In order to test these manufacturing ideas and the ones expected to be proposed by industry, demonstration prototypes are under preparation. These prototypes will also include all the features of the final parts: kinematic mountings, heat shield, ...

## 6. Conclusion.

The barrel is probably the most challenging part of the CMS Inner Tracker. A first design has been

defined, but a lengthy optimisation process, coupling design, calculations and manufacturing techniques, should lead to a cost-effective solution.

## Acknowledgements

Daniel Lacroix has drawn and refined the successive versions of the design. His work is warmly acknowledged by the authors.

## References

- [1]. A. Onnala, Feb. 1993, *Development of the Mechanics of a Silicon Strip and Micro-Strip Gas Chamber Tracker*, CMS TN/93-70.
- [2]. Oct. 1992, *CMS, the Compact Muon Solenoid*, Letter of Intent, CERN/LHCC 92-3.
- [3]. Oct. 1993, *CMS Status Report and Milestones*, CERN/LHCC 93-48.
- [4]. M. Koutchouk and B. Nicquevert, Jul. 1993, *Etude de la stabilité d'une solution par états composites*, CMS TN/93-99.
- [5]. R. Ribeiro, Feb. 1994, *Material Budget calculation of the CMS inner tracker*, CMS TN/94-145.
- [6]. R. Ribeiro, Mar. 1994, *Barrel support structure, precision and radiation length*, PPE-TA1/94-10.
- [7]. M. Koutchouk, Apr. 1994, *Etude de stabilité de la structure du trajectographe interne de CMS*, CMS TN/94-167.
- [8]. P. Virtanen, Sept. 1994, *Structural analysis and optimization of the CMS central tracker barrel wheel*, to be published as a PPE-TA1/94-20.
- [9]. Z. Sun, C. Hauviller, Sept. 1994, *3D finite element analysis of the CMS central tracker barrel wheel using Ansys*, PPE-TA1/94-19.

# The Mechanical Structure of the Inner Tracker for ATLAS

About Fallou<sup>(1)</sup>, Eric Perrin<sup>(2)</sup>, Geoffrey Tappern<sup>(3)</sup>

1. CPPM, CNRS, France

2. Université de Genève, Switzerland

3. Rutherford Appleton Lab, England

## Abstract

To achieve the long term stability requirements in the low mass precision Inner Tracker detectors which will operate in high radiation environment of the Large Hadron Collider (LHC) at CERN demands innovative design, and use of advanced technology materials. It is the intention of this paper to state the present concepts of the proposed engineering design, and the materials under consideration at the present time. It is at this stage of early design and prototyping that advice from industry is welcomed to help achieve the design goals.

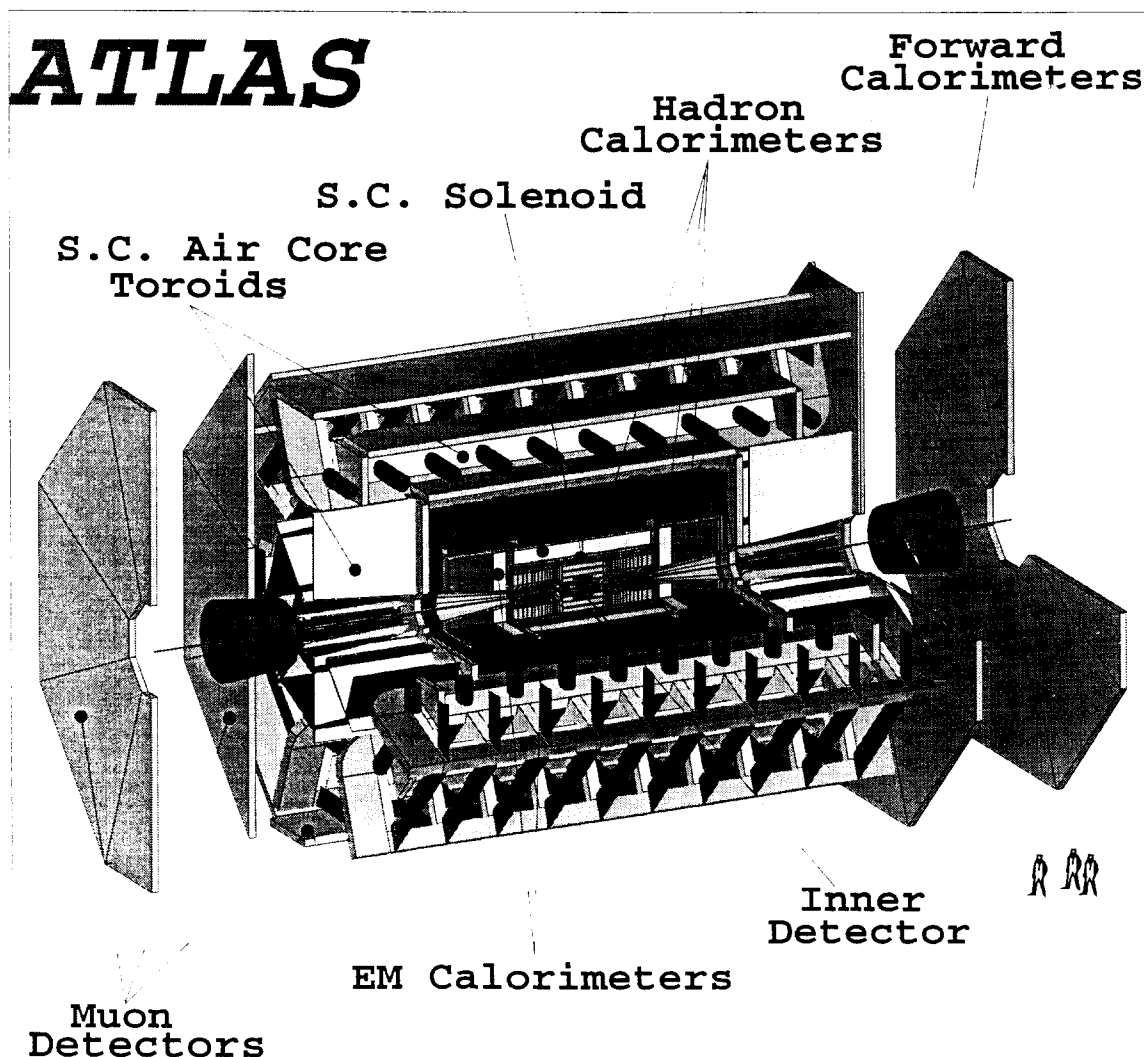


Fig. 1

## 1. Introduction

The Atlas experiment (see Fig 1) is one of the two new Large Hadron Collider (LHC) experiments proposed for construction at CERN with an operating date of the year 2003. The cost of the experiment is budgeted for 300 million Swiss Francs. Part of this overall detector is the central system referred to as the Inner Tracker Detector. The physics design goals can be found in the Atlas Letter of Intent section 3 (Ref 1). As no single tracking detector fulfills these physics requirements, several detector techniques are used. This makes the design, presently at an early stage, and construction more challenging from the engineering point of view. It is the intention of this paper to highlight some of the engineering problems which are expected to be encountered during the design, prototype and construction phases, and in particular the use of high technology materials.

## 2. Inner Tracker Engineering

The Inner Tracker occupies a space 6.9 metres long by 2.3 metres diameter (see Fig 2) and weight 1500 kg. (representing an average specific weight of less

than 55 kg/m<sup>3</sup>) It is composed of three sub-assemblies, a central barrel region with most detectors arranged in concentric cylindrical arrays and two forward regions with radial detector arrays. Stability of the very low mass structure to the ten microns level is of paramount importance. Instability is likely to be caused by temperature change, humidity and creep effects. The complete tracker has been optimised for minimum multiple scattering. Each sub-assembly has four wheels which run on two rails, a vee and a flat, which are both mounted on the inside wall of the Liquid Argon Calorimeter cryostat. The three sub-assemblies are linked together to form one unit, but must be easily demountable to give independent movement for installation and maintenance purposes. Dead space between Barrel and Forward regions are to be kept to a minimum. Services, support of the beam pipe, installation and access scenarios are also important consideration in the design.

### 2.1 Barrel region

The engineering requirements of the barrel are to :  
a) Support 42.5 m<sup>2</sup> of pixel/silicon detectors with a stability at the 10 micron level, at constant

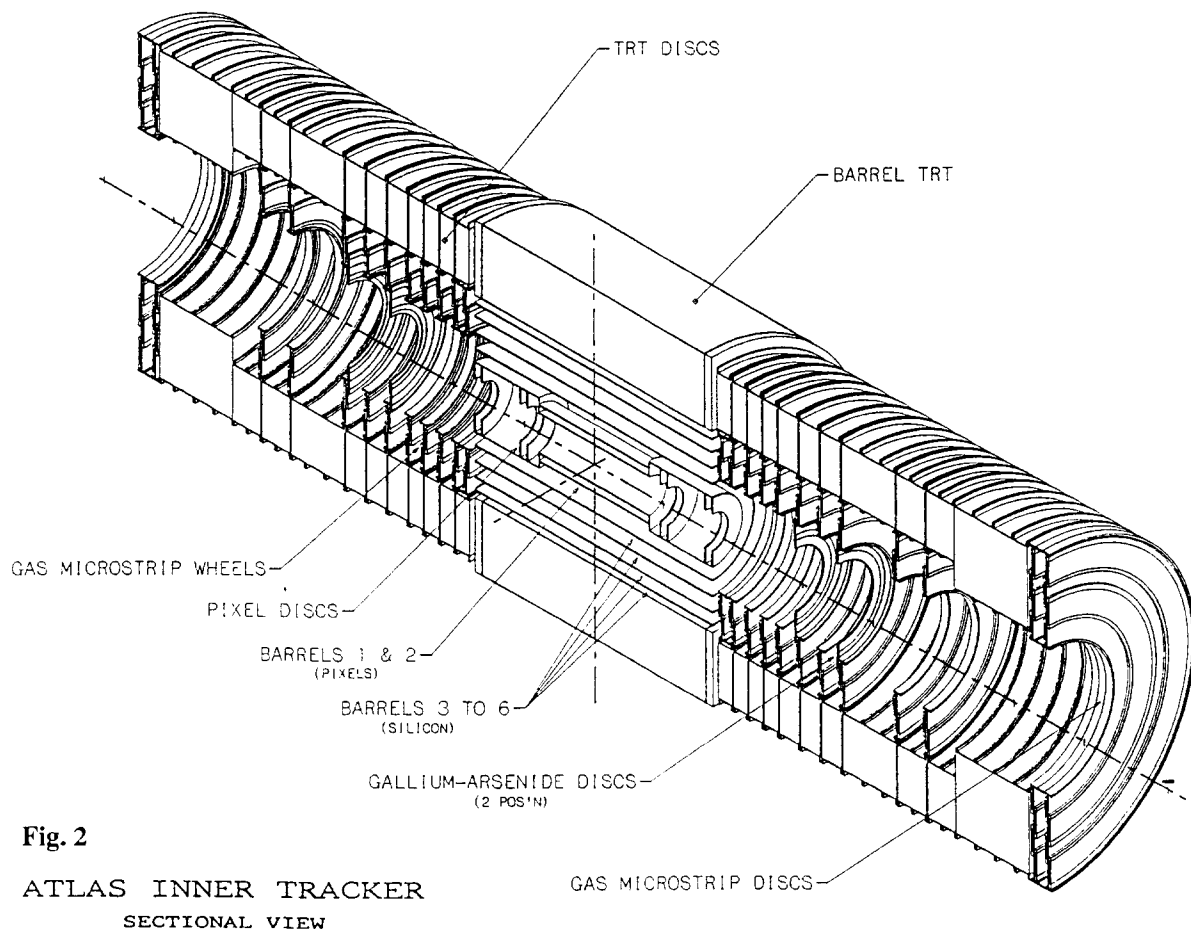


Fig. 2

ATLAS INNER TRACKER  
SECTIONAL VIEW



temperature and support 100,000 straw tubes for the TRT detector with a stability of 50 microns.

b) Use only low mass and low Z radiation hard materials in the construction of the detector.

c) Remove the heat dissipated by local electronics (15 kW), so as to operate the pixels and silicon detectors at a stable temperature of 0 degree C by using a fluid cooling system, and the TRT at the tracker ambient of 21 degree C. An insulating enclosure, flowed with dry nitrogen at a temperature of 0 degree C will be required around the pixels and silicon to prevent any condensation.

The two inner pixel layers are supported on a brazed beryllium structure. The design aim is to maintain stability of the structure to better than 10 microns when running at an operating temperature of 0 degree C.

Overlap in Z and R-phi is provided to insure good hermeticity of the detector. The pixel barrel and the four 1.7 m long silicon barrel assemblies at radius 300 to 600 mm are tested individually and then assembled by means of end discs to one another and to the TRT, and then to the rail system. It is intended that each cylinder is self supporting in its own right and that interlinking is via a kinematic mount system.

The TRT straws are axially orientated and embedded in a foam radiator. An outer carbon fibre structure provides the mechanical stability of the barrel, each straw is designed to support the tension of its sensitive wire. The ionization gas, a mixture of xenon, CO<sub>2</sub> and CF<sub>4</sub> is contained within a closed system. There is also a forced flow of CO<sub>2</sub> around each straw to remove the heat dissipated in the gas.

## 2.2 Forward region

The engineering requirements of the forward regions are: a) Support 66 m<sup>2</sup> of gas microstrips detectors (MSGC), 1.5 m<sup>2</sup> of gallium arsenide detectors, and 285,000 straw tubes of the TRT.

b) Remove the heat generated by the local electronics, (16 kW each end), so as to operate these detectors at the tracker ambient of 21 degree C. The forward TRT (18 discs) structure consists of inner and outer wheels of carbon fibre. The outer wheel providing the inertia and the inner only the tension of the radial straws. TRT, gas microstrips assemblies (ten wheels and two discs) and the gallium arsenide detectors (two discs) are interlinked after testing to form the forward detector sub-assembly.

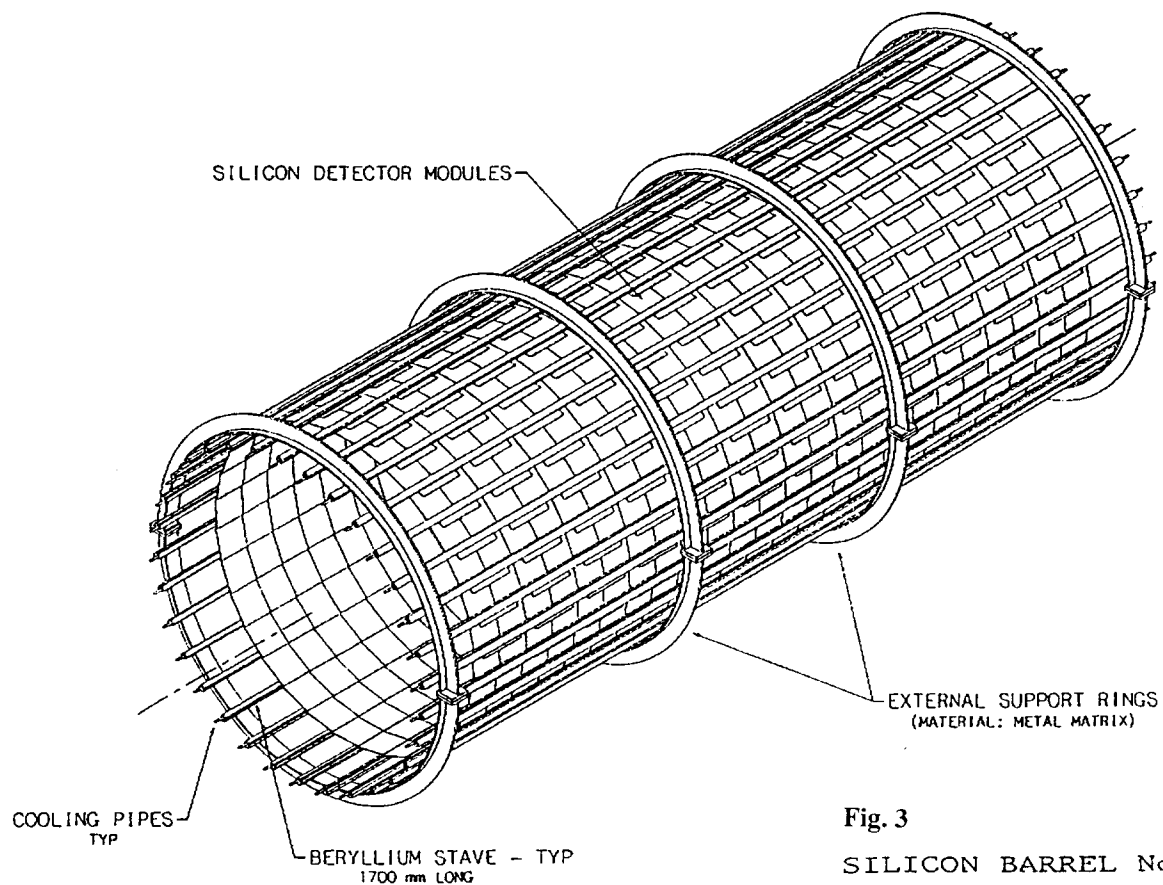


Fig. 3

SILICON BARREL No. 3  
ATLAS INNER TRACKER

Fig. 4

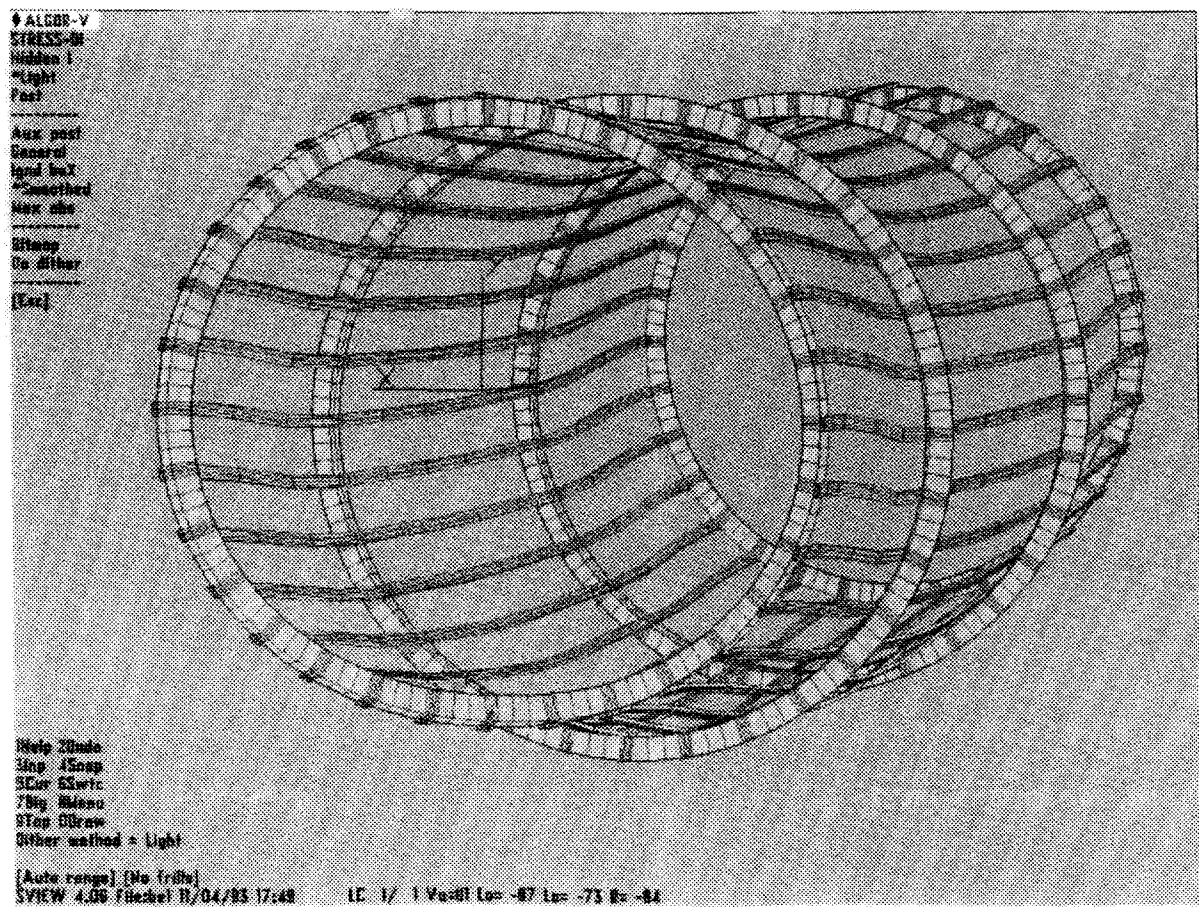
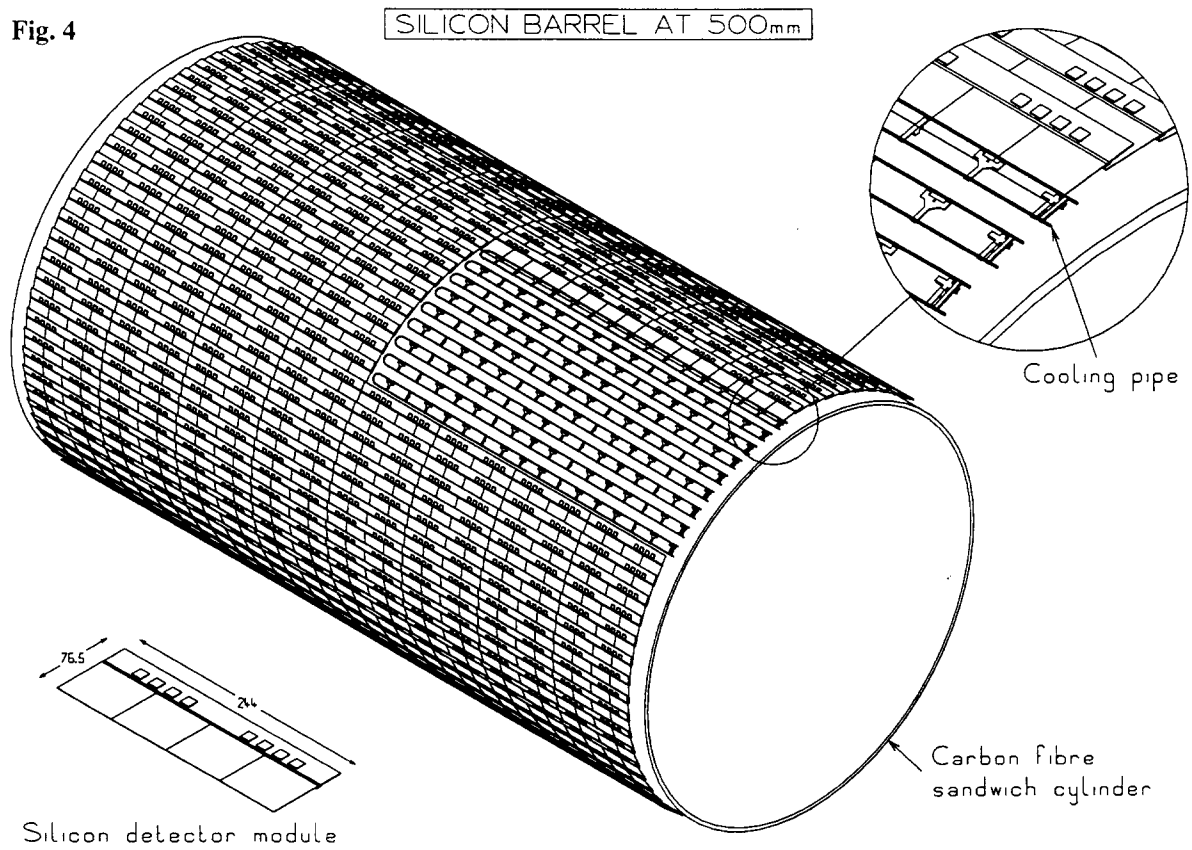


Fig. 5

### 3. Structure studies

The Atlas Inner Tracker is still at an early stage of design and structures have to be adapted to the type of detector they have to support. Two design are being evaluated for the silicon barrel structure (see Fig. 3 and 4). One using a carbon fibre composite construction and the other using extruded beryllium staves and metal matrix composite support rings. The Beryllium stave design also incorporates the cooling channel and in close proximity to the local electronics heat source. Dimensional stability of beryllium is well known and by using zero CTE metal matrix support rings a high quality support structure can be achieved to meet the specification requirements. Finite elements analysis has been carried out on the proposed structure with resulting deflections of approx. 60 microns (see Fig. 5)

Industry has been approached and quotes obtained for a possible stave design to be manufactured by extrusion techniques.

The comparison of cost versus stability achieved will be made between Beryllium and the carbon fibre cylinders described below.

For the carbon fibre sandwich cylinders for the barrel silicon, structural impact of different skin core combinations are under evaluation. The target being to be as low as 1 kg/m<sup>2</sup>. Minimum skin thickness is clearly related to the number of plies needed. (anisotropic skins, with fibres laid up only at 0/90 degree for example may be well thinner than quasi isotropic ones). For a given geometry, the influence

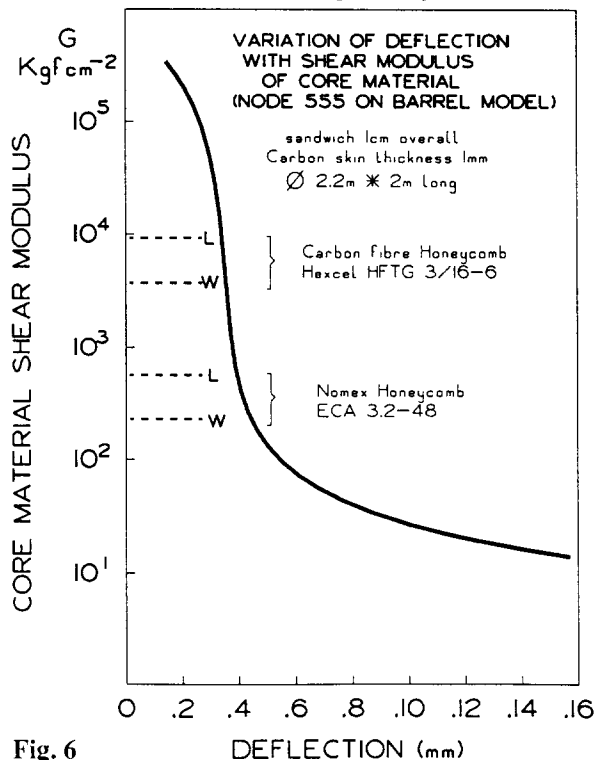


Fig. 6

of the core material in the overall performance of the cylinder has been studied. (see Fig.6) The mechanical studies related to the sandwich cylinders were made for different geometries, proposed in an earlier Tracker layout. Therefore needing to be reevaluated. Fig 6 shows that a standard nomex honeycomb core has a sufficient shear modulus to fulfill the specification.

Manufacturing techniques were also envisaged in contact with industry. Typically a steel mandrel is required on which the inner skin plies (prepregs) are laid up with the required fibre orientation, then the core material is added and the outer skin plies laid up in a similar way as the inner. Vacuum bag technique is well adapted to the thin skin proposed sandwich to apply the pressure during the curing cycle. In case more pressure is required for curing, an autoclave could be used. Expansion of the mandrel to the curing temperature has to be taken into account in the design. In sandwich construction, the adhesion of skins on the core material is a key point. For sandwiches skinned with high modulus fibre, high fibre percentage plies, a resin rich adhesion layer has to be interlayered. Moisture barrier coatings can be integrated during fabrication or added later. At both ends of the cylinder, carbon fibre rings will be integrated during fabrication to provide extra circumferential stiffness and attachment points for the end structures.

Each cylindrical shell will be equipped with numerous precision fixation points (fasteners) for the silicon modules. Mechanical mounting of the detector modules is foreseen, allowing for interchangeability during assembly, test of the single cylinders, and at a later stage for maintenance. A method which allows for these fixation points to be added after fabrication of the cylinders. A precise jig, supporting one or several longitudinal rows of fasteners will be positioned accurately with respect to the cylinder. Once this is achieved glue is injected in small holes in the purpose designed fasteners. Operation is repeated for other rows. (see Fig. 7)

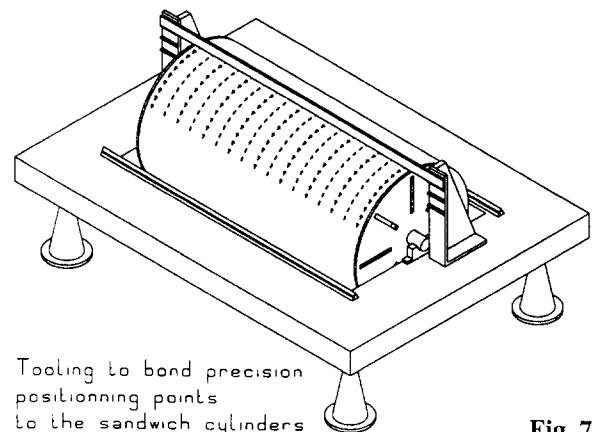


Fig. 7

After curing, fixation points are permanently bonded to the cylinder shell. This method was prototyped and may compensate radially up to 500 microns thus not requiring high precision in the dimension of the sandwich itself. This technique is also compatible if a moisture barrier coating is used and introduces no break in the barrier. The fasteners themselves will be mass produced mouldings in thermoplastic resin reinforced with short fibres. They may also serve as cooling pipe support. The aluminium alloy pipe being clipped in place but allowed to move longitudinally thus avoiding thermal strains to be transmitted to the silicon modules. A good thermal contact is assured using a heat sink compound like the Dow Corning DC 340.

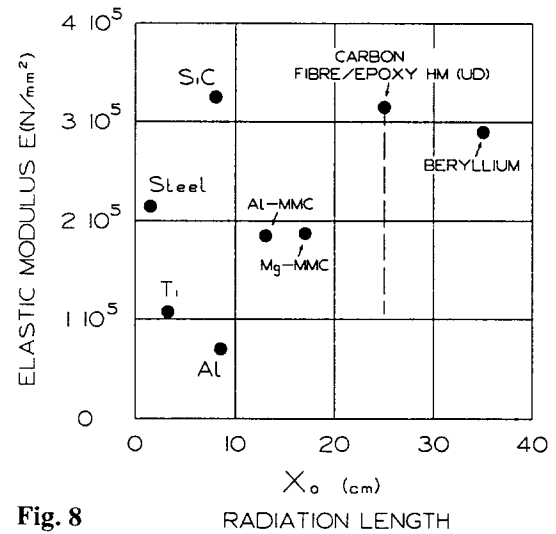


Fig. 8

#### 4. Materials

A survey has been carried out of lightweight materials with high specific stiffness and of the ones that are, or were proposed to be used in other Trackers throughout the world (Ref. 2). Typically boron, fibre-glass, metallic foams, Rohacell, nomex, whisker aluminium, and aluminium alloys. After extensive study, the materials available for use in the support structure have been optimised to carbon-fibres, nomex, metal matrix composite materials, and beryllium. Table 1 gives typical values for materials used in lightweight construction, and figure 8 shows Elastic modulus and radiation length for some of them.

Carbon fibre composites are good candidates, specially if used in sandwich type of structure which exhibit a very high stiffness to weight ratio. This type of construction is widely used in air and spacecraft manufacture. Another feature of carbon fibre for stable structure applications is that its coefficient of thermal expansion (CTE) can be tuned to essentially zero (in the laminate plane), or even to match the CTE of silicon but in this case losing considerably on the Young's modulus. (see Fig. 9 showing the Elastic modulus - CTE dependence for several quasi-isotropic carbon fibre laminates) (Ref. 2)

<b>Table 1</b> <b>TYPICAL MATERIAL PROPERTIES</b> <b>and selecting chart for elastostatic stability criteria</b>									
	ELASTIC MODULUS E (N/mm <sup>2</sup> )	DENSITY ρ (g/cm <sup>3</sup> )	CTE (ppm/K)	THERMAL CONDUCT K (W/mK)	RAD LENGTH X <sub>0</sub> (cm)	RELATIVE SPECIFIC STIFFNESS E'/ρ'	E' = E/E <sub>ALU</sub> ρ' = ρ/ρ <sub>ALU</sub> E' <sup>2</sup> /3ρ' E' <sup>1</sup> /2ρ' E' <sup>1</sup> /3ρ'		
St. Steel	2.1 · 10 <sup>5</sup>	7.85	11	15	1.76	1.02	0.71	0.59	0.49
Titanium alloy	1.05 · 10 <sup>5</sup>	4.5	9.4	7-16	3.56	0.89	0.78	0.73	0.68
Aluminium alloy	7.1 · 10 <sup>4</sup>	2.7	23	100-200	8.9	1.00	1.00	1.00	1.00
Magnesium alloy	4.5 · 10 <sup>4</sup>	1.8	25	60-130	14	0.95	1.11	1.18	1.29
Beryllium	2.9 · 10 <sup>5</sup>	1.85	11,6	145	35.4	6.0	3.75	2.96	2.34
Carbon-fibre/Epoxy/M60J 1)	3.5 · 10 <sup>5</sup>	1.7	- 1.1		25	7.8	4.60	3.52	2.7
Carbon-fibre/Epoxy UHM2)	9.6 · 10 <sup>4</sup>	1.6	0.2		25	2.28	2.06	1.96	1.87
Fiberglass EPG11	2.1 · 10 <sup>4</sup>	1.9	10-15		19.4	0.42	0.63	0.77	0.94
Silicon	1.3 · 10 <sup>5</sup>	2.3	2.6	129	9.37	2.15	1.76	1.59	1.43
Mg-MMC <sup>3)</sup>	1.9 · 10 <sup>5</sup>	2.0	-0.3	412	16.8	3.6	2.60	2.21	1.87
Al-MMC <sup>3)</sup>	1.95 · 10 <sup>5</sup>	2.4	0	409	13.2	3.08	2.20	1.86	1.58
1) Unidirectional properties 65 % vf 2) quasi-isotropic 3) P120/MMC, quasi isotropic ~ 60 % fiber						Eigenfrequency for similar structures	Buckling of round tubes	Buckling round bars	warping plates compr.+ shear

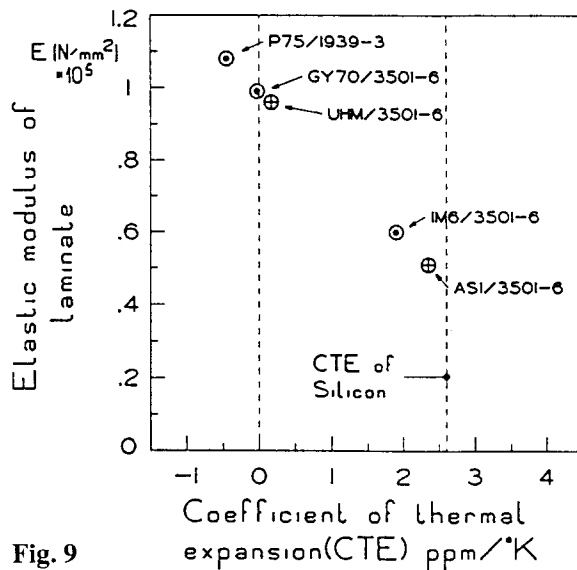


Fig. 9

There is a concern regarding the humidity effects on the stability of carbon fibre shells. Here, the use of low moisture intake resins e.g. Cyanate ester or Polyimide will make the laminate considerably less prone to swelling. The use of moisture barrier coating is another method used to reduce humidity effects.

Beryllium is an excellent material for stable support structures, and is widely used in aerospace applications for precision instrumentation such as inertial guidance systems and space telescope structures. As well as its mechanical properties the dimensional repeatability after thermal cycling and zero humidity effects make the choice of Beryllium a serious contender for the support structures. In the case of the silicon barrel structure the cooling channels is also integrated into the support structure.

#### 4.1 Material tests

Dimensioning and specially optimising sandwich panels or shells with so many parameters to play with is a difficult task. So, several sandwich plates, using different carbon fibre skins - core combinations, ranging from general use to sophisticated aerospace types were manufactured for test purposes. (Fig. 10) Four point bending tests were carried out to ASTM spec C393 to determine the flexural properties of these test sandwich plates. Comparisons were also made with calculations and were in good accordance. With the extremely high stability required for the structures, dimensionnal changes induced by moisture absorption or desorption is also a concern. So, moisture absorption tests have been carried out to ASTM specification C272 on samples cut from the

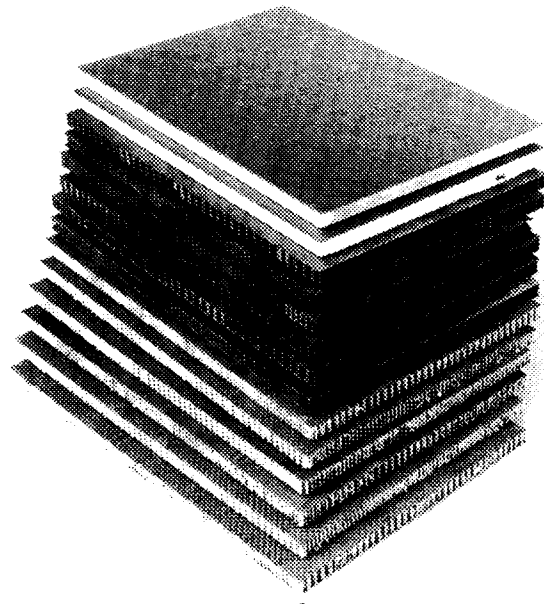


Fig. 10

same plates used for bending tests. Results as per Table 2.

**Table 2** Typical dimension change due to humidity

Core	Skin	Dimension change over 70 mm in microns
1 Rohacell 31	EP104 2 plies 0/90	25
2 Nomex 3.2-48	UHM/3501 4 plies	5
3 Hexcel HFTG	EP104 2 plies 0/90	15
4 Hexcel HFTG	UHM/3501 4 plies	5
5 Hexcel HFTG	YLA RS-3 XN-70A	<4

It has to be emphasised that these moisture absorption tests which combine high temperature and wet atmosphere are very severe and induce moisture saturation in the resin matrix. This will normally never be the case with the real structure. So movements induced by change from ambient to working conditions are expected to be smaller than the ones observed in these tests.

Regarding Beryllium structural parts, which have cooling pipes integrated, corrosion tests have also been carried out to check any possible effect.

Heat sink compound DC340 samples were exposed to radiation up to fluence of  $6 \times 10^{13}$  neutrons/cm<sup>2</sup> without showing significant change in texture and thermal conductivity.

## 5. Cooling

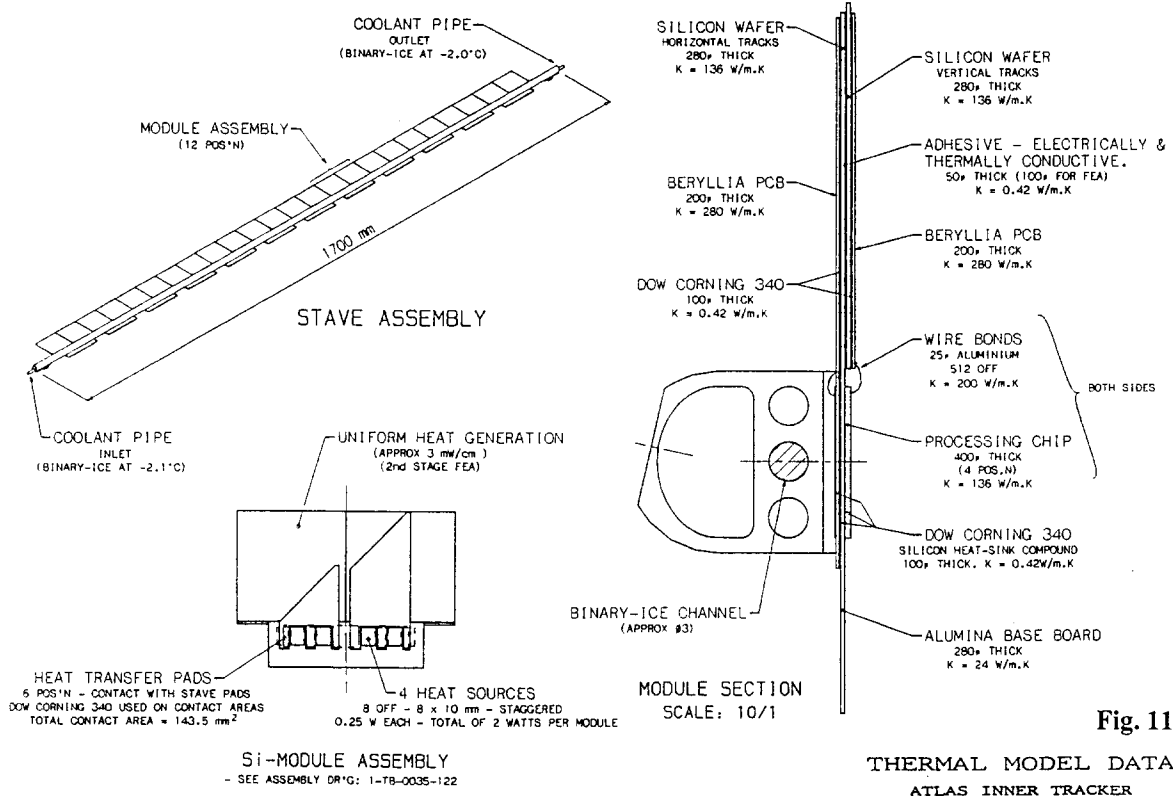
A fail-safe, leak free system with uniform temperature is of prime importance. Fluid cooling, for example Binary ice or water, is being studied for use in all detectors. A flow of cold (approx 0 C), dry nitrogen is anticipated in the silicon barrel to eliminate the risk of condensation. Alternative schemes of evaporative and bi-phase fluid cooling are also under investigation for both silicon and pixel sub-detectors. The susceptibility of the materials and fluids to radiation damage will be studied.

Temperature monitoring will be carried out on all detectors. The information provided will be used to control the cooling system.

Successful tests have been performed in cooling single sided silicon detector modules using ultralight 1mm square aluminium tubes. (Ref. 3)

Thermal modelling to the parameters shown in Fig. 11 have been produced and are shown in Fig. 12.

The cooling must cope, not only with the basic power load of the front-end electronics, but also with the heat dissipated in the power cables and in the detector elements. This last component is expected to rise as a function of integrated dose.



## 6. Installation and access

The Inner detector will be first assembled and tested on the surface in a transport cradle providing the same rail system as in the cryostat. Services from the barrel will be supported from a light weight structure to allow the removal of the Forward regions.

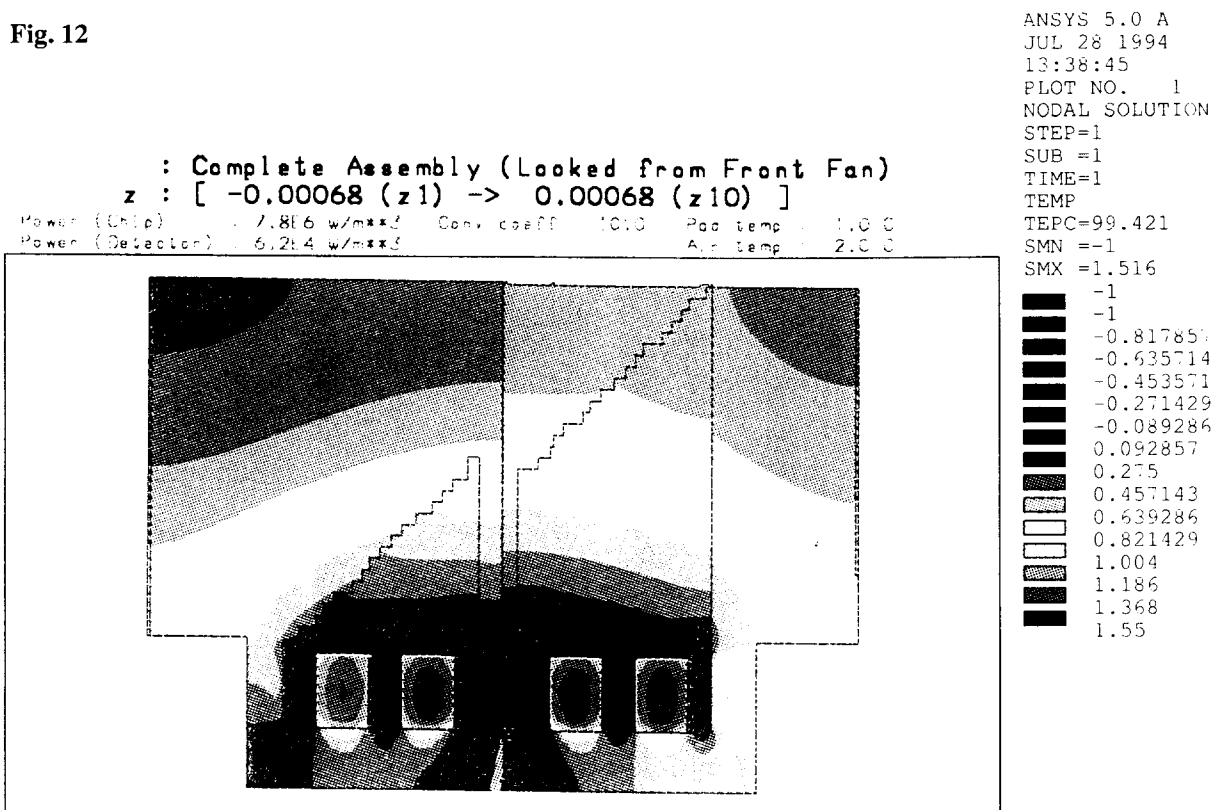
The maintenance scenario will be:

A) short access, typically one week will allow access to both ends of the Inner detector and the patch panels.

B) medium term, typically three weeks which will allow for the Forward region to be pulled out giving access to the Barrel ends. C) long term, typically once a year which would involve the removal of the complete Inner Tracker to the surface for major maintenance or upgrade.

CERN rules of safety will be strictly followed in the Inner Tracker. Problems regarding use of beryllium have already been discussed with the safety group.

Fig. 12



## 7. Prototyping

Extensive prototype work is underway on many aspects of the proposed design:

- A) Detector modules of the different technologies.
- B) An aluminium stave and later in the year a beryllium stave.
- C) A carbon fibre sandwich cylinder using the appropriate skin core combination and manufacturing technique will be made and its mechanical as well as thermal behaviour will be checked and compared with calculations. Module fixation methods and heat transfer to the cooling system have also to be prototyped very accurately.
- D) Prototypes of the interlinking and cylinder mounting points are also needed.
- E) A complete TRT wheel is in a well advanced state.
- F) A mock up to study service routing is also foreseen, specially inside the barrel to study interconnections with the modules, at barrel end face to optimise connectivity, routing and feedthrough to pass the pixel and silicon enclosure.

## 8. Programme

A programme has been produced assuming an installation date of mid 2002 and beam running in

2003. This shows that prototyping including testing must be completed by end of 1996 and manufacture start in 1997.

## 9. Acknowledgements

The authors would like to thank Dave Evans and Dave McPhail from RAL, Alan Holmes from the University of Oxford, Gérard Barbier from the University of Geneva, Bill Miller and Tim Thompson from the Los Alamos National Laboratory and also the Fonds National Suisse de la Recherche Scientifique for financial support.

## 10. References

- 1) ATLAS letter of intent 1/10/92  
CERN/LHCC/92-4
- 2) Superconducting Super Collider Silicon Tracker system. R&D dec 90 LA-12029
- 3) RD2 Status report 12/8/94  
CERN/DRDC 94-34

# Detailed Design and Manufacture of the Support Frames for a Transition Radiation Tracker Detector for the LHC

**Jürgen Enz and Gerhard Lippmann**  
**Dornier GmbH**  
**D 88039 Friedrichshafen - Germany**

## Abstract

The detector for the transition radiation tracker eventually will consist of 50 identical modules, each containing 16 planes of 600 Kapton straws of 500 mm length. These straws are supported by circular cylindrical frames, so-called wheels, an inner wheel (diameter 1000 mm, height 130 mm) made of aramid fibre composite and an outer wheel (diameter 2000 mm, height 130 mm) made of carbon fibre composite. The selection of the materials had to be made under the prerequisites of high "transparency" to particles, high mechanical and thermal stability, high electric resistivity for the inner wheel and sufficient radiation resistance of the resins. By using an appropriate resin system and by applying a non-crossing winding technique, a roundness tolerance  $\leq 0.1$  mm for the inner wheel and  $\leq 0.2$  mm for the outer wheel could be achieved.

For each frame, 9600 holes had to be drilled with high precision in order to position the straws and related equipment. The required accuracy, which is crucial for the performance of the detector, was  $\pm 10''$  for the circumferential and  $\pm 0.02$  mm for the axial positioning. This task also was managed satisfactorily.

## 1. Introduction

The application of fibre composite materials has a long tradition in aerospace industry. The main characteristics of one of the most prominent materials - carbon fibre composite (CFC) - are high stiffness and strength, low density, low thermal expansion, and resistivity to corrosion and fatigue. These properties are the driving factors for application of CFC for aircraft components or for satellite structures - applications in which low mass combined with high mechanical performance are of predominant importance.

Most of these properties are also relevant for application of fibre composites for high energy

physics equipment. In addition to the above mentioned advantages, the high radiation length of carbon fibre - which nearly matches that of Be - makes this material suitable e. g. for the construction of vacuum chambers for the interaction regions of particle accelerators [1, 2]. Thus, also the support frames of the transition radiation detector (TRD) tracker were to be made out of fibre composites in order to achieve the required, rather stringent specifications and tolerances.

The TRD eventually will form an instrument at the planned LHC (Large Hadron Collider) at CERN. Its task will be to detect high energetic leptons and track their way by means of a very high number of single wire chambers, each represented by a Kapton straw



with a charged concentric tungsten wire (Figure 1). The TRD will be composed of an array of some 50 modules which are separated from each other by a 15  $\mu\text{m}$  polypropylen foil; each module consists of two

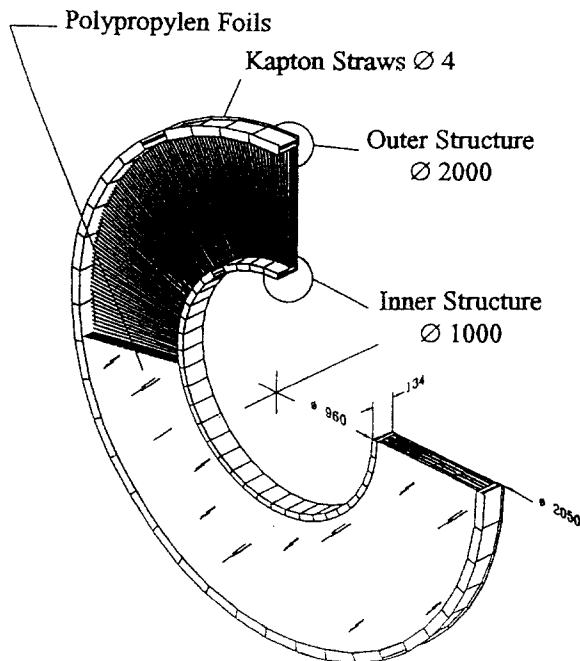


Figure 1: Sketch of one TRD tracker module

cylindrical frames - the so-called inner and outer wheel - with 130 mm height and about 1m and 2 m in diameter, respectively. These wheels provide the support for 16 rows of 600 "straws" each which are part of the wire chambers described above.

The task of the development work described in this paper was the detailed design and the manufacture of the first prototype module for a TRD tracker. The finished frames are shown in Figure 2.

## 2. Design

The first task was to select the suitable materials for the wheels which had to meet the following specifications:

- high stiffness
- high transparency for particles
- high thermal stability
- high electric resistivity for the inner wheel
- good processibility of the material

In principle, fibre composites can meet those requirements and thus the following materials were selected (supplier in parentheses):

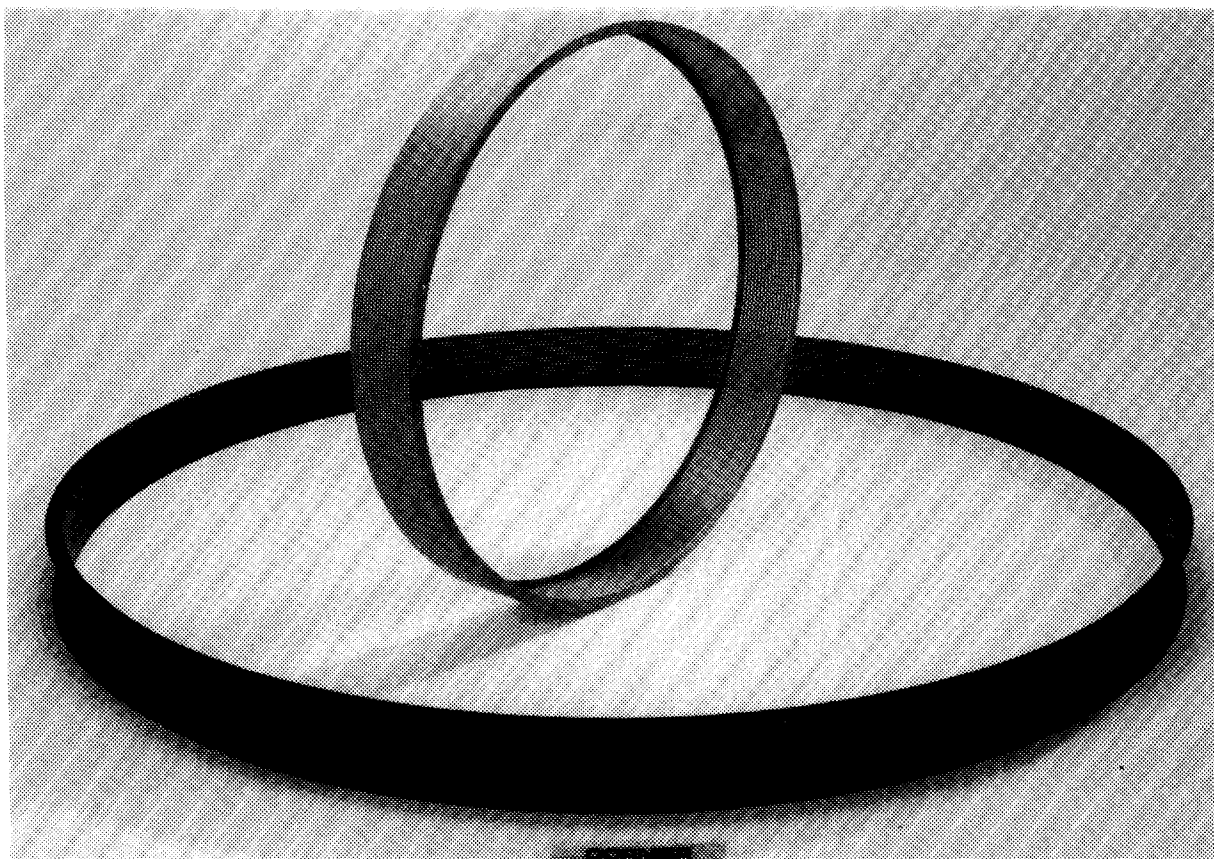


Figure 2: Inner and outer wheel with 9600 holes each

**Table 1: Results of Laminate Calculations**

	Fibre / Resin	Lay-Up	Young's modulus (N/mm <sup>2</sup> ) <sup>(4)</sup>		proportion of fibre [%]
			axial	circumfer.	
Inner Wheel	Kevlar 49 / Epoxy	quasi isotropic <sup>(1)</sup>	30 000	30 000	60 + 5
		quasi cross-ply <sup>(2)</sup>	40 000	40 000	60 + 5
	Nextel 440 / <sup>(5)</sup> Epoxy	quasi isotropic <sup>(1)</sup>	44 000	44 000	60 + 5
		quasi cross-ply <sup>(2)</sup>	54 000	54 000	60 + 5
Outer Wheel	T 800 / Epoxy	anisotropic <sup>(3)</sup>	45 000	130 000	60 + 5
	M 40 J / Epoxy	anisotropic <sup>(3)</sup>	59 000	158 000	60 + 5
Cells	E-Glas / Epoxy	quasi cross-ply	-	-	60 + 5
note: circumferential coefficient of thermal expansion $\alpha \approx 0$ (1) quasi isotropic: $\pm 67,5^\circ / \pm 22,5^\circ$ (2) quasi cross-ply: $\pm 10,0^\circ / \pm 80,0^\circ$ (3) anisotropic: $90,0^\circ / \pm 67,5^\circ / \pm 22,5^\circ$ (4) because of the holes, the listed young's moduli are already reduced by 5 % (5) fibre material: 70 % Al <sub>2</sub> O <sub>3</sub> , 28 % SiO <sub>2</sub> , 2 % B <sub>2</sub> O <sub>3</sub>					

- inner wheel:
  - fibre: aramid fibre Kevlar 49, type 968 2400 dtex (Dupont)
  - resin/hardener: L 20/SL (Bakelite)

- outer wheel:
  - fibre: carbon fibre M40 3B-6 K-50 B (Toray)
  - resin/hardener: LY 556/HY 932 (Ciba Geigy)

Low temperature resins were applied due to the stringent geometrical tolerances; high temperature resins might have caused inhomogeneities or thermal stresses during hardening which may yield deformations of the work pieces after de-moulding.

The computation of the fibre lay-up was done with the Dornier laminate programme "LAMA". The main design parameter were the required structural stiffness, no thermal expansion in circumferential direction and a fibre content of 60 to 65 %. The results of this laminate calculation are shown in Table 1. In order to improve the mechanical behaviour during machining, thin glass fibre layers were designed to cover both sides of the wheels. The drawings of the inner and outer wheel are shown in the annex.

### 3. Processing technology and Manufacture

#### 3.1 Winding of the Wheels

The specified tolerances for roundness and flatness were  $\leq 0.1$  mm each for the inner wheel and  $\leq 0.2$  mm each for the outer wheel.

In order to achieve these requirements a manufacturing technique had to be selected which allowed the application of a low temperature resin system (cf. ch. 2). This manufacturing technique had to fulfil the following criteria:

- achievement of highest accuracy of shape
- endless lay-up of circumferential layers (90°)
- exact inlaying of rovings between the grooves for the outer wheel
- reshaping of the sides during the uncured state
- high precision and reproducibility suitable for a cost-effective series production

These requirements essentially are only met by an automated winding technique. Therefore the wheels were manufactured at a CNC controlled winding machine at Dornier. Before winding, the mandrels were mounted on the winding machine, and were inspected and adjusted with respect to roundness. In order to extend the processing period of the resin the space temperature was lowered to 17 to 18 °C during winding. For the outer wheel the resin supply was heated up in order to improve the impregnation of the rovings.

At first, the wheels were wound cylindrically (Figure 3); then the sides were reshaped into a U-profile shape during the uncured state. For this process several steel jigs were needed, such as separable winding mandrels, flank forming tools and pressure plates. The thermal expansion during hardening was taken into account in the mandrel design.

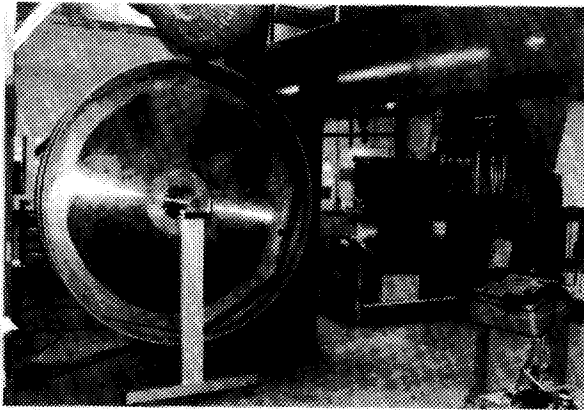


**Figure 3: Mandrel for the outer wheel mounted on the CNC winding machine**

The cylinders were cured in an autoclave by using a checked plane support structure. The achieved geometrical accuracies were within the required tolerances.

### **3.2 Drilling and milling**

For the final processing of the wheels, the sides had to be milled into a U-shaped profile and 9600 holes (quality H 9) had to be drilled into each wheel. The specified accuracy for the positioning of the holes was  $\pm 0.0028^\circ$  (i.e.  $\pm 0.024$  mm for the inner wheel) in circumferential direction and  $\pm 0.02$  mm in axial direction.

To work CFC or even aramid fibre composite (AFC) on a lathe is not without problems. The tools and working parameters had to be adjusted and optimized in order to achieve the required accuracies. An extra difficult job was the drilling of the holes with fitting tolerances H9 at the inner wheel made of AFC; apart from the difficult handling of this material, the small distance of the edges of the holes from each other (about 1 mm) was a special challenge. Before drilling and milling - which was done in an air-conditioned workshop - the drilling jigs and facilities were measured and readjusted. The suitable tools and parameters were determined during tests.

A hard alloyed spiral drill  $120^\circ$  turned out to be the best drilling tool for certain parameters with respect to forward feed, rotational speed and tool life. A new drill was used after 50 holes. - The best milling tool was an AFC milling cutter with counterrotating cutting edges.

The fraying out of the inner and outer rim of the holes had to be avoided during drilling. This could only be managed by a special coating of the wheels.

All machining work was done on a CNC manipulator (working range 5 m  $\phi$ , see Figure 4) in automatic operation in an air-conditioned workshop.

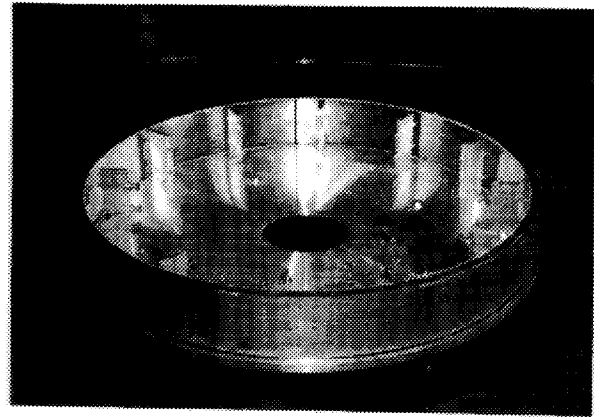


**Figure 4: Inner Wheel mounted on the CNC manipulator for machining**

### **3.3 Assembly of the Cells**

The cells were manufactured out of glass fibre prepreg material separately from the wheels. By means of special fixtures they were glued accurately precision into the U-shaped wheels such that a nearly gas-tight connection is achieved.

## **4. Conclusion and future Aspects**

In the static load tests the required accuracies could be verified. This proved that the selection of materials and the detailed design of the wheels were correct. Nearly all of the specified tolerances could be achieved. Thus, the manufacturing techniques are qualified and, in our opinion, seem to be the only way to achieve such accuracies.

One point needs further investigation: The diameters of the 9600 holes of the inner Kevlar ring shrank considerably during time. Even though the exact reasons still are unclear, this effect might be caused by a moisture induced swelling of the material or by a standing up of the cut fibres in the drill-hole; also a lateral displacement of the webs due to the small distances between holes might be possible. A further reason for this effect could be a small deformation of the total structure after drilling. All these possibilities had to be checked systematically before working further AFC wheels on a lathe. A concept for such a test programme is available at Dornier.

Generally, we believe that a future small series production of such wheels can be performed without major risk and within a reasonable time and cost frame.

## 5. Acknowledgement

The continuous communication during this development work with CERN engineers involved in this project, especially with Claude Hauviller, provided a valuable dialogue and feed-back between manufacturing needs and physical requirements and therefore is gratefully acknowledged.

## 6. References

- [1]. O. Gröbner, C. Hauviller, 1990, "LEP Vacuum Chambers for Experimental Regions: Experience with the first Generation, Prospects for the second Generation", *Proceedings of the 1990 European Particle Accelerator Conference*, 1326-1328
- [2]. H. Betzold, G. Lippmann, 1991, "Application of Carbon Fibre Composite Materials for the Collision Sections of Particle Accelerators", *Proceedings of the 1991 Particle Accelerator Conference*, 598-600

## 7. Annex

Drawings of inner and outer wheel





# Inner Tracking System for ALICE: Conceptual Design of Mechanics, Cooling and Alignment

G.A.Feofilov  
*St.Petersburg University*

P.Giubellino, L.Riccati  
*INFN, Torino*

J.Schukraft  
*CERN*

V.M.Dobulevitch, V.M.Fedorov, O.N.Godisov, S.N.Igolkin, M.I.Yudkin  
*Meson, St.Petersburg*

S.F.Gerasimov, I.A.Novikov, L.F.Vitushkin  
*Mendeleev Institute for Metrology, St.Petersburg*

## Abstract

We present here the basic ideas for the design of the support and cooling system for the Inner Tracking System of the ALICE experiment at the LHC. The cooling scheme, which must provide 5 kW heat drain from the electronics situated inside the tracking volume and stabilise the temperature field for the Si-drift detectors within 0.1 °C, is the starting point of the design. The choice of candidate materials for the mechanics support and integrated cooling structures is done under the general constraint of the total mass minimization. We discuss here some of the ideas for the precise positional alignment and monitoring, and the alternative options which we are considering for the mechanical layout of the Inner Tracker. We also present some first results of prototype tests and of calculations of the gravitational sagging for the ladders.

## 1 Introduction

The ALICE collaboration has proposed to build a dedicated detector to exploit the exciting physics opportunities of ultra relativistic Heavy-Ion collisions at the LHC [1, 2]. The experiment will study hadrons, electrons and photons of  $P_t$  up to 10 GeV/c in the central rapidity region, in order to detect the expected formation of a new phase of matter, the Quark-Gluon-Plasma.

The ALICE detector will be composed of a central part, consisting of an inner tracking system, a cylindrical TPC, a particle identification array (TOF or RICH) and a single-arm electromagnetic calorimeter, embedded in a weak solenoidal field, complemented by a Zero Degree Calorimeter and a large acceptance multiplicity detector.

Given the very large multiplicities, tracking will be a formidable task; the Inner Tracking System is supposed to ensure the reconstruction of secondary vertices and of the low-momentum particles, for which it will have to provide also identification capability via  $dE/dx$ . Since for the bulk of the interesting tracks the momentum resolution will be limited essentially by multiple scattering, the minimization of the material thickness is an absolute priority for tracking inside ALICE.

Thus the ITS must satisfy very stringent requirements in terms of the high spatial accuracy, momentum resolution, particle type identification, stability and reliability of operation, meeting at the same time the most contradictory demand of matter minimization in the region of interest.

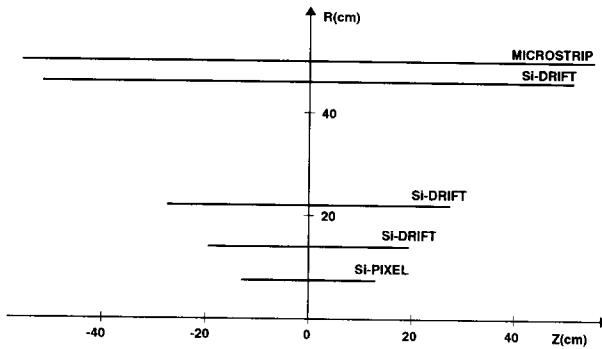


Figure 2.1: Transverse half-section of the Inner Tracking System

## 2 System Overview

The Inner Tracking System (ITS) will measure charged particles at radii up to 50 cm. Its main purpose is the detection of secondary vertices and the momentum measurement of low- $p_t$  particles, down to a  $p_t$  of  $\approx 20$  MeV/c for electrons. It will also improve the momentum resolution at large momenta. In addition, it will perform the identification of the low-momentum particles which do not reach the outer particle identification devices, via  $dE/dx$  in the  $1/\beta^2$  region.

The system will consist of five cylindrical layers, covering the central rapidity region ( $|\eta| \leq 0.9$ ) for vertices located within the length of the interaction region ( $2\sigma$ ), i.e. 10.6 cm along the beam direction ( $z$ ). A half-section of the system is shown in Fig. 2.1, while the nominal dimensions are summarized in Table 2.1.

Layer	$r$ (cm)	$\pm z$ (cm)	Area ( $\text{m}^2$ )
(1)	7.5	12.8	0.12
(2)	14	19.3	0.34
(3)	22	27.3	0.75
(4)	46	51.3	2.97
(5)	50	55.3	3.47
Total Area = 7.65 $\text{m}^2$			

Table 2.1: Dimensions for the Inner Tracking System

The criteria which led to the definition of the number and location of layers are the results of the simulated performance and can be found in the Letter of Intent for ALICE [3].

The granularity required for the innermost planes can be achieved only with silicon micropattern detectors with two-dimensional readout, such as Silicon Pixel Detectors (SPDs) and Silicon Drift Detectors (SDDs).

As a baseline design, we consider using SPDs for the innermost plane, the most demanding one in terms of granularity and resolution, and SDDs for the following two. A configuration in which only one of these technologies would be applied might still be considered, if it could be proven to satisfy all the requirements at all radii, and to provide a system which would be simpler to construct and operate.

At larger radii, the requirements in terms of granularity are less stringent, so that for at least one or possibly both planes we foresee the use of a more standard, well-proven and cheaper technique, like double-sided silicon strip detectors [5] or MicroStrip Gas Counters (MSGCs) [6]. The outer layers have large areas, and involve the use of a large number of detectors, so that reliability, ease of operation, and established capability of industrial production become major points in favour of a conservative choice. The MSGCs are cheaper than Si-strips, but have a lower two-track resolution for inclined tracks; also, double-sided silicon microstrips offer the possibility of matching the signals read out from the two sides, to help resolve ambiguities. The final choice will be determined on the basis of simulations using optimized track finding algorithms.

The main parameters of each of the four detector types considered are indicated in Table 2.2: spatial precision, two-track resolution, pixel size, size and number of channels of an individual detector and number of output lines from a detector module.

In Table 2.3 the main parameters of the various layers are summarized, including the number of detecting elements, the number of electronic channels and the dissipated power. The different detector technologies require specific front-ends, and we foresee the unification of electronic standards (type of links, protocols) at the level of optical links, i.e. at the front-end outputs.

## 3 Materials

As mentioned in the introduction, in the ALICE experiment we are interested mainly in the measurement of low- $p_t$  particles, for which the momentum resolution is dominated by the effects of multiple scattering in the detectors and their support structures. Therefore it is essential that in the design of the ITS only minimal quantities of low- $Z$ , long radiation length materials are used. At the same time those materials must provide the necessary rigidity and mechanical stability of the construction and be radiation hard and thermostabilized. In addition, the coolants must be safe, nonaggressive and satisfy the CERN safety regulations [7].

In accordance to the experience accumulated in



Type	Spatial precision ( $\mu\text{m}$ )		Two-track resolution ( $\mu\text{m}$ )		Cell size ( $\mu\text{m}$ )	Module size (mm)	Channels per module	Output lines
	$r\phi$	$z$	$r\phi$	$z$				
Pixel	22	78	150	540	75x270	4.8x69	16384	32
Drift	25	25	500 <sup>a</sup>	200 <sup>a</sup>	–	57x70	448	448
Si Strip <sup>c</sup>	30 <sup>b</sup>	1000	200	7000	100x50000	75x50	2x750	24
MSGC <sup>c</sup>	60	1000	800	12000	200x25000	100x50	2x1000	32

<sup>a</sup> Can be improved with waveform analysis

<sup>b</sup> Can be improved with centroid finding

<sup>c</sup> Layer at  $r = 50$  cm

Table 2.2: Parameters of the various detector types

Layer	Type	Detector modules	Electronic channels (k)	Barrel dissipated power (W)	Endplates dissipated power (W)
(1)	Pixel	400	6550	160	
(2)	Drift	96	45	75	430
(3)	Drift	192	90	150	860
(4a)	Drift	765	350	600	3400
(4b)	Si Strip	900	1440	1850	
(5a)	Si Strip	924	1400	1800	
(5b)	MSGC	700	1400	1800	
			$\approx 8500$ to $\approx 9600$	$\approx 2800$ to $\approx 4000$	$\approx 4700$

Table 2.3: Physical parameters of layers

various labs in the design and exploitation of vertex detectors [8, 9, 10, 11, 12, 13, 14, 15, 16, 17] the choice of materials that can be used as components of supporting structures, cooling systems, interconnections, etc., is rather limited.

The main parameters of some of the materials that can be applied for the mechanical support and other structures are summarized in Table 3.1.

As can be seen from this table the main candidates can be considered to be Be, BeO and carbon fiber composites.

The use of Be is disfavoured due to the potential health hazards during mechanical processing (although these hazards can be controlled and the protective coating [20] can be used afterwards). In addition, the CTE of Be is rather different from the one of Si, which is a serious disadvantage for a large mechanical structure like the ITS. Therefore we foresee the application of Be only for the central part of the beam pipe and possibly for some micro refrigerators for the heat drain from the front-end electronics.

The BeO is an insulator that has rather high thermoconductivity. Thus it can be used e.g. in some local heat drain devices.

As to the global mechanical structure of the ITS, we foresee the wide implementation of high modulus Carbon Fiber Composites both to the space-frame Si ladders support and to the general support of the Tracker. The use of Carbon Fibers is preferred due to their high mechanical properties and very low CTE that can be matched (if needed) with that of Silicon by using metal additives. Besides, there are quite new materials that possess outstanding properties, like the Super Thermoconductive Graphite fiber THORNEL [18], that has a thermoconductivity 3 times larger than copper. Using such a material one can think about a possible integration of the local heat drain from the front-end electronics and the ladder support structure for Si-strip and MSGC detectors.

Among the materials there is a quite new one which has very interesting properties: the boron carbide foam; it possesses along with high mechanical properties also a CTE that is well matched to that of Si and has the density  $\approx 0.07$  of the solid boron carbide. The radiation length is of the order of 2 m. This material was proposed to be used in a U-form support structures for the CLEO vertex detector [9]. We consider the possibility of implemen-

Material	Rad Length cm	Density g/cm <sup>3</sup>	CTE ppm/K	Elastic modulus E-GPa	Thermo- conduc- tivity W/m/K	Ref.
Si	9.37	2.33	2.6-4.2	131	129	[8]
Be	35.43	1.84	11.6	290.0	146.0	[8]
BeO			9		260	[19]
Carbon fiber composites	18	1.9	down to -0.5	>390 (axial)	10-100	[21]
THORNEL graphite K1100X composite		2.15		806 (axial)	1050	[18]
Boron carbide foam	200		5.5			[9]

Table 3.1: Parameters of some materials and substances.

tating such foam (or some other porous materials) for the end-caps.

## 4 Detector Concept

### 4.1 Cooling

The design of such a complex detector, involving the use of several different detection techniques, and with very demanding requirements for the temperature stability, the positioning precision and the total material thickness in the sensitive volume, is a task that requires a unified approach.

The cooling scheme ( $\approx 3-5$  kW heat drain in the tracking volume) determines the overall mechanical construction and is in fact a key point to the design of the ITS. Preliminary studies of different cooling schemes (gaseous, liquid, evaporative) have been done [22] for a higher heat load (10 kW) and two options were selected for further development:

- localized, evaporative cooling in a closed system under atmospheric pressure for the Si-drift and Si-strip (or MSGCs) detectors, that is expected to provide uniform temperature fields (within 3–4 °C in the detector volume) and a thermostabilization of the whole ITS of the order of 0.1 °C at ambient temperature. Such an ambient-temperature evaporative cooling scheme, should allow a uniform and stable temperature, with minimal stresses at turn-on and switch-off.

- uniform gas cooling of the first layer of pixel detectors with reasonable air flow.

We will only give here a brief outline of these systems, which are described in detail elsewhere [23].

#### Evaporative cooling system.

The temperature stability required by the Si-drift detectors (of the order of 0.1 °C) is one of the major reasons for the evaporative cooling choice. In addition, it was shown [22] that the use of one of ozon-safe freons as a coolant can optimize the total amount of material compared to the other liquid cooling options. Each of the possible cooling freons has its own temperature vs. pressure working field; in particular C3F7I is suitable ambient temperatures under 1 bar pressure in the system (the boiling temperature is 25–20 °C). Freon C4F10 can be used under 1 bar for temperatures from -2 to +5 °C, C4F8 from -10 to 0 °C and C3F8 for -30 to -25 °C.

The minimum total amount of condensed coolant in the volume of the ITS can be estimated roughly from the total waste of coolant fluid (0.1 kg/s) to be 0.5–1.0 kg. These values were obtained for saturated vapor pressure 1 bar and a total heat drain of 10 kW.

#### Cooling of the first layer.

In the first layer of sensitive Si-surface, composed of pixel detectors overlayed with the readout electronics, the heat will be produced uniformly with a density of 0.13 – 0.17 W/cm<sup>2</sup>. Keeping in mind that the working temperature gradients for pixels are limited only by the requirements of alignment and mechanical stability, we consider gas cooling of this layer possible. The cylinder gap (1.5 cm) between the first layer and the beam pipe can be used as a natural channel for the gas flow

To simplify the system and minimize the material, we would make it an open one; the gas trans-

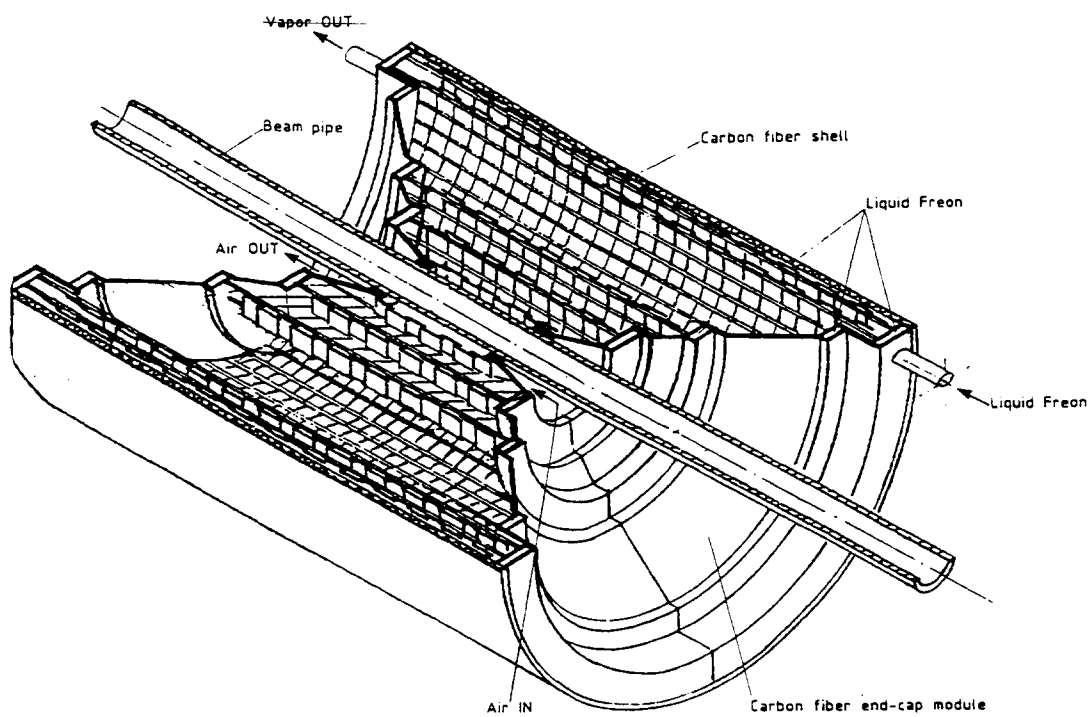


Figure 4.1: General view of one half of the Inner Tracking System

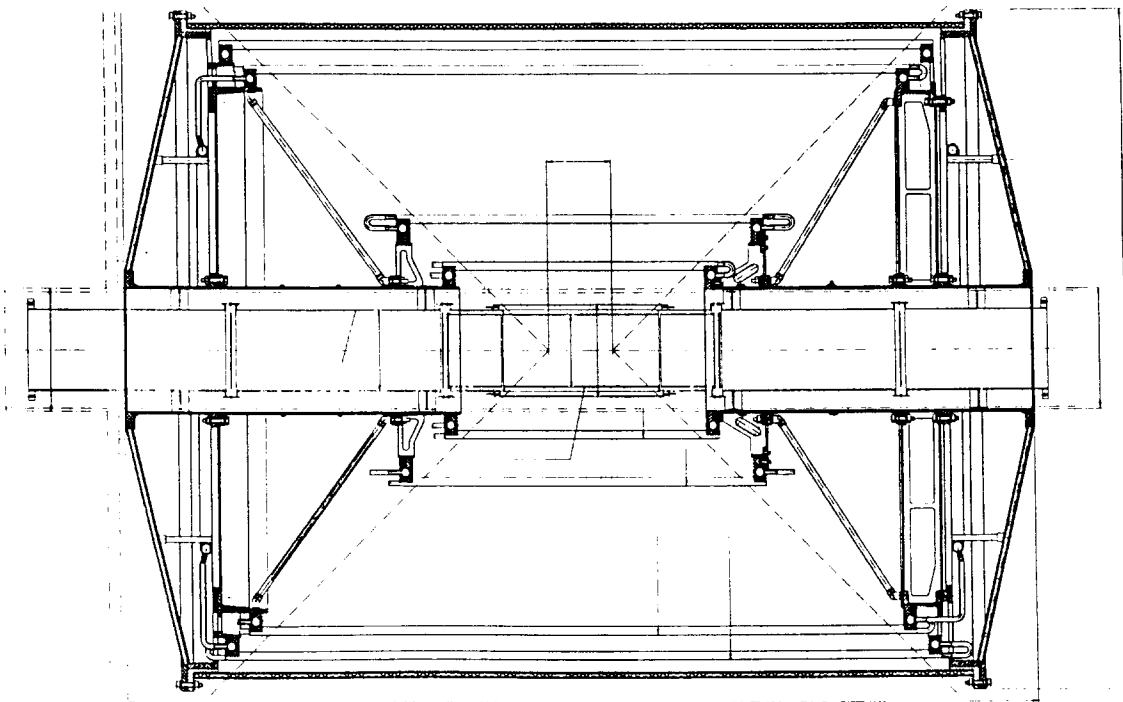


Figure 4.2: General setup of the mechanical support of the ITS. Side view. The independent 1st (pixel) layer is situated directly on the central part of the beam pipe

port may be done under fairly high pressure, i.e. 1.5-2 bar, to diminish the volume of gas wastes.

## 4.2 General Layout

The general layout of the ITS is shown in Fig. 4.1. To ensure a flexible system, we are developing a structure which is mechanically independent from the outer detectors, and can be preassembled and measured accurately before final installation in the experiment.

The general idea is to remove the material of supporting and cooling structures from the central region to the end-caps and to the outer layer to the maximal extent. To this purpose, we are studying a support structure in which the material is concentrated in the conical endplates, covering a minimum solid angle, and the detectors are organized in ladders, parallel to the beam direction and held by linear structures (ribs) that are possibly also used as flow channels for the cooling fluid and possibly as substrate for power distribution. With this design, we plan to keep the total average thickness, including detectors, below 0.6% of  $X_0$  per layer.

The mechanical design for the ITS is not finalised yet and at this stage we are studying three possible options, which arise mainly from different assembly schemes for the ITS:

- rigid end-caps (integrating support, cables to the outer world, connectors, coolant collector) and outer honeycomb carbon fiber cylinder that form a space structure to support Si ladders;
- clamshell design;
- five relatively independent cylinder detectors supported by the cone end-caps and the outer honeycomb carbon fiber cylinder.

The last option is represented in Fig. 4.2 and in Fig. 4.3

## 4.3 The integrated unit for support, cooling, power bus and data bus

### The 1st ladder design

The 1st option of the basic linear supporting structure, which must be thermostabilized by the integrated cooling channels, is represented in Fig. 4.4. It is formed by a carbon fiber semicylinder shell (diameter 5 mm, thickness 0.5 mm), which houses the Be (or 100  $\mu\text{m}$  wall Al) pipe of 3 mm in diameter that serve as cooling channel and as a power (or ground) bus.

The thermoconductive Be (or Al) cooling channel is expected to provide a uniform temperature along the line, avoiding the formation of hot spots. The multichannel data bus cables (Be or Al on kap-

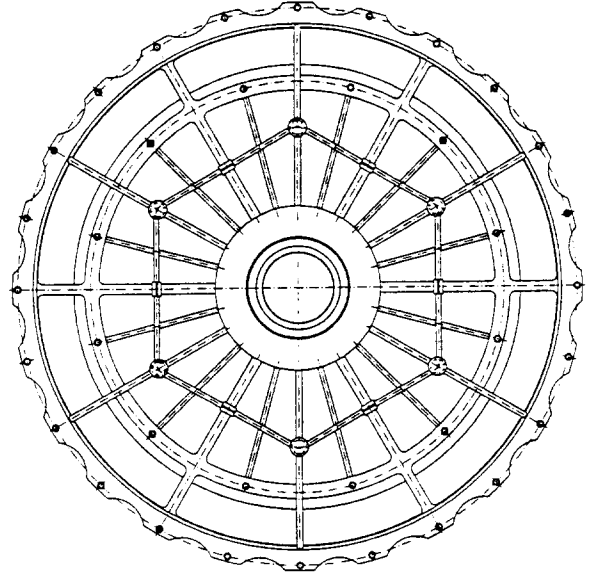
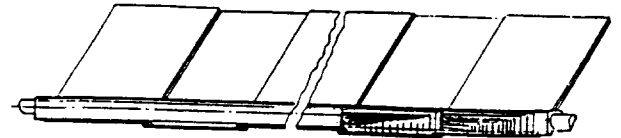


Figure 4.3: General setup of the mechanical support of the ITS. End-cap view.



Side View

Figure 4.4: Scheme of the ladder, integrated cooling, power and data bus

ton) are embedded into the body of the carbon-fibre support structure.

The cooling channel contains the mixture of gas/vapor and condensed liquid. The amount of the condensed liquid is controlled by the pressure of saturated vapor in the channel and can be kept very low (1-2 mm thick).

The first 0.5 m prototype of the long ladder support was manufactured according to the described geometry, see Fig. 4.5. We got 400  $\mu\text{m}$  wall thickness using three layers of the carbon fiber and a cold process. In fact during mass production one can expect the reduction down to 200  $\mu\text{m}$ .

The first prototype tests were done with 1 meter heat drain prototype of the ladder based on the freon cooling artery of 3 mm in diameter. There were 20 localised heaters that simulated the local heat drain from the front-end electronics. Tests have confirmed our calculations on the evaporative freon cooling up to 25 W power per one ladder providing temperature gradient along the ladder within 0.8  $^{\circ}\text{C}$ .

#### Calculations of the Gravitational Sagging

The maximal sagging of the uniformly loaded long bar can be evaluated from the formula:

$$f = k \frac{ql^4}{EJ} \quad (4.1)$$

where  $k$  is a coefficient that depends on whether the ends of the bar are fixed or free.

We consider here the case in which both ends of the bar are fixed ( $k=0.0026$ );

The other parameters in the formula are:

$l$  - the length ( $l=1.1 \cdot 10^3$  mm)

$q$  - a uniformly distributed load

$E$  - the module of elasticity of the bar in the direction of its axis

$J$  - the moment of inertia of the transverse cross section of the bar.

The cross-section of the bar is a semicircle with inner diameter  $d$  and outer diameter  $D$ . We consider here a bar with  $D=5.5$  mm and  $d=5$  mm, with a 0.5 mm wall, made of high modulus carbon fiber composite ( $E=20000 \text{ Kg/mm}^2$ ). Our calculations for a 1.1 meter length supporting structure loaded by the Si, the coolant (35 g in this calculation) and its own weight and in the most unfavorable ladder position ("flat horizontal"), give a gravitational sagging of 6.6 mm (not including the silicon rigidity), which we consider excessive.

Since the sagging of the rib grows as the fourth power of the length, in the initial stage of the design we foresaw for the outer layers two intermediate annular ladder supporting membranes, made of thin carbon-fibre foil. The same structure supported by a membrane at every 30 cm will provide

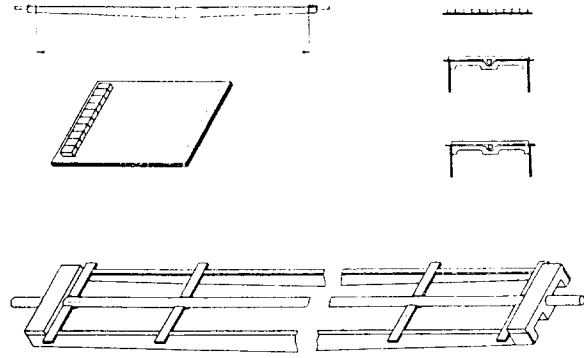


Figure 4.6: Design of the 1.1 m length carbon fiber ladder with the integrated central cooling artery and perpendicular super thermoconductive heat drain bars

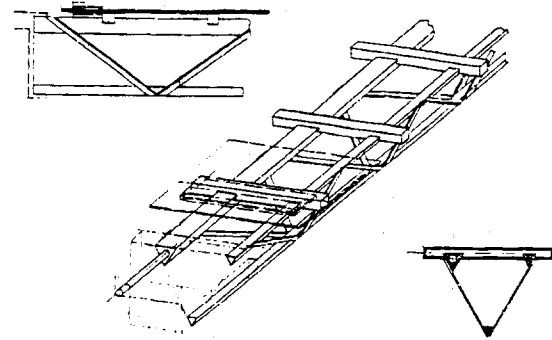


Figure 4.7: Design of the space-frame carbon fiber ladder support

approximately 40  $\mu\text{m}$  of sagging that already can be considered tolerable.

#### The new ladder design studies

Afterwards, we have investigated several alternative possibilities of ladder design. One of the new designs, shown in Fig. 4.6, is based on lateral blade ribs and a central cooling artery; super thermoconductive graphite fibers are used for the local heat drain from the electronics to the cooling arteries.

The further development of the ladder concept is the transition from the bar-supported ladder to a space-frame carbon-fiber ladder support structure (with the same amount of material as in the previous case). A first concept is represented in Fig.4.7.

The first estimates done for the new structure have shown 20  $\mu\text{m}$  sagging without any additional support. A full scale prototype of this new space-

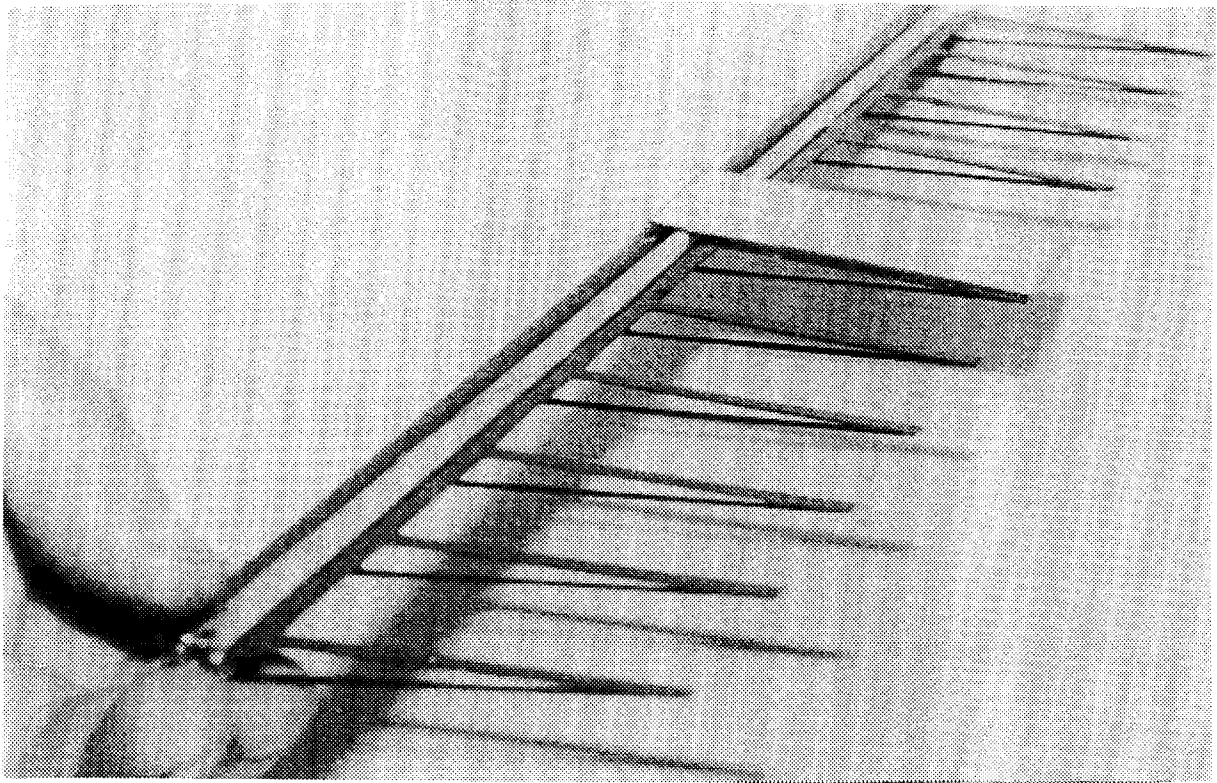


Figure 4.5: Photo of the 1st 0.5 m length 0.4 mm wall carbon fiber ladder prototype with the integrated cooling artery (Al 50  $\mu\text{m}$  foil).

frame 1.1 m ladder support is being manufactured now for the future mechanical tests.

#### 4.4 Estimate of the total amount of material

In the proposed configuration, the material will be distributed non-uniformly in each layer, being concentrated along the ribs. The assembly will be done so that the ribs in the different layers will not be collinear when seen from the vertex point.

The exact amount of material in each layer will be fixed only after the finalization of the design, but we give here the estimate of material for a realistic case, which has been calculated to provide enough mechanical precision and satisfy the cooling requirements. The values, in  $X_0$ , averaged over a whole layer, are:

- 0.03% for the carbon-fibre ribs
- 0.15% for the coolant fluid.
- 0.03% for the BeO foil.
- 0.03% for the Be power bus.
- 0.03% for the kapton data bus.

The material in the tracker is about 0.27% of  $X_0$  per layer in addition to the detector modules, which are on average 0.33%, giving a total of 3% of  $X_0$  for the ITS with five layers.

#### 4.5 Radiation effects

Thanks to the open geometry of the experiment, we expect the primary particles produced in the interaction to be the major source of radiation damage to the tracking elements, albedo neutrons giving a minor contribution. We estimate a maximum yearly dose of 12 kRad for the innermost plane, not including beam losses; these might ultimately be the main source of radiation, but are at present very hard to evaluate. The above-mentioned levels are not very severe, and should not create a specific problem for the components discussed here, yet care will be taken in avoiding materials and devices known to be sensitive to these radiation levels.

### 5 Positioning and Assembly

#### 5.1 Assembly of the ladder.

In order to get reliable positioning at the level of 10  $\mu\text{m}$  and to decrease the misalignment errors for the individual Si-wafers in the whole sensitive 1 meter length volume of the Tracking System, the ladder assembly is considered to be done wafer-by-wafer at an optically controlled Working Station -I (WS-I) using fiducial marks located on the Si wafers.

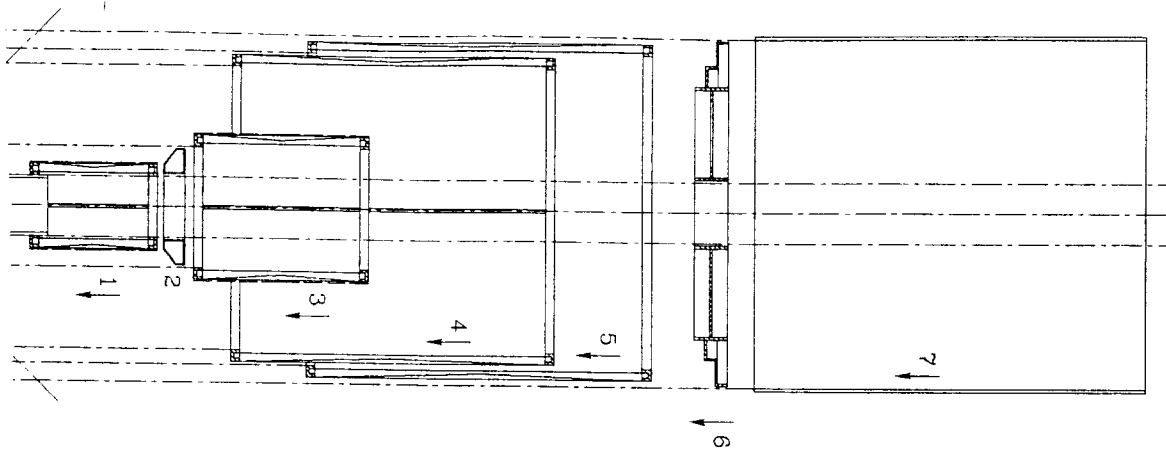


Figure 5.1: Scheme of the module-by-module assembly of the ITS

This station is based on a laser controlled automated movable (photoelectric) microscope that can be adjusted in two coordinates to the prescribed position with the required accuracy by a microdrive. Thus the negative feedback from the laser controlled traditional device is expected to give a rather cheap method of controllable motion along the 1 meter base.

This system will be the analog of the Laser interferometric comparators of National Metrology centers that are used for the length measurements of line scale. For the national primary standards of length unit the international comparison show  $0.11 \mu\text{m}$  for 1 meter [24] For the present task a precision of about  $3 \mu\text{m}$  can be achieved in a straightforward way.

The assembled ladder (with integrated cables, buses and cooling channels) should be wirebonded (chips to buses) with the help of Working station - I and one of the modified traditional Bonding Machines. Then operation of the ladder is supposed to be completely tested before final assembly in the system.

## 5.2 Assembly of Cylinder Modules and of the ITS.

The overall assembly of the Inner Tracker System is supposed to be done either ladder-by-ladder or module-by-module at a Working Station-II analogous to WS-I, using part of the same fiducial marks. In Fig. 5.1 is shown a possible option for the overall ITS assembly done by separate independent cylinder modules.

## 5.3 Multichannel Temperature Monitoring of the ITS.

In order to monitor the temperature and thermal gradients inside the ITS it is possible to use an au-

tomated multichannel temperature measuring system that can give the necessary information on the operational temperature of any part of the detector. The temperature at a definite point is monitored by a thin film planar sensors, made of 2 to  $5 \mu\text{m}$  Pt meander directly spread over the Si-plate, on an area of  $2 \times 2 \text{mm}^2$ . They can provide  $0.02\text{--}0.03^\circ\text{C}$  accuracy of measurements in the  $\pm 10^\circ\text{C}$  interval from the working detector temperature in the  $-10^\circ\text{C}$  to  $+40^\circ\text{C}$  region.

The number of thermosensors, their place and the way of positioning on the wafer, the points of the ITS that are necessary to monitor, etc. are now under study.

The same multichannel system of temperature measurements can be used for the temperature fields mapping and the temperature control of the working station for the precise alignment of the Tracking System.

Fixation of the wafer on the supporting structure is supposed to be done by traditional epoxy glue.

## 6 Conclusions

The future R&D for the ITS design will be concentrated mainly on local specific problems that require innovative approaches:

- the heat drain from the front-end electronics to the cooling arteries;
- the thermostabilization and temperature field uniformity of SDD;
- the local liquid freon supply to the ladder cooling arteries.

All the other problems of the design can be solved on the base of existing technologies and experience. A full scale 1.1 m Si ladder prototype is expected to be produced during the next year to test the proposed mechanics, cooling and alignment scheme.

### Acknowledgments

The authors are grateful to M. Price, K. Ratz, L. Leistam and O. Runolfsson for the numerous useful discussions and to H. Gutbrod for his help and kind support.

### References

- [1] Design study of the Large Hadron Collider (LHC), CERN 91-03.
- [2] J.Schukraft, Proceedings of the General Meeting on LHC Physics and Detectors, Evian-les-Bains, 5-8 March 1992, 479-511.
- [3] N.Antoniou et al., CERN/LHCC/93-16,LHCC/I 4 , 1 March 1993
- [4] P.Giubellino, ALICE note/SIL/92-3, Aug.1992
- [5] G. Batignani et al., IEEE Trans. Nucl. Science, Vol. 36, No. 1, Feb 1989.
- [6] F. Angelini et al, "MicroStrip Gas Chambers with true two-dimensional and pixel read-out"; int. report of Università Degli Studi di Pisa, INFN PI/AE 92/01.
- [7] CERN Safety Note TIS N°23.
- [8] STAR collaboration, Conceptual Design Report for the Solenoidal Tracker At RHIC.
- [9] J.Alexander et al., preprint CLEO,1992
- [10] C.Adolphsen et al.,NIM A313(1992),63)
- [11] G.Anzivino et al., NIM A256 (1987)65
- [12] G. Batignani et al., NIM A326 (1993) 183-188.
- [13] C.J.S.Damerell et al., NIM A288 (1990) 236-239
- [14] W.C.Carithers et al., NIM A289 (1990) 388
- [15] L3 Collaboration, CERN-LEPC 91-5,LEPC P4.Add.1,April 1991.
- [16] Silicon Tracking Conceptual Design Report, SCIPP 92/04, 1992; SDC Technical Design Report, SSC 92-201.
- [17] Letter of Intent for a General-Purpose pp Experiment at the Large Hadron Collider at CERN,CERN/LHCC/92-4,LHCC/I 2, 1992
- [18] AMOCO Performance Products, Inc., Developmental Product,1992
- [19] "Encyclopedia of Material Science and Engineering", Ed.M.B.Bever,MIT,USA.
- [20] NIM,A319(1-3),1992,228-232
- [21] "Engineered Materials Handbook" - "Composites", ASM International, Metals Park, Ohio,44073,1987
- [22] V.M.Dobulevitch et al., Further ideas on the first approach to the conceptual design of the cooling, mechanical and alignment systems of the vertex tracker for the H.I. experiment at the LHC, LHC-HI internal note, Nov. 1992.
- [23] O.Godisov et al., " Concept of the Cooling System of the ITS for ALICE: Technical Proposals, Theoretical Estimates, Experimental Results" , submitted to the WELDEC, First Int. Workshop on Electronics and Detector Cooling, Oct.1994, Lausanne, Switzerland
- [24] Metrologia,v.24,pp187-194, (1987).



# High Specific Stiffness Beryllium and Beryllium Alloys

Nancy F. Levoy, Kevin R. Raftery, and Raymond L. White

Nuclear Metals, Inc.

2229 Main St., Concord, Massachusetts 01742, USA

## Abstract

Beryllium has a unique combination of properties that include low density, high elastic modulus and strength, and good corrosion resistance. However, beryllium is difficult to fabricate due to its low ductility and high anisotropy. Nuclear Metals, Inc. has developed advanced beryllium extrusion technology over a forty year period and is a leading producer of extruded beryllium products. Products available include seamless tubing ranging in size from 3.2 mm O.D. by 0.076 mm wall up to 130 mm O.D. by 3 mm wall, as well as customized shaped extrusions. Small diameter tubing and complex shaped extrusions are produced by a novel filled billet approach. Typical properties of extruded beryllium tubing include a Young's modulus of 290 GPa, ultimate tensile strength of 690-830 MPa, 0.2% offset tensile yield strength of 410-520 MPa, and elongation of 5.5 to 7.5%. Extrusion of tube from new specialty grades of beryllium can result in product having an 0.2% offset tensile yield strength of up to 655 MPa with only a modest decrease in elongation when compared with extruded tubing from standard grade beryllium.

For applications requiring good ductility and lower cost, new beryllium-aluminum extruded alloy products are being developed at Nuclear Metals, Inc. These products combine the high strength and stiffness of beryllium with the ductility and toughness of aluminum. The beryllium-aluminum alloys contain approximately 65 weight percent beryllium, have densities less than 2,160 kg/m<sup>3</sup>, elastic moduli in excess of 210 GPa, and ultimate tensile strengths of 440 to 480 MPa. Technology is currently being developed for the extrusion of seamless beryllium-aluminum tubing and for the direct extrusion of complex shapes.

## 1. Introduction

The metal beryllium has a unique combination of properties that include low density, high elastic modulus, high strength and good corrosion resistance. In addition, beryllium retains useful properties at elevated temperatures. This introduction will give a general review of the properties and applications of beryllium, while subsequent sections of this paper will give more detailed information on the processing and properties of extruded beryllium and beryllium-aluminum alloy products.

The density of beryllium is 1,855 kg/m<sup>3</sup>, making it the lightest structural metal except for magnesium. With a room temperature elastic modulus of 290 GPa in tension or compression, beryllium is exceptional for its high stiffness to density ratio as illustrated in Table 1 [1]. Based on its strength to density ratio, beryllium is also competitive with

common engineering metals.

**Table 1.** Modulus to Density Ratio for Various Metals (m-N/kg × 10<sup>5</sup>) (after reference 1).

Metal	Temp.: 294 K	477 K	811 K
beryllium	1664	1642	1419
steel	268	251	218
titanium	236	209	142
aluminum	259	204	--
magnesium	244	160	--

Major limitations to more extensive application of beryllium metal include its high cost, low ductility, and high degree of anisotropy of structure and properties. Current technology for production of beryllium parts with optimized properties involves vacuum hot pressing beryllium powder of controlled size and purity to form fully dense fine-grained beryllium block. Parts can either be machined directly from the block, or the block can be further processed, e.g. by rolling or extrusion.

While isotropic percent elongation of beryllium in block form has historically been limited to approximately 1%, modern practice can now consistently produce beryllium block with 4% or better elongation [2]. However, even with these improvements in measured percent elongation, beryllium still fractures in a brittle mode. Since brittle fracture is believed to be inherent in the crystal structure of beryllium, further potential improvements to the ductility of beryllium are expected to be limited [3]. Percent elongation measured in wrought material may be significantly greater than in hot pressed block, but will vary greatly depending on the direction of property measurement due to texturing effects. For example, it is possible to achieve 20% elongation in extruded beryllium when properties are measured in the extrusion direction; however, percent elongation measured normal to the extrusion direction is typically less than 1%.

Beryllium is well suited to applications where high strength and stiffness are required in combination with severe weight restrictions. Extruded beryllium tubing is used extensively for structural support components in communications satellites based on its outstanding stiffness to weight ratio. Other structural applications for beryllium include use in satellite antenna booms, missile re-entry vehicles, and space telescopes. Additionally, beryllium is used in nuclear applications as reflectors and moderators based on its nuclear properties and low density.

Beryllium is also suited to many high stability instrument applications such as in inertial guidance components and optical platforms, which require high stability and resistance to micro-creep. The high elastic modulus of beryllium is important in instrument applications where beryllium is used because of its rigidity and retention of dimensional accuracy. Instrument grades of beryllium have been developed for high micro-yield strength (defined as the stress required to produce the first micro-inch of permanent strain, also known as the precision elastic limit or PEL), which contributes to excellent dimensional stability for these applications. Further, beryllium has a relatively low coefficient of thermal expansion (average measured as  $10.7 \times 10^{-6}/\text{K}$  in the temperature range of 275 to 311 K for instrument grade block [4]), giving it good dimensional stability over a wide temperature

range. However, for wrought material where texturing occurs, the coefficient of thermal expansion may vary with direction by up to 15% [4].

## 2. Beryllium extrusion technology

### 2.1. Overview

Extrusion is the major metalworking technique used for production of long lengths of wrought beryllium metal. Advanced beryllium extrusion technology has been developed at Nuclear Metals, Inc. (NMI) over a forty year period. Special extrusion techniques are required for beryllium due to its particular physical and mechanical properties. These properties of beryllium include: (1) a lack of triaxial ductility and a high degree of anisotropy; (2) a tendency to gall and stick when extruded through steel extrusion tooling under normal extrusion conditions; (3) very high stiffness at temperatures less than 873 K; and (4) rapid oxidation in air at temperatures above 1,073 K [1,5].

Many of the extrusion problems associated with the material properties outlined above have been eliminated by application of elevated temperature canned billet extrusion technology. For beryllium, canned billets are typically formed by placing the beryllium billet inside a can of low carbon steel. Low carbon steel is selected because at typical extrusion temperatures for beryllium, the steel and beryllium have similar stiffnesses (i.e. they are mechanically compatible) and they don't react with each other (i.e. they are chemically compatible). Furthermore, steel cans can easily be removed from beryllium after extrusion by pickling in nitric acid. The canned billets are evacuated and the can sealed to isolate the billet from the atmosphere. Evacuation is done at slightly elevated temperatures to remove potential organic contaminants.

An important relationship basic to the extrusion process relates the pressure required to perform the extrusion to the reduction of cross sectional area of the billet that occurs during extrusion, and to the material flow characteristics of the extrusion billet. The expression for this relationship is

$$P = K \ln R \quad (1)$$

where  $P$  is the required extrusion pressure,  $R$  is the reduction ratio or the ratio of the cross-sectional area of the starting billet to that of the extruded rod, and  $K$  is the extrusion constant, which is a measure of the billet's resistance to plastic flow through the extrusion die, and is a strong function of extrusion temperature.

Extrusion of canned billets must be done under conditions of streamlined flow in order to maintain the uniform enclosure of the beryllium billet inside the can material. In streamlined flow, the outside of the billet becomes the outside of the extruded rod [6]. When streamlined flow is achieved, any shape within the cross-section of a cylindrical extrusion billet is reproduced exactly in a reduced size in the cross-section of a rod extruded from this billet through a round die. The resulting linear reduction is equal to the square root of the reduction ratio  $R$ . Figure 1 shows a "streamlined flow" extrusion as well as the uniform flow of canning material over the core material. Streamlined flow is accomplished by use of an extrusion die with a conical approach, combined with good lubrication and tightly fitting tooling [5].

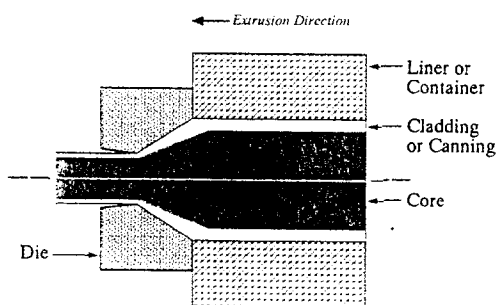


Figure 1: Example of streamlined flow extrusion

Beryllium billets for extrusion are usually made from high density vacuum hot pressed blocks of beryllium powder. This powder metallurgy route avoids problems that result when starting with ingot cast beryllium billets; namely, that cast beryllium ingots generally have large grains which, combined with high crystal anisotropy, form a very rough surface on extruded beryllium product when the steel can is removed. Extrusion of consolidated powder, on the other hand, results in a smooth surfaced

product with significantly better mechanical properties.

## 2.2. Processing and properties of extruded beryllium tubing

To date, over 1,200 meters of seamless beryllium tubing have been delivered by NMI for use in modern satellite structures. Seamless beryllium tubing is produced in sizes ranging from 3.2 mm outer diameter by 0.076 mm wall thickness up to 130 mm outer diameter by 3 mm wall thickness, and lengths of up to 4.25 m. Several examples of seamless beryllium tubing are shown in Figure 2.

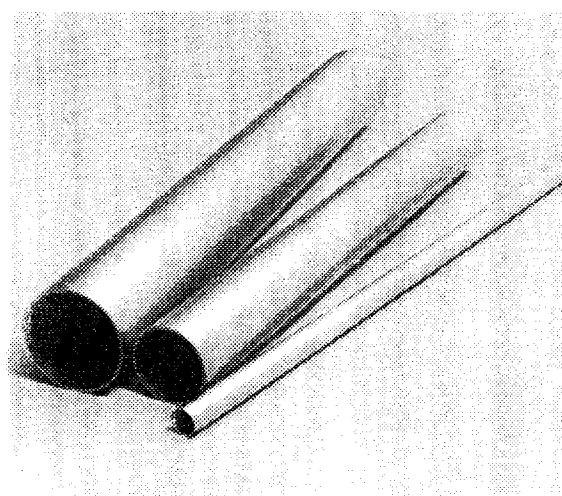
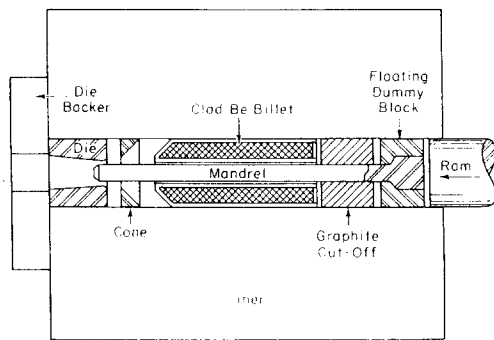


Figure 2: Examples of seamless beryllium tubing

Two extrusion methods are used at NMI to produce beryllium tubing. Small diameter tubing is produced by a novel filled billet approach, which is discussed in section 2.3. The more commonly used method of tubing production involves extrusion of a hollow billet over a floating mandrel, and is illustrated in Figure 3 [7]. This method is used for production of tubing greater than 13 mm diameter. The input billet for this method is canned as described in section 2.1, but with the addition of an inner sleeve of can material to accommodate the mandrel, as illustrated in Figure 4. Dimensional tolerances for extruded beryllium tubing are typically as follows:

wall thickness	+/-0.127 mm
outer diameter	+/-0.127 mm
inner diameter	+0.000/-0.762 mm
length	+3.2 mm/-0.0
straightness	0.83 mm/m
surface finish	<3.2 $\mu\text{m}$ .



**Figure 3:** Extrusion of hollow billet over floating mandrel [7]

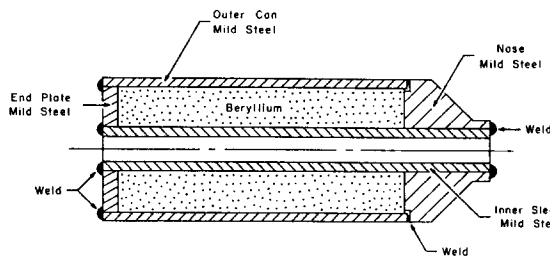


**Figure 4:** Diagram of canned billet for tube extrusion

Extrusion processing of the canned beryllium billets for tubing consists of preheating the billet assembly to the extrusion temperature inside a protective atmosphere furnace in order to minimize oxidation of the can material, which would otherwise increase friction during extrusion. Extrusion temperature is selected between 980 K and 1,250 K, depending on the tube size, can material and required tolerances. The billets are lubricated prior to assembly inside the extrusion press. The extrusion press container is preheated and lubricated prior to extrusion. Ram speed is selected in the range of 11 to 80 mm per second, depending on the final product reduction ratio. Higher speeds are used when the extrusion press capacity is limited to reduce the amount of billet cooling during processing. Lower speeds are necessary for high reduction extrusions to reduce adiabatic heating from friction.

The reduction ratio for a given extrusion is selected in the range of 5x to 60x, and may be limited by the force available from the extrusion press, as described above by equation 1. Reductions of less than 5x result in material with poorer properties, while reductions of greater than 60x generate excessive adiabatic heating due to frictional effects, leading to poor

dimensional control and potential reaction between the beryllium and the can material.

After the extruded tube is cooled, the canning material is removed by etching, usually with nitric acid. The tubes are then dimensioned, warm straightened, machined to length and chemically etched to remove surface twinning effects. This last step is necessary since surface twinning in beryllium can have a detrimental effect on mechanical properties.

Extruded beryllium tubing typically has an ultimate tensile strength of 690-830 MPa; a 0.2% offset yield strength of 415-520 MPa; and an elongation in a 25.4 mm section of 5.5-7.5%, all measured in the extrusion direction. Mechanical properties of the tubing are a function of the extrusion conditions and of the input material. For example, significantly higher than typical strength levels with only a modest decrease of ductility have recently been demonstrated in extruded tubing produced from a new instrument grade of beryllium, which may thus be of interest for structural applications as well. A comparison of properties for a typical structural grade of beryllium tubing vs. this higher strength beryllium tubing is provided in Table 2. The tubes tested for this comparative data were both extruded from canned hot pressed powder billets that were extruded with a 22:1 reduction ratio to produce tubes with a final size of 26.7 mm outer diameter by 1.27 mm wall thickness.

**Table 2.** Mechanical Properties of Extruded Tubing

	Type 1	Type 2
Ultimate tensile strength (MPa)	761	906
0.2% tensile yield strength (MPa)	428	658
% Elongation (in 25.4 mm)	6.7	5.1
1.0% compressive yield strength (MPa)	435	652
Tensile modulus (GPa)	294	300

Mechanical test results reported in Table 2 were measured for the material oriented in the extrusion direction. There is a pronounced difference in properties for extruded beryllium

when measured in the extrusion direction compared with the direction normal to the extrusion direction. Differences in properties increase with increasing reduction ratio used in the extrusion process, since an increase in reduction results in increased crystallographic orientation in beryllium and a concomitant increase of ductility in the extrusion direction. Increases in extrusion temperature are also typically accompanied by increases in ductility combined with decreases in strength.

### 2.3. Filled billet extrusion

The technique of filled billet extrusion is used for producing complex shapes or shapes with small dimensions that cannot be produced by conventional means. This technique is particularly useful for processing beryllium since post-extrusion working of beryllium is difficult. Filled billet extrusion is an extension of canned billet extrusion technology, which was described in section 2.2. As previously described, if extrusion is done under conditions of streamlined flow, any shape within the cross-section of a cylindrical billet extruded through a round die will be exactly reproduced with reduced dimensions in the extruded product. The filled billet extrusion technique involves preshaping a billet of the material to be extruded to an enlarged cross-section of the finished part. Filler material, selected for ease of removal after extrusion by chemical or mechanical means, is shaped to fit around the product material to form a cylindrical billet, as illustrated in Figure 5. The cylindrical billet is then extruded as a single entity. In the case of beryllium, the filler material is usually steel, or a suitable nonferrous alloy that matches the stiffness of beryllium at the extrusion temperature. Post-extrusion, the filler material is removed by chemical etching, leaving the extruded product of the desired shape [5,6].

The filled billet shown in Figure 5 is modified with a hollow center for extrusion over a floating mandrel. Figure 6 shows a billet of this configuration in the partially extruded condition and as the fully extruded finned tube product, after removal of the filler material. This extrusion was processed with a 16x reduction ratio.

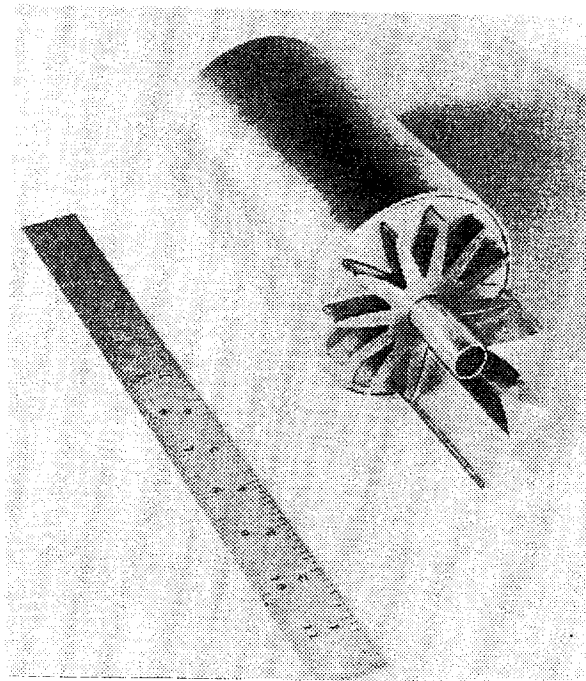


Figure 5: Example of formation of modified filled billet

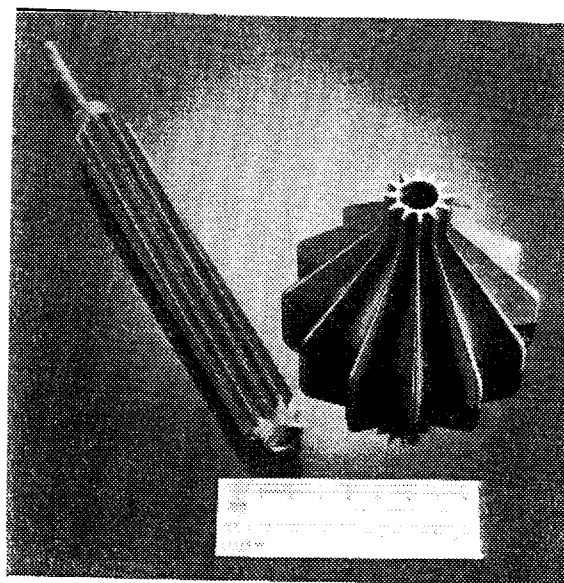
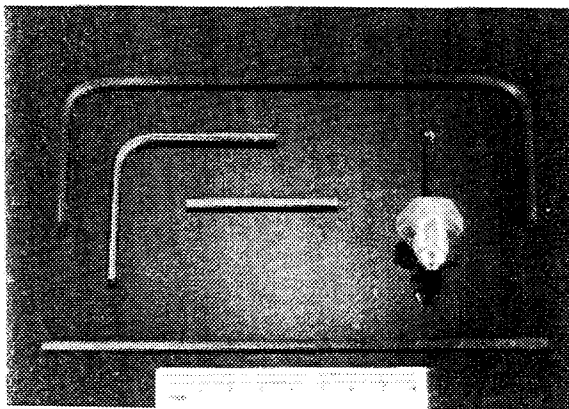


Figure 6: Partially and fully extruded finned beryllium tube, produced by the filled billet technique

Small diameter beryllium tubes are produced by a variation of the filled billet technique. For their production, a sacrificial core of filler material is extruded within a beryllium rod, then removed by chemical etching. For long tubes of small diameter, a water soluble inner core may also be used to aid removal of the filler material by chemical

etching. Beryllium tube is generally produced by the filled billet technique when the inner diameter is less than 12.7 mm.

An example of small diameter beryllium tube produced by this technique is shown in Figure 7. This tubing, which was produced for a heat exchanger application, has an outer diameter of 3.2 mm and a wall thickness of 0.08 mm, and can be produced in lengths of up to 3 m. The tubing illustrated in Figure 7 was produced using both an inner and outer filler, and double extruding the composite billet. The reduction ratio (ratio of the cross-sectional area of the starting billet to the cross-sectional area of the extruded billet) for the primary extrusion was 16:1; the reduction ratio for the secondary extrusion was 25:1. A water soluble salt inner core with a post extrusion diameter of typically 0.4 mm is used in this type of extrusion, and is rapidly removed after extrusion by use of high pressure water fed into the extrusion through a hypodermic needle. After the salt is removed, nitric acid is pumped through the tube and the inner steel filler is uniformly removed. Without the soluble core, etching to remove the inner filler could take 60 hours. By using the soluble core, etching time is dramatically reduced.



**Figure 7:** Small diameter (3.2mm) beryllium tube, produced by the filled billet technique

### 3. Beryllium Aluminum Alloy Extruded Product

#### 3.1 Applications

For applications where greater ductility, good stiffness and lower cost are required,

extruded beryllium-aluminum alloys under development at NMI offer an alternative to pure beryllium. These alloys combine the high strength and stiffness of beryllium with the ductility and toughness of aluminum. At present, this technology is of greatest interest to the aerospace industry, for structural applications such as ground and space based interceptor and tracking systems, which require minimum weight, high stiffness, good damping capacity, and thermal stability. However, this technology may also find applications in commercial markets where lightweight, high strength materials show an advantage over existing materials. Potential commercial applications include recreational sporting goods, and electromechanical machinery that can take advantage of high stiffness and light weight to achieve improved performance.

#### 3.2 Processing and properties

Beryllium-aluminum alloys date from the 1960's. The beryllium-aluminum alloy known as Lockalloy (62Be-38Al) was developed by NMI for Lockheed Missiles and Space Corporation under contract to NASA and was produced by Kaweicki Berylco Inc. (KBI). Due to the state of casting technology for reactive metals and two phase alloys at that time, Lockalloy was produced by powder metallurgical (P/M) processes, similar to those used for pure beryllium. However, recent alloy and process development work has resulted in the casting of high quality beryllium-aluminum alloys. This development leads to the possibility of producing beryllium-aluminum composites through conventional metal casting and metal working technologies. Metal casting is a significantly more cost-effective method than P/M processing for beryllium-aluminum alloy production since it is a less process intensive manufacturing technique that affords a higher product yield. In addition, preliminary data indicate that cast and extruded beryllium-aluminum alloys will have properties superior to those of P/M based alloys.

Current development efforts are focused on extrusion of cast beryllium-aluminum ingots having a nominal composition of 65 weight percent beryllium and 35 weight percent aluminum, and which contain small elemental alloying additions that improve the castability and properties of this material.

The microstructure for cast ingots of this material includes a primary beryllium phase for strength and stiffness surrounded by a ductile aluminum matrix. These alloys have a density of less than  $2,160 \text{ kg/m}^3$  and an elastic modulus in excess of 210 GPa.

Vacuum induction melting is used to produce beryllium-aluminum ingots of varying geometries up to 152 millimeters in diameter. Since both beryllium and aluminum have a tendency to gall and stick when extruded through steel extrusion tooling under normal extrusion conditions, beryllium-aluminum ingots are canned in a ductile metal can prior to extrusion. The can, typically formed from copper or aluminum, reduces surface cracking and aids lubrication during extrusion. Although beryllium-aluminum alloys are more ductile than pure beryllium, they still must be extruded hot to obtain uniform deformation and properties in the product. Additional factors that affect the choice of extrusion conditions for beryllium-aluminum alloys are the lower melting temperature and lower stiffness of aluminum relative to beryllium. Because of these factors, extrusion of beryllium-aluminum alloys must be done at temperatures less than 755 K. Reduction ratios may also be limited by these factors.

Properties of extruded beryllium-aluminum rod are shown in Table 3. These properties were measured in the extrusion direction from extruded rods produced from cast ingot of two different alloys, both of which contain 65 weight % beryllium. The 40.6 mm diameter ingots were canned in copper and extruded at 723 K with a 9x reduction ratio. Higher reductions would be expected to further enhance properties. Properties are also shown for both alloys after annealing at 823 K for 24 hours.

Beryllium-aluminum alloy ingots can be extruded into seamless tubing in a manner similar to that described for pure beryllium. Due to its higher ductility, beryllium-aluminum also has the potential to be directly extruded through shaped dies into complex configurations. This type of shaped die extrusion for beryllium-aluminum is currently under development at NMI.

**Table 3.** Properties of extruded cast billets

(NOTE: A-E = As-extruded, AN = Annealed)

	Alloy 310		Alloy 311	
	A-E	AN	A-E	AN
0.2% yield strength(MPa)	342.4	321.8	365.2	351.4
Tensile strength(MPa)	440.3	447.2	467.8	485.1
% E (in 25.4 mm)	12.6	16.7	12.5	12.5
modulus (GPa)	237.0	227.4	239.8	243.2
density ( $\text{kg/m}^3$ )	2,131	2,131	2,131	2,131

#### 4. Summary

Beryllium is used in a variety of structural aerospace applications where high strength and stiffness are required in combination with severe weight limitations. Beryllium is also well suited to many high stability instrument applications that take advantage of its rigidity and retention of dimensional accuracy. Beryllium extrusion technology is well developed and can be used to produce extruded products such as thin wall seamless tubing as well as products with complex cross-section produced by the filled billet extrusion technique. For applications requiring higher ductility and lower cost, extruded beryllium-aluminum alloys under development at NMI offer an alternative to pure beryllium products.

#### 5. References

- [1]. Gerald FRIEDMAN, 1967, "Problems in the extrusion of structural beryllium shapes", *Technical Paper MF-67-204*, American Society of Tool and Manufacturing Engineers, Dearborn Michigan.
- [2]. A.J. MARTIN and D.R. ADOLPHSON, 1979, "Introduction" in *Beryllium Science and Technology 1*, D. Webster and G.J. London, eds., Plenum Press, NY, 1-5.

- 
- [3]. H.J. SAXTON and G.J. LONDON, 1979, "Flow and fracture of polycrystalline beryllium", in *Beryllium Science and Technology 1*, D. Webster and G.J. London, eds., Plenum Press, NY, 115-144.
- [4]. Norman P. PINTO, 1979, "Properties", in *Beryllium Science and Technology 2*, Dennis R. Floyd and John N. Lowe, eds., Plenum Press, NY, 319-350.
- [5]. Paul LOEWENSTEIN, 1979, "Metalworking II: Extrusion", in *Beryllium Science and Technology 2*, Dennis R. Floyd and John N. Lowe, eds., Plenum Press, NY, 67-82.
- [6]. William T. NACHTRAB and Paul LOEWENSTEIN, 1989, "'Filled billet' extrusion: complex shapes from simple extrusions", in *IEXTRU '89*, J.S. Gunasekera, ed., Ohio University, Athens, Ohio, 343.
- [7]. Paul LOEWENSTEIN, A.R. KAUFMAN, and S.V.ARNOLD, 1955, "Mechanical working of beryllium by extrusion", in *The Metal Beryllium*, D.W. White Jr., and J.E. Burke, eds., The American Society for Metals, Cleveland, Ohio, 245.



# High Dimensional Stability Structure

## Continuous Fibre Metal Matrix Composites

J.-F. Peltier\*, J. Pernon\*, M. Rabinovitch\*

\* AEROSPATIALE Espace & Défense  
Les Mureaux 78133 - France

\* ONERA  
Châtillon 92322 - France

### Abstract

AEROSPATIALE has been involved for many years in the development of light weight structural materials. In that respect light alloys metal matrix composites were early considered as promising materials for such applications, which require high dimensional stability.

One way of making Metal Matrix Composite (MMC) parts is inspired of organic prepreg route. It consists of a lay up of unidirectional carbon-metal prepreps, heat treated under pressure. It is a Solid Phase Processing technology (SPP). Another way consists of using sized fibres and preforms. These preforms are infiltrated with molten alloy. It is a Liquid Phase Processing technology (LPP).

Tensile strength around 1000 MPa and Tensile modulus around 300 GPa are obtained with unidirectional materials using ultra high modulus (UHM) fibres.

A prepreg pilot production line has been operating since 1993 for C/Mg and C/Al. A liquid production line will be operational in 1995.

### 1. Introduction

The present paper successively presents the expected advantages for development of light alloy matrix composites and AEROSPATIALE activities in terms of materials, processes results and applications.

AEROSPATIALE is investigating Metal Matrix Composites, in respect with their exceptional characteristics, for high stability space structures in order to manufacture structural supports for telescopes. For such applications, satellite material requirements are characterized by a high stiffness, low expansion, high conductivity, low moisture absorption, no outgassing and high microyielding strain.

Compared to polymer composites, metal matrix confers good tensile strength to MMCs, together

with higher thermal and electrical conductivity and no moisture expansion. Compared to non reinforced metals, carbon fibre reinforcement allows weight saving, higher rigidity, strength and dimensional stability. Graphite fibre reinforced metal matrix composites give rise to a new class of metal materials.

### 2. MMCs Materials

Characteristics of fibres are of prime importance, because they govern the composite properties.

To achieve highest values in specific stiffness, specific strength and dimensional stability, continuous UHM graphite filaments are particularly suited. Tensile modulus and strength are mainly controlled by the structure of the fibre. The choice

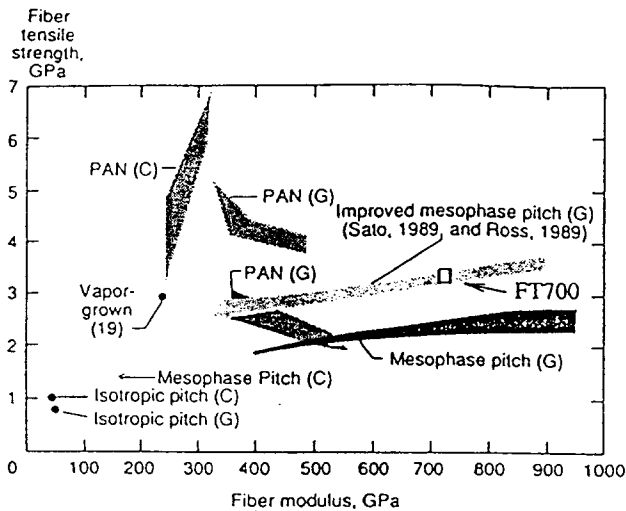


**Figure 1. Tensile strength and modulus of various types of carbon fibres**

of the carbon fibre was done considering different characteristics (see Figure 1).

- PAN (PolyAcrido Nitril) -based fibres have high tensile low modulus and positive coefficient of thermal expansion (CTE).
- Pitch-based fibres have low tensile high modulus and negative CTE.
- Improved Pitch-based fibres have higher tensile strength.

That is the reason why mesophase pitch-based carbon fibres are preferred to PAN based carbon fibres for parts designed for stability. Our choice ended on a TONEN FT700 product which is a 700 GPa class fibre and offers a good compromise for both modulus and strength (see Table 1).

AEROSPATIALE has developed a family of MMCs materials. Both aluminium and magnesium have been primary used to manufacture composites with oriented continuous fibres. Particles are never used for reinforcement.

Table 2 compares the unidirectional mechanical properties of C/Mg and C/Al versus a C/organic resin frequently used in space structures.

The advantages of MMCs materials are:

**1. over organic matrix composites:**

- no moisture absorption,
- better behaviour at high temperature (high temperature resistant structures)<sup>(1)</sup>,

<sup>1</sup>. will be characterized in 1996

**Table 1 : Typical properties of Tonen Forca FT700 carbon fibres**

	Properties	FT 700
Form of fibre	Filament diameter	10 $\mu\text{m}$
Tow	Yield (3K base)	0.52 g/m
Physical properties	Density	2.16 g/cm <sup>3</sup>
Mechanical properties	Tensile strength	3300 Mpa
	Tensile modulus	700 GPa
	Elongation	0.5 %
Thermal properties	Coefficient of Thermal Expansion	$-1.5 \cdot 10^{-6} \text{ K}^{-1}$
	Thermal Conductivity	360 W.m <sup>-1</sup> .K <sup>-1</sup>
	Specific Heat	0.71 J.g <sup>-1</sup> .K <sup>-1</sup>
Electrical Properties	Electrical Resistivity	$5 \cdot 10^{-4} \Omega \cdot \text{cm}$
Oxidation Resistance	Weight loss after 2 hours at 650°C	1.7 %

- better transverse and longitudinal thermal conductivity,
- no outgassing

**2. over metals:**

- coefficient of thermal expansion near zero, leading to a good dimensional stability control,
- better specific modulus,
- lower density.

From the point of view of the design and mounting:

- dimensioning rules are similar to organic matrix composites,
- concept is flexible due to the laying-up, and machining is well controlled,
- mounting is possible by bolting, riveting, bonding...

Metal matrix composites materials are very suited for high dimensional stability structure but also for thermal control applications.

### 3. Manufacturing Processes

Several methods for manufacturing continuous fibre MMCs were investigated. Two ways were selected:

1. the first one is derived from the organic prepreg route. It is a Solid Phase Processing technology (SPP), well suited for thickness lower than 3 mm;
2. the second one is a Liquid Phase Processing technology (LPP) similar with resin transfer moulding process, well suited for thickness greater than 1.5 mm.

#### 3.1. The Solid Phase Process Technology (SPP)

##### 3.1.1. Prepreg Elaboration

Prepreg processing steps are:

1. a removal of fibre sizing,
2. a spreading step,
3. a conditioning of the spread tow on a spool.

Figure 2 shows a schematic of the unit which insures these first three steps. Spools of 50 to 200 m of spread tows are then loaded in a Multi-

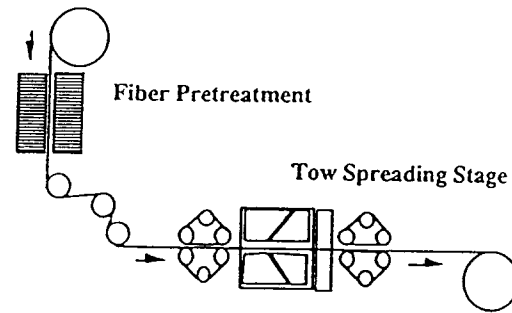


Figure 2. Fibre treatment (sizing degradation) and spreading line

layer Magnetron Physical Vapour Deposition apparatus (MMPVD) (Figure 3). Temperature, pressure, deposition rate of the coating and matrix proportion ratio are controlled to provide an industrial semi-product.

Morphology of prepreg has been investigated. Depending on pulverisation power and substrate temperature, metal layer was found to grow with a radial columnar morphology or with a multiaxial polycrystallisation. Figure 4 a and b present micrographs of filaments metallized with magnesium under different conditions. In figure 6b parameters have been set to provide an hermetic

Table 2 : Comparison of mechanical properties

Unidirectional Properties	Carbon/ Magnesium FT700/Mg	Carbon/ Aluminium FT700/Al	Carbon/ Organic resin M55J/M18
Moisture absorption	0	0	0.8 %
Coefficient of Moisture Expansion	0	0	$-100 \times 10^{-6} \%^{-1}$
UV, atomic oxygen aging	as titanium <sup>(a)</sup>	as aluminium	
Coefficient of Longitudinal Thermal Expansion	$-0.2 \times 10^{-6} \text{ K}^{-1}$	$+0.5 \times 10^{-6} \text{ K}^{-1}$	$-1.5 \times 10^{-6} \text{ K}^{-1}$
Coefficient of Transverse Thermal Conductivity	$90 \text{ W.m}^{-1}.\text{K}^{-1}$	$150 \text{ W.m}^{-1}.\text{K}^{-1}$	$<10 \text{ W.m}^{-1}.\text{K}^{-1}$
Specific gravity	2	2.4	1.6
Longitudinal Young's modulus	330 GPa	275 GPa	300 GPa
Longitudinal ultimate tensile strength	1000 MPa	600 MPa	1700 MPa
Void content	<1%	<1%	<3%
Outgassing: Total Mass Loss	0	0	0.31%
Collated Volatile Condensable Mat.	0	0	0.03%

a. A titanium sheet (integrated during processing) surrounds the C/Mg in order to avoid oxidation.

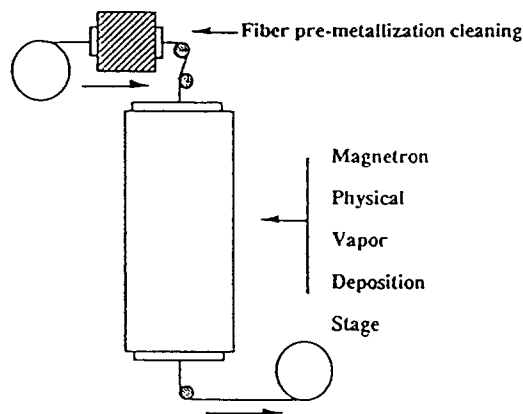


**Figure 3. Multilayer Magnetron Assisted Physical Vapour Deposition Liner**

coating with a thickness related to the desired fibre volume ratio.

This process is validated as an industrial process.

### 3.1.2. Densification

Metallized tows are conditioned in unidirectional prepreg to make preforms. If complex geometry preform is needed, a polymeric binder is used to keep the shape of the preform (Figure 5).

A preform is densified by diffusion bonding in a hot press with specific heating tools. This technique allows a lower manufacturing temperature

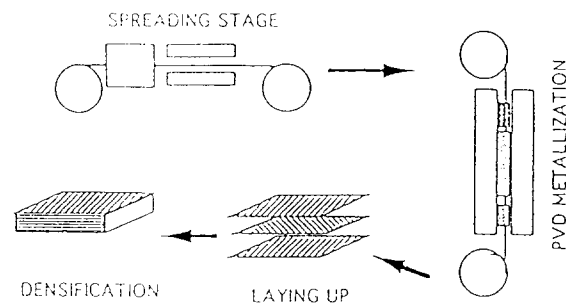
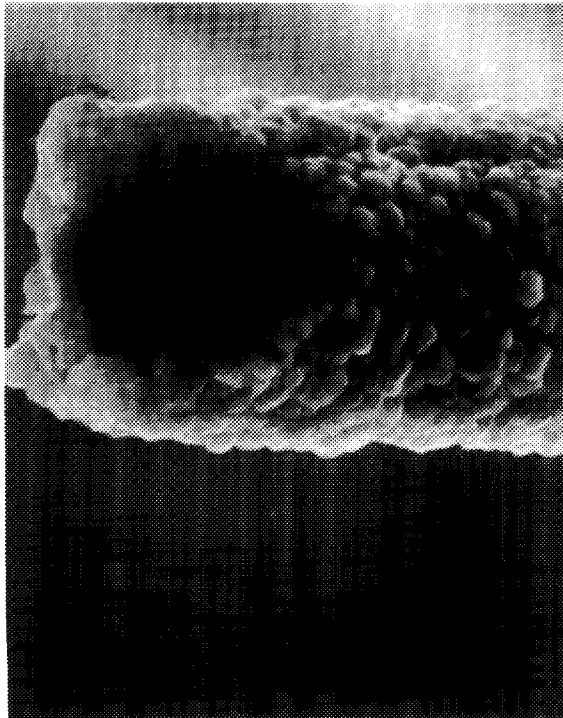


**Figure 5. MMCs processing with solid technology**



a. Low temperature metallization



b: High temperature metallization

**Figure 4. FT700 fibres metallized with magnesium by PVD process**

than liquid phase infiltration. Therefore, in the case of reactive systems it reduces chemical reactions activation, such as carbide formation. Pressures from 15 to 30 MPa are applied, at temperatures between 500 to 600°C. Unidirectional plates of TONEN FT700/Mg with tensile strength of 1000 MPa and tensile modulus of 300 GPa are obtained. See annex 1 for the characteristics of unidirectional plates.

### 3.2. Liquid Phase Process Technology (LPP)

AEROSPATIALE and ONERA have developed a C/Al and C/Mg manufacturing process using hot pressing under medium pressure (150 to 300 bars) in liquid phase.

This process is particularly well suited for plates and tubes manufacturing.

Figure 6 shows the block diagram for the principal stages of the process.

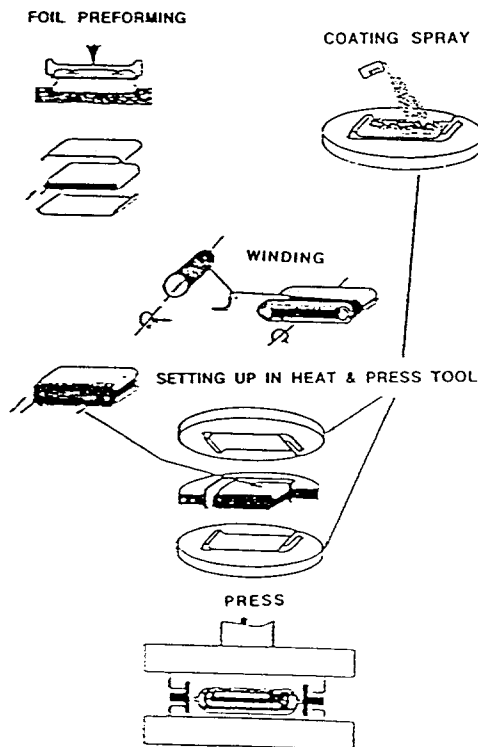


Figure 6. Manufacturing Process of MMC by Liquid Phase Process Technology

- The preform is made of fibre laying obtained by carbon yarn winding around a metallic mandrel.
- The metallic foils (Al or Mg) surround the preform.
- The assembly is placed with a tool between two heating plates on an hydraulic press.

The temperature and pressure cycles are computer controlled in order to optimise the manufacturing process, to obtain a very good reproducibility and to avoid chemical reactions (especially for Aluminium).

Figure 7 presents a typical manufacturing cycle.

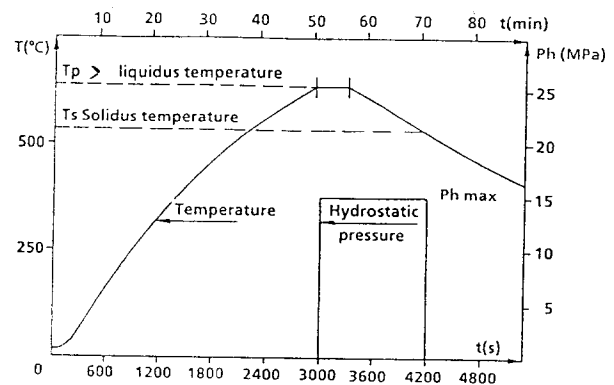


Figure 7. Schematics of manufacturing cycles

An improved liquid phase processing technology is now going on. Thick quasi isotropic plates and quasi unidirectional tubes have been successfully manufactured (See precision data in annex 2).

## 4. MMCs Industrial Capabilities

### 4.1. In SPP Technology

Prepreg elaboration unit: 60 kg/year.

Hot press: diameter of 0.8 m, maximal area of 0.5 m<sup>2</sup>.

Autoclave and furnace (specific for tube manufacturing) of 2 m.

### 4.2. In LPP Technology

Capacity: 150 kg/year.

Hot press: diameter of 0.8 m, maximal area of 0.5 m<sup>2</sup>.

It is possible, with this process, to reach higher dimensions with specific facilities and by using the same heating process.

## 5. MMCs Applications For Spacecraft Structures

It is possible to manufacture high stability truss structures with some devices like tubes, omega shapes and stiffeners.

In SPP technology, AEROSPATIALE has manufactured plates, omega and tubes.

In LPP technology, AEROSPATIALE has manufactured or will manufacture:

- plates (300 x 300 x 1.5 mm) in 1993;
- plates (500 x 300 x 5 mm) in 1995;
- L profiles;
- 200 mm long, 25 mm diameter and 2 mm thick tubes.

The SPP advantages versus LPP process are a more accurate laying up, and a lower processing temperature. The LPP advantages versus SPP process are a cheaper price, and a higher thickness.

Other future applications are possible: for thermal control, wave guides, reflectors...

Figure 10 shows a tube manufactured by solid way.

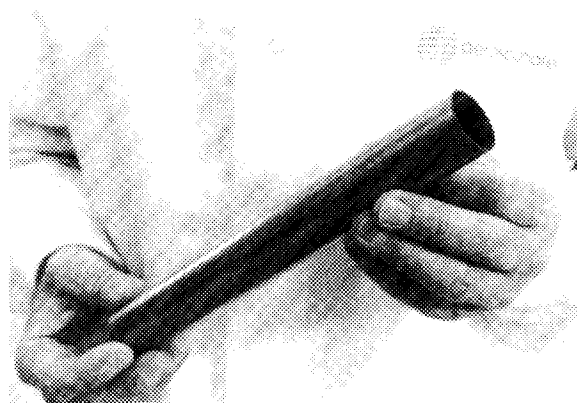


Figure 8. MMC Tube

The technical data of this tube are:

Length: 1000 mm

Diameter: 32 mm

Thickness: 1.4 mm

Lay-up:  $(0_2/\pm 25/0_2)_s$

Fibre volume: 50%

Compression ultimate strength: 260 MPa

Compression Young's modulus: 260 GPa

Coefficient of thermal expansion (longitudinal):  $+1.4 \cdot 10^{-6} \text{ K}^{-1}$

## 6. Conclusions

After a six years effort, two kinds of processes for manufacturing MMCs parts (C/Al and C/Mg) are now mastered. The prepreg pilot production line needed by the Solid Phase Process Technology has been operating since 1993. The liquid production line for the Liquid Phase Process Technology will be operational in 1995. Aerospace application fields are closely investigated. Corrosion resistance, thermal cycling and microstrain behaviours are carefully looked at.

The two processes are not only restricted to the manufacturing of aerospace parts. MMCs (C/Al and C/Mg) materials could have many applications in other fields because of their exceptional characteristics.

## References

- [1]. M. Rabinovitch, J.-C. Daux, J.-C. Raviart, M.-H. Vidal-Sétif, R. Hevrel, H. Abiven et J.-F. Peltier, Proc. Internat. Symp. "Advanced materials for light weight structures", ESTEC, Noordwijk, The Netherlands, 25-27 March 1992, ESA SP 336, October 1992, pp. 135-139.
- [2]. M. Rabinovitch, M.-H. Vidal-Sétif, J.-C. Daux, J.-L. Raviart, J.-L. Gerard, R. Hevrel, L. Lancin, O. Perez, Proc. I.C.C.M. 9, Madrid, 12-16 July, 1993, pp. 683-690.

## Annex 1 - Solid Way Process

The quasi-tropic plate is a 72-ply plate; its layout is  $(0, 45, 90, -45, 0, 45, 90, -45, 0)_{4,s}$ .

**Table 1 : Requested and Measured Values for C/Mg Plates**

Properties	Requested (unidir)	Measured (unidir)	Measured (quasi-iso)
Void Content	3%	0.7%	
Longitudinal features			
CTE	$0.0 \pm 0.5 \times 10^{-6} \text{ K}^{-1}$	$-0.22 \times 10^{-6} \text{ K}^{-1}$	$3 \times 10^{-6} \text{ K}^{-1}$
Young's modulus	$300 \text{ GPa} \pm 30 \text{ GPa}$	290 GPa	92 GPa
Ultimate tensile stress	> 900 MPa	943 MPa	170 MPa
Transverse features			
Ultimate tensile stress	> 20 MPa	90 MPa	
Young's modulus	> 20 GPa	54 GPa <sup>(a)</sup>	
Shear tensile stress	> 20 MPa	38 MPa	
Poisson's coefficient	-	0.324	
Microyielding stress	-	50 MPa <sup>(b)</sup>	

a. Sample dimensions  $37 \times 7.86 \times 1.09 \text{ mm}$  (in transverse the titanium foil predominates).

b. Corresponding residual deformation  $< 2 \mu\text{m.m}^{-1}$ .

## Annex 2 - Liquid Way Process

For a quasi isotropic lay up  $(0, \pm 45, 90)_s$  and a FT700/Mg with AZ61 matrix, the measured values are:

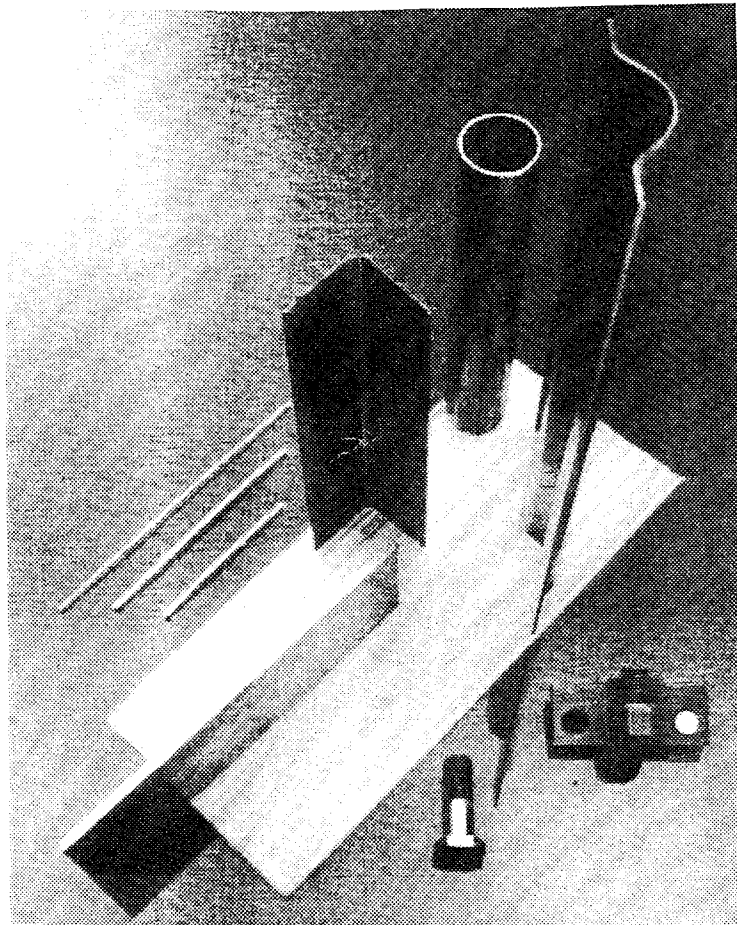
**Table 2 : Mechanical and thermal measured properties**

Type of test	Properties	Measured value
Tensile at 0°C (4 tests)	Young's modulus	$106 \pm 16 \text{ GPa}$
	Ultimate tensile stress	$294 \pm 44 \text{ MPa}$
Compression at 0°C (5 tests)	Ultimate stress	$84 \pm 7 \text{ MPa}$
3 points bending (8 tests)	Ultimate shear stress	$9.8 \pm 1.4 \text{ MPa}$
Shear plan (type losipescu, 3 tests)	Ultimate shear stress	$71 \pm 3 \text{ MPa}$
	Shear modulus	$24 \pm 2 \text{ GPa}$
Titanium foil shear	Ultimate tensile stress	$20 \pm 2 \text{ MPa}$
from 23.3°C to 44.1°C	CTE	$1.67 \pm 0.09 \times 10^{-6} \text{ K}^{-1}$
from 44.1°C to 22.5°C	CTE	$1.76 \pm 0.09 \times 10^{-6} \text{ K}^{-1}$
	Long. thermal conductivity	$95 \text{ W.m}^{-1}.\text{K}^{-1}$
	Transverse thermal conduct.	$17 \text{ W.m}^{-1}.\text{K}^{-1}$

**Table 3 : Average geometrical characteristics (12 recurring plates AZ61)**

Fibre volume	$49.5 \pm 1.5\%$
Thickness	$7.1 \pm 0.2 \text{ mm}$
Flatness (upper side)	$0.20 \pm 0.07 \text{ mm}$
Flatness (lower side)	$0.18 \pm 0.04 \text{ mm}$
Parallelism	$0.3 \text{ mm} \pm 0.1 \text{ mm}$ (100 mm length)

## Annex 3 - MMC Products





# High Performance Polyarylates under radioactive, cryogenic, and high temperature conditions

Peter R. Fialla  
ISONOVA, Technische Innovationen GmbH  
A-2355 Wiener Neudorf, Austria

## Abstract

Fully aromatic, amorphous polyesters, i. e. polyarylates (ISARYL® 15 and ISARYL® 25) have been developed to meet advanced needs for electrical insulation materials. This paper presents the mechanical, thermal, and electrical data of parts and films. Data on cryogenic tests are given and properties after exposure to nuclear radiation up to a dose of  $10^8$  Gray are given. Examples and a survey of applications are given, including experiences made at CERN.

**KEY WORDS:** polyarylates, high performance plastics, cryogenics, nuclear radiation, electrical insulators, transparent films, injection molded parts, sintered parts

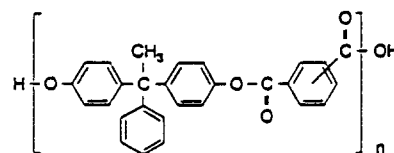
## 1. Introduction

ISARYL® 15 and ISARYL® 25 are amorphous polyarylates consisting of carbon, oxygen, and hydrogen only. ISARYL®s are high performance plastics opening new application possibilities, especially where e. g. a combination of properties such as high temperature resistance, resistance to nuclear radiation, good mechanicals at cryogenic temperatures, good electrical insulating properties, low moisture uptake and low flammability together with a low specific gravity of 1.2 is required.

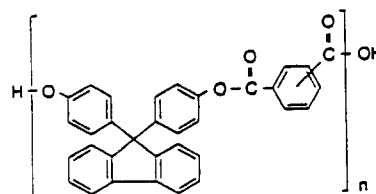
These polymers are produced by interfacial polycondensation. The polymer powder can be converted into: solvent cast films, injection molded parts, and sintered net shapes.

polyesters containing a bisphenol and an aromatic dicarboxylic acid. In the case of ISARYL® 15 it is a combination of 1,1-bis(4-hydroxyphenyl)-1-phenylethane and a mixture of iso- and terephthalic acid and ISARYL® 25 is a combination of 9,9-bis(4-hydroxyphenyl)-fluorene plus phthalic acid with the following structures:

ISARYL® 15



ISARYL® 25



## 2. ISARYL® polyarylates

### 2.1 What are polyarylates?

Why are they interesting? What do they compare with? Polyarylates are fully aromatic

When these materials were first developed the main interest was in the electrical insulation properties at elevated temperatures together with an inherent flame resistance, i. e. without the use of additives, without halogenes, without phosphor and so on. After having developed the interfacial polycondensation synthesis to a degree of perfection to tailor-make molecular weights from very low to very high, what means from 2,000 to over 1 million we found by further testing:

- (i) very low moisture uptake, thus excellent dimensional stability and very low outgasing under high vacuum
- (ii) very good mechanicals under cryogenic conditions - tests down to 4.2 K
- (iii) very good resistance against nuclear radiation (gamma)
- (iv) constant electrical properties over a wide range of temperatures, frequencies and humidity
- (v) especially ISARYL® 15 (unfilled) shows interesting tribological characteristics like high friction and low wear
- (vi) good processability: film casting out of solution, injection molding, sintering

There is no identical material to those polyarylates. Pricewise the ISARYL® polyarylates range between PEEK and polyimides.

Performancewise ISARYL® is in some aspects, like temperature resistance, similar to polyimides in others, like water absorption, solvent resistance, very different to polyimides.

## 2.2 The polymer synthesis

The interfacial polycondensation [1,2,3] can be either a batch polymerization [4,5] or a continuous polymerization [6]. The batch polycondensation allows a lot of freedom what concerns the ratio of the iso- to terephthalic acid and will probably be ideal for quantities up to 100 tons a year. The continuous polymerization

will be used for production quantities exceeding 100 tons. ISONOVA has built a pilot plant at Wiener Neudorf, Austria with a capacity of 5 tons, including a solvent recovery facility. The scale-up study for a much larger production facility has been completed and will be realized.

ISONOVA produces also the bisphenolic monomers following their patents and know-how [7].

## 2.3 The conversion of the polymer powder into products

### 2.3.1 Films [8]

At LONZA-Folien at Weil/Rhein, Germany clear and transparent and colourless films are cast out of solution. These foils come in standard thicknesses of 25 µm, 50 µm, and 100 µm. Trials have been made to produce extremely thin films down to 2 µm and very thick films up to 700 µm. The standard width is 1 m.

The casting technique [8] guarantees a minimum surface roughness compared to extruded films.

Those films are sold by ISONOVA under ISARYL® 15F and ISARYL® 25F and by their licensee LONZA-Folien GmbH under ARYPHAN 15 and 25.

### 2.3.2 Injection molded parts

For the moment being only ISARYL® 15 can be injection molded and/or extruded. The colour of those parts is amber and show a very good elasticity and elongation at break of up to 10 %. Trials are now made to modify ISARYL® 25 and to make polymer blends so that also this material can be injection molded.

### 2.3.3 Sintered net shapes [9]

Both ISARYL® 15 and 25 can be sintered to form blocks, rods and slabs. Out of these net shapes parts can be easily machined. The net shapes come in the following standard sizes: 240 x 410 mm and 115 x 165 mm with thicknesses between 5 and 60 mm. The sintering technique has proven to be ideal for prototyping.

## 2.4 Properties

### 2.4.1 Thermal properties

PROPERTIES ISARYL® 15	unit	film	IM/sinter
Glass Transition Temperature	[°C]	250	243
Heat Deflection Temperature (Method A, 1.85 N/mm <sup>2</sup> )	[°C]	-	237
Thermal Conductivity (30 °C)	[W/mK]	0.19	0.19
5 % Weight Loss (10°C/min, air)	[°C]	452	457

PROPERTIES ISARYL® 25	unit	film	sinter
Glass Transition Temperature	[°C]	325	325
Heat Deflection Temperature (Method A, 1.85 N/mm <sup>2</sup> )	[°C]	-	307
Thermal Conductivity (30 °C)	[W/mK]	0.25	0.25
5 % Weight Loss (10°C/min, air)	[°C]	475	480

Table 1.

Typical values for films, injection molded and sintered parts [11,12,13]

Figure 1 shows the difference between a conventional bisphenol A type polyarylate [10] like Ardel® from Amoco or U-Polymer® from Unitika and ISARYL® polyarylates which are based on bisphenols containing a higher amount of aromatic rings than bisphenol A.

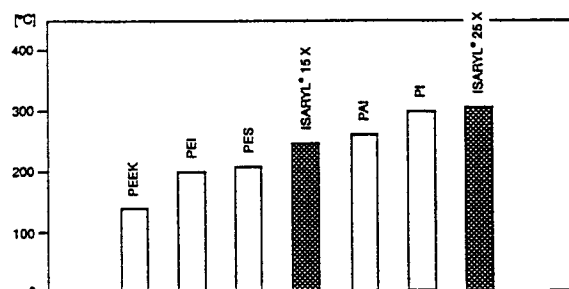
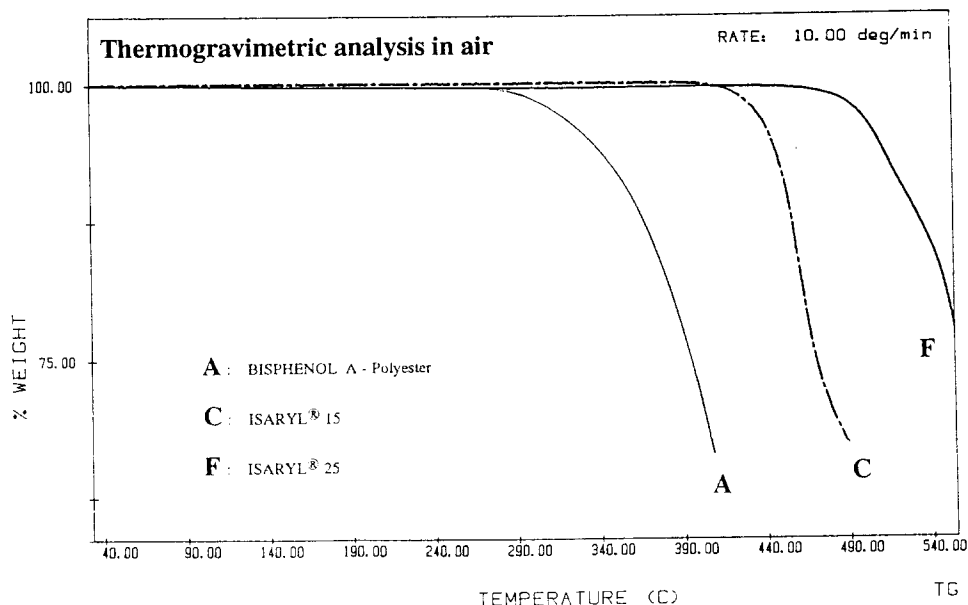


Fig. 2.: Comparison of Heat Deflection Temperature of High Performance Plastics

Fig. 1.: Thermogravimetric analysis



### 2.4.2 Mechanical Properties

Typical values for films, injection molded  
and sintered parts [11,12,13]

*at ambient temperature:*

ISARYL® 15		film	IM/sinter
Tensile Strength	[MPa]	76	77
Tensile Modulus	[MPa]	2,100	2,350
Elongation at Break	%	115	10.1
Flexural Strength	[MPa]	-	no break
Flexural Modulus	[MPa]	-	2,350

ISARYL® 25		film	sinter
Tensile Strength	[MPa]	100	72
Tensile Modulus	[MPa]	2,750	2,800
Elongation at Break	%	70	4.2
Flexural Strength	[MPa]	-	82
Flexural Modulus	[MPa]	-	2,800

Table 2

Fig. 3.: Tensile Strength at Elevated Temperature

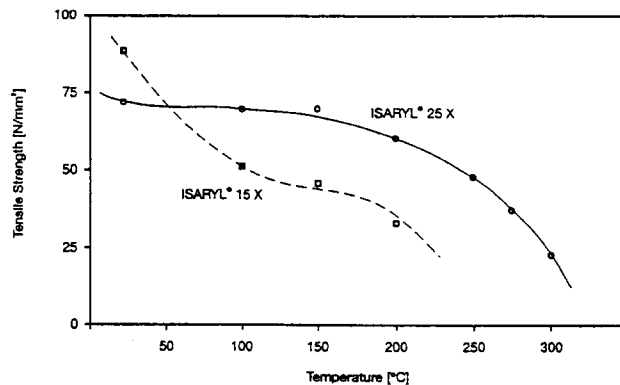


Fig. 5.: Flexural Strength at Elevated Temperature

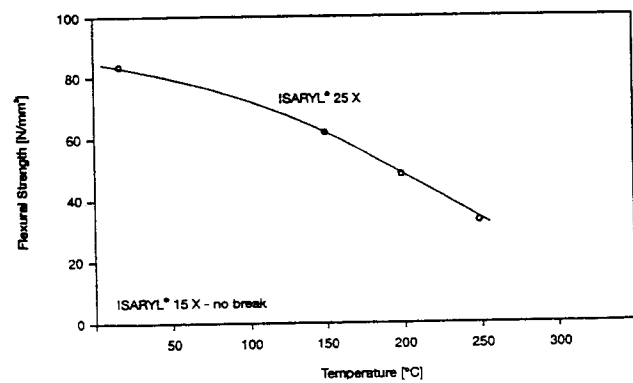


Fig. 4.: Ultimate Elongation at Elevated Temperature

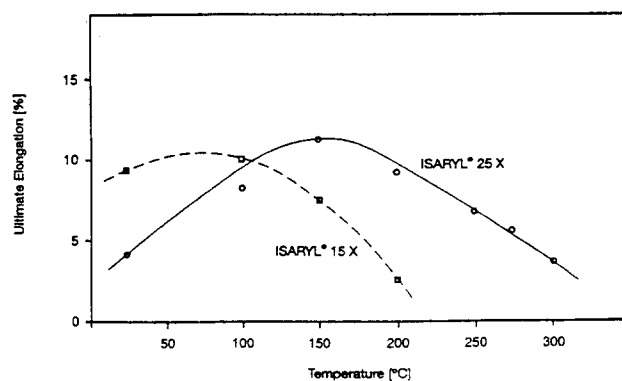


Fig. 6.: Compressive Strength versus Temperature

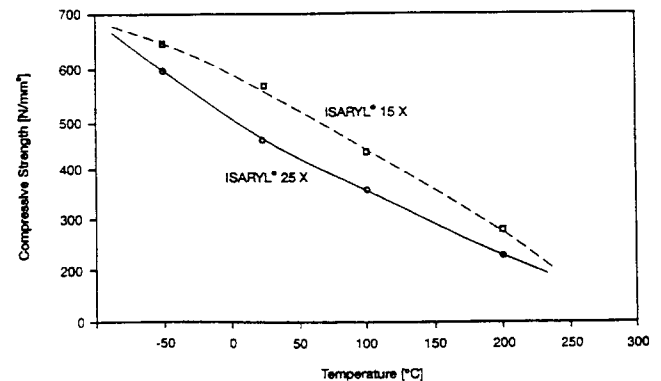


Table 3. **ISARYL®15X**  
at cryogenic temperatures

tempe- rature [K]	modulus of elasticity [GPa]	ultimate tensile strength [MPa]	elongation at break [%]
293	1.2	77	13.3
77	2.7	138	5.9
4.2	2.7	124	4.9

Table 4. **ISARYL®25X**  
at cryogenic temperatures

tempe- rature [K]	modulus of elasticity [GPa]	ultimate tensile strength [MPa]	elongation at break [%]
293	1.5	37	2.6
77	2.9	73	3.0
4.2	2.6	61	2.3

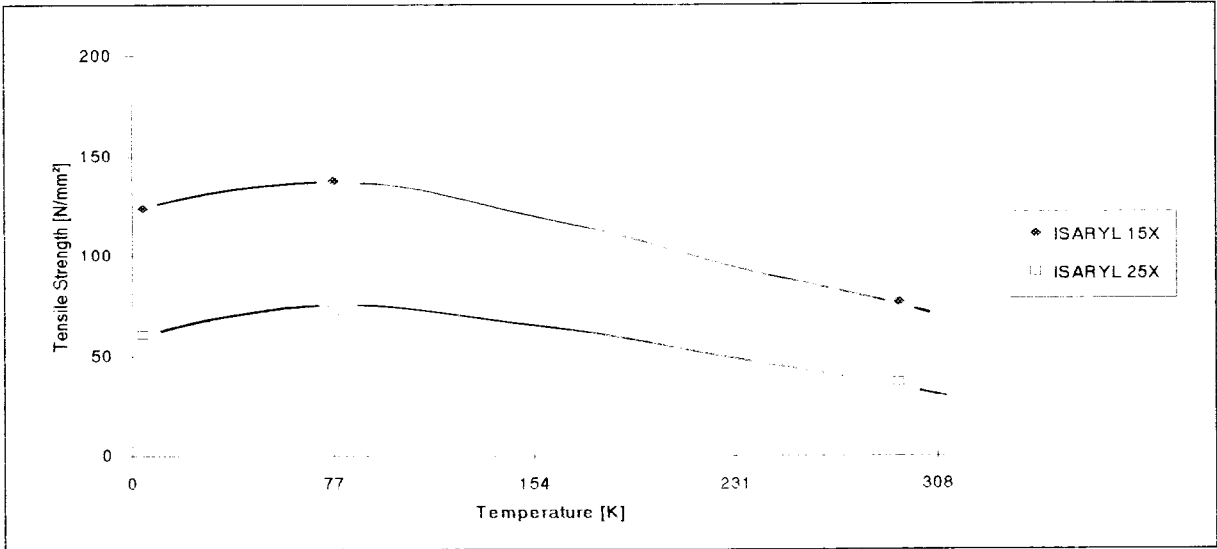


Figure 7: ultimate tensile strength at cryogenic temperatures

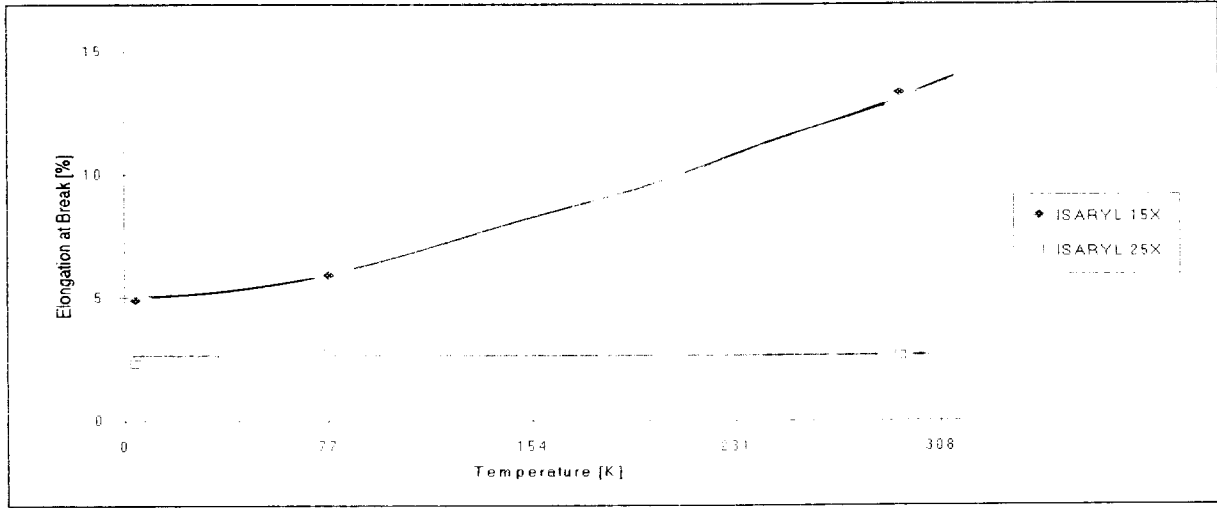


Figure 8: elongation at break at cryogenic temperatures

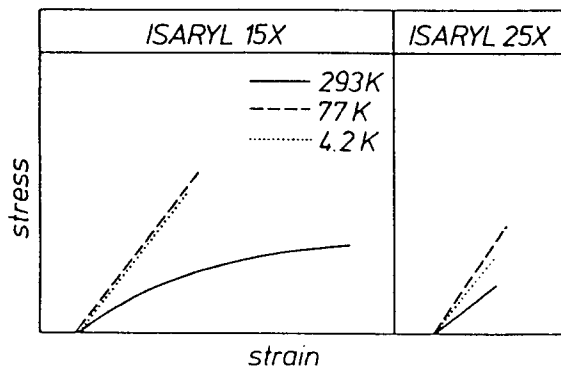


Figure 9: Qualitative illustration of stress strain diagrams of ISARYL<sup>®</sup>15X (left) and ISARYL<sup>®</sup>25X (right) at 4.2 K ( ···· ), 77 K ( - - - ) and at 293 K ( ——— )

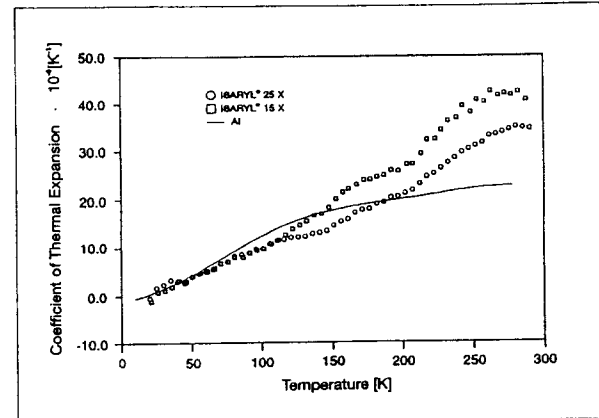


Figure 10: Comparison of coefficient of thermal expansion between ISARYL<sup>®</sup> 15X (□), ISARYL<sup>®</sup> 25X(o), and aluminium ( ——— )

Table 5: Coefficient of thermal expansion [ $K^{-1}$ ] of ISARYL<sup>®</sup>15X and ISARYL<sup>®</sup>25X

Temperature [K]	ISARYL <sup>®</sup> 15X	ISARYL <sup>®</sup> 25X
20 - 100	$0.1 - 13 \times 10^{-6}$	$0.6 - 10 \times 10^{-6}$
100 - 200	$13 - 27 \times 10^{-6}$	$10 - 21 \times 10^{-6}$
200 - 290	$27 - 37 \times 10^{-6}$	$21 - 35 \times 10^{-6}$

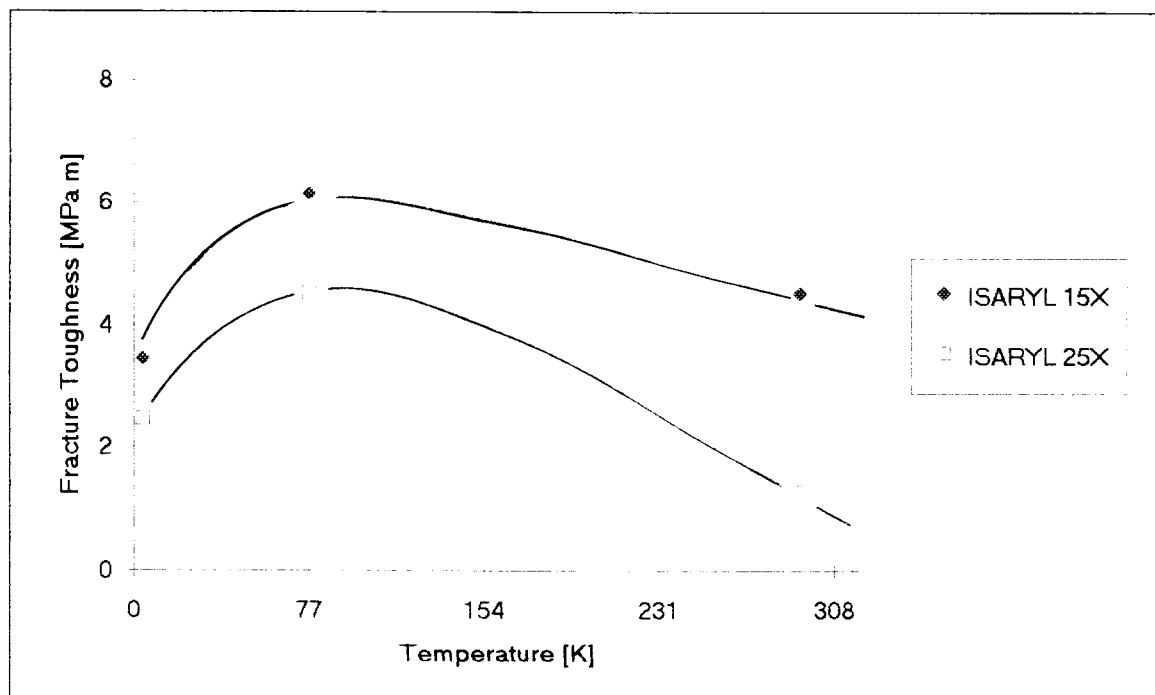


Figure 11: Fracture toughness of ISARYL<sup>®</sup> 15X and ISARYL<sup>®</sup> 25X at cryogenic temperatures

Fig. 12.: **Torsional Oscillation Test**  
**ISARYL® 15 X**

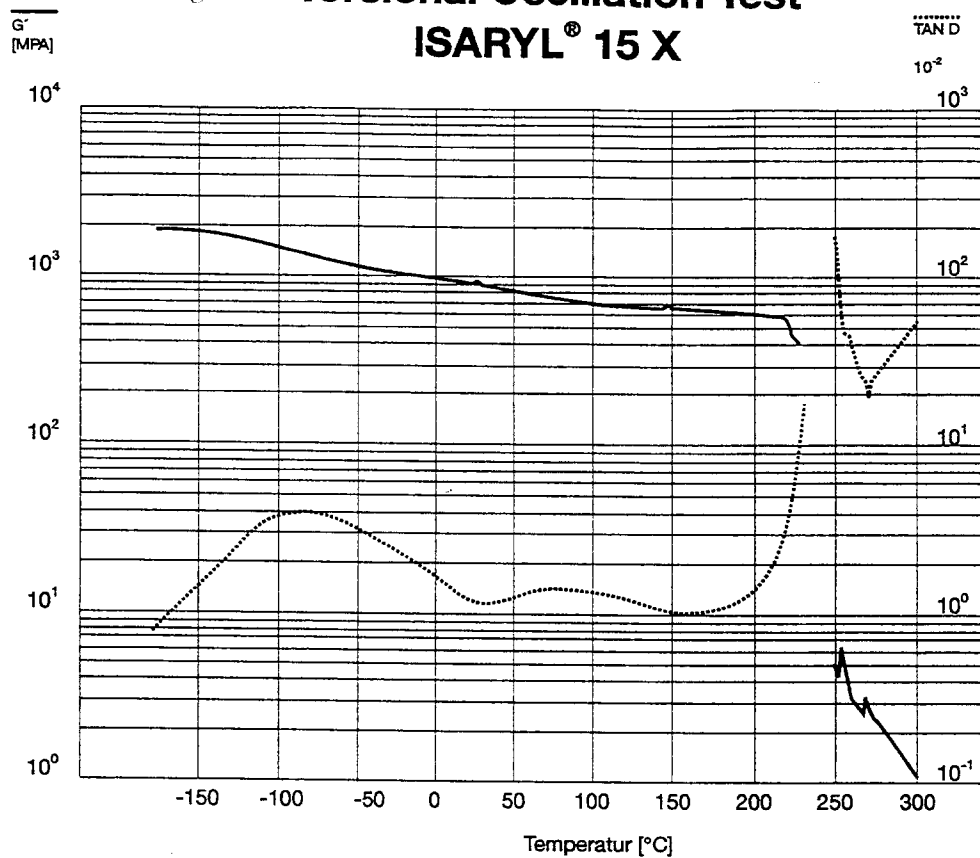
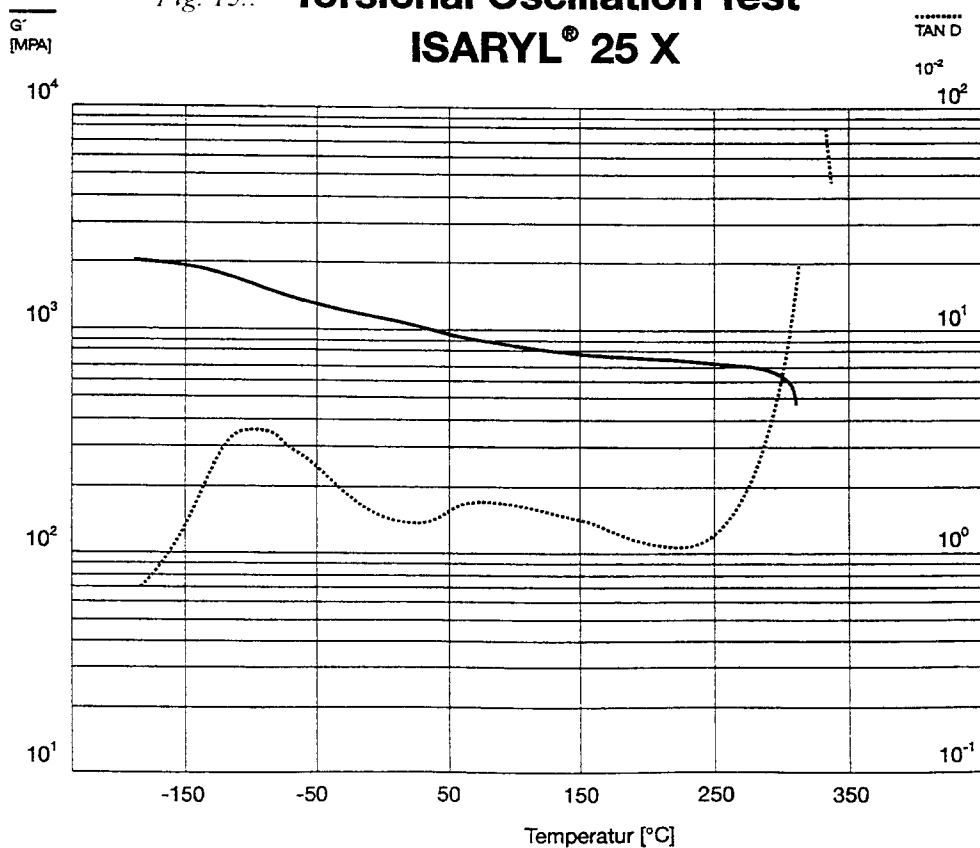


Fig. 13.: **Torsional Oscillation Test**  
**ISARYL® 25 X**



## 2.4.3 Electrical Properties

ISARYL® 15	unit	film		IM/sinter	
Dielectric Strength	[kV/mm]	(50 µm)	220	(3.02 mm)	15
Dielectric Constant		(1 kHz)	3.5	(1 MHz)	4.3
Dissipation Factor	[10 <sup>-3</sup> ]	(1 kHz)	7.0	(1 MHz)	16
Surface Resistance	[Ω]		5.0x10 <sup>12</sup>		1x10 <sup>14</sup>
Spec. Vol. Resistivity	[Ω.cm]		7.0x10 <sup>15</sup>		5x10 <sup>16</sup>

ISARYL® 25	unit	film		sinter	
Dielectric Strength	[kV/mm]	(50 µm)	320	(3.02 mm)	17
Dielectric Constant		(1 kHz)	3.2	(1 MHz)	4.1
Dissipation Factor	[10 <sup>-3</sup> ]	(1 kHz)	3.1	(1 MHz)	16
Surface Resistance	[Ω]		5.5x10 <sup>16</sup>		3x10 <sup>13</sup>
Spec. Vol. Resistivity	[Ω.cm]		2.5x10 <sup>17</sup>		5x10 <sup>16</sup>

Table 6

## 2.4.4 Physical Properties

Appearance: films are clear, transparent and colourless;

sintered and injection molded parts are of amber colour.

	ISARYL® 15	ISARYL® 25
Density [g/cm <sup>3</sup> ]	1.21	1.22
Refractive Index	1.65	1.66
Water Absorpt. (23°C/24h Imm.)	0.2%	0.25%

Table 7

## 2.4.5 Combustion properties

	ISARYL® 15X	ISARYL® 25X
LOI [%]	33.5	40.0
Heat Release [kW/m <sup>2</sup> ]		
Peak	93	29
Total HR [kW.min/m <sup>2</sup> ]	2	0
Smoke Density (4.3mm, 4min)	7	1
Vertical Test (4mm)		
Burn Length [mm]	49	42
Burn Time [s]	5	3
UL94 (3.18 mm)	V-0	V-0

Table 8

## 2.4.6 Radiation Resistance [15]

The samples were irradiated at the research reactor at Seibersdorf, Austria at level 1 in the nuclear reactor, i. e. at a distance of 35 cm from the nuclear core. At that level the radiation consists of 98 % hard (gamma) radiation and 2 % neutrons. The energy is in the range of 0.1 MeV to 1 MeV. The samples were exposed to a dose rate of 0.2 MGy/h.

The following measurements were made at Seibersdorf.

## ROCKWELL - HARDNESS M

Iridation dose [Gy]	ISARYL® 15X	ISARYL® 25X
0	98	118
1x10 <sup>7</sup>	86	114
2x10 <sup>7</sup>	86	111
6x10 <sup>7</sup>	92	108
x10 <sup>8</sup>	99	108

Table 9



## ISARYL® 15X

Irradiation dose [Gy]	Flexural strength [MPa]	Elongation at break [%]	Flexural modulus [MPa]
0	no break	no break	2100
$1 \times 10^7$	108	5.8	2900
$2 \times 10^7$	83	3.2	2900
$6 \times 10^7$	46	1.6	3300
$10^8$	37	0.8	3500

## ISARYL® 25X

Irradiation dose [Gy]	Flexural strength [MPa]	Elongation at break [%]	Flexural modulus [MPa]
0	89	4.0	2550
$1 \times 10^7$	88	3.0	3100
$2 \times 10^7$	60	1.9	3350
$6 \times 10^7$	31	0.9	3600
$10^8$	29	0.7	3900

Table 10

At CERN the following measurements were evaluated: ( 100 micron film ISARYL® 25F)

Dose (MGy)	Dose rate (Gy/h)	Tensile properties		Hardness Shore D H (Degree)
		Strength R (MPa)	Elongation E (%)	
0.000	—	$79.7 \pm 8.9$	$12.1 \pm 3.3$	$44.0 \pm 0.0$
0.200	4800.0	$83.6 \pm 4.5$	$8.3 \pm 3.8$	$44.0 \pm 0.0$
0.500	4800.0	$87.7 \pm 4.2$	$7.9 \pm 2.5$	$51.0 \pm 0.0$
1.000	4800.0	$86.1 \pm 3.5$	$7.5 \pm 2.2$	$52.0 \pm 0.0$
5.000	$2.4 \times 10^4$	$87.5 \pm 2.6$	$6.8 \pm 1.4$	$46.0 \pm 0.0$

RADIATION INDEX (  $2.4 \times 10^4$  Gy/h ) > 6.7

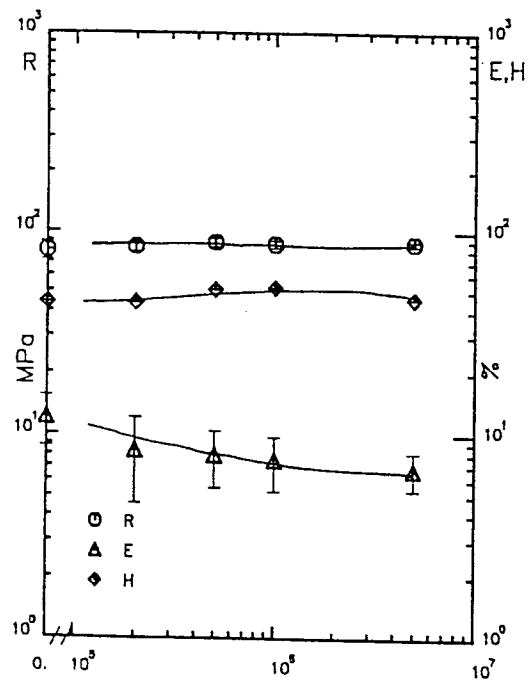


Fig. 14. ABSORBED DOSE (Gy)

### 3. Applications

#### 3.1 Examples

Applications  
for ISARYL® films and/or parts

Industry	typical application	requirements
CERN	detectors: wire guides superconductors: end spacers electrical insulation, films	cryo, radiation resistance mechanical, electrical properties
electrical and electronic industry	insulators, plug connectors, reflectors, cable insulation, flexible circuit, capacitors, LCD	high temperature resistance, good electrical insulation, low moisture uptake, good mechanicals, low outgasing, low electric dissipation, high transparency, low retardation, inherent flame resistance, no toxic combustion gases
adhesive tapes	pressure sensitive, electrical tapes	heat resistance and electrical insulation
chemical process	membranes, diaphragm	selective permeability, low temperature resistance
mechanical engineering	plasma and spot welding	heat shock resistance
space	solar sails	cryo, radiation resistance, thin films

### 3.2 At CERN

Here injection molded and sintered parts were tested, e.g. in detectors as wire guides and as prototype-endspacers in super conductors. Furthermore films have been sampled for insulation of cables and coils. Here ISARYL® can be used mainly because of its good mechanical properties from elevated temperatures to cryogenic temperatures because of very low outgasing at high vacuum and - last but not least - very good resistance to nuclear radiation.

### 4. Standards

	ISO/ IEC	DIN	ASTM
Tensile Test	527	53455	
Bending Test	178	53452	
Modulus of Elasticity	527	53457	
Rockwell M	2039-2		
Shore D	868	53505	D2240
Coeff. of Therm. Exp.		TMA	
Glass Transition Temp.		DSC	D3418-82 <sup>(1)</sup>
Dielectric Strength	243	53481	
Surface Resistance	93	53482	
Spec. Vol. Resistivity	93	53482	
Dielectric Constant	250	53483	
Dissipation Factor	250	53483	
Density	R1183	53479	
Water Absorption	62	53495	
LOI			D2863
Heat Release			E662 <sup>(2)</sup>
Smoke Density			E906 <sup>(3)</sup>
Burning Behaviour <sup>(3)</sup>			
Heat Deflect. Temp.		53461 <sup>(1)</sup>	
5 % Weight Loss		TGA	

<sup>(1)</sup> according to

<sup>(2)</sup> also FAR 25853 (a-1) resp. (a)

<sup>(3)</sup> also Airbus ATS 1000.001

### 5. Acknowledgement

The author wishes to express his sincere thanks to the following persons for their contributions and commitment: Mr. David, Mr. Hauviller, Mr. Schönbacher, Mr. Szeless, Mr. Tavlet, and many others within CERN as well as to my co-workers especially Mr. Oberlehner.

### 6. References

- [1] P.W. Morgan, Condensation Polymers: By Interfacial and Solution Methods, Interscience, New York (1965)
- [2] F. Millich, Ch. E. Carraher, Jr., Interfacial Synthesis, Vol. 1, Marcel Dekker Inc., New York - Basel (1977)
- [3] F. Millich, Ch. E. Carraher, Jr., Interfacial Synthesis, Vol. 2, Marcel Dekker Inc., New York - Basel (1977)
- [4] AT 392475
- [5] US 4.967,306
- [6] AT 386 217
- [7] AT 393 502
- [8] EP 64 972
- [9] AT 395 431
- [10] F. Zahradnik, Hochtemperatur-Thermoplaste, VDI-Verlag, Düsseldorf (1993)
- [11] ISARYL® High Performance Plastics, folder by ISONOVA (1993)
- [12] ISARYL® High Temperature Polyarylates, New Sintered Polyarylates, brochure by ISONOVA (1992)
- [13] K. Humer, E.K. Tschegg and H.W. Weber, Tensile, fracture and thermal properties of polyarylates at room and cryogenic temp., Cryogenics Vol. 33, No. 7 (1993)
- [14] ISARYL® at cryogenic temperatures, brochure by ISONOVA (1994)
- [15] ISARYL® under nuclear radiation, brochure by ISONOVA (1994)

# Advanced Composite Stable Structures, Appropriate Materials for High Precision Detectors

Susan Robitaille, Gary Patz, Sean Johnson  
YLA Inc.  
Benicia, Ca., USA

## Abstract

The use of cyanate ester resin in concert with high modulus pitch fibers has gained broader acceptance in satellite and space structures in the last five years. Their use as a replacement for metal structural materials such as aluminum, beryllium and titanium in stable structures and for thermal management in space has begun to produce a design data base which may result in lowering the risk associated with these new materials and lead to their acceptance into other applications. This paper will present current material data which can be used to support the use of cyanate ester/pitch fiber material in stable structure designs for high precision detectors. The properties of Coefficient of Thermal Conductivity, Coefficient of Moisture Expansion, radiation resistance and thermal conductivity of commercially available cyanate ester composite materials will be discussed along with a summary of the mechanical properties associated with these materials.

## Introduction

The development of ultra high modulus graphite fibers which exhibit a more negative coefficient of thermal expansion (CTE) than other carbon fibers has allowed the designer to produce near zero CTE structures. These same fibers also have excellent thermal conductivity and are being evaluated for thermal management in environments where thermal cycles can approach -250 to + 280 °F.

The teaming of cyanate ester formulated resins with these high modulus fibers further improves the design flexibility. The polymers' low moisture absorption, CME, low degree of microcracking with thermal cycles, radiation resistance and ease of processing make it more attractive than standard epoxy resins which have been base lined for many stable structures.

## Cyanate Ester Resins Properties

The first patents on cyanate esters were filed in Germany in the mid 1960's. Initially developed for applications in the electronic industry, they provided improved electrical properties and

moisture absorption compared to other available materials. In the late 1960's, cyanate esters were investigated for the first time as modifiers for epoxy resins in fiber reinforced composites for structural applications. Synthesis of many cyanate monomers, both di- and monofunctional, was sponsored by US Air Force at Wright Patterson Air Force Base. This work was later intensified by Celanese. Celanese concentrated their development efforts on the Bisphenol A based polymers.

It was not until the early 1980's that the first commercially available cyanate blend resin (BT) or bismaleimide-triazine resin was introduced by Mitsubishi Chemicals. This was a bismaleimide/cyanate ester blend and was targeted to the high performance circuit board industry. Since that time, several other formulated cyanate blend resins have become available for use in structural composites usually a blend of either Bismaleimide (BMI) or epoxy. In the mid 1980's, Dow USA introduced its cyanate ester chemistry based on a cyclopentadiene backbone and later offered a core shell toughened version of the same chemistry. It

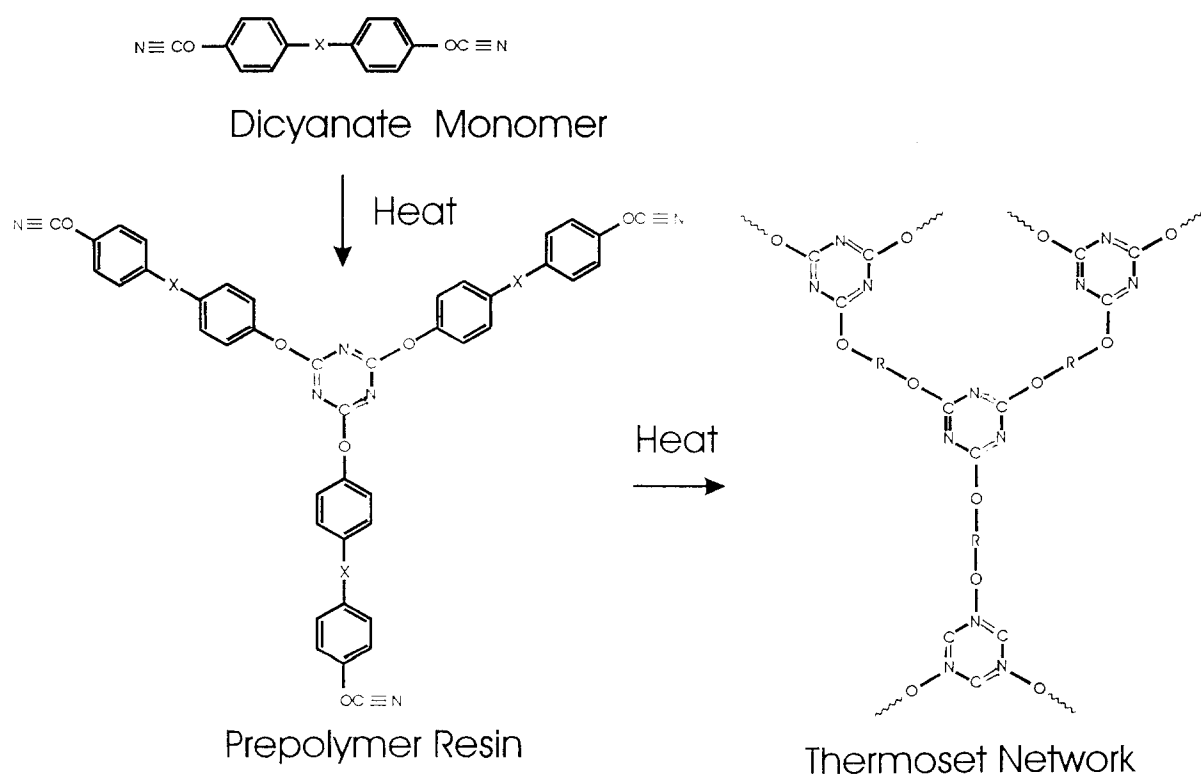


**Figure 1. Representative Cure Chemistry of Dicyanates**

was the first 100% cyanate ester resin system qualified for use in space by Space Systems Loral and is the base polymer for all of the cyanate ester resins discussed in this paper.

The advantages of polycyanate resins are directly related to the chemical structure of the polymer. Their low moisture absorption, CME, dielectrics and outgassing characteristics result from their non-polar structure and the lack of hydroxyl groups that favor hydrogen bonding [1].

Table 1 shows a comparison of moisture diffusivity and its effect on the glass transition temperature, coefficient of moisture expansion and modulus between a polycyanate resin system,

RS-3 and a space qualified epoxy systems, Fiberite 934. The effect of moisture absorption on the modulus of cyanate esters is minimal. At saturation, the polymer weight gain is approximately 1.4%, compared to the epoxy absorption that is in the 7% absorption range. Excellent retention of modulus is seen even under extreme conditions, due to the hydrophobicity of the polymer. The high diffusivity of cyanate esters also allow the composite structure to reach moisture equilibrium quickly in a given environment.

The coefficient of moisture expansion of a composite structure is dependent upon the total amount of moisture absorbed, resin expansion

RESIN	Moisture Diffusivity $\text{K}^{\text{H}}\text{m}^2/\text{s}$	Max. Moisture Cont. (%)	Coefficient of Moisture Expansion	Tg (°C) Before → After absorption	Young's Modulus (GPa) Before → After absorption
Fiberite 934	2.69	7.4	0.267	225 → 134/212	3.62 → 3.21
Fiberite PST	2.97	7.1	0.267	229 → 139/217	4.10 → 3.47
RS-3	11.1	0.9	0.173	207 → 213	2.63 → 3.58
RS-3 PST	13.4	1.5	0.156	245 → 243	3.10 → 3.20

**Table 1 : Physical properties**

due to this absorption and the in-plane modulus of the composite. Table 2 shows the data obtained from several different resin systems and fiber types using a constant humidity chamber held at 24°C.

The initial length of each specimen was measured against an invar standard. Weight gain was measured daily on pre-dried specimens and recorded. CME was calculated by dividing the strain at saturation by the percent moisture pickup at saturation. The results have not been normalized to a constant fiber volume [2].

**Table 2 : CME (ppm/%RH)**

Vendor	YLA	Fiberite	Amoco	Amoco
Fiber	XN50	FT500	P75s	P75s
Matrix	RS-3	954-3	ERL 1999	ERL 1962
35% RH	160	150	162.5	162
55% RH	171.4	176.5	123.1	162
75% RH	227.8	227.77	158.8	162
FVF	57.8	58.2	59.0	n/a

## Cure and Processing

Cyanate esters cure by trimerization using a transition metal as a coordination catalyst in low concentrations. With the exception of the phenol triazine resins from Allied Signal and Ciba Geigy, they produce an intermediate crosslink density polymer and give excellent glass transition temperatures in the 220°C range. The ether linkage between triazine ring allows some degree of flexibility in the polymer structure [1]. This may contribute to the low degree of microcracking with thermal cycling seen in composite structures using the more highly negative CTE fibers. Their increase in free volume during cure gives the polymer a low percent shrinkage during cure, reducing cure induced stresses and resulting in structures with good dimensional stability.

The standard cure for cyanate esters is 180°C with an optional postcure. Autoclave processing is recommended, however the cure produces no by-products and the viscosities during cure are low, allowing excellent consolidation and high fiber volumes.

## Radiation Effects

While the effect of radiation exposure on the polymer has not been fully investigated, some comparison data has been generated between epoxy and polycyanate resin systems. The radiation exposure level and its effect on the storage modulus of the polymers is shown in Figure 2. (1 MGy or Mega-gray = 108 rad). Rather than a decrease in the modulus of the polymer as seen in typical epoxy systems, cyanate esters show an initial increase in modulus after exposure. Work currently being performed will evaluate the effect of thermal cycling after radiation exposure on the mechanical properties of the composite systems and should give a better understanding of the influence of radiation exposure.

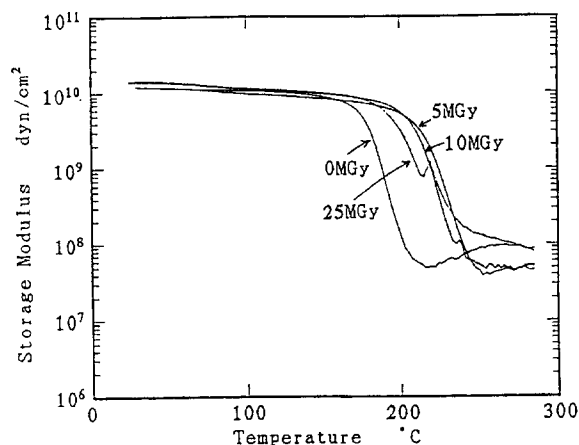


**Figure 2. Dynamic Mechanical Analysis of Irradiated RS-3**

## Composite Structures and Properties

For stable structures, the advantages of high modulus fibers, pan or pitch, have allowed material designers greater versatility. Structures which historically have been made using metals are now produced using anisotropic materials. The resulting weight savings, high stiffness properties, good thermal conductivity and low CTE have driven the use of these composite materials for stable structures. The ability to produce light weight graphite honeycomb core (0.8 lb./ft³) with high modulus fibers and very thin unidirectional tape skins, less than 0.025 mm per ply, has further added to the materials versatility.

In stable structures that are exposed to wide temperature ranges or gradients, the CTE of the struc-

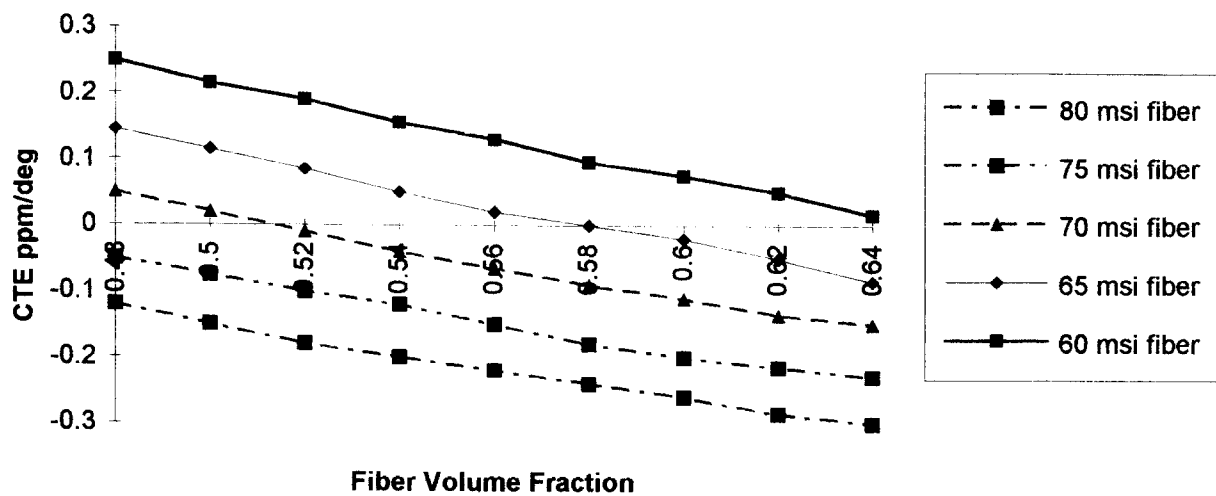


Figure 3. CTE vs. Fiber Volume Fraction

ture becomes a very important material property to control. Using prepregs with negative fiber and positive resin CTEs, the CTE of the structure can be targeted through the lay-up configuration and fiber volume control. Figure 3 shows the trends associated with changes in fiber volume for various fiber moduli on the CTE of quasi-isotropic laminates made with cyanate esters.

Typically, fiber volumes in the 55 to 65% range are easily obtainable and report excellent mechanical properties.

Figure 3 shows the CTE in ppm/°F, versus fiber volume for a variety of fibers with different moduli [3].

Table 3 is comparison data generated on quasi-isotropic composites, all using 75msi fibers and cyanate ester resins. This data was predicted using supplied data from vendors, micro-

mechanics techniques, actual test data and lamination theory. The data is based on laminates containing a 60 % fiber volume [3].

## Thermal Conductivity

The axial or longitudinal thermal conductivity found in the ultra high modulus fibers increases with fiber modulus. Thermal conductivity can further be enhanced by orientating the crystalline or platelet structure produced during the graphitization process. Longitudinal orientation improves the thermal conductivity of the fiber but decreases the tensile strength and compressive strength of the fiber. New fibers are quickly being developed to improve the balance of strength and conductivity. The use of metal matrix composites are being used to improve the conductivity in

Table 3 : Normalized quasi-isotropic CTE (ppm/°F)

Panel	YLA XN50 RS3	YLA P75s RS3	Fiberite FT 500 954-3	Fiberite P75s 954-3	Amoco P75s ERL 1999
0.040	-0.085 / -0.11	-0.142 / -0.13	0.15 / 0.075	-0.094 / -0.13	-0.329 / -0.30
0.060	-0.086 / -0.053	na	0.164 / 0.071	na	-0.231 / -0.256
0.080	-0.09 / -0.075	-0.127 / -0.12	0.170 / 0.059	-0.131 / -0.169	-0.192 / -0.299

applications where through thickness thermal conductivity is important.

Comparison data of thermal and mechanical properties of several pitch fibers are found in Table 4. The theoretical thermal conductivity of pitch fiber is 2400 W/m.K with the K1100 (P130X) fiber from Amoco Performance Products, the best in this area. However, for designs which are compressive strength driven, the use of fibers with a better balance of properties may be necessary. It

should also be noted that the thermal conductivity of fibers is not linear. Therefore identification of the service temperature of the structure is important when designing structures with pitch fibers.

Mechanical properties of several of the CE/pitch fiber materials which are qualified for space structures are shown in Table 5. All data has been normalized to a 60% fiber volume for comparison, and all systems are cured at 177°C.

**Table 4 : Fiber Comparison Properties**

	P-75	XN-50A	P100	XN-80A	XN-70	P120	P130
Thermal conductivity (W/m. K)	185	180	520	425	320	640	1120
CTE (ppm/K)	-1.46	-1.40	-1.48	-1.46	-1.6	-1.5	-1.55
Tensile modulus (GPa)	517	517	758	785	720	827	900
Tensile strength (MPa)	1900	3862	2200	3630	3630	2400	3100
Density	2.16	2.14	2.16	2.17	2.16	2.19	2.2

**Table 5 : Typical Mechanical Properties**

	P-75	XN-50A	K139	K135	XN-70A	XN-80A
ILLS	56	76	81	76	81	72
0° Tensile strength (MPa)	1083	1724	1490	2000	1669	1793
0° Tensile modulus (GPa)	297	296	410	379	429	452
0° Compression strength (MPa)	421	406	432	406	333	330
0° Compression modulus (GPa)	241	275	400	275	423	423

## Summary

Many of the requirements for stable structures in space applications are also consistent with those for high precision detectors. The data base and knowledge gained by the successful deployment of these space structures may reduce the risk involved in using these or similar materials for high precision detectors. While more testing is required to determine the limits of these materials, they do offer a low CTE, CME, good radiation resistance, thermal conductivity and excellent processing and handling characteristics.

## Acknowledgments

The Authors would like to thank the support of Geoff Tappern from Rutherford Appleton Laboratories, Nippon Oil Company, Amoco Performance Products and Composite Optics.

## References

- [1]. Shimp, D.A. et al., "Cyanate Ester Resin Chemistry, Properties and Applications", Product Brochure, Hitek Polymer Brochure, Hitek Polymer Inc., 1989.

- [2]. T. Matsumoto, M. Mohri, A Oshima. "Moisture Absorbing Properties of Thermosetting Matrix Resins for Composites," Proceedings of the Second Japan International SAMPE Symposium and Exhibition, Dec. 1991.
- [3]. Nippon Oil Company, Granoc Brochure, 1993.
- [4]. Sidwell, D.R. "New Generation Space Qualified Materials. Proceedings of the Second Japan SAMPE International Symposium, 1991.



# The dimensional stability of composite laminates: sensitivity to gradients in fibre content and misalignment

Patrick Kim, Richard Phillips, Staffan Toll, Jan-Anders E. Månson  
Laboratoire de Technologie des Composites et Polymères  
Ecole Polytechnique Fédérale de Lausanne  
CH-1015 Lausanne, Switzerland

## Abstract

The anisotropic structure and heterogeneous nature of laminated structural composites may cause dimensional instabilities, as constituent properties mismatch and processing factors lead to the development of internal stresses. The effect of two types of microstructural imperfections is examined in this work: heterogeneities in the fibre content and deviations from the designed fibre orientations. Variations in the fibre content through the thickness of a laminate are simulated by introducing thin layers of neat polymer film between certain plies before consolidation. Lamina misalignments up to  $5^\circ$  are introduced in various plies to simulate the displacement of fibres that can occur during processing. The resulting warpage is measured by interferometry and related to the fibre distribution observed by microscopy. The warpage upon cooldown of the unsymmetrical laminates created by these two methods demonstrates the sensitivity of the part geometry to fibre arrangement, and thus the importance of a close control of layup, flow and fibre content in producing high-precision composite parts. A numerical model verifies how precisely the amount of warpage in both cases can be predicted.

## 1. Introduction

An appreciable advantage of fibre-reinforced composite materials is the design flexibility they offer, especially when specific, anisotropic material properties are desired. The engineer has at his disposal a set of constituent materials, and can arrange them so as to obtain not only a customised structure, but also tailor-made, locally varying mechanical and thermal properties of the material in a part. The two principal design parameters for a given choice of constituents are the content of fibres and their orientation. It is usually assumed that the fibre content is homogenous throughout the region considered, and that the layup angles are ensured as designed. In reality, however, this is rarely the case, and deviations from the design values occur. Such discrepancies may lead to manufacturing-related warpage during curing of the matrix, when thermoset systems are used [1-3], or during cooldown for composites processed at temperatures above those expected during their service life [4-6]. Additional internal stresses and deformation may occur when the curing of the composite is not uniform [7] or as a result of rapid cooling [8-10].

Local variations in fibre content can occur for a number of reasons, the principal ones being uneven prepreg quality, fibre/matrix segregation due to flow or resin percolation in a pressure gradient during processing, and resin accumulation at the mould surface [11]. This problem can be as important in thermoplastic matrix composites as in thermosetting systems.

Deviations from the designed fibre orientation are often more difficult to control than fibre content gradients. They are mainly due to extensional flow or interlaminar shear during forming, and shortcomings in production quality control, such as accuracy of prepreg orientation during cutting and layup of the individual plies. These misalignments are usually small, of the order of a few degrees, and are difficult to detect, especially in sub-surface layers.

In most applications global dimensions are assured by geometrical constraints, and empirical tolerance specifications of fibre arrangement are sufficient. High-precision components, however, call for tolerance specifications based on a systematic sensitivity analysis. This is especially important for thin structures such as plates and shells, whose

dimensional stability is particularly sensitive to perturbations in the fibre content distribution and ply angles [12]. This work presents the results of a study examining the effects on dimensional stability of small perturbations from specified values in the two principal design parameters, the fibre content and the fibre orientation in a composite.

## 2. Materials and sample preparation

Samples were made of an 0.3mm thick unidirectional glass fibre-reinforced polyetherimide (PEI) prepreg (TenCate) with a fibre content of 52% by volume, and a 0.1mm thick PEI film (GE ULTEM 1000). The glass transition temperature of the amorphous PEI matrix material is 216°C. Thermal stress development occurs between the glass transition and room temperature, thus over a temperature range of 193°C. Thermal expansion curves for the neat PEI and the composite were obtained on a Perkin-Elmer TMA and are reproduced in Fig. 1, in the form of thermal strains, Eq. 1:

$$\varepsilon^T = \frac{(L - L_{RT})}{L_{RT}} \quad \text{Eq.1}$$

where  $L_{RT}$  is the sample length at room temperature.

In order to verify the predictive capability of composite warpage based just on knowledge of constituent properties and microstructure, the composite properties were also calculated using the Composite Cylinder Assemblage (CCA) model, details of which can be found in [13]. The average measured and calculated properties of the materials relevant to the present study are given in Table 1.

**Table 1. Properties of the neat PEI and PEI/glass fibre composite ( $\phi=52\%$ ) at 25°C.**

Property	neat PEI	PEI/glass composite	
		exper.	calc. (CCA)
$E_L$ [MPa]	3'000		37'860
$E_T$ [MPa]			9'850
$\nu_{LT}$	0.37		0.284
$\alpha_L$ [ $\times 10^{-6}/^\circ$ ]	51.9	7.9	7.5
$\alpha_T$ [ $\times 10^{-6}/^\circ$ ]		39.7	35.5
Tg [°C]	216	216	

The prepreg was cut into 70 x 70mm squares with different controlled angles of the fibres with respect to

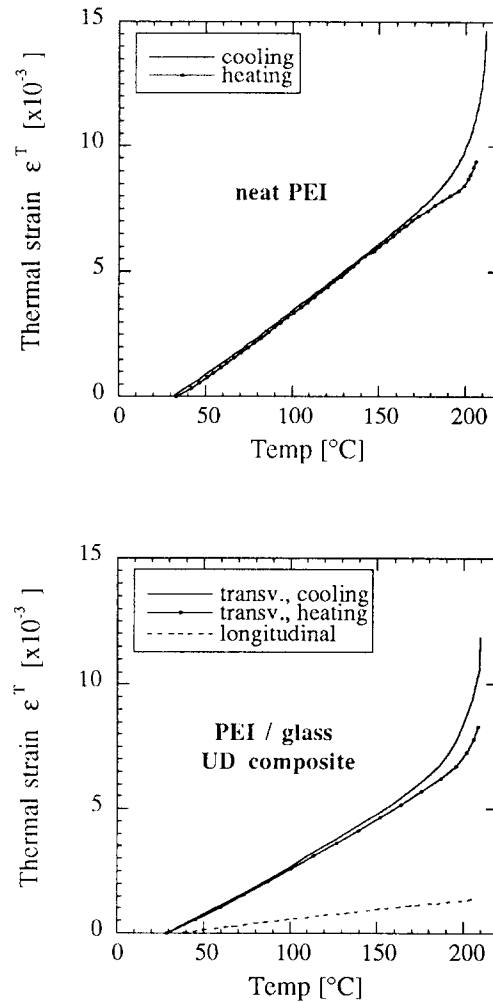


**Fig. 1. Thermal expansion curves for neat PEI (top) and the PEI/glass composite transverse and parallel to fibre direction (bottom)**

the principal axes of the sample. The precision of the cutting angle was estimated to about one fifth of a degree. The prepared materials were placed in a 70x70mm mould, heated to 310°C, and compression moulded on an instrumented press at 4MPa closing pressure. The consolidation was carried out with practically no long-range resin flow. The samples were cooled at an average rate of 20°C/min and demoulded at about 50°C. After demoulding and cooling to room temperature, the surface was prepared for interferometric shape measurements by spray application of a thin layer of chalk powder.

Two types of samples were produced: laminates with neat PEI leaves intercalated between composite layers, to produce fibre content heterogeneities through the thickness, and laminates with a deliberate fibre misalignment up to 5° in certain plies. In what follows, the sample stacking sequence is given as ( $O_a$ ,

$P_b, \dots$ ) or  $(0_4, A'_2)$ , where "0" designates a composite ply at  $0^\circ$ , "P" is a neat polymer layer, "A" gives the fibre angle of misaligned composite plies, and the subscripts indicate how many layers are in a group of same orientation or composition. The thicknesses of the moulded plates depended on the layup, with a thickness contribution of the consolidated composite of about 0.16mm per layer and, given the negligible resin flow, a thickness contribution of 0.1mm per layer of PEI film.

### 3. Experimental methods

The shape of the samples was measured by projection moiré interferometry using a Newport MP/MV-1000 analysis system. A regular grid of black and white lines at a defined pitch is projected onto the object, and the interference with a second grid placed in the viewing system is recorded by a CCD camera. By taking a first interference image of the object and tracking the change in the interference pattern with respect to a second image of a plane surface, one may determine the height of any point on the object in the viewing direction, also called the optical axis (Fig. 2). Image analysis software allows the evaluation of the interference phase diagrams along a selected line or over the entire surface of the object. A similar method was used in Ref. [14], with the difference that a single grating was placed just in front of the object.

In a first step, the deformation of the 70x70mm samples was measured in order to check the symmetry of the sample as an indicator of minimal flow during consolidation. The edges were then trimmed to reduce the sample size to 50x50mm, in order to remove the effects due to the small amount of resin flow at the edges of the mould, and the measurement were repeated. Transverse curvature effects in samples with fibre content gradients were reduced to a minimum by further trimming the plates into 6mm wide strips transverse to the fibre direction. In each case, shape

measurements were made in an initial position, after which the samples were rotated by  $90^\circ$  and a second measurement was made. The measurements were repeated if the two results differed excessively. The twist of sample with misaligned plies was calculated from the deformation of the diagonals of the 50x50mm samples. The values given in the following are the average of the different measurements.

Information on the fibre content distribution through the thickness of the section was obtained from micrographs of polished sections on one hand and by ashing of the sample to obtain total fibre contents on the other. In the first case, the fibre distribution and presence of resin-rich areas could be determined visually. In the second case, the fibre content distribution was reconstituted by comparing the overall fibre content of modified layups containing added layers of neat resin with laminates consisting exclusively of the composite. This information was then combined with knowledge of the layup sequence and the assumption that fibre content within a prepreg layer was constant. At least two sections were taken in different locations for each sample, in order to check the amount of variation in the fibre content distribution along the length of the sample. The fibre content values obtained by ashing are the average of three samples.

### 4. Theory and calculations

The moduli and the coefficients of thermal expansion (CTE) of the unidirectional lamina can be predicted fairly accurately using micromechanical models such as the Halpin-Tsai equations or the CCA, for example. Such models make assumptions on the microstructure of the material, and thus give slightly varying results.

Given the heterogeneous nature of the materials, it is important to define to which level of detail the microstructure must be characterised. Short range variations of the fibre arrangement over a distance of a few fibre diameters usually need not be considered. Variations over a longer range, of the order of a ply thickness, as were observed in the present study, must however be accounted for by a description of the local average of the fibre content. For a laminate, it is most useful to describe the variation of properties through the thickness on a ply-by-ply basis. The appropriate level of detail is that which allows an accurate calculation of all the required moments of effective property distribution of the section. For in-plane loading, only the global average of the effective properties need to be determined. In the case of the

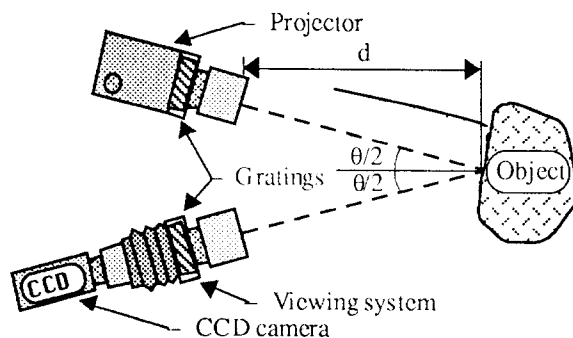


Fig. 2. Schematic of the moiré interferometry setup.

bending of a laminate, higher moments are needed, as can be seen in Eqs. 2a and 2b below.

Although material properties can be measured on standard samples, such results only give a global average of the properties. An analytical approach gives the lamina properties as a function of the fibre content and thus allows the assignment of properties locally, according to the observed fibre contents. The transverse modulus and CTE of the unidirectional PEI/glass lamina as calculated by the CCA are plotted in Figs. 3 and 4. A fluctuation of fibre content between 50 and 78% was observed in the composite plies. Within this range, the calculated modulus changes by 118%, while the CTE changes by 47%.

In the present case, it was assumed that the

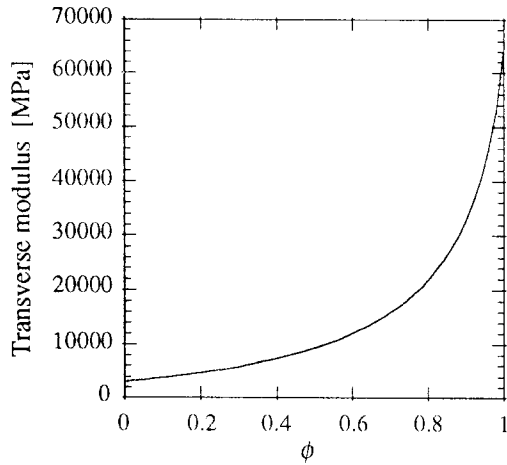


Fig. 3. Transverse modulus of the unidirectional PEI/glass lamina as a function of fibre content.

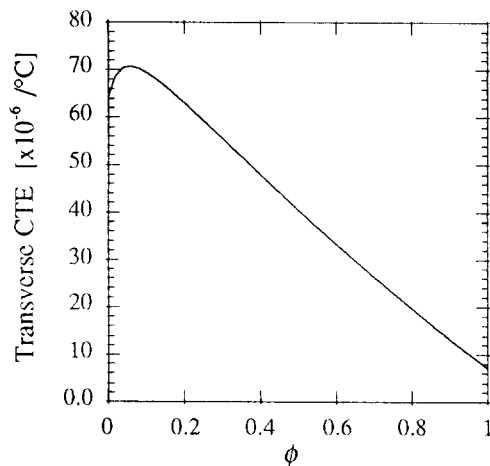


Fig. 4. Transverse CTE of the unidirectional PEI/glass lamina as a function of fibre content.

laminate consisted only of composite layers with a homogeneous fibre content distribution and neat resin layers. Graphs as in Figs. 3 and 4 are however extremely useful when the structure/property definition are to be done in more detail and values for local properties are needed.

Once the lamina properties are known, classical lamination theory (CLT) may be used for the analysis of the laminate, as long as deformations are kept small and elastic shape instabilities are avoided [11, 15]. The force and moment resultants for a laminate subjected to mechanical and thermal loads can be formulated as:

$$\{N\} = \int [\bar{Q}] (\{\epsilon\} + z\{\kappa\} - \Delta T\{\alpha\}) dz \quad \text{Eq.2a}$$

$$\{M\} = \int [\bar{Q}] (z\{\epsilon\} + z^2\{\kappa\} - z\Delta T\{\alpha\}) dz \quad \text{Eq.2b}$$

where  $[\bar{Q}]$  is the reduced plane stress stiffness matrix of the composite layer at  $z$ ,  $\{\epsilon\}$  and  $\{\kappa\}$  are the mid-plane strains and curvatures,  $\{\alpha\}$  the thermal expansion coefficients, and  $\Delta T$  is the temperature change to which the laminate is subjected. Details on classical lamination theory may be found in any text on composite materials mechanical analysis.

For an unconstrained laminate subjected to a temperature difference, the applied forces and moments  $\{N\}$  and  $\{M\}$  are zero. The integral for temperature effects is then the only source of stresses and warpage. Eqs. 2 can thus be solved for the mid-plane strains and curvatures due to a temperature differential. Various programs for the solution of laminate equations are readily available for this. Alternatively, one may resort to an FE solution, using a simple thermoelastic calculation module, as was also done for the present work. In this case, the layered structure of the laminate can be modeled using 4-node isoparametric elements under plane strain conditions.

The important issue at this point is to apply an accurate description of the actual microstructure in the solution of the laminate equations. The approaches that can be taken and the results of the calculations using Eqs. 2 are given in the next section along with experimental results.

## 5. Results

The inhomogeneity in fibre content lead to a warpage of the plate samples in two principal directions corresponding to the axes parallel and transverse to the fibres. Since the material with a lower fibre content has a higher coefficient of thermal

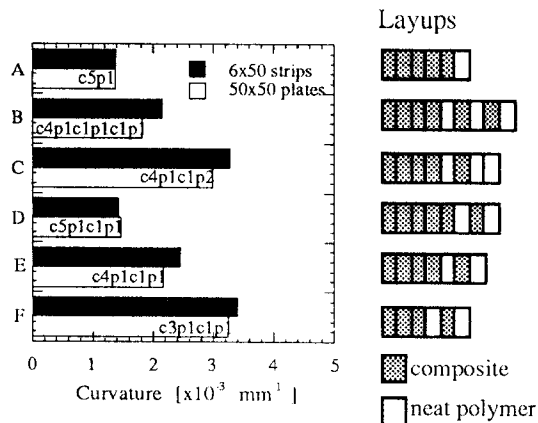


Fig. 5. Principal curvature of the 50x50mm plate and 6x50mm strip samples with inhomogeneous fibre content distributions.

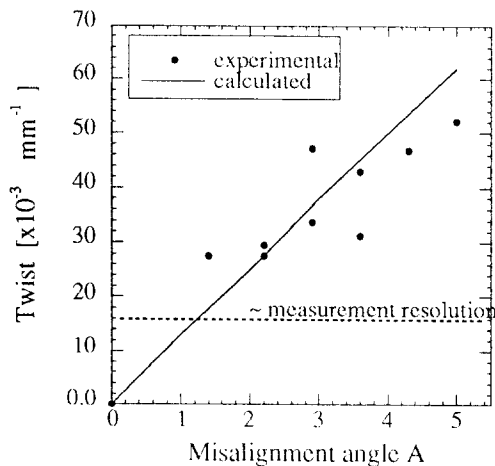


Fig. 6. Twist as a function of the misaligned ply angle for the 50x50mm plate samples with a  $(0^\circ/4, A^\circ/2)$  layup.

expansion, the plates developed, when cooled from the processing temperature, a concave curvature toward the side on which extra neat resin layers were added. The curvature in the direction transverse to the fibres was always larger and is the one considered here. The maximum principal curvature of the 50x50mm plates and the curvature of the strip samples transverse to the fibre direction are reported in Fig. 5. The largest measured curvature of  $3.29 \times 10^{-3} \text{ mm}^{-1}$  corresponds to a deflection of 1mm of a 50mm long strip. It is quite clear from a comparison of the three samples at the bottom of the diagram in Fig. 5 (D, E, and F) that samples with a higher overall flexural stiffness with respect to their thickness have the least warpage. Furthermore, as is expected, neat resin or resin-rich layers cause a greater warpage when they are close to

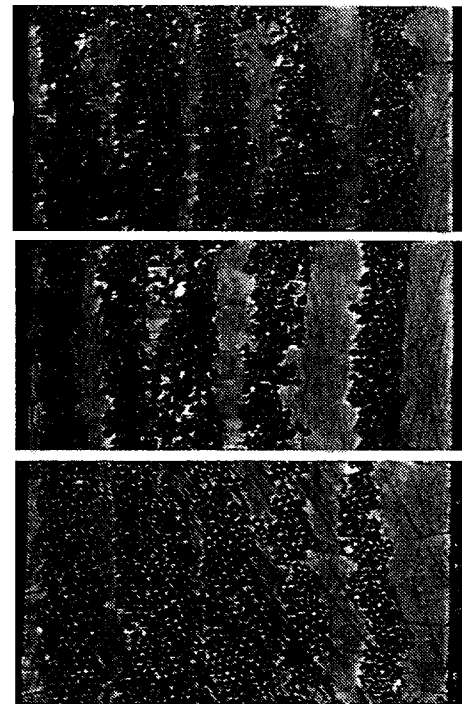


Fig. 7. Micrograph of a cross section of the laminate, Sample E, transverse to the fibre direction in three location.

the surface. In fact, that is often where they occur in practice.

The samples with misaligned plies twisted when cooled after moulding. The amount of twist is expressed in radians per unit length  $[\text{mm}^{-1}]$  for a plate of a given dimension. The amount of twist is plotted in Fig. 6 as a function of fibre angle  $A$  for a layup  $(0_4, A_2)$ . For the calculations of the twist, it was assumed that the fibre content was homogeneous through the thickness of the laminate. The amount of twist can be expressed as a linear function of the misalignment angle for the range of angles considered. The twist is evidently also a function of the number of misaligned plies, but this relationship was not examined here.

A micrograph of the cross section in different locations of a typical sample having an inhomogeneous fibre content distribution (Sample E, layup C4P1C1P1) is shown in Fig. 7. The layup sequence in the samples could generally be fairly easily recognised in the micrographs. Some slight variations in the position of the layers are seen to occur along the length of the sample. These are attributed mainly to thickness and fibre content variations in the prepreg. It can furthermore be seen that the different plies are separated by a thin layer of neat polymer that results from the resin-rich surface of the prepreps.



The thermal expansion curves (Fig. 1) are fairly linear over most of the range of temperatures considered. It has been found that using this linear portion of the curve extrapolated to the glass transition temperature suffices for the warpage calculation and does not lead to any significant error. This can be explained by the fact that the modulus drops off near the glass transition and the product  $E(t)\alpha(t)$  remains fairly constant during all of cooldown. Viscoelastic relaxation is negligible for this type of material and the fairly rapid applied cooling rates.

Calculation of the twist in samples with misaligned plies is less sensitive to modeling assumptions about the exact microstructure than calculation of the warpage in samples where a description of the fibre content distribution is necessary. It can be seen from the preceding results that such a description is difficult to make accurately, and that statistical methods may be needed to obtain a meaningful profile of the fibre content through the thickness of the laminate and over the area of the part.

## 6. Discussion

The results presented above illustrate the difficulty in producing composite parts of high geometric precision. They show that the dimensional stability of laminates is quite sensitive to even small fibre misalignment and inhomogeneities in fibre contents. Although the former effect can be predicted quite accurately by simple laminated plate theory, the latter effect is more difficult to analyse by simple models. One of the main difficulties is describing the actual spatial distribution of fibre content.

The microscopic analysis of the composite sections showed that the microstructure in a real composite can be quite different from the idealised case on which mechanical analysis and design are based. Already in the prepreg ply, the fibres are inhomogeneously dispersed throughout the matrix, and further fibre/matrix segregation can arise as a result of processing conditions.

Obviously, the position of the perturbations in fibre content is as important as the amount of variation in fibre content through the thickness of the laminate. A resin-rich layer at the surface of the laminate, as occurs at mould surfaces, is often desired for the aesthetic quality of a part, but is also most detrimental to the overall dimensional stability. The total warpage is a function of the overall flexural stiffness with respect to the laminate thickness, and of the amount, position, and spatial extent of perturbations. Thus, thicker parts are less subject to warpage, as variations in the material structure and

properties lead to internal stresses rather than flexural dimensional instabilities.

The magnitude of the perturbations introduced into the laminates in this study is of the order of that which may be found in industrially produced composite parts under reasonable quality control standards. For many flat or slightly curved parts with simple curvature, the warpage is accepted as it can be accommodated, e.g. by fixing the panel to a stiffer frame. For parts with important double curvature or thicker sections and high-precision components, however, the observed warpage may be unacceptable. Since the warpage can be predicted fairly accurately, as was seen, tolerances on the fibre content distribution and fibre orientation may be defined based on the required dimensional tolerances for the final part and a knowledge of the degree of precision in microstructure control that can be guaranteed in the part construction. The degree of error in the end combines the idealised tolerance and the precision in processing. The latter may become less important when measures are applied to ensure a consistent microstructure of the laminate.

One factor that can be controlled in order to obtain a more homogeneous microstructure is the thickness of the plies used to build up the laminate [16]. A resin-rich layer is often found on the surface of prepregs. This layer can in some cases, when plies are stacked, amount to a thickness close to that of the fibre-reinforced layer. By increasing the number of plies for a constant section thickness, one can achieve a more even distribution of the fibres and matrix through the thickness of the laminate. This would reduce the imbalance and thus the warpage, and has the additional benefit of increasing the interlaminar toughness of the laminate. Production time and cost is however increased as a result of the higher number of plies to be positioned. The main tradeoff that must be taken into account is then between construction cost and high geometric precision of the part.

A different approach to improvements in the homogeneity of the fibre reinforcement microstructure is through a better control of the prepregging process. Commercial prepregs come in a limited range of thicknesses. Extending the range to thinner plies is desired for high-precision composites, as was discussed above. Yet better would be a higher precision in the production of the prepregs in order to avoid intraply fibre content fluctuations, resin-rich surface layers, and fibre misalignments.

Two approaches exist to achieve solutions to the problem of composite part warpage: one is through design, and the other through constructive means. In the first case, the laminate's sensitivity to perturbations in the designed microstructural parameters such as fibre orientation and content can be

reduced by choosing an appropriate layup sequence with a higher bending stiffness in the directions of concern. Furthermore, processing characterisation must be included as part of the design process. The goals are a reduced or more closely controlled flow during forming and consolidation and optimised thermal cycles. Constructive solutions include methods such as a closer control of the prepreg cutting and positioning, for example through numerical control machines, the use of thinner prepreps, and correct matching of tool and part materials.

## 7. Summary and conclusions

The present study has shown the importance of quality control in processing of composite parts. This points to a need for a good understanding and control of material and processing parameters in order to achieve a high geometric precision through a close control of the composite's reinforcement microstructure.

The effects of small deviations from design values of fibre content distribution and layup angle on the dimensional stability of PEI/glass laminates have been examined. Laminates with intercalated resin layers and small fibre angle perturbations were prepared and the measured shapes were analysed and compared to results of calculations using simple laminate theory.

Small deviations from the designed fibre content or layup angle can lead to significant departures from the desired geometry. These dimensional instabilities result from the anisotropic properties of the lamina and the thermal expansion mismatch between the matrix and the reinforcing fibres. They occur as a symmetric warpage along two principal axes corresponding to the principal axes of the fibre orientation for unidirectional samples and as a twist for samples with a misalignment of the fibres in certain plies. The amount of warpage for similar layups decreases with section thickness, as the overall section stiffness increases.

Simple laminate theory or an analogous FE calculation can be combined with an approximate characterisation of the fibre microstructure, for example on polished sections, to predict the warpage due to an inhomogeneous microstructure or misaligned reinforcing fibres. This approach is sufficient for evaluating the sensitivity of the dimensional tolerance of the part to microstructural parameters and relating it to the deviations from the designed fibre microstructure.

## 8. Acknowledgements

The authors thank the Fonds National Suisse de la Recherche Scientifique for its financial support of the present work.

## 9. References

1. Radford, D. W., *Manufacturing warpage in flat uni-axial composite laminates*, Composite Materials in Transition, Proceedings of the American Society for Composites 5th Technical Conference, East Lansing, MI, USA, American Society for Composites, 1990.
2. Wang, T. - M., Daniel, I. M., and Gotro, J. T., *Thermoviscoelastic analysis of residual stresses and warpage in composite laminates*, Journal of Composite Materials, Vol. 26, No. 6, pp. 883-899, 1992.
3. Tseng, S. - C. and Osswald, T. A., *Predicting shrinkage and warpage of thin compression molded fiber reinforced thermoset parts*, SAMPE Quarterly, Vol. 24, No. 4, pp. 40-48, 1993.
4. Nairn, J. A. and Zoller, P., *The development of residual thermal stresses in amorphous and semicrystalline thermoplastic matrix composites*, Toughened Composites, Johnston, N. J., ed., ASTM, Philadelphia, PA, USA, pp. 328-341, 1987.
5. Lawrence, W. E., Manson, J. - A. E., and Seferis, J. C., *Thermal and morphological skin-core effects in processing of thermoplastic composites*, Composites, Vol. 21, p. 475ff., 1990.
6. Manson, J. - A. E. and Seferis, J. C., *Process simulated laminate (PSL): a methodology to internal stress characterization in advanced composite materials*, Journal of Composite Materials, Vol. 26, pp. 405-431, 1992.
7. Kau, H. T. and Petruska, L. A., *Dimensional stability and property gradients in thick sheet molding compound (SMC) sections*, Polymer Engineering and Science, Vol. 30, No. 14, pp. 805-812, 1990.
8. Chapman, T. J., Gillespie, J. W. Jr., Pipes, R. B., Manson, J. - A. E., and Seferis, J. C., *Prediction of process-induced residual stresses in thermoplastic composites*, Journal of Composite Materials, Vol. 24, pp. 616-643, 1990.



9. Barnes, J. A., Byerly, G., Lebouton, M. C., and Zahlan, N., *Dimensional stability effects in thermoplastic composites-towards a predictive capability*, Composites Manufacturing, Vol. 2, No. 3/4, p. 171ff., 1991.
10. Unger, W. J. and Hansen, J. S., *The effect of cooling rate and annealing on residual stress development in graphite fibre reinforced PEEK laminates*, Journal of Composite Materials, Vol. 27, No. 2, pp. 108-137, 1993.
11. Radford, D. W., *Cure shrinkage induced warpage in flat uni-axial composites*, Journal of Composites Technology & Research, Vol. 15, No. 4, pp. 290-296, 1993.
12. Krumweide, G. C. and Brand, R. A., *Attacking dimensional instability problems in graphite/epoxy structures*, Optomechanics and Dimensional Stability, San Diego, CA, USA, SPIE, 1991.
13. Rosen, B. W. and Hashin, Z., *Analysis of Material Properties*, Engineered Materials Handbook, Vol. 1: Composites, ASM International: Metals Park, OH, USA, pp. 185-205, 1987.
14. Daniel, I. M., Wang, T. - M., Karalekas, D., and Gotro, J. T., *Determination of chemical cure shrinkage in composite laminates*, Journal of Composites Technology & Research, Vol. 12, No. 3, pp. 172-176, 1990.
15. Hyer, M. W., *Calculations of the room-temperature shapes of unsymmetric laminates*, Journal of Composite Materials, Vol. 15, pp. 296-310, 1981.
16. Manders, P. W., *Thin carbon fiber prepregs for dimensionally critical structures*, Advances in Optical Structure Systems, Orlando, FL, USA, SPIE, 1990.

# Interfacial Moisture Transport In Composite Materials

Wahid Benhamida<sup>†</sup>, Hélène Dumontet<sup>†</sup>, Ahmed Lekhder<sup>†‡</sup>

<sup>†</sup> Laboratoire de Modélisation et Mécanique des Structures

U.R.A. C.N.R.S. 1776 - Université P. et M. Curie - E.N.S.A.M. - E.N.S.C. -  
Tour 66, 5<sup>e</sup> étage. 4 Place Jussieu. 75252 PARIS CEDEX 05. FRANCE

<sup>‡</sup> Laboratoire de Mécanique et des Matériaux  
Faculté des Sciences. RABAT. MAROC

## Abstract

When composite materials are exposed to humid environments for long periods of time, their mechanical properties can be altered. In particular, moisture has been observed to cause damage by delamination in stratified composites or by debonding at fiber-matrix interfaces in reinforced composites. It has also been observed that moisture initially penetrates into the structure following preferential pathes along the interfaces between the constituents. The objective of this work is to modelize this preferential diffusion, in order to investigate interfacial regions with high levels of moisture and to predict the interfacial stresses which can be induced.

## 1. Introduction

Composite materials are increasingly used for designing complex structures because of their excellent mechanical properties. Using composite materials in humid environments, however, may lead to water absorption and to the damage of the structure. In particular, moisture has been observed to cause delamination in stratified structures or debonding at fiber-matrix interfaces in reinforced composites, [4], [8], [9]. As a consequence, modelling moisture transport in composite materials along interfaces is important from a practical and developmental point of view. In this paper, we derive a model for interfacial diffusion by using multiscaled asymptotic expansions.

In section 2, we first derive an interfacial law asymptotically equivalent to transmission conditions through thin diffusive layers. In section 3, we use the homogenization theory of periodic media in order to obtain the equivalent macroscopic be-

havior for stratified and fiber reinforced materials. Finally, in section 4, we present various numerical results with comparison to experimental data.

## 2. Interface asymptotic analysis

In this section, we consider fibers reinforced materials as a typical exemple. The results that are obtained are easily generalized to other type of structures like stratified composites or composites with spherical inclusions.

### 2.1 Governing equations

In order to simplify the presentation, we assume that the fibers and the matrix have an isotropic homogeneous diffusive behavior. We will denote by  $c(x, t)$  the concentration of humidity at point  $x$  and time  $t$ , where  $x = (x_1, x_2, x_3)$  are cartesian coordinates, and by  $q(x, t)$  the humidity flux vector. The water conservation equation can then be

written in the form

$$\frac{\partial c}{\partial t} + \operatorname{div} \mathbf{q} = 0,$$

and the water flux vector is given by Fick's law

$$\mathbf{q}(x, t) = -\mathbf{D} \operatorname{grad} c,$$

where  $\mathbf{D}$  is the hygrometric tensor which is spherical and constant in each constituent by assumptions.

Interfaces between the fibers and the matrix are preferential diffusive pathes and are modeled by thin layers of thickness  $\epsilon$  and diffusivity  $\mathbf{D}^\epsilon$  that is taken in the form

$$\mathbf{D}^\epsilon = \frac{\tilde{D}}{\epsilon} \mathbf{I},$$

where  $\tilde{D}$  is a finite scalar quantity. Finally, we will denote by  $R$  the radius of the fibers and by  $\mathbf{e}_3$  their alignment direction.

### 2.2 The thin interface limit

By using asymptotic expansions, the following asymptotic behavior can be obtained, [1]

*Proposition 1.* The interfacial law at the interface  $\Gamma : \{r = R\}$  between a fiber and the matrix

$$\begin{aligned} [c] &= 0, \\ [\mathbf{q} \cdot \mathbf{n}] &= \tilde{D} \left( \frac{1}{R^2} \frac{\partial^2 c}{\partial \theta^2} + \frac{\partial^2 c}{\partial z^2} \right), \end{aligned}$$

is asymptotically equivalent to transmission through a thin diffusive layer when its thickness  $\epsilon$  goes to zero.

In these relations,  $(r, \theta, z)$  denotes the cylindrical coordinates,  $[g]$  the jump of a quantity  $g$  through the interface, that is to say  $[g] = g^m - g^f$  where the superscripts  $m$  and  $f$  refer to the matrix and the fiber, respectively, and where  $\mathbf{n}$  is the unit normal external to the fiber.

*Remarks :* In the case of stratified materials along direction  $\mathbf{e}_3$ , the asymptotically equivalent flux interfacial law becomes

$$[\mathbf{q} \cdot \mathbf{n}] = \tilde{D} \left( \frac{\partial^2 c}{\partial x_1^2} + \frac{\partial^2 c}{\partial x_2^2} \right),$$

whereas for more complex geometries, we get

$$[\mathbf{q} \cdot \mathbf{n}] = \tilde{D} \Delta_T c,$$

where  $\Delta_T$  denotes the surfacic laplacien operator.

## 3. Macroscopic diffusive behavior

In this section, we now consider a fiber reinforced material with a thin periodic structure; the interfaces between the fibers and the matrix are modeled as in section 2. Our goal is to obtain the homogeneous equivalent behavior of this composite structure.

### 3.1 Homogenization

Among the various homogenization methods, we have chosen the homogenization theory of periodic media which provides a mathematical framework for the homogenization process. Let  $\epsilon$  be the small parameter characterising the size of the heterogeneities. The homogenous equivalent behavior is defined by the limit behavior obtained as  $\epsilon$  goes to zero, [2], [3], [7].

We will denote by  $Y$  the basic period which can be reduced in the case of fiber reinforced composites to a bidimensional period  $Y = ]0, Y_1[ \times ]0, Y_2[$ .

### 3.2 Equivalent transversal diffusion

The homogenized transverse diffusive behavior can first be interpreted as the relation between macroscopic quantities, [1].

*Proposition 2.* Let  $\mathbf{G}$  be the macroscopic gradient of water concentration and consider the following problem on the cell  $Y$

$$\begin{aligned} \operatorname{div} \mathbf{q}(y) &= 0, & \text{in } Y, \\ \mathbf{q}(y) &= -\mathbf{D}(y) \operatorname{grad} c(y), & \text{in } Y, \\ [c] &= 0, \quad [\mathbf{q} \cdot \mathbf{n}] = \tilde{D} \Delta_T c, & \text{on } \Gamma, \\ \langle \operatorname{grad} c(y) \rangle &= \mathbf{G}, \\ \operatorname{grad} c(y) \text{ and } \mathbf{q}(y) &\text{ are } Y\text{-periodic.} \end{aligned}$$

The macroscopic water flux vector  $\mathbf{Q}$  is then defined as

$$Q_\alpha = \langle q_\alpha \rangle_{Y-\Gamma} + \frac{1}{|Y|} \int_\Gamma [\mathbf{q} \cdot \mathbf{n}] y_\alpha ds, \quad \alpha = (1, 2),$$

where the microscopic flux  $\mathbf{q}$  is the solution of the above cell problem and the equivalent transverse diffusion coefficients  $D_{\alpha\beta}^h$  are then given by

$$Q_\alpha = D_{\alpha\beta}^h G_\beta, \quad (\alpha, \beta) = (1, 2).$$

In practice, we reformulate the above cell problem by using a change variable and the linearity,

[6]. The following expression is then obtained for the equivalent transverse diffusion coefficients

$$D_{\alpha\beta}^h = \frac{1}{|Y|} \left[ \left( \int_Y D(y) dy \right) \delta_{\alpha\beta} - \int_Y D(y) \frac{\partial \chi^\beta}{\partial y_\alpha} dy \right] + \frac{1}{|I|} \left[ \tilde{D} \pi R - \int_I \tilde{D} \frac{n_\alpha}{R} \chi^\beta ds \right],$$

where the periodic functions  $\chi^\beta$ ,  $\beta = (1, 2)$ , are solutions of the variational problem

$$\begin{cases} \chi^\beta \in W/\mathbb{R} \\ a(\chi^\beta, v) = L_\beta(v), \quad \forall v \in W/\mathbb{R}. \end{cases}$$

The bilinear form of the variational problem is given by

$$a(u, v) = \int_Y D(y) \frac{\partial u}{\partial y_\alpha} \frac{\partial v}{\partial y_\alpha} dy + \int_I \tilde{D} \frac{\partial u}{\partial y_\alpha} \frac{\partial v}{\partial y_\beta} \tau_\alpha \tau_\beta ds,$$

where  $\tau$  is the unit tangent vector of the interface, the linear form by

$$L_\beta(v) = \int_Y D(y) \frac{\partial v}{\partial y_\beta} dy + \int_I \tilde{D} \frac{n_\beta}{R} v ds,$$

and the space  $W$  is defined by

$$W = \{v \in H^1(Y), v|_I \in H^1(I), v \text{ } Y\text{-periodic}\},$$

where  $W/\mathbb{R}$  denotes the space  $W$  quotiented by the constant functions.

*Remark :* The homogenized coefficients appear as the sum of a classical term [2], [3], [7] and an additional term due to the microscopic flux discontinuity at the interface.

### 3.3 Equivalent longitudinal diffusion

By using a similar homogenization procedure, the expression of the equivalent longitudinal diffusion coefficients is also obtained analytically.

*Proposition 3.* The equivalent longitudinal diffusion coefficients are given by

$$D_{33}^{hom} = \frac{1}{|Y|} \left[ \int_Y D(y) dy + \tilde{D} |I| \right], \\ D_{\alpha 3}^{hom} = 0, \quad \alpha = (1, 2).$$

The equivalent macroscopic hygrometric tensor  $\mathbf{D}^h$  is then completely determined from Propositions 2 and 3.

### 3.4 Practical calculations

From the precedings sections, the homogenized behavior is obtained after the resolution of two cell

problems with periodic boundary conditions. However, when the cell presents material symetries, we only have to solve one problem on a subcell with Dirichlet and Neuman boundary conditions, [6]. In addition, in the case of fiber rectangular arrays, one can show that the homogenized behavior is orthotropic, i.e.,

$$\mathbf{D}^h = \begin{pmatrix} D_{11}^h & 0 & 0 \\ 0 & D_{22}^h & 0 \\ 0 & 0 & D_{33}^h \end{pmatrix}.$$

Furthermore, in the case of square or hexagonal arrays, one can show that the homogenized behavior is transverse isotropic, i.e.,  $D_{11}^h = D_{22}^h$ .

Finally, for periodically stratified materials along the direction  $\mathbf{e}_3$ , the homogenized behavior is explicitly given by

$$D_{11}^h = D_{22}^h = \frac{1}{|Y|} \left[ \int_Y D(y_3) dy_3 + \tilde{D} \right], \\ D_{33}^h = \frac{1}{\frac{1}{|Y|} \int_Y \frac{1}{D(y_3)} dy_3},$$

the other coefficients being zero.

## 4. Numerical results

We first consider a stratified structure composed alternatively of two homogeneous isotropic layers of equal tickness. The structure, initially dry, is instantaneously exposed to water concentration  $c_a$  at one of its boundary. The ratio  $D_2/D_1$  of the layer diffusion coefficients is taken to be 2. The interfacial diffusion coefficient  $\tilde{D}$  is taken to be  $20 D_1 h$ , where  $h$  is the thickness of the cell.

We first investigate water transport in a cell domain of the structure directly exposed to the humid boundary which is perpendicular to the direction of stratification. The water transport evolution problem is solved by using the finite element method for spacial discretization and a multistep method for time discretization. Special lineic finite elements are introduced at the interfaces in order to take into account the interfacial discontinuity of the flux vector  $\mathbf{q}$ .

Figure 1 presents the water concentration isopleths  $c(x, t)/c_a$  at the beginning of the process. In order to validate the interfacial law, we also present the same result at the same time in the case where the interface is modeled by a thin layer of thickness  $e = 0.02 h$  and of high diffusivity  $D^c = 1000 D_1$ , (Figure 2) and in the case where the interface is perfect, ( $\tilde{D} = 0$ ), (Figure 3). Although the water progressively penetrates into the structure nearly parallell to the exposition front in Figure 3, we observe that it penetrates rapidly by following the interface path in Figures 1 and 2. The

very good agreement between the water isopleths obtained with the asymptotic interfacial law and with a thin diffusive layer observed in Figures 1 and 2, is again observed with the time dependence of the global quantity

$$M(t) = \frac{\text{humid weight} - \text{dry weight}}{\text{dry weight}} \quad (\text{in } \%),$$

which represents the relative weight gain of the structure, (Figure 4).

These numerical results clearly show the asymptotic equivalence between the interfacial law and a thin diffusive layer. It validates the use of this interfacial law which suppresses the difficulties associated with thin domain discretizations.

Next, we consider a fiber reinforced material with an hexagonal array of circular fibers. The diffusion coefficient of the matrix  $D^m$  is taken to be  $10^3 D^f$  and the coefficient  $\tilde{D}$  to be  $30. D^m R$ .

Figure 5 presents the water concentration isopleths  $c(x, t)/c_a$  in a subdomain of the structure near the humid boundary which is perpendicular to

the fiber direction. We again observe a preferential water penetration tangentially to the interfaces. A very good agreement is also achieved with the case of a thin diffusive interface, as for stratified structures.

Figures 6 and 7 finally present the dependence of the homogenized equivalent coefficients—normalized by the matrix coefficient—on the fiber volume fraction. The transverse diffusion coefficient is given in Figure 6 and the longitudinal diffusion coefficient in Figure 7. These coefficients, obtained by the homogenization process described in section 3, are compared with experimental data [4] and with the coefficients obtained with other homogenization procedures [5], [8], [9]. The diffusion coefficients obtained in the case of a perfect interface corresponds exactly to these given by [8]. The gap observed between these models and the experimental data shows the importance of interfacial diffusion. Finally, by adjusting the interfacial coefficient  $\tilde{D}$ , our model gives an excellent agreement with the experimental data, far superior than that of the classical models.



Figure 1 : Water concentration isopleths with the interfacial law model.



Figure 2 : Water concentration isopleths with a thin diffusive layer interface.



Figure 3 : Water concentration isopleths with a perfect interface.

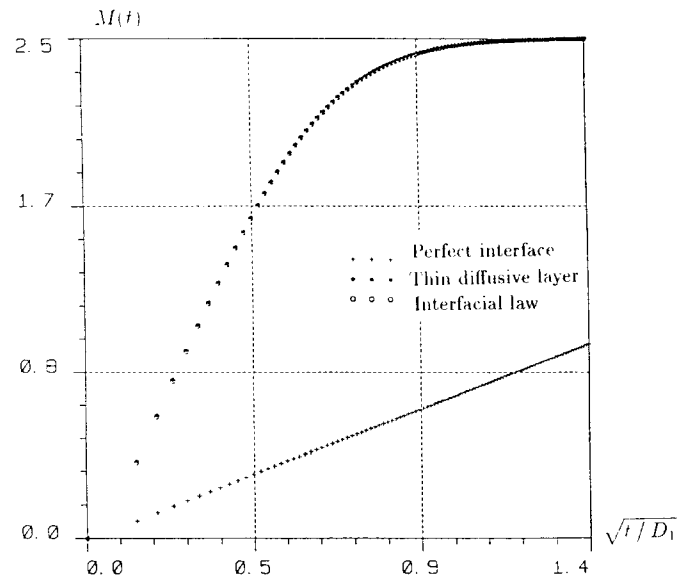
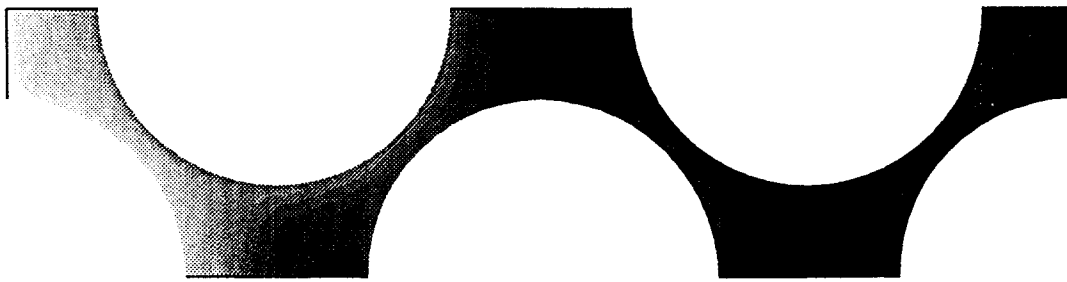
Figure 4 : Time dependence of the relative weight gain  $M$ .

Figure 5 : Water concentration isopleths with the interfacial law model.

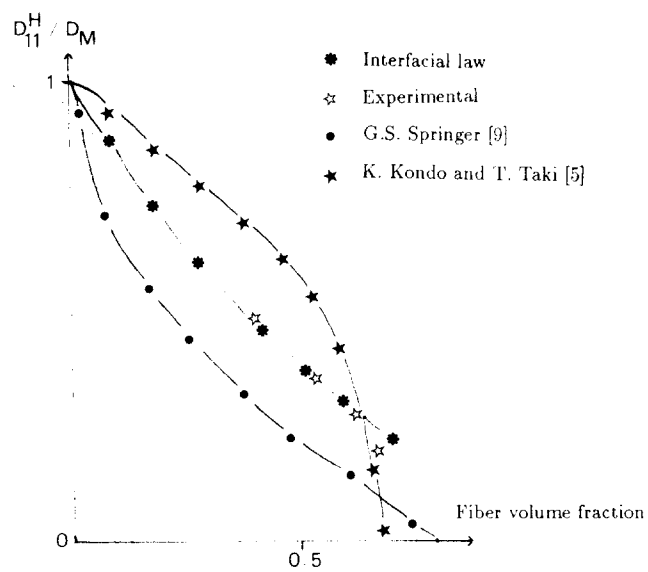


Figure 6 : Dependence of the equivalent transverse diffusion coefficient on the fiber volume fraction.

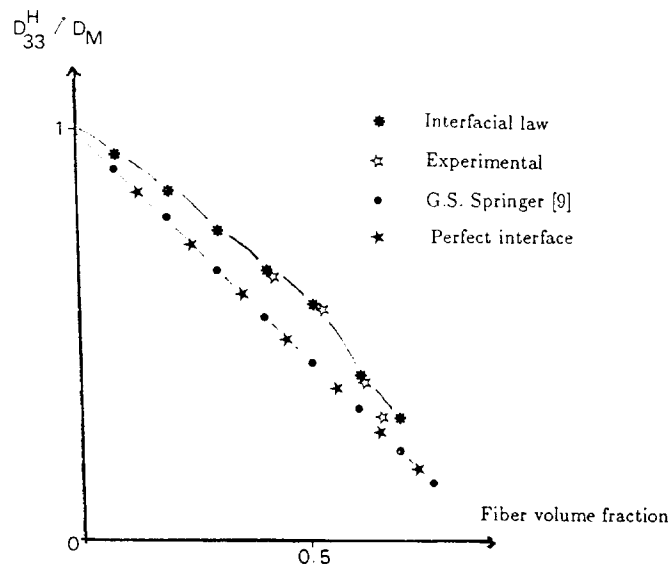


Figure 7 : Dependence of the equivalent longitudinal diffusion coefficient on the fiber volume fraction.

## Acknowledgment

This work was supported by the Institut Français de Recherche pour l'Exploitation de la Mer under research contract (U.R.M. n°12). The authors wish to express their thanks to P. Chauchot and Y. H. De Roeck of the Direction de l'Ingénierie de la Technologie et de l'Informatique (IFREMER) for their fruitful discussions on the problem.

## References

- [1]. A. BENHAMIDA, H. DUMONTET, N. LEBRIS and A. LEKHDER, (1995), "Hygroscopic Behavior of Composite Materials", (to appear)
- [2]. A. BENSOUSSAN, J.L. LIONS and G. PANICOLAOU, (1978), "Asymptotic Analysis for Periodic Structures," *North-Holland Editor, Amsterdam*.
- [3]. G. DUVAUT, (1976), "Analyse Fonctionnelle et Mécanique des Milieux Continus", *Theoretical and Applied Mechanics, W. Koiter Editor, North-Holland*, pp.119-132.
- [4]. J.P. FAVRE and J.N. DEWAS, (1984), "Diffusion of Water in Carbon Epoxy Composite Materials. Evaluation of a Model Based on Matrix Absorption", *Comptes Rendus des Quatrièmes Journées Nationales sur les Composites, Pluralis Editor*, pp. 631-644.
- [5]. K. KONDO and T. TAKI, (1981), "Moisture Diffusivity of Unidirectional Composites", *Environmental Effects on Composite Materials, G.S. Springer Editor*, pp. 288-298.
- [6]. F. LENE, (1984), "Contribution à l'Etude des Milieux Composites et de leur Endommagement", *Thèse de Doctorat d'Etat, Paris 6*.
- [7]. E. SANCHEZ-PALENCIA, (1980), "Non Homogeneous Media and Vibration Theory", *Lectures Notes in Physics, Springer-Verlag Editor, Berlin*, 127.
- [8]. C.H. SHEN, G.S. SPRINGER, (1981), "Moisture Absorption and Desorption of Composite Materials", *Environmental Effects on Composite Materials, G.S. Springer Editor*, pp. 15-33.
- [9]. G.S. SPRINGER, (1981), "Introduction", *Environmental Effects on Composite Materials, G.S. Springer Editor*, pp. 1-6.

# Radiation Effects on Structural Materials for High-Energy Particle Accelerators and Detectors

H. Schönbacher, M. Tavlet  
CERN - TIS  
CH 1211 Geneva 23 - Switzerland

## Abstract

This paper gives a review of radiation effects and radiation damage for a number of materials which are frequently used in high-energy particle accelerator and detector construction. The main emphasis is put on polymers. Representative examples of commercially available materials suitable for use within the dose range from  $10^5$  Gy to  $10^8$  Gy are given. For completeness, basic radiation effects in ceramics and metals are also described, but no radiation damage problems can be expected from these materials in this dose range.

## 1. Introduction

Material selection for future high-luminosity collider detectors is a challenge to design engineers and physicists. Many operational and safety aspects need to be taken under consideration. One of the key parameters is radiation. In the past, radiation damage studies were concentrated on materials in the primary beam areas of the accelerators and practically no attention had to be given for detector materials because the radiation doses in experiments were far below any damage level. For the CERN Large Hadron Collider (LHC) the accelerator will have to operate with low beam losses and hence low radiation doses for the large majority of the machine part, whereas in the collision region of the 8 TeV proton beams the radiation doses will be in the order of  $10^4$  to  $10^6$  Gy per year [1].

This report will give an overview of radiation effects on detector construction materials, mainly polymers, used for insulation, supports, tubing, cables and, although much less radiation sensitive, on ceramics and metals [2]. The report will not cover materials used for the detector operation

such as semi-conductors, electronics, optical fibres and crystals.

## 2. Polymers

Extensive work has been done on radiation effects on polymers mainly for nuclear reactor application and radiation processing [3] but also for materials used in high-energy particle accelerator construction such as the CERN Super Proton Synchrotron (SPS) or the Large Electron Positron storage rings (LEP) [4].

As polymers degrade under the influence of high-energy radiation, they can suffer from loss of their mechanical, electrical, chemical and optical properties. The major cause of changes in the macroscopic mechanical properties of polymers results from scission of polymer chains and/or from crosslinking between neighbouring polymer chains.

The rate of degradation can strongly be influenced by the presence of oxygen and corrosive gases such as  $O_3$  and  $NO_x$ . This increases the difficulty in predicting long term (low dose rates) radiation degradation beha-



viour. In many cases, lower dose rates result in comparatively higher mechanical degradation at the same integrated dose. Therefore, if the material is in service over a long time at low dose rate it may degrade faster than would be expected from short time tests.

This effect is particularly pronounced in some currently used thermoplastics for cable insulation such as polyolefins. Table 1, taken from Ref. 4 is a typical example. The dose limit for this type of materials is around  $10^5$  Gy and therefore in the central part of the detector more radiation resistant materials such as polyimide (Kapton®) or polyether-etherketone (PEEK) have to be used which can stand doses up to a factor of 100 higher.

Among the thermosetting polymers, a number of materials are available, especially high-temperature cured epoxy resins, which exhibit excellent radiation resistance up to  $10^7$  Gy for the pure resins and up to  $10^8$  Gy when filled with glass fibres, carbons fibres or mica. Radiation damage in polymer-based composites has two origins: the degradation of the polymer matrix as explained above, and the debonding between the fibres and the matrix leading to delamination. The latter effect is in particular influenced by  $(n, \alpha)$  reactions in boron containing fibres, as do thermal cycles.

Some typical examples of suitable radiation resistant materials for LHC are given in Table 2 for pure epoxy resins [4], in Table 3 for epoxy molding compounds [5] and in Table 4 for epoxy resins filled with glass and carbon fibres [4].

Three papers presented at this Workshop give some more specific data on glass fibre epoxy laminates [6] polyarylates [7] and high performance plastics [8].

Table 5 gives a more general overview and classification of a number of polymers and composites which are frequently used in high-energy particle accelerator and detector construction.

The appreciation of radiation resistance is based on mechanical tests, more precisely on flexural strength for rigid polymers and elongation at break for flexible polymers for which experience has shown that they are the most radiation sensitive properties [8].

All cited doses refer to energy absorption in a  $\text{CH}_2$ -type material (polyethylene). For polymers, the radiation damage can be related directly to absorbed dose, irrespective of the radiation type.

Finally, it should be noted that for reasons of low smoke density, low toxicity and corrosivity of gases in case of a fire, halogen containing polymers are forbidden at the LHC. This excludes some very commonly available materials such as polyvinyl chloride (PVC), chlorosulphonated polyethylene (Hypalon®), polychloroprene (Neoprene®), fluorocarbons (e.g. Teflon®) and other halogenated or sulphur containing compounds [9, 10].

Table 6 summarizes the test standards and specifications for polymers as regards to radiation and fire resistance [9].

**Table 1: Elongation at break of polyolefin 862 irradiated to  $5 \times 10^5$  Gy at various dose rates [4]**

Dose Gy	Dose rate ( Gy/h)	Elongation (%)
Zero	Zero	$140 \pm 29$
$5 \times 10^5$	$1.7 \times 10^5$	$90 \pm 3.7$
$5 \times 10^5$	7160	$79 \pm 10.8$
$5 \times 10^5$	100	$30 \pm 5.6$

**Table 2: Mechanical properties of some very commonly used epoxy resins (Araldite®) irradiated up to  $2.5 \times 10^7$  Gy [4]**

Material	Dose (Gy)	Ultimate flex. strength (MPa)	Deflexion at break (mm)	Modulus of elasticity (GPa)
Araldite 300 CY 205 + HY 905 + DY 061	0	$144.2 \pm 10.8$	$13.1 \pm 0.9$	$3.57 \pm 0.29$
	$5 \times 10^6$	$109.9 \pm 15.7$	$7.4 \pm 1.2$	$3.93 \pm 0.10$
	$1 \times 10^7$	$59.8 \pm 12.8$	$3.7 \pm 0.7$	$4.14 \pm 0.16$
	$2.5 \times 10^7$	$12.8 \pm 2.0$	$1.1 \pm 0.1$	$3.22 \pm 0.16$
Araldite 299 MY 745 + HY 906 + XB 2687	0	$107.7 \pm 20.6$	$7.9 \pm 2.0$	$3.84 \pm 0.15$
	$5 \times 10^6$	$114.9 \pm 34.3$	$9.3 \pm 3.3$	$3.76 \pm 0.12$
	$1 \times 10^7$	$68.7 \pm 21.6$	$4.4 \pm 1.3$	$4.02 \pm 0.16$
	$2.5 \times 10^7$	$36.3 \pm 8.8$	$2.2 \pm 0.5$	$4.25 \pm 0.24$

**Table 3: Mechanical properties of epoxy molding compounds irradiated to  $5 \times 10^7$  Gy [5]**

Material (see Ref. 5)	Flexural strength		Deflexion		E-modulus	
	$S_o$ MPa	$S_E/S_o$ %	$D_o$ mm	$D_E/D_o$ %	$M_o$ GPa	$M_E/M_o$ %
XB 3183	158	102	2.0	90	17.4	107
NU 461	117	98	1.7	71	18.4	116
XB 3192	73	93	1.0	80	14.6	108
XB 3097	121	92	1.7	77	17.6	114

**Table 4: Mechanical properties of epoxy resins filled with glass and carbon fibres irradiated up to  $1 \times 10^8$  Gy [4]**

Material	Dose (Gy)	Ultimate flex. strength (MPa)	Deflexion at break (mm)	Modulus of elasticity (GPa)
EPOXY + GLASS FIBRES 409 LEP-QP	0	$433.3 \pm 22.2$	$3.8 \pm 0.1$	$21.5 \pm 0.6$
	$5.0 \times 10^6$	$453.2 \pm 14.9$	$4.1 \pm 0.1$	$22.1 \pm 0.4$
	$1.0 \times 10^7$	$444.8 \pm 13.1$	$3.9 \pm 0.1$	$22.2 \pm 0.5$
	$5.0 \times 10^7$	$408.0 \pm 7.8$	$4.0 \pm 0.2$	$21.7 \pm 0.3$
	$1.0 \times 10^8$	$360.0 \pm 26.2$	$3.7 \pm 0.4$	$21.7 \pm 0.6$
EPOXY + CARBON FIBRES 552 LY556/HY 917/DY 070	0	$928.6 \pm 187.4$	$4.1 \pm 0.9$	$80.5 \pm 2.6$
	$3.0 \times 10^6$	$815.7 \pm 99.1$	$3.5 \pm 0.6$	$81.5 \pm 2.1$
	$1.0 \times 10^7$	$857.3 \pm 113.6$	$4.0 \pm 0.5$	$82.2 \pm 1.4$
	$6.2 \times 10^7$	$836.7 \pm 90.1$	$3.9 \pm 0.4$	$83.0 \pm 1.2$

**Table 5: Radiation dose limits in air for commonly used polymers [4]**

Organic Materials	Radiation Dose Limits
Epoxy resin, cured at ambient temperature (Araldite D®) Cross-linked PE (XLPE) Ethylene-acrylate rubber (EAR) Ethylene-propylene rubber (EPR) Ethylene vinyl acetate (EVA) Polyethylene terephthalate (PETP) Polyethylene (PE) Polyolefin (PO) Polyamide (PA, e.g. Nylon®)	$10^5 - 10^6$ Gy
Epoxy resins aromatic hardener (Araldite B®, Araldite F®, Epikote® Novolac) Paints based on epoxy or polyurethane resins Polyimide film (Kapton®) Polyethersulfone (PES) Polysulfone (PSU) Polyarylates (PAr)	$10^6 - 10^7$ Gy
Polyether-ether-ketone (PEEK) Polyetherimide (PEI) Glass or carbon fibre filled resins: - Epoxy, aromatic hardener - Phenolic - Polyester - Polyimide (PI) - Polyurethane (PUR) - Polyphenylene sulfide (Ryton®, PPS) - Polyphenylene oxide (PPO) - Silicone	$10^7 - 10^8$ Gy

### 3. Ceramics [11]

Exposure of ceramic materials to ionizing radiation affects the crystal lattice of the ceramic by displacement of atoms within the lattice, transformation of atoms to different species by nuclear reactions, and ionization and electronic excitation.

A variety of effects are produced in ceramic materials as a result of lattice displacement. The introduction of interstitial atoms into the lattice produces swelling which may proceed to the point of causing the material to disintegrate. Defects in the lattice reduce the thermal conductivity of the ceramic. Thermal spikes produced particularly near the end of the path of the particle through the lattice lead to localized regions of high temperatures.

The conversion of atoms in the lattice to other species by reactions with neutrons and high-energy particles (HEP) produces impu-

rity atoms. This is generally not of great importance except in the cases where gases are formed, such as the neutron reaction with beryllium which produces helium. Such gases in the lattice may nucleate to form gas pockets or bubbles and cause severe swelling. All these effects occur in frequently used structural or insulating materials such as aluminium oxide ( $\text{Al}_2\text{O}_3$ ) or beryllium oxide ( $\text{BeO}_2$ ) at very high doses exceeding  $10^{10}$  Gy and neutron fluences above  $10^{21}$  n/cm<sup>2</sup> ( $E > 0.1$  MeV).

Ionization and electronic excitation produced by the passage of fast particles or electromagnetic radiation through the lattice do not affect the general mechanical properties of ceramics to any great extent. However, electrons stripped from atoms in the lattice may be trapped at defects to form colour centers, or regions of altered optical absorption characteristics. This effect can be of great importance in applications where optical glasses and optical glass fibres are utilized.

**Table 6: Test standards and specifications for polymers as regards to radiation and fire resistance**

(Cables, connectors, terminals, boards, cards, foils, films, tapes, conduits, tubings, mouldings, coatings, supports, frames, covers and similar parts)

TEST	STANDARD	REQUIREMENTS
<b>Radiation resistance</b>	IEC 544 Parts 2 and 4	Tensile strength or Flexural strength or Elongation at break: 50% of initial value at a specified absorbed dose between $10^6$ Gy and $10^7$ Gy at high dose rates (greater than 1 Gy/s) when applicable
<b>Flame and fire propagation of cables</b>	IEC 332-2 IEC 332-1 IEC 332-3	Pass for all single wires Pass for all cables and all single wires $> 0.5 \text{ mm}^2$ Pass for all cables with outer diam. $> 10 \text{ mm}$ , category CF
<b>Flame and fire propagation of sheets</b> a) Needle-flame test  b) Flammability test	IEC 695-2-2  IEC 707 or UL 94V	Duration of flame application 60 s unless otherwise stated according to Clause 5. Time to extinction: 30 s Damaged length (mm) must be measured  FV0 or FV1 94 V0, 94V1
<b>Temperature Index of sheets</b>	BS 2781 Part 1	$>260^\circ\text{C}$ , no burning or glowing after T + 12s
<b>Smoke density</b>	ASTM-E-662 or ASTM-F-814	$D_s < 250$ for flaming and non-flaming modes
<b>Toxicity of fire gases</b>	ATS 1000.001	HF $<100$ HC1 $<150$ HCN $<150$ SO <sub>2</sub> + H <sub>2</sub> S $<100$ CO $<3500$ NO + NO <sub>2</sub> $<100$ Mean value in ppm of at least 3 samples obtained within 4 minutes under flaming and non-flaming conditions
<b>Corrosivity of fire gases</b>	IEC 754-2	pH $> 4$ conductivity $<100 \mu\text{S/cm}$

## 4. Metals [11]

The mechanism of radiation effects in metals is essentially related to neutrons and HEP which in a primary collision with an atom create vacancies. The neutrons continue to bounce about knocking atoms out of place until their energy is dissipated. A secondary effect results from the energy imparted to the knocked-on-atom. This atom collides with other atoms in the lattice knocking them out of position and imparting energy to them. Finally, these "knocked-on" atoms lose all energy and come to rest in an interstitial position in the lattice. Hence, two types of point defects are formed by the collision between neutrons, HEP and elastic atoms: vacancies and interstitials.

A further secondary effect of neutron and HEP bombardment is the change in structure caused by "thermal spikes". It is postulated that in some instances the energy of the knocked-on atoms can be dissipated locally as a thermal pulse, which can produce extremely high temperatures for very short periods of time. The area affected by such a "spike" could contain interstitial vacancies, misoriented regions, and dislocation loops.

Fission processes produce a variety of foreign atoms, the effect of these atoms on interstitial positions will also contribute to property changes. In certain materials, the same effect can be achieved by the transmutation of the basic material to atoms of another element. Of all transmutation products the inert gases cause some of the most notable effects in metals by swelling which is produced by retained gas.

As in the case of ceramics, these effects occur only at very high doses exceeding  $10^{10}$  Gy and  $10^{21}$  n/cm<sup>2</sup> ( $E > 0.1$  MeV). The main problem in high-energy particle accelerator application is the creation of radioactive isotopes.

## 5. Summary and conclusions

Table 7 summarizes for the groups of materials discussed in this paper the damage mechanisms and the radiation types which cause the damage.

Figure 1 shows a very general appreciation of radiation damage of materials for dose ranges and neutron fluences where they undergo no damage, mild to moderate damage and where they are unusable. Semiconductors were added for completeness. For LHC accelerator and detector construction materials, it can be concluded:

1. Some of the thermoplastics, in particular cable insulations will have to be carefully selected when radiation levels exceed  $10^6$  Gy.
2. A number of carbon and glass fibre reinforced thermosetting resins are available on the market with a radiation resistance up to  $10^8$  Gy.
3. No radiation damage problems shall arise for ceramics and metals. For the latter however the induced radioactivity will have to be taken seriously into consideration when designing for access and maintenance for the central and forward part of the detectors.

Table 7: Radiation effects to Materials

Material	Damage mechanism	Damage due to
Polymers	Main and side chain rupture Cross-linking and degradation, gas evolution, radical production, reaction with environment	Total dose
Ceramics	Displacements, trapped charge carriers, thermal peaks colour centres	Neutrons, high energy particles  Total dose
Metals	Displacements Dislocations Nuclear reactions producing clusters (Helium), voids and bubbles	Neutrons, high energy particles

## GENERAL APPRECIATION OF RADIATION DAMAGE TO MATERIALS

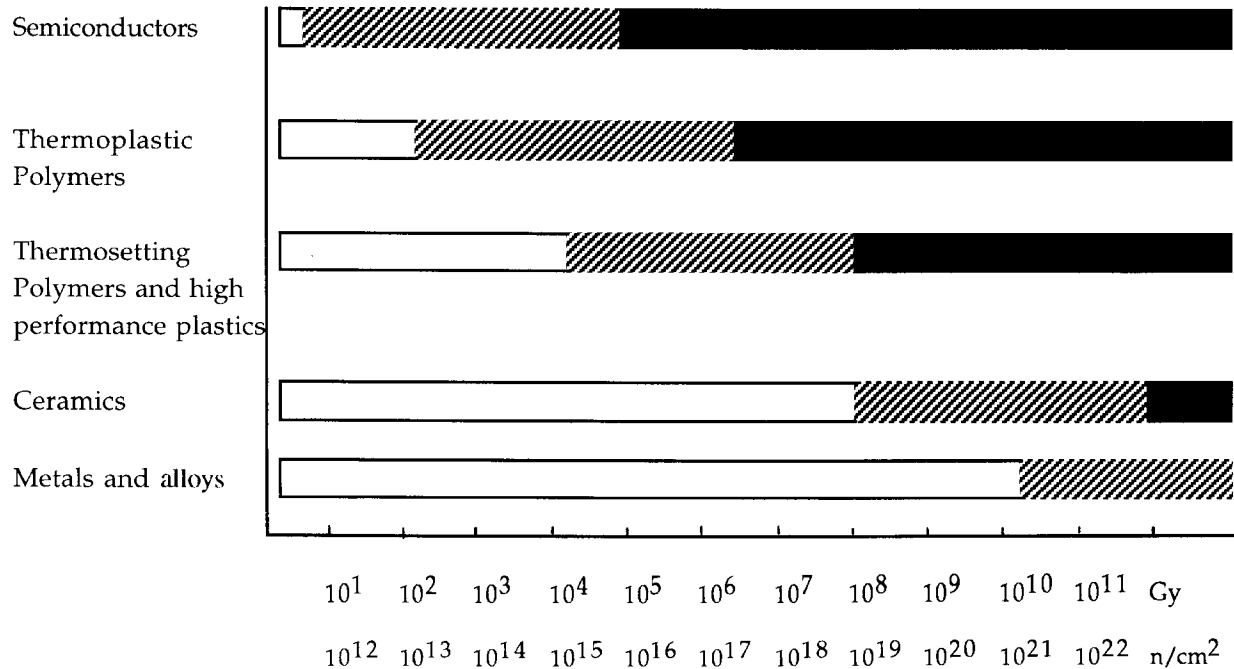


Figure 1: General appreciation of radiation damage to materials. Shown are ranges where materials undergo no damage (blank) mild to severe damage (shaded) or destruction (black).

## 6. References

- [1] G.R. STEVENSON and H. SCHÖNBACHER, 1988, "Radiation dose to a collider detector", **CERN 88-02**, 39-40.
- [2] H. SCHÖNBACHER, 1993, "Materials in the radiation environment of high-luminosity colliders", *Supercolliders and Superdetectors*, World Scientific Publishing, Singapore, 327-336.
- [3] D.W. CLEGG and A.A. COLLYER, 1991, "Irradiation effects in polymer", Elsevier Science Publishers Ltd., New York.
- [4] P. BEYNEL, P. MAIER, H. SCHÖNBACHER, A. STOLARZ-IZYCKA and M. TAVLET, "Compilation of radiation damage test data, Part I: Cable insulating materials" 2nd edition, 1989, **CERN/89-12**, Part II: "Thermo-setting and thermoplastic resins", 1979, **CERN 79-08**, PART III: "Materials used around high-energy accelerators," 1982, **CERN 82-10**.
- [5] H. SCHÖNBACHER, B. SCHREIBER, R. STIERLI, 1986, "Radiation resistance of epoxy molding compounds" *Kunststoffe, German Plastics*, **76**, 14-16.
- [6] W. EICHBERGER, 1994, "Radiation resistant epoxy glass fibre laminates", *Proceedings of this Workshop*.
- [7] P. FIALA, 1994, "High-performance polyarylates under radioactive, cryogenic and high-temperature conditions", *Proceedings of this Workshop*.
- [8] M. TAVLET, H. VAN DER BURGT, 1994, "Radiation resistance and other safety aspects of high-performance plastics of ERTA", *Proceedings of this Workshop*.
- [9] CERN TIS-COMMISSION, 1993, "Criteria and standard test methods for the selection of electric cables, wires and insulated parts with respect to fire safety and radiation resistance", *Safety Instruction 23*.
- [10] CERN TIS-COMMISSION, 1994, "The use of plastics and other non-metallic materials at CERN with respect to fire safety and radiation resistance", *Safety Instruction in preparation*.
- [11] J.F. KIRCHER and R.E. BOWMAN, 1964, "Effects of Radiation on Materials and Components", Reinhold Publishing Corporation, New York.

# Radiation resistant Epoxy Glass fibre Laminates

**W. Eichberger  
ISOVOLTA AG  
A 2355 Wr. Neudorf**

## **Abstract**

Isovolta, one of the leading European manufacturers of insulating materials, can look back at a long co-operation with CERN. Large detector frames were made of ISOVAL, the epoxy glass laminate, which exhibits the best thermal and radiation resistance. For the LEP, Isovolta supplied all the insulation of the excitation bars made of ISOPREG EP. Also experience in the field of superconduction was gained, when Isovolta delivered the prepreg for the coils of the superconducting magnets for the HERA project at DESY. Similar products are being used in all prototypes for the LHC.

Different tests of radiation resistance on Isoval-laminates and Isopreg-prepregs have been carried out and the results are reported and discussed. All results show a radiation resistance of  $10^8$  Gy. The relation between chemical, thermal and radiation resistance depending of the chemical structure of the cross linking is discussed.

Low temperature behaviour of Isoval laminates compared with other epoxy laminates is discussed using the results of Dhalerup and Perrot (CERN) and Prof. Weber et al. (T.University of Vienna).

ISOVAL 10 is introduced: The epoxy laminate showing the same temperature and radiation resistance as the other high cross linked Isoval laminates, but having better machining properties with good dimensional stability.

## **1. Introduction**

Isovolta has been producing glass fibre based prepregs and laminates according to international standards as well as custom tailored products for many years and the company is one of only a few composite manufacturers which have internal resin development and manufacturing facilities at their disposal. This lead to the development of products which are successfully being sold into specialized market segments. For example, one resin developed by Isovolta is used to manufacture a prepreg for the interior of the European Airbus. Another resin is used for manufacturing prepregs for the production of skis and tennis-rackets exhibiting excellent fast curing properties, glass and Mica based prepregs and laminates.

Efforts in the field of epoxy resin chemistry led to the development of a special resin - hardener system, the so called ISOVAL - system, which is used to produce laminates that have served the electrical industry for many years. Continuing improvements of the resin system and in depth studies of the properties of those laminates showed, that they posses vastly superior temperature and chemical resistance in comparison to standard epoxy resin composites. Laminates and prepregs based on this resin system. (Isoval and Isopreg) offer composites, which are economical, have long-term temperature endurance between 180 and 200 °C and can be heated to temperatures up to 300 °C for short periods of time.

## 2. Co-operation with CERN

This lecture deals with Radiation resistant Epoxy Glass fibre Laminates. Of course, the testing of these materials has been done in a close co-operation with CERN.

The first contact the author had with CERN was in 1978, when Isovolta produced the frames of the wire chamber detector of the "European Hybrid System" - project ordered by the Austrian Academy of science represented by its Institute of High Energy Physics. These frames were made from ISOVAL 11, a material which was developed just at that time. ISOVAL 11 was tested regarding radiation resistance and outstanding radiation resistance up to  $10^{10}$  rad were found.

### 2.1. Insulation of the LEP excitation bars

This was the reason for the company to keep further contact with CERN and so we were involved in the LEP project since the first steps of development. The insulation of the excitation bars required

- ) a high grade of safety as it is directly accessible for human contact
- ) a high humidity resistance, because the humidity in the tunnel is nearly 100 %
- ) a high radiation resistance because of secondary radiation caused by the beam.

All these requirements were well known and covered by our ISOVAL laminates. But of course the excitation bars could not be insulated by laminates, even the first idea for the insulation was the application of pultruded profiles. When the decision was made at CERN to use glass fibre prepreps for the wrapping of the bars and additional heat curing - a technique which was well known for the insulation of conductors used for high voltage machines - the development of ISOPREG EP, using the Isoval - resin system was just finished. Introduced to the CERN-laboratories, the outstanding qualities combined with a reasonable price level made this prepreg qualified and proposed to magnet suppliers.

ANSALDO/Genova got the order for all excitation bars and when they started to wrap the first prepreps, they found it to be a little bit stiff and got difficulties in wrapping. This problem could be solved by modifying the prepreg using a softer resin without external modification. This new version was put in the Austrian reactor at Seibersdorf during Christmas holidays and within three weeks we got the radiation results and a new qualification.

This advantage of the radiation resistance being independent of the degree of cross linking will be discussed later on.

### 2.2. LHC project

While the magnets were built for the LEP, Isovolta was involved in the next big collider project, the superconducting magnets for HERA at DESY in Hamburg. For this application the behaviour at low temperature was studied.

With this experience it was obvious, that Isovolta was invited to cooperate concerning the insulation of the superconducting coils of the LHC project at CERN. A lot of development work was necessary to improve the HERA prepreg to cover the new requirements caused by the design of the LHC - magnet coils. Some variations of ISOPREG EP were developed and used in the prototype magnets of LHC.

## 3. Results of Irradiation Tests

### 3.1. Test conditions

Most of the tests were carried out in accordance to IEC 544 (Determination of Effects of Ionizing Radiation on Insulating Materials) in the ASTRA 8 MW pool reactor in Seibersdorf, Austria in the position "plane 1" where the  $\gamma$ -dose rate was about  $1,7 \times 10^5$  Gy/h. In this position also CERN carried out most of its tests.

Some recent results of Isoval 10 were obtained at the 250 kW TRIGA - MARK II reactor of the "Atominstitut of the Austrian Universities" in Vienna using  $\gamma$ -dose rates of  $10^6$  Gy/h.

Already cut specimens for the bending test were irradiated to a total dose of  $10^7$  Gy,  $5 \times 10^7$  Gy and  $10^8$  Gy.

The resistance against ionizing radiation acc. IEC 544 is defined as the dose, at which the flexural strength is reduced to 50 % of the initial value.

### 3.2. Results of the Irradiation Tests

The results of internal tests and CERN- tests of Isoval- and Isopreg-laminates were compared with the results of other glass fibre reinforced laminates published by CERN (1, 2). Whilst Isoval and Isopreg-laminates show radiation resistance of  $1-2 \times 10^8$  Gy, other epoxy glass laminates show only  $10^6$  to  $10^7$  Gy, depending on their chemical composition. Therefore, the radiation resistance of Isoval and Isopreg is in the range of Silicone- and Polyimide-Laminates (fig. 1)



### 3.3. Influence of the degree of cross linking

It is a common rule in the field of Epoxy chemistry, that the thermal and chemical resistance is increased with higher degree of cross linking. This degree of cross linking is given by the curing agent and the functionality of the epoxy resin and is usually expressed by the  $T_G$  (Temperature of the Glass transition).

Regarding the radiation resistance, the standard epoxy laminates seem to follow that rule, but it could be shown, that the high radiation resistance of the Isoval- and Isopreg-Laminates is not correlated with their  $T_G$ . According to the authors interpretation the thermal and chemical behaviour of the epoxies is mainly influenced by the chemical structure of the cross linking and mostly the mechanical properties at elevated temperature are depending on the  $T_G$ .

The independence of the thermal endurance of Isoval laminates from their glass transition temperature was already published (3). The irradiation results can be interpreted in the same way and figure 1 shows the general parallelism between the radiation resistance and thermal resistance, which is expressed also by figure 2, whilst no dependency to the  $T_G$  can be seen.

As explained in 1.2. as an example in practice, the flexibilizing of the first Isopreg named VP288 (similar to Isoval 11,  $T_G = 170^\circ\text{C}$ ) only by reducing the degree of cross linking to the low  $T_G$ -product Isopreg EP ( $130^\circ\text{C}$ ) made it suitable for the wrapping process for the insulation of the LEP - excitation bars. Figure 3 and 4 show the results of the irradiation tests of these two products.

Fig. 5 shows the radiation resistance of Isopreg EP 1037/I DT, the prepreg used in the superconducting coils of the LHC prototype magnets. The resistance obtained is higher than  $10^8$  Gy although it is difficult to press porous free specimens because of the extremely low resin content.

## 4. Isoval 10 as radiation resistant G 10 laminate

In the field of electrical insulating materials the G 10 epoxy glass fibre laminate (according NEMA standard Li 1) is known as the better mechanical grade at ambient temperatures, whilst the G 11 laminate is designed for higher working temperatures but is more brittle at ambient temperature and more difficult to machine. The disadvantage of the standard G 10 - laminate is its very low thermal and chemical

resistance and, as shown in figure 1, its low radiation resistance.

To avoid these disadvantages, Isovolta has introduced successfully Isoval 10, that combines the advantages of both grades. At a first glance it appears that Isoval 10 is not suited as construction material for high temperatures due to its lower glass-transition temperature. This however is not the case. The decline in flexural strength and modulus is not very pronounced around the  $T_G$  region so that the values are still above those of other, more expensive high temperature resistant materials (3).

This conditional thermal stability can be explained as follows: Figure 6 shows the shear modulus curve as measured by torsional braid analysis for different products. The dynamically good standard low-temperature epoxy resin exhibits a very strong decline in modulus at the glass transition temperature and, in comparison, the dynamically equally good version of the Isoval system shows a decline, which is similar to the more thermally stable and higher cross linked products.

## 5. Irradiation tests and low temperature behaviour of Isoval 10

### 5.1 Test conditions

For the use as insulating and construction material in superconducting magnets, the mechanical behaviour at low temperature after irradiation is one of the most important parameter.

Although the irradiation in that case also takes place at the same low temperature, it seems to be not necessary to carry out the irradiation tests at the low temperature. M. Van de Voorde reported very soon the effects on some organic materials including epoxy resins after irradiation at 77 K as approximately the same as after room temperature irradiation (4). The same result was obtained by K.Humer et al (5) after irradiation of some glass fibre epoxy laminates at 5K.

Of course, the characterisation of materials as well as the irradiation effects should be studied by mechanical tests at low temperature.

In a fundamental investigation serie of the mechanical properties of fibre reinforced plastics at low temperature after irradiation H.W. Weber, E.K. Tschegg and K. Humer (6) used Isoval 10 to study basic problems in describing the mechanical behaviour by the means of more detailed cracking mechanism (7,8.). The evaluation of the Crack Opening Mode and the Shear Mode shall give more

information about the damage mechanism during irradiation.

## 5.2 Irradiation effects

In the meantime it is known that the damage process is caused by increasing brittleness of the resin similar to the effect of postcuring, especially at the resin - fibre interface. So one will expect, that the damage after irradiation is more obvious when measured at low temperature.

This was confirmed for some fibre reinforced epoxy laminates including Isoval 10 by the results of S. Spießberger (9) using the tensile strength and crack opening mode and shear mode also at cryogenic temperature for the characterisation of the damage process. In figure 7,8,9, the damage factor is expressed for all three test methods carried out at different temperatures. Generally the damage is more significantly expressed, when the test temperature is lower. So it can be seen, that all three test methods show an increase of the mechanical strength of Isoval 10 at room temperature and 77 K after irradiation to  $10^8$  Gy, but a decrease at 4.2 K.

This behaviour is caused by the relative elastic resin system of this laminate. A certain increase of brittleness during the irradiation increases the mechanical strength (like postcuring), but the additional increase of brittleness by the low temperature of 4.2 K weakens the laminate (but on a very high level because the initial value at 4.2 K is very high).

## 5.2 Mechanical properties at low temperature

If the cryogenic properties are compared, it has to be taken under consideration that the mechanical strength of fibre reinforced laminates is significantly higher at lower temperatures, even at 4 K than at ambient temperature. This fact was already published by Dhalerup and Perrot (10) in a very complete study of the tensile strength of a variety of fibre reinforced plastics at 293, 77 and 4 K. Similar results were obtained for Isoval 10 by E.K. Tschegg (7) not only by using tensile tests but also by shear fracture tests and crack opening mode (fig. 10 and fig. 11).

## 5.3. Influence of Boron in the glass fibre

The influence of the Boron in the glass fibre was studied by testing Isoval 10 with E-glass (Boron content was 2,2 % in the fibre) and with S-glass (boron free) as reinforcement (9).

Because of the high reactivity of the Boron with neutrons it was expected, that very serious damage mechanism occur at the glass fibre surface. But no

significant differences between S-glass and E-glass were obtained. The remaining differences may occur from the different laminating processes (The S-glass laminate was produced in a laboratory scale).

The samples were irradiated up to a dosage of  $10,1 \times 10^8$  Gy and the mechanical strength was measured at ambient temperature, 77K and at 4K. The results are presented in figure 12.

## 6. Conclusion

The resin system of the Isoval laminates allows the production of tailor made epoxy laminates and prepregs with high radiation resistance. Isoval 10 is composed with the relative elastic version of this resin system and shows very high mechanical strength after irradiation of  $10^8$  Gy even at cryogenic temperatures.

## 7. References

- (1) CERN Publ. 79-08 - Health and Safety Division : "Compilation of Radiation Damage Test Data, Part II.
- (2) CERN Publ. 85-02 - Technical Inspection and Safety Commission: "Radiation Tests on selected electrical insulation materials for high-power and high voltage application".
- (3) W. EICHBERGER: "Temperature resistant glass fibre - epoxy composites", *Composites Structures* 24 (1993).
- (4) M.van de VOORDE, "Low temperature irradiation effects on materials and components for superconducting magnets for high energy physics application", CERN Publ. 77-03, 1977
- (5) K. HUMER, H.W. WEBER, E.K. TSCHEPP, Sh. EGUSA, R. C.BIRTCHER, H. GERSTENBERG, "Tensile and shear fracture behaviour of fibre reinforced plastics at 77 K irradiated by various radiation sources.", *Advanced cryog. Eng.* 40,
- (6) H. W. WEBER and E.K.TSCHEGG, "Test program for mechanical strength measurements on fibre reinforced plastics exposed to radiation environment", *Advanced cryog. eng.*, 36 - 863
- (7) E. TSCHEGG, K.HUMER and H.W. WEBER, "Influence of test geometry on tensile strength of fibre reinforced plastics at cryogenic temperature", *Cryogenics* 31(1991), 312 - 318
- (8) K.HUMER, E.K. TSCHEGG, H.W. WEBER, "Small specimens and new testing techniques for fibre reinforced plastics in the crack opening mode (Mode I) and in the shear mode (mode II), *Adv.Cryog.Eng* 40
- (9) S. SPIESSBERGER, "Temperatur- und Strahlungseinfluß auf die mechanischen Eigenschaften glasfaserverstärkter Kunststoffe", Diplomarbeit am Inst. für angew. und techn. Physik der TU Wien.
- (10) CERN Publ. 79 -05 (Dhalerup and Perrot), 1979

Material	Radiat.resist.	TG	Temp.Index
	MGy	°C	°C
Isoval 10	100	130	180
Isoval 11	100	170	180
G 10 - Epoxy	5	130	135
G 11 - Epoxy	20	170	155
Epoxy-Anhydrid	20	130	155
Silikon-Glass	100	100	180
Polyimid-Gl.	100	220	180

Fig. 1. Radiation resistance, TG and temperature index of some glass fibre based laminates

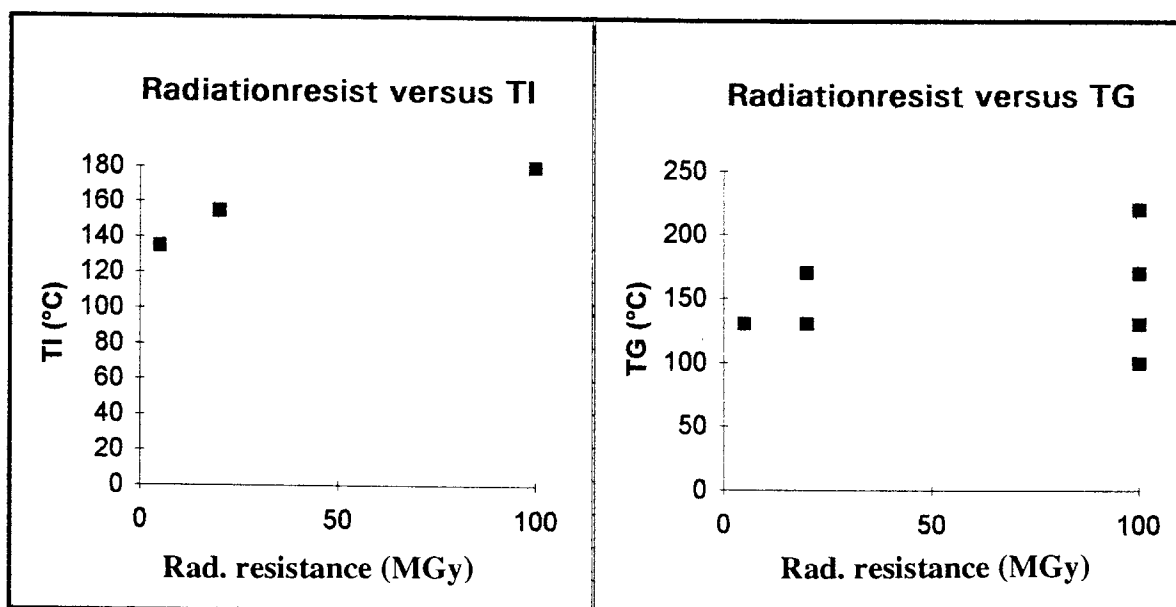


Fig. 2. Correlation of Radiation resistance to TG and TI

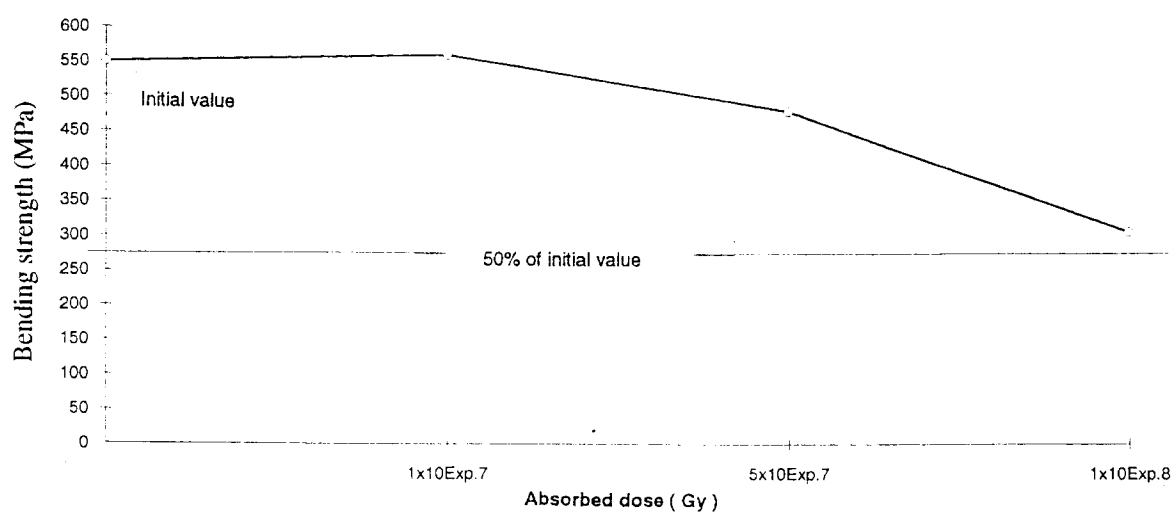
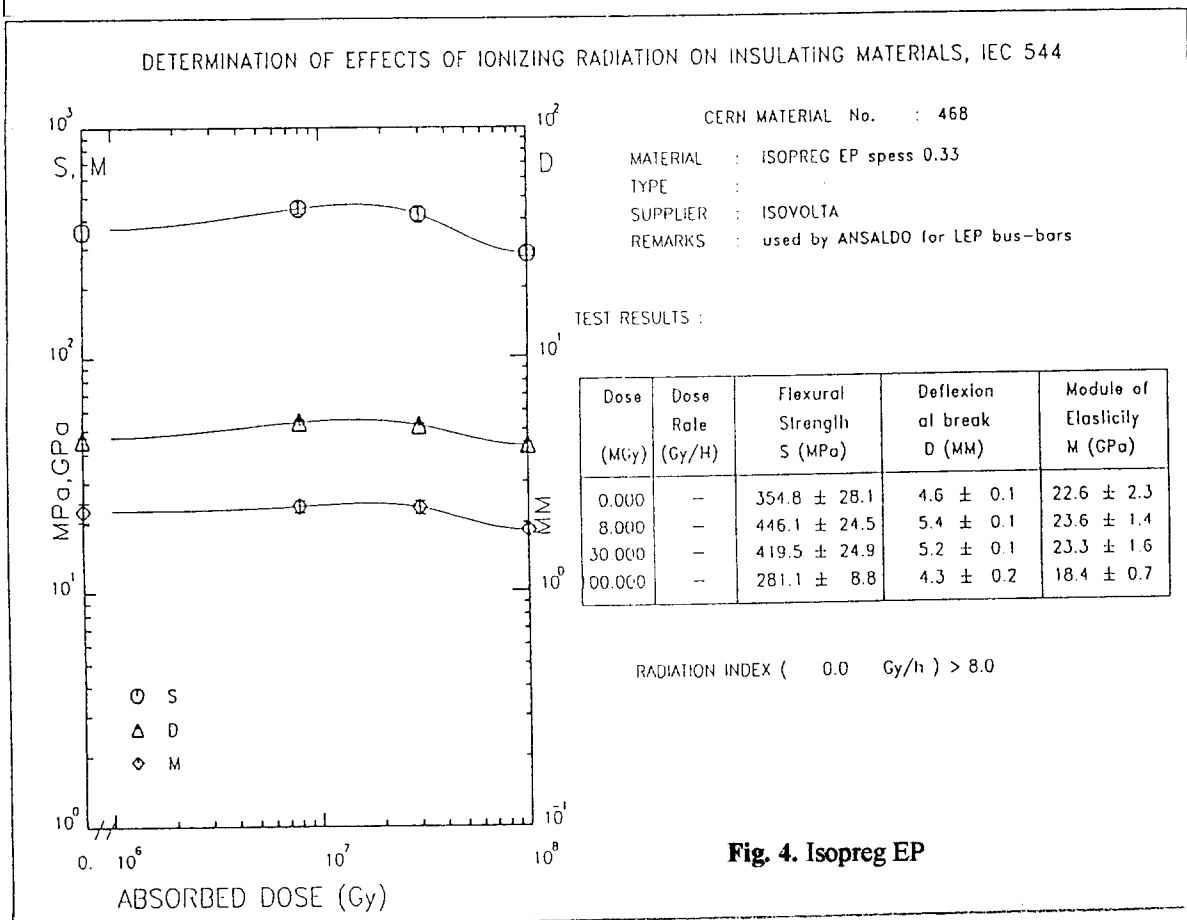
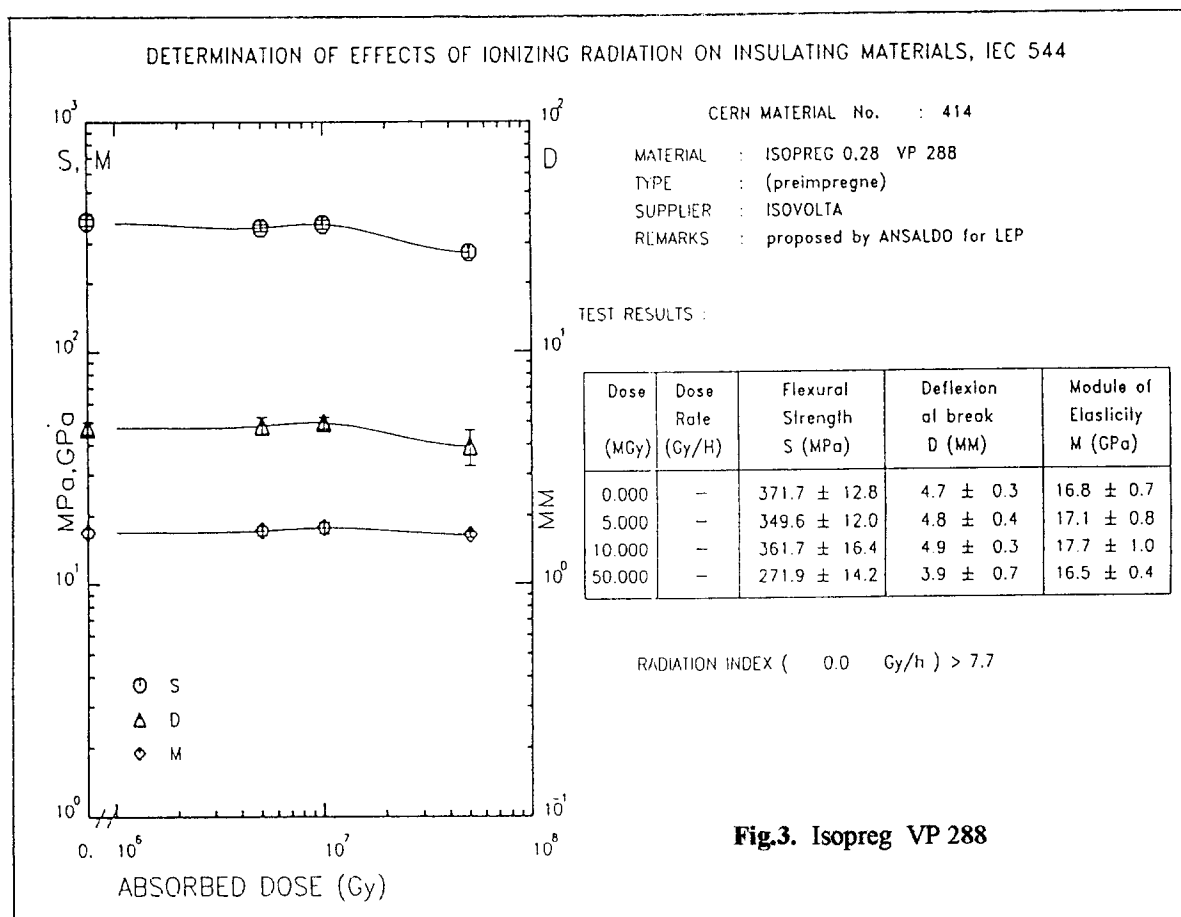


Fig. 5. Radiation resistance of Isopreg EP 1037 / I DT



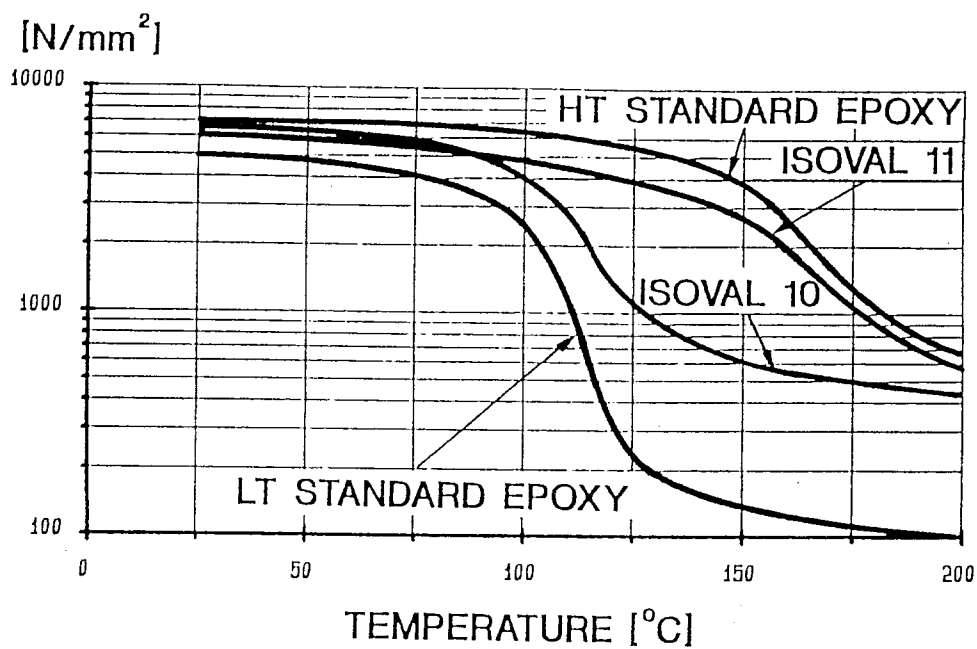


Fig. 6. Shear modulus of Isoval and standard epoxy laminates

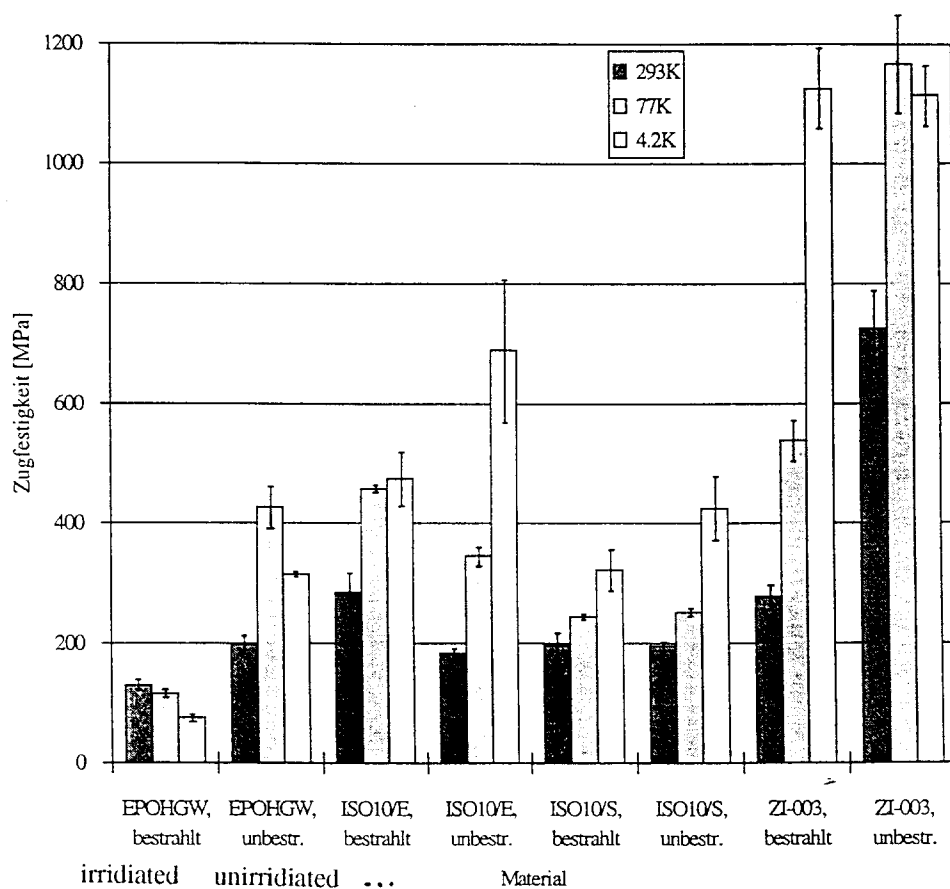
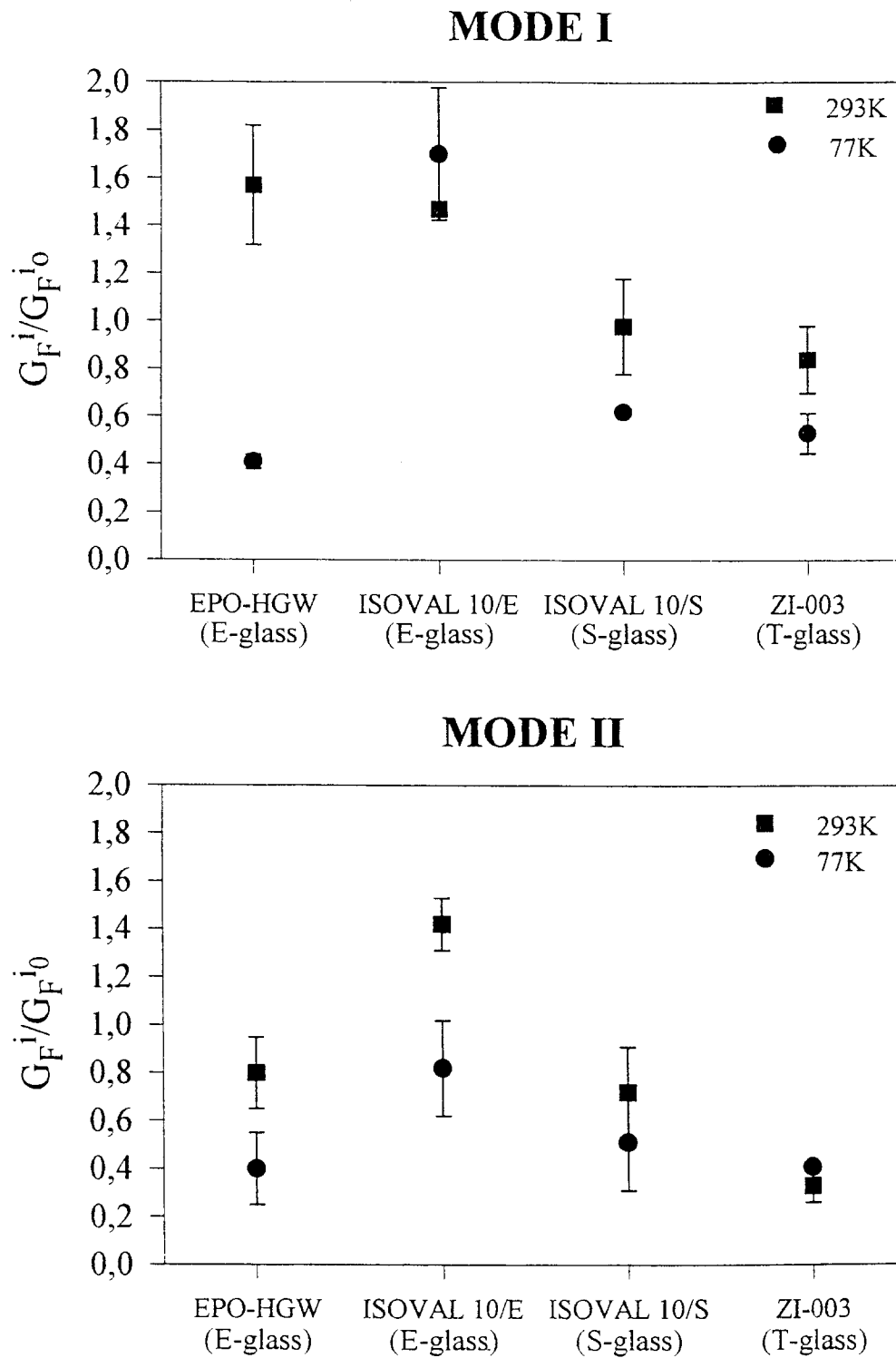


Fig. 7. Radiation damage effects characterised by tensile strength at 293K, 77 K and 4 K



**Fig. 8. and 9.** Damage factor of epoxy laminates determined by the crack opening mode ( mode I ) and the shear mode ( mode II )

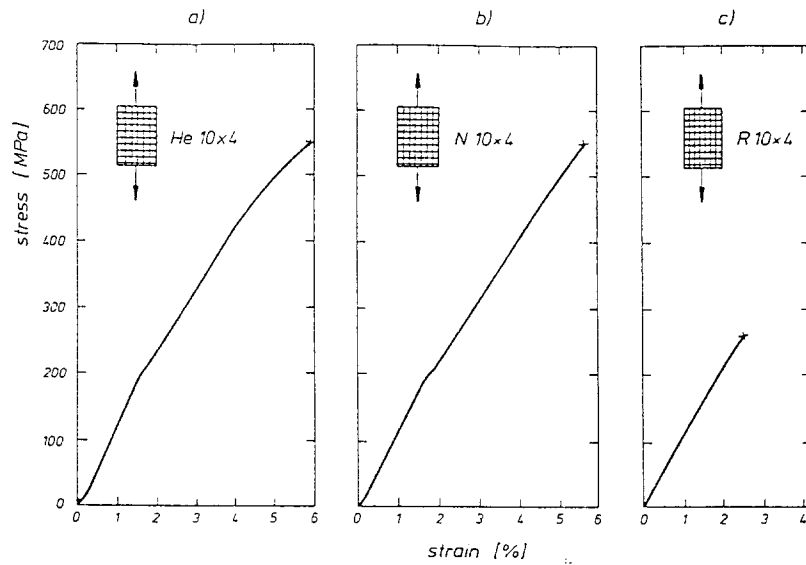


Fig. 10. Isoval 10 : Stress - strain diagrams at a) 4.2 K; b) 77 K; c) room temperature

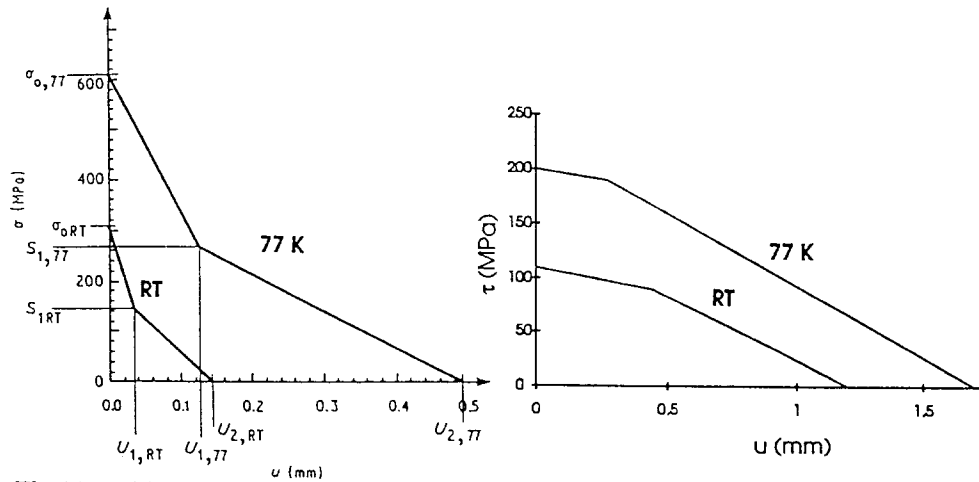


Fig 11. Bilinear strain-softening diagram of Isoval 10 for mode I (left) and mode II (right) at room temperature and at 77 K

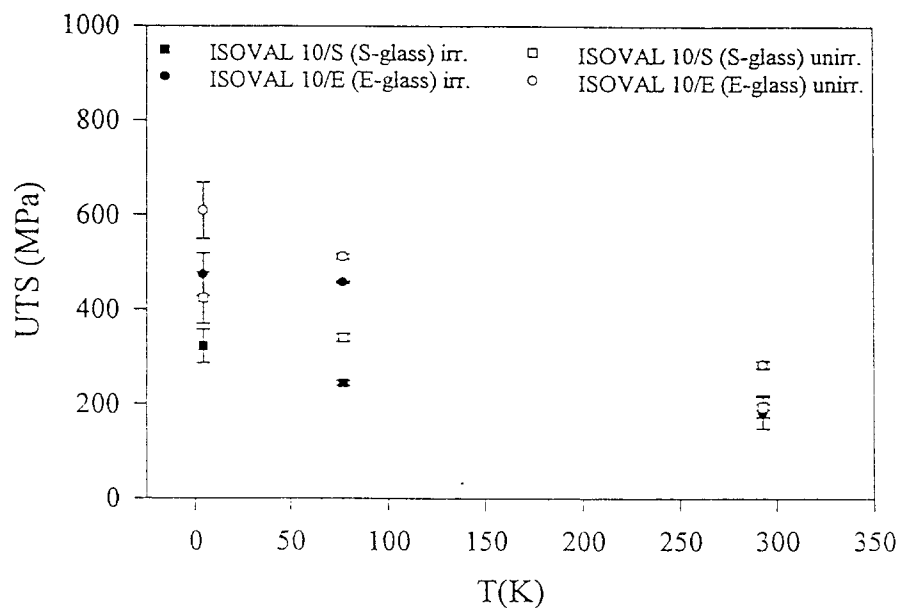


Fig. 12. Tensile strength of Isoval 10 reinforced with E-glass and S-glass irradiated and unirradiated

# Radiation resistance and other safety aspects of high-performance plastics by ERTA

M. Tavlet, CERN – TIS, CH-1211 Geneva 23  
and

H. van der Burgt, ERTA-EPEC, B-8700 Tielt

## Abstract:

High-performance plastics, PEEK (polyether-ether-ketone), Ertalon 4.6 (polyamide PA 4.6), PEI (polyether-imide), PES (polyether-sulfone) and PSU (polysulfone), were supplied to CERN by ERTA-EPEC (B) for testing of their radiation resistance. The fire behaviour of pure PEEK and PEI complies with the requirements of the CERN Safety Code and Instructions. PES and PSU could emit toxic and corrosive fumes when involved in a fire; PA 4.6 is not flame retardant in the standard grade. PEEK, PEI, PES and PA 4.6, as well as PSU to a lower extent, are usable at high temperature, but they are often brittle at cryogenic temperature. Mechanical tests have been carried out, prior and after irradiation up to doses as high as 100 MGy, to assess the radiation resistance; flexural strength, deformation at break, limit of elasticity and modulus of elasticity have been measured. The results show that the modulus and the limit of elasticity are usually not affected by radiation. They also allow to sort the materials from the most resistant one to the most sensitive one: PEEK, PEI, PA 4.6, PSU and PES.

## 1. Introduction

The selection of insulating and structural materials is an important part of the CERN Large Hadron Collider (LHC) project. The selected materials have to fulfil the CERN safety requirements which means that in addition to their mechanical, electrical, thermal, and environmental endurance properties, they have to present a good radiation resistance, and a good fire behaviour: they must be flame retardant, and in the event of a fire, the smoke emission must be low and the resultant gases must be non-toxic and non-corrosive, this implies that they be halogen-free.

Numerous mechanical tests have been carried out at CERN and in many other institutes to assess the radiation resistance of various types of materials, and a lot of data is now available [1, 2]. Most of this data concerns glass-fibre reinforced thermosets. Since a few years, high-performance thermoplastics are available on the market. These products present interesting properties on a mechanical point of view, as well as good radiation resistance. They are still often more expensive than common thermosets, but

the possibility to mould complicated pieces of equipment makes their process faster and cheaper. The semi-crystalline ones (PEEK and PA 4.6) also present a better wear resistance and a lower friction coefficient. With respect to the standard engineering plastics (PA, POM, PETP and PC) the high-performance thermoplastics also offer a better chemical and hydrolysis resistance especially PEEK which has a chemical resistance almost comparable to PTFE.

## 2. Selected engineering thermoplastics

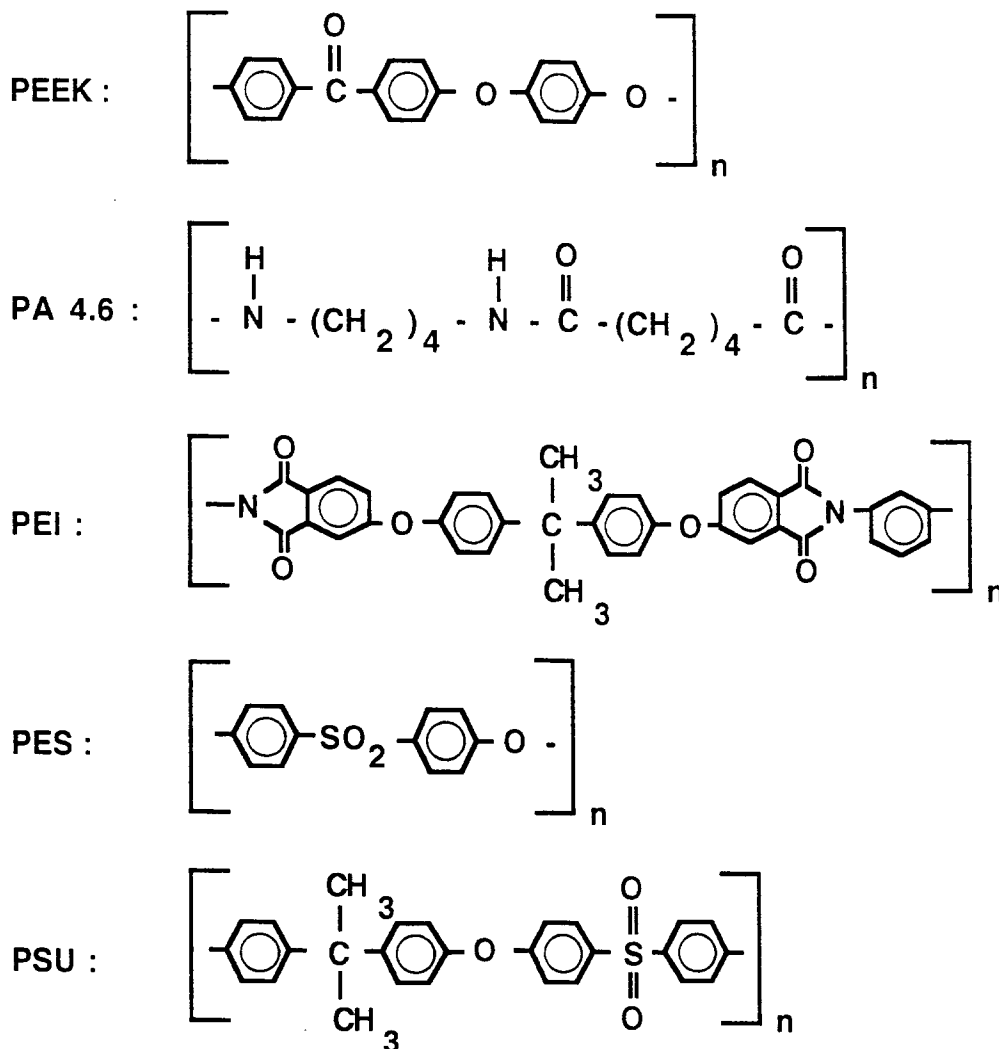
ERTA-EPEC (B) supplies stock shapes in high-performance thermoplastics (EPEC stands for 'Engineering Plastics, Extruded and Cast), five of them have been selected for testing of their radiation resistance: PEEK (polyether-ether-ketone), Ertalon 4.6 (polyamide PA 4.6, also commercialized under the trade-name Stanyl), PEI (polyether-imide), PES (polyether-sulfone) and PSU (polysulfone). All of them are pure plastics, but PEEK is also available in the carbon-black grade, in



a lubricated reinforced bearing grade, or with 30% of glass-fibers.

Their chemical structures appear in Fig.1 below.

Figure 1: Chemical structures.



Their main physical properties appear in Table 1 [3]. Some of their thermal properties, such as CTE and thermal conductivity are comparable to the best epoxies. They are usually more sensitive to water absorption and moisture, especially PA 4.6 which is very sensitive.

### 3. Fire behaviour criteria and tests

At CERN, the requirements for fire safety are described in the Safety Code E and its appendices, among them, the Safety Instruction IS 23 and the Safety Note NS 11 [4, 5, 6]. The requirements and the

corresponding standards are summarized in another paper of this conference [7].

The UL rating and the limit of oxygen index (OI) appear in Table 1. The data about the toxicity and the corrosiveness of fire gases as well as the smoke density are general data for these types of materials, taken from [8], they are summarized below.

PA 4.6, as other polyamides, burn readily exhibiting dripping. Its use must be restricted in components where fire propagation is impossible because of confinement. Flame retardant grades are sometimes available but their smoke and toxic fume emission should be controlled before selection.

PEEK and PEI present good heat resistance and very good fire retardancy without resort to the use of additives. When involved in a fire, it emits low smoke and toxic and corrosive fume.

PES and PSU also present good heat resistance. PES is rated V-0 in the UL test, PSU is rated V-1 or HB that indicates a rather poor flame-propagation behaviour, even if both types of materials are difficult to ignite. When involved in a fire, they emit sulphur dioxide at high temperature.

## 4. Radiation-test methods

### 4.1. Irradiation conditions

The samples have been irradiated either in a cobalt source ( $^{60}\text{Co}$ ) at a dose rate of the order of 1 Gy/s, up to 1 MGy, or in a nuclear reactor at a dose rate of the order of 50 Gy/s up to 100 MGy. In both cases the irradiations took place in air, at temperatures between 15°C and 60°C which are well below the glass-transition temperatures of the materials.

PEEK and PA 4.6 have also been irradiated in the cobalt source at the same dose rate, but up to 7 MGy, in several times spread over a period of two years.

More details about the irradiation conditions can be found in [9].

### 4.2. IEC 544 Standard

The international recommendations for radiation damage tests are described in the IEC 544 standard, "Guide for determining the effects of ionizing radiation on insulating materials" [10]. As it has been observed that electrical breakdown of insulating materials is usually a consequence of severe mechanical deterioration (see e.g. [2]), the recommended test procedures for permanent effects are testing of mechanical properties, which in the case of structural materials is the only valid method.

The IEC standard recommends that flexible plastics (e.g. cable insulations) be submitted to tensile tests (according to ISO/R527 and ISO/R37) and that rigid plastics, including composites and prepregs, be submitted to flexural tests (ISO 178). IEC 544 recommends that these tests are carried out to rupture of the material: flexural strength and ultimate deformation are measured at the breaking point. This is an appropriate way for assessing the severe mechanical deterioration and the consequent electrical possible failure of an insulator.

In real life, the structural materials are never used up to their breaking point; the strain is usually limited to less than 1% (usually between 0.2% and 0.6%) to minimize long-term creeping (which may never be neglected for plastic materials). If stress and strain are limited, the modulus is often an important property to be considered for the behaviour of the material; the flexural modulus is calculated from the slope of the stress-strain curve at its origin.

IEC 544 recommends that the limit of usability of a material is the absorbed dose at which the critical property (the most sensitive one; often the flexural strength) is reduced to 50% of its initial value, and defines a radiation index (RI) as the logarithm (base 10) of this dose.

### 4.3. Mechanical tests at CERN and criteria

At CERN, the flexural tests are based on a three-point loading system carried out on an Instron 1026 machine, with a crosshead speed of 5 mm/min. It is known that the three-point loading test creates local stresses opposite to the central loading support, but as all samples are tested the same way, the observed reductions of properties are well representative of the degradation of the materials. More details about our test methods can be found in [9].

From the recorded load-displacement curves it is possible to calculate the stress-strain curves, the modulus of elasticity and to determine the limit of the pseudo-elastic region.

The flexural strength at maximum load, the ultimate deformation (at break), the limit of proportional deformation and the flexural modulus of elasticity are given in the results below (Table 2). They are defined as follow :

Flexural strength at maximum load :

$$\sigma_x = (3 \cdot L \cdot P_x) / (2 \cdot B \cdot T^2) \quad (\text{in MPa})$$

Flexural modulus of elasticity :

$$E = (L^3 \cdot F/Y) / (4 \cdot B \cdot T^3) \quad (\text{in MPa})$$

Ultimate deformation (at break) :

$$\epsilon_x = 6 \cdot D_x \cdot T / L^2 \quad (\text{in \%})$$

Limit of proportional deformation :

$$\epsilon_p = 6 \cdot D_p \cdot T / L^2 \quad (\text{in \%})$$

With, L the span length between the outer supports (= 67.065 mm),



Table 1 (continued): Main physical properties of the "High Performance Materials"

PROPERTIES	STANDARD	UNITS	PEEK	PA 4.6 (1)	PEI	PES	PSU
<b>MECHANICAL PROPERTIES at 23°C</b>							
Tensile test (6)	ISO						
- tensile stress at yield	R 527	N / mm <sup>2</sup>	95	100 / 55	105	85	70
- elongation at break (7)	R 527	%	> 25	25 / 100	> 50	> 25	> 50
- modulus of elasticity (8)	R 527	N / mm <sup>2</sup>	3600	3100 / 1500	3000	2700	2500
Flexural test:							
- modulus of elasticity	178	N / mm <sup>2</sup>	4100	-	3300	2800	2700
Compression test (9):	604	N / mm <sup>2</sup>	130	92	130	105	90
- 1%-offset yield strength (8)							
Tensile creep test:							
- stress to produce 1% elongation in 1.000 h							
( $\sigma_1/1.000$ ):- at 23°C	899	N / mm <sup>2</sup>	30	22 / 7.5	30	23	22
- at 60 / 100°C (dry)	899	N / mm <sup>2</sup>	26 / 22	14 / 9	23 / 18	19 / 17	18 / 14
- at 125 / 150°C(dry)	899	N / mm <sup>2</sup>	12 / 5	7 / 6.5	13 / 7	13 / 10	9 / 5
Impact strength - Charpy	179/2D	kJ / m <sup>2</sup>	-	no break	no break	no break	no break
Notched impact strength:- Charpy	179/2C	kJ / m <sup>2</sup>	6	20	4	4	4
- Izod	180/A	kJ/m <sup>2</sup> ; J/m	8 ; 80	25 ; 250	5 ; 50	5 ; 50	4 ; 40
Ball indentation hardness H 358/30 or H 961/30 (10)	2039-1	N / mm <sup>2</sup>	230	165	170	160	155
Rockwell hardness (10)	2039-2	-	M 105	M 92	M 114	M 104	M 91
<b>ELECTRICAL PROPERTIES at 23°C</b>							
Dielectric strength (11)	IEC	kV / mm	30	60 / 25	30	30	30
Volume resistivity	243	Ohm.cm	10 <sup>16</sup>	10 <sup>15</sup> / 10 <sup>13</sup>	10 <sup>16</sup>	10 <sup>16</sup>	10 <sup>16</sup>
Surface resistivity	93	Ohm	10 <sup>14</sup>	10 <sup>14</sup> / 10 <sup>12</sup>	10 <sup>14</sup>	10 <sup>14</sup>	10 <sup>14</sup>
Dielectric constant:- at 10 <sup>3</sup> Hz	250	-	3.3	4 / 10	3.2	3.6	3.1
- at 10 <sup>6</sup> Hz	250	-	3.3	3.8 / 4.3	3.1	3.6	3.1
Dissipation factor tan $\delta$ :- at 10 <sup>3</sup> Hz	250	-	0.003	0.013 / 0.3	0.001	0.002	0.001
- at 10 <sup>6</sup> Hz	250	-	0.003	0.012 / 0.15	0.006	0.011	0.005
Resistance to tracking	112	-	CTI 150	CTI 425	CTI 150	CTI 150	CTI 150
Note:							
1 N / mm <sup>2</sup> = 1 MPa	(6) test samples of type 1 (ISO)						
1 kV / mm = 1 MV / m	(7) test speed = 5 mm / min						
	(8) test speed = 1 mm / min						
	(9) test samples: cylinders Ø 12 x 30 mm						
	(10) test samples 10 mm thick						
	(11) electrodes P25/P75 on 1 mm thick samples						

- B the width of the test piece (= 10 mm),  
 T the thickness of the test piece  
 (=  $5.04 \pm 0.05$  mm),  
 P<sub>x</sub> the maximum load (N),  
 F/Y the slope of the load–displacement  
 curve in its early linear region,  
 D<sub>x</sub> the deflexion at break (mm),  
 D<sub>p</sub> the limit of proportional deflexion (mm),

Note that for technical reasons, the maximum deflexion, in the flexural cage, is 23 mm, the corresponding ultimate deformation is 15 %. The radiation indices will be calculated on the base of the reduction of the flexural strength at break and of the reduction of the deformation at break; the value to be taken for the limit of usability is the most restrictive one.

## 5. Radiation test results

### 5.1. Flexural test results

The variation of the mechanical properties with dose appears in the tables and graphs in appendix, they are summarized in Table 2 for the five selected materials. Two values of the radiation index are given for each material: one based on the reduction of the ultimate flexural strength, the other one based on the reduction of the ultimate deformation; the latter is the lowest one (based on the most sensitive property), it is the value to be considered for the limit of usability of the materials.

### 5.2. Tensile tests on PEEK film

Insulating films made of PEEK (not supplied by ERTA), of 130 and 25 micrometre thicknesses, have been submitted to tensile tests (according to ISO R37, which is not the appropriate standard for films, but which can be used to observe the radiation degradation). After irradiation in the nuclear reactor, it appears that the films are more degraded than the bulk material; the degradation is even more pronounced for the 25 micrometre film which suggest an oxidative effect; RI = 6.8 (see in appendix).

### 5.3. Long-term irradiation

After the long-term irradiations up to 7 MGy, one sample of PEEK has been tested and show no degradation. The four samples of PA 4.6 have been

tested; the results show that it is heavily degraded (see the results with an asterisk in Table 2).

### 5.4. Mechanical tests at low temperature

It is known that the flexibility of the polymers is reduced at cryogenic temperature; their modulus as well as their strength increase slightly or significantly, their ultimate strain as well as their impact resistance decrease. A literature survey has shown that the reduction of the mechanical properties with irradiation is about the same whether the material has been irradiated at room temperature or at cryogenic [11]. For example, Spindel et al. found that the strength and modulus of PEEK and PEI increase sensibly at cryogenic temperature (4 K), and that the irradiation up to 10 MGy still increases these values [12]. ERTA materials, PEI, PES and PSU have been included in a radiation test programme carried out at low temperature (77 K) at the Atominstitut der Österreichischen Universitäten [13]; the same behaviour has been observed, their ultimate deformation prior to irradiation is of the order of 5%. Regarding their ultimate deformation, PES and PSU have an RI of 6.3 which is higher than after a room-temperature irradiation.

The 130 micrometre film has also been included in the same programme. Its ultimate elongation prior to irradiation is of the order of 6%, and is unchanged up to 60 MGy. This confirms that PEEK is prevented from radio-oxidative degradation when irradiated in liquid nitrogen.

## 6. Discussion and conclusion

### 6.1. Validity of the tests

As said in 4.2., if stress and strain are limited, the modulus of elasticity and the limit of the pseudo-elastic region (quasi-proportional) are important properties to be considered for the behaviour of the material. The radiation test results show that these properties are almost not affected by radiation.

On the other hand, the decrease of the flexural strength and of the ultimate deformation are representative of the degradation of the material), the ultimate flexibility is always the critical parameter.

Ageing of polymers, due to time–temperature degradation as well as other environmental factors such as radiation combined with fatigue, appears as a change in the fracture mode, from ductile to fragile.

Table 2 : Variation of mechanical properties of High Performance Plastics

TIS No	Trade name	Dose (MGy)	Strength (MPa)	Deformation (%) at break	prop. (%)	Modulus (GPa)
520	<b>Erta PEEK</b>	0.0	177	> 15	2.4	4.3
		5.0	179	> 15	2.9	4.1
		7.0*	187	> 15	1.6	3.0
		10.	161	11.6	2.7	4.2
		50.	111	3.8	1.5	4.3
		100.	143	5.8	1.9	4.2
		<b>RI</b>	<b>&gt; 8.0</b>	<b>7.0</b>		
526	<b>Ertalon 4.6</b>	0.0	126	3.7	1.2	5.8
		3.0	133	3.4	1.6	5.9
		7.0*	50	1.2	1.0	3.0
		10.	64	1.4	1.5	3.7
		50.	33	1.5	1.0	1.9
		<b>RI</b>	<b>7.0</b>	<b>6.8</b>		
533	<b>Erta PEI</b>	0.0	171	> 15	2.1	3.1
		1.0	174	> 15	2.0	3.2
		3.0	179	> 15	2.1	3.3
		10.0	158	10.9	1.2	3.2
		50.0	102	3.3	2.2	3.3
		<b>RI</b>	<b>&gt; 7.7</b>	<b>7.0</b>		
534	<b>Erta PES</b>	0.0	141	> 15	2.9	2.7
		0.5	134	> 15	1.9	2.8
		1.0	132	11.7	2.0	2.9
		3.2	47	1.7	1.6	3.1
		10.0	14	0.5	0.4	3.3
		<b>RI</b>	<b>6.3</b>	<b>6.0</b>		
535	<b>Erta PSU</b>	0.0	120	> 15	2.1	2.6
		0.5	114	> 15	1.9	2.7
		1.0	102	9.6	1.8	2.8
		3.2	58	2.1	2.0	3.0
		10.0	19	0.7	0.6	3.0
		<b>RI</b>	<b>6.4</b>	<b>5.9</b>		

\* long-term irradiations

The measurement of the ultimate properties as done in the tests recommended by the IEC 544 standard is representative of the transition in this rupture mode

and hence of real ageing of the material. Therefore, the reduction of one of these properties is a valid base for the limit of usability.

## 6.2. Cryogenic behaviour under radiation

At cryogenic temperature, polymers are not ductile and their fracture always occurs in the fragile mode. Irradiation at constant low temperature does not increase the degradation compared to a room temperature irradiation, the presence of the cryogenic fluid even impedes the radio-oxidative degradation.

## 6.3. Long-term behaviour under radiation

As other polyamides, PA 4.6 is sensitive to radio-oxidative degradation and to moisture. Its fire behaviour characteristics prohibit its use in places where fire propagation presents a danger. All of this restricts the use of this high-performance thermoplastic in confined vessels without oxygen and where the atmosphere is controlled.

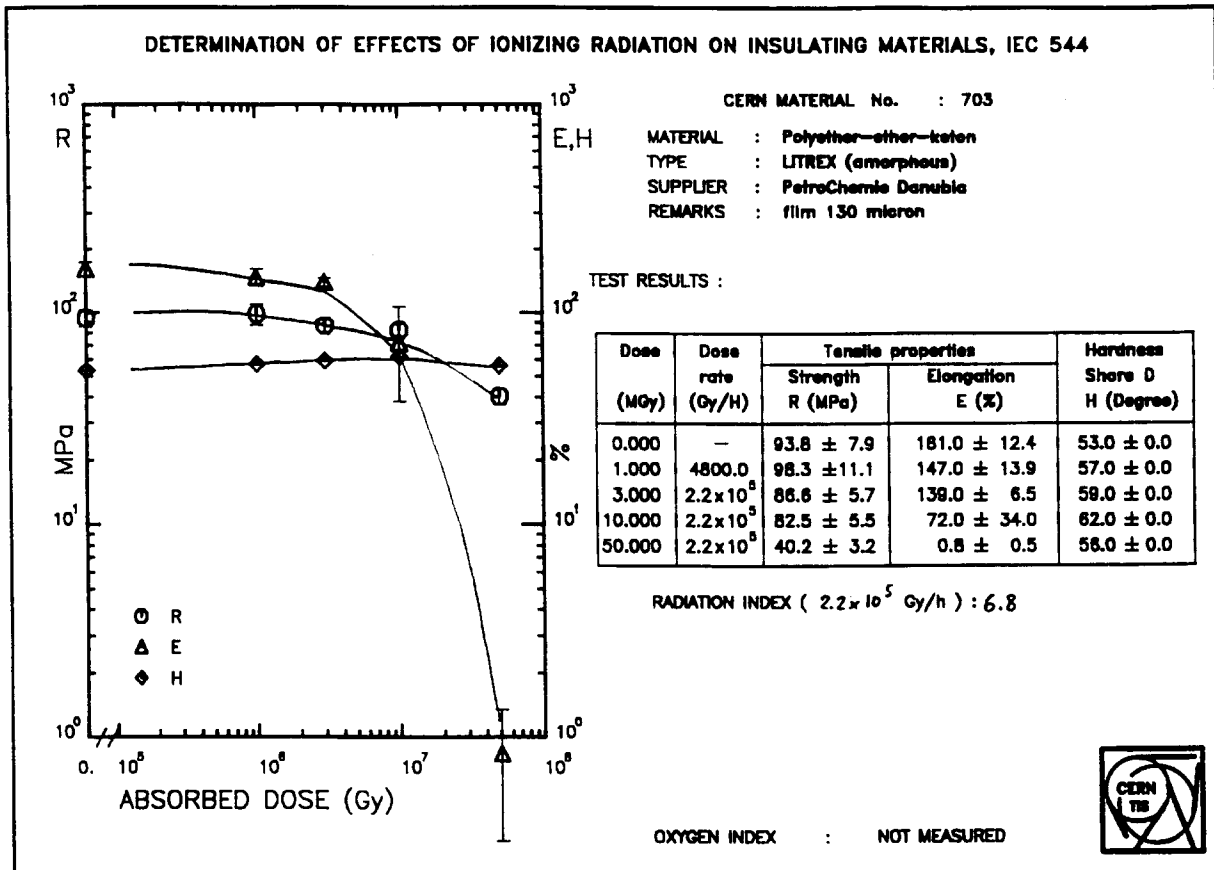
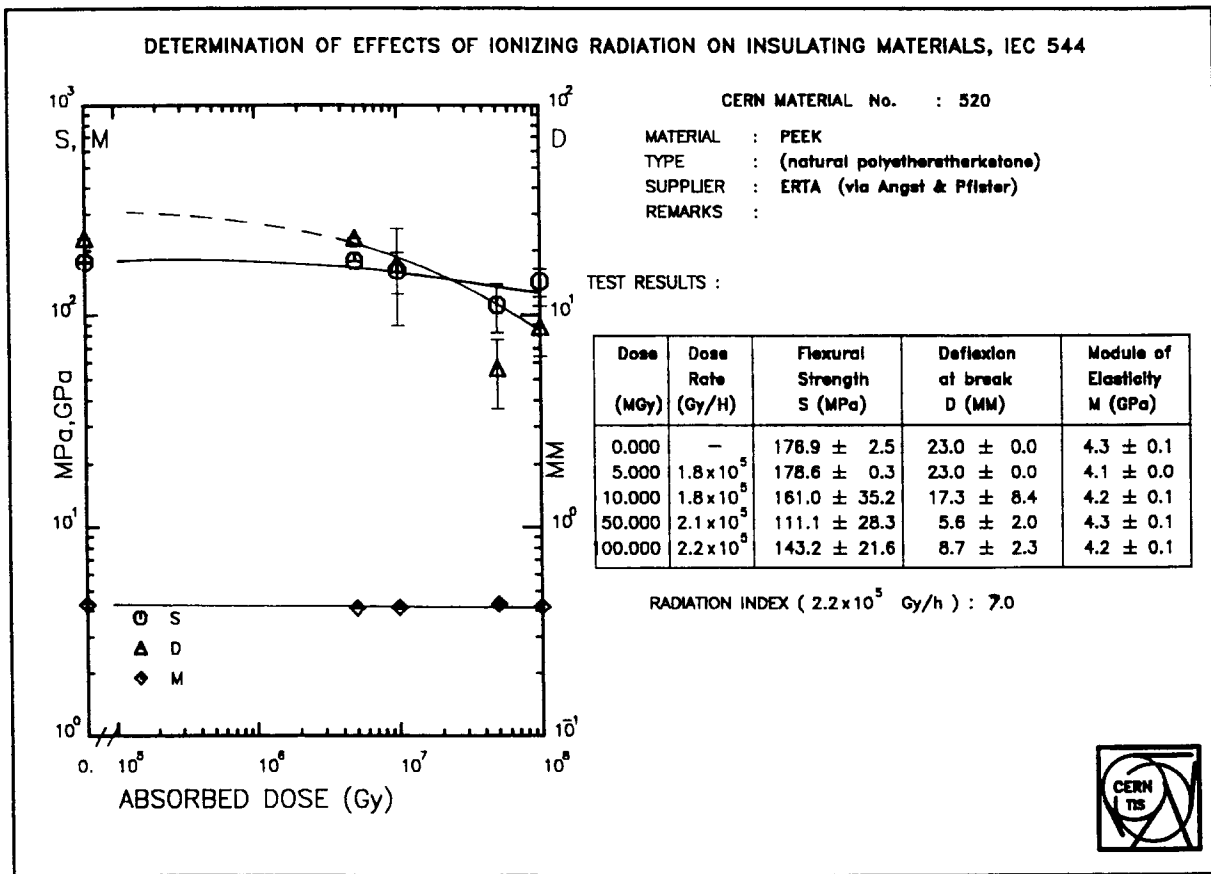
## 6.4. Ranking

The results show that the modulus and the limit of elasticity are usually not affected by radiation, the flexural strength is slightly affected, the deformation at break is the critical property.

The results also allow to sort the materials from the most resistant one to the most sensitive one: PEEK, PEI, PA 4.6, PSU and PES.

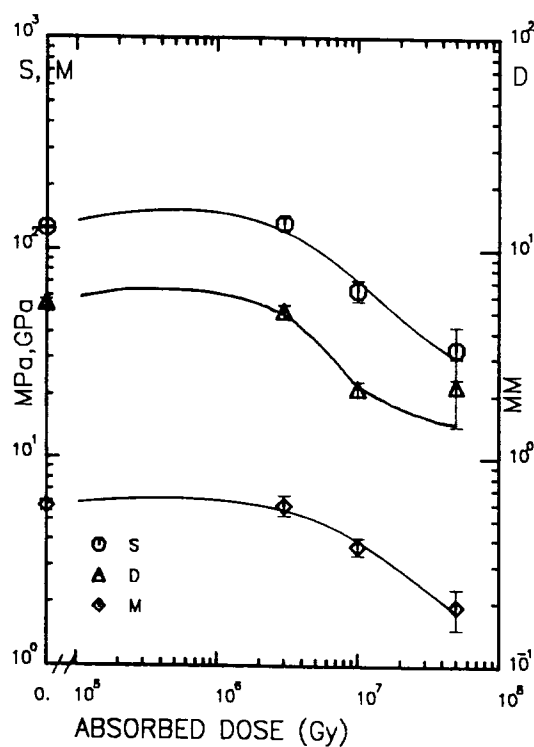
## References

1. H. Schönbacher et al.: Compilation of radiation damage test data; Part I: Cable insulating materials, CERN 79-04, 2nd ed.: Halogen-free cable-insulating materials, CERN 89-12, Part II: Thermosetting and thermoplastic resins, CERN 79-08, Part III: Materials used around high-energy accelerators, CERN 82-10.
2. G. Lipták et al.: Radiation tests on selected electrical insulating materials for high-power and high voltage applications. CERN 85-02
3. ERTA, Delivery Programme of Engineering Plastics (1991)
4. CERN, Safety Code E; Fire Protection. (1991)
5. CERN, Safety Instruction IS 23 Rev.; Criteria for the selection of electrical cables and equipment with respect to fire safety and radiation resistance. (1992)
6. CERN, Safety Note NS 11; Recommendations on the use of plastic and synthetic materials in areas where the products of combustion in a fire may cause material damage or threaten life or health of affected persons. (1986)
7. H. Schönbacher and M. Tavlet: Radiation effects on detectors structural materials. (this conference)
8. J. Troitzsch: International Plastics Flammability Handbook, Hanser Publishers, NY, USA (1993)
9. G-P. Tartaglia and P. Beynel: Radiation damage to insulation materials; test and data evaluation procedures following IEC Standard 544. CERN/TIS-RP/180 (1986)
10. IEC 544, four parts; I : Radiation interaction (1977), II : Procedures for irradiation (1979), III : Test procedures for permanent effects (1979) IV : Classification system for service environments (1985)
11. P. Suva and M. Tavlet: Review of radiation tests on polymers at cryogenic temperatures. CERN/TIS-CFM/IR/94-04 (1994)
12. A. Spindel: Report on the program of 4 K irradiation of insulating materials for the SSC. SSCL-635 (1993)
13. H. W. Weber: Low-temperature neutron and gamma irradiation of plastics: influence on their mechanical properties at 77 K. Wien, May 31, 1994





## DETERMINATION OF EFFECTS OF IONIZING RADIATION ON INSULATING MATERIALS, IEC 544



CERN MATERIAL No. : 526

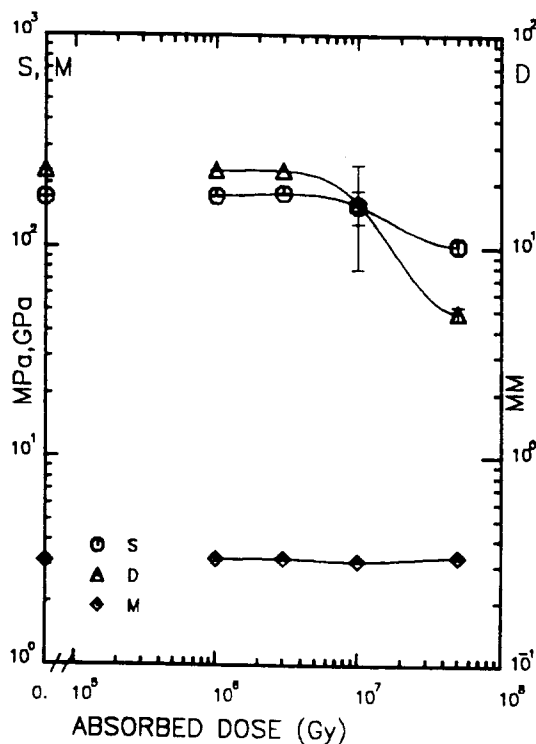
MATERIAL : Polyamide 4.6  
 TYPE : Ertalon 4.6  
 SUPPLIER : ERTA (via A & P)  
 REMARKS : = Stanyl by DSM

## TEST RESULTS :

Dose (MGy)	Dose Rate (Gy/h)	Flexural Strength S (MPa)	Deflexion at break D (MM)	Module of Elasticity M (GPa)
0.000	—	128.1 ± 1.4	5.5 ± 0.2	5.8 ± 0.3
3.000	2.4 × 10 <sup>5</sup>	133.1 ± 8.9	5.0 ± 0.4	5.9 ± 0.7
7.000	1000.0	50.4 ± 5.8	1.9 ± 0.2	3.0 ± 0.1
10.000	2.1 × 10 <sup>5</sup>	64.0 ± 7.5	2.1 ± 0.2	3.7 ± 0.4
50.000	2.1 × 10 <sup>5</sup>	33.3 ± 9.4	2.2 ± 0.8	1.9 ± 0.4

RADIATION INDEX ( 2.4 × 10<sup>5</sup> Gy/h ) : 6.8

## DETERMINATION OF EFFECTS OF IONIZING RADIATION ON INSULATING MATERIALS, IEC 544



CERN MATERIAL No. : 533

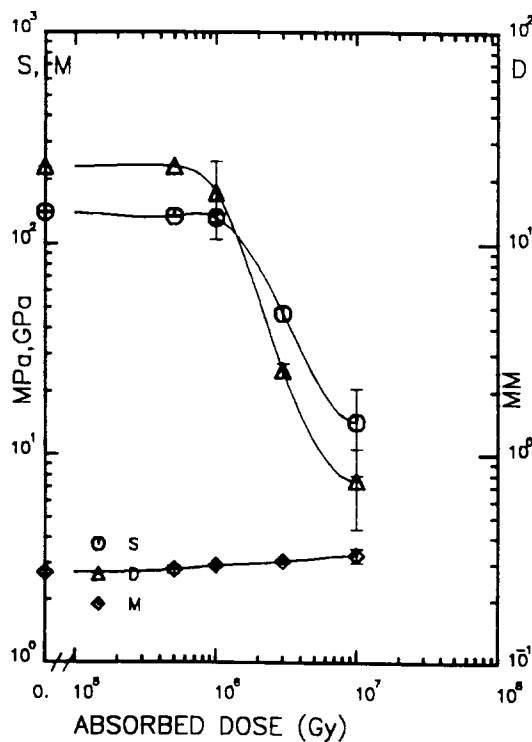
MATERIAL : Polyetherimide  
 TYPE : Ertal PEI  
 SUPPLIER : ERTA  
 REMARKS : based on Ultem 1000

## TEST RESULTS :

Dose (MGy)	Dose Rate (Gy/h)	Flexural Strength S (MPa)	Deflexion at break D (MM)	Module of Elasticity M (GPa)
0.000	—	171.0 ± 1.2	23.0 ± 0.0	3.1 ± 0.1
1.000	4000.0	174.1 ± 1.5	23.0 ± 0.0	3.2 ± 0.1
3.000	2.2 × 10 <sup>5</sup>	179.2 ± 1.2	23.0 ± 0.0	3.3 ± 0.1
10.000	2.2 × 10 <sup>5</sup>	157.9 ± 28.6	16.2 ± 8.4	3.2 ± 0.0
50.000	2.2 × 10 <sup>5</sup>	101.8 ± 6.8	4.9 ± 0.4	3.3 ± 0.0

RADIATION INDEX ( 2.2 × 10<sup>5</sup> Gy/h ) : 7.0

## DETERMINATION OF EFFECTS OF IONIZING RADIATION ON INSULATING MATERIALS, IEC 544



CERN MATERIAL No. : 534

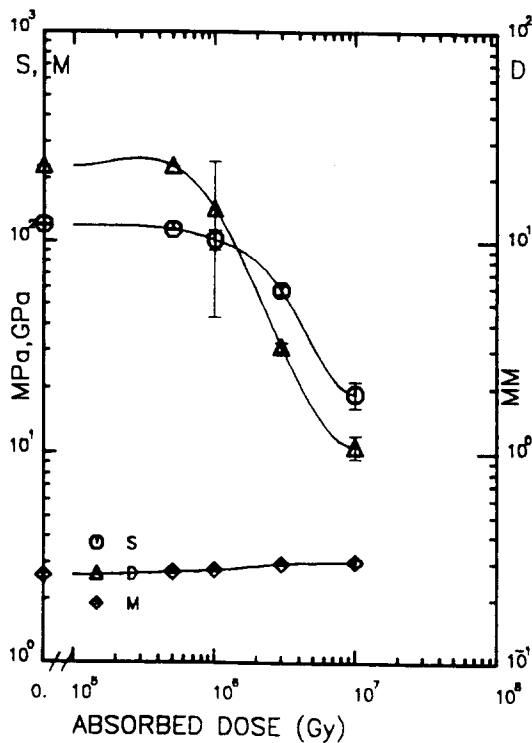
MATERIAL : Polyethersulfone  
 TYPE : Ertal PES  
 SUPPLIER : ERTA  
 REMARKS : based on Victrex

## TEST RESULTS :

Dose (MGy)	Dose Rate (Gy/h)	Flexural Strength S (MPa)	Deflection at break D (MM)	Module of Elasticity M (GPa)
0.000	—	140.7 ± 1.4	23.0 ± 0.0	2.7 ± 0.0
0.500	4000.0	134.4 ± 0.8	23.0 ± 0.0	2.8 ± 0.1
1.000	4000.0	132.0 ± 5.5	17.4 ± 6.9	2.9 ± 0.1
3.000	2.2 × 10 <sup>5</sup>	46.8 ± 3.4	2.5 ± 0.2	3.1 ± 0.1
10.000	2.2 × 10 <sup>5</sup>	14.3 ± 6.3	0.7 ± 0.3	3.3 ± 0.3

RADIATION INDEX ( 1.1 × 10<sup>5</sup> Gy/h ) : 6.0

## DETERMINATION OF EFFECTS OF IONIZING RADIATION ON INSULATING MATERIALS, IEC 544



CERN MATERIAL No. : 535

MATERIAL : Polysulfone  
 TYPE : Ertal PSU  
 SUPPLIER : ERTA  
 REMARKS : based on Udel P 3500

## TEST RESULTS :

Dose (MGy)	Dose Rate (Gy/h)	Flexural Strength S (MPa)	Deflection at break D (MM)	Module of Elasticity M (GPa)
0.000	—	120.1 ± 0.8	23.0 ± 0.0	2.6 ± 0.1
0.500	4000.0	113.9 ± 0.9	23.0 ± 0.0	2.7 ± 0.0
1.000	4000.0	101.6 ± 11.4	14.3 ± 10.0	2.8 ± 0.0
3.000	2.2 × 10 <sup>5</sup>	58.2 ± 2.5	3.1 ± 0.1	3.0 ± 0.0
10.000	2.2 × 10 <sup>5</sup>	18.8 ± 2.6	1.1 ± 0.1	3.0 ± 0.1

RADIATION INDEX ( 1.1 × 10<sup>5</sup> Gy/h ) : 5.9

# Influence of Processing Parameters on the Dimensional Stability of Polymer Composites

Richard Phillips, Patrick Kim, Paul Sunderland, Jan-Anders E. Månson

Laboratoire de Technologie des Composites et Polymères  
Ecole Polytechnique Fédérale de Lausanne,  
CH-1015 LAUSANNE,  
Switzerland

## ABSTRACT

The prediction of internal stresses and of post-moulding warping is crucial to the design of dimensionally-stable thermoplastic composite parts. In this study the warping caused by internal stresses resulting from thermal effects within a part during cooling has been studied. Balanced and unbalanced cooling profiles were applied to unidirectional composite plates based on amorphous and semi-crystalline thermoplastic matrices; asymmetric cross-ply laminates with an amorphous thermoplastic matrix were also studied. Experimental results show that the dimensional stability is dependent upon the cooling rate, and is strongly governed by the viscoelastic behaviour of the composite. A numerical model based on a linear thermoviscoelastic formulation has been developed to calculate the internal stress build-up during cooling. Results obtained by this modelling approach correlate well with the experiments.

## 1) INTRODUCTION

The conditions under which polymer composites are processed strongly influence the morphology and the final properties of manufactured components. This is particularly true for internal stresses. These stresses are inherent to almost all processes used for the transformation of polymers and polymer composites. Many advanced production techniques involve strongly non-isothermal conditions, high thermal gradients, unbalanced cooling profiles and high pressure gradients. Advanced processes running at high production rates impose more severe conditions upon the material and thus lead to a greater likelihood of internal stresses.

Internal stress generation in composites is governed in part by the intrinsic material properties, which are inherently viscoelastic, heterogeneous and anisotropic [1-3]. Whereas these stresses are not necessarily detrimental, their presence is most often noticed as a source of

defects such as warping, voids and micro-cracks.

This study focuses on thermally-generated internal stresses and their effect on the dimensional stability of a part after demoulding. Two factors influencing stress generation have been examined: cooling rate and cooling profile across the part thickness. A numerical model has been developed in parallel with an experimental programme, with the aim of providing a predictive capacity for stress and warping effects.

## 2) EXPERIMENTS

### 2.1) Materials and sample preparation

Two materials were used in this study: APC2/AS4 (PEEK/carbon fibre, ICI-Fiberite), a semi-crystalline matrix with a fibre volume fraction of 61%, and PEI/glass fibre (TenCate), an amorphous matrix containing 52% glass fibres

(GF) by volume. Both prepregs contained unidirectional fibres.

Samples were consolidated with negligible resin flow in a 70x70mm matched-die mould on an instrumented press. The prepregs were heated in the mould. Table 1 shows consolidation parameters; temperatures were monitored by two K-type thermocouples, one placed on each surface of the sample.

**Table 1: Consolidation parameters**

	APC2/AS4	PEI/GF
Temperature (°C)	400	330
Time (min)	1	2
Pressure (bar)	40	40

## 2.2) Influence of cooling rate on dimensional stability

The influence of the cooling rate was investigated on specimens of PEI/GF, since with the amorphous matrix crystallisation effects can be avoided. To amplify the effect of cooling rate, experiments were performed on an asymmetric  $[0_5, 90_{15}]$  laminate. After consolidation, the laminates were cooled slowly in the mould and cut into 10mm-wide beams, which were then heated to 230°C in an oven. At this temperature the sections can be considered to be stress-free. The beams were then cooled at three different cooling rates; **rapid** (quenched in an ice/water bath), **medium** (cooled in air) and **slow** (cooled in an oven).

## 2.3) Influence of cooling profile on dimensional stability

The effect of cooling profile across the thickness of  $[0]_{20}$  UD laminates of both materials was studied. After consolidation according to the conditions shown in Table 1, two cooling conditions were applied: unbalanced, where the two mould halves were subjected to different cooling rates, one medium and one slow, and balanced, where the cooling rate in the two mould halves was the same.

## 2.4) Curvature determination

The curvature of the parts was measured indirectly with a dial test indicator, as Figure 1 shows. The measured deflection  $d$  was converted to the curvature  $\kappa$  using Equation (1).

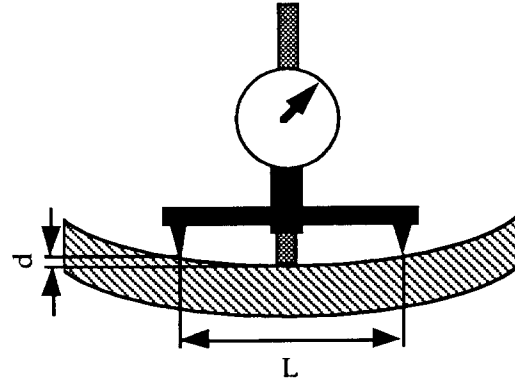


**Figure 1: Experimental apparatus for curvature determination**

$$\kappa = \frac{8d}{L^2 + 4d^2} \quad (1)$$

## 2.5) Properties for modelling

### a) Coefficient of thermal expansion

The coefficient of thermal expansion (CTE) is determinant in the calculation of the thermally-induced strain. In a unidirectional composite it is dependant upon fibre orientation. The CTE transverse and parallel to the fibres as a function of temperature were determined by thermomechanical analysis (Perkin Elmer TMA7).

### b) Thermoelastic properties

Thermoelastic properties were measured using a dynamic torsion rheometer (RDA2, Rheometrics Inc.) on rectangular prism samples for the shear modulus, and with a dynamic solids analyser (RSA2, Rheometrics Inc.) in three point bending for the tensile modulus. Longitudinal and transverse properties were measured as a function of temperature at a frequency of 1Hz, at which frequency the storage modulus corresponds to the steady-state modulus [4].

### c) Relaxation behaviour

For the viscoelastic relaxation behaviour of PEI/GF, the relaxed and unrelaxed shear and tensile moduli were determined as a function of temperature from relaxation tests performed at a range of temperatures in rectangular torsion for the shear modulus and in three point bending for the tensile modulus.

### 3) RESULTS OF EXPERIMENTS

#### 3.1) Influence of the cooling rate

Figure 2 shows the evolution of the temperature as a function of time at the surface of the sample for the three cooling rates. The difference in the coefficient of thermal expansion between the 0° and 90° layers induces warping. Table 2 gives the induced curvatures.

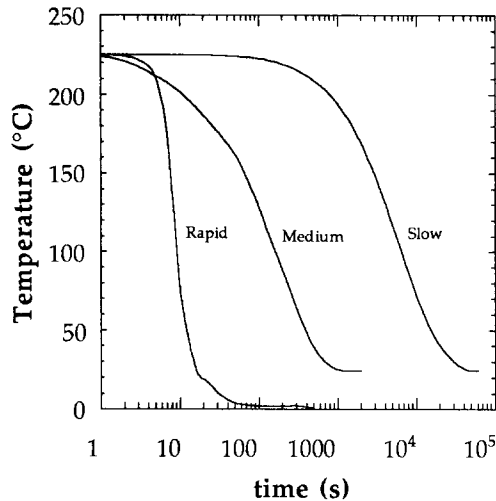


Figure 2: Temperature evolution as a function of time at the surface of a sample

Table 2: Curvature of PEI/GF [0<sub>5</sub>,90<sub>15</sub>] as a function of cooling rate

	Rapid	Medium	Slow
Curvature [10 <sup>-3</sup> mm <sup>-1</sup> ]	2.1	1.6	1.4

#### 3.2) Influence of the cooling profile

Figure 3 shows the temperature evolution at the surface of a sample as a function of time for the two cooling profiles for PEI/GF. The curves for APC2 were qualitatively similar, the initial temperature being 400°C and the time to cool to ambient temperature 2700 seconds.

The curvatures induced by the cooling profile are listed in Table 3.

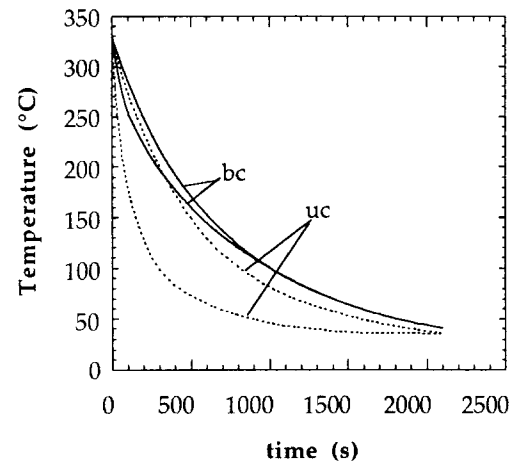


Figure 3: Temperature evolution on the surfaces of PEI/GF samples as a function of time for balanced (bc) and unbalanced (uc) cooling

Table 3: Curvature of PEI/GF and APC2 as a function of the cooling profile

	PEI/GF bc	PEI/GF uc	APC2 bc	APC2 uc
Curvature [10 <sup>-3</sup> mm <sup>-1</sup> ]	0.17	0.81	0.24	2.4

### 4) ANALYSIS OF DIMENSIONAL STABILITY

Short-term dimensional instabilities occur as internal stresses built up during cool-down are relieved upon demoulding [1,3]. If the internal stress distribution inside the part just before demoulding is known, the unconstrained warping can be predicted [2].

Internal stresses which develop during processing may originate from the thermal conditions and from the polymer structure, so the temperature distribution and the mechanical properties as a function of time and of the three spatial co-ordinates must be known. Heat transfer during the processing of composite parts can be modelled using the heat equation, expressed as:

$$\frac{\partial}{\partial t}(\rho C_p T) = \text{div} \left[ k_{th} \cdot \left( \frac{\partial T}{\partial x} + \frac{\partial T}{\partial y} + \frac{\partial T}{\partial z} \right) \right] + \dot{Q} \quad (2)$$

For a semi-crystalline matrix the heat generated by crystallisation is denoted by the

source term  $\dot{Q}$ . Knowing the temperature distribution through the part as a function of time, the thermally-induced internal stresses can be predicted with the expression [2,3]:

$$\underline{\sigma} = \int_0^t \underline{K}(T(\tau)) \frac{\partial}{\partial \tau} (\underline{\varepsilon} - \underline{\varepsilon}^{th} - \underline{\varepsilon}^{cr}) \partial \tau \quad (3)$$

where  $\underline{K}$  is the stiffness matrix,  $\underline{\varepsilon}$  is the vector of the effective deformation of the part and  $\underline{\varepsilon}^{th}$  and  $\underline{\varepsilon}^{cr}$  are the vectors of the thermal and morphological contractions. The morphological contraction occurs as a result of the crystallisation of the matrix.

Several relations exist in the literature to predict viscoelastic behaviour [4,5]. In this work, the viscoelastic effect is taken into account by using a Prony series expansion of the relaxation modulus,

$$K_{ij}(t, T) = K_{ij}^0 \sum_{i=1}^n k_i \exp\left(-\frac{t}{\tau(T)_i}\right) \quad (4)$$

where  $K_{ij}^0$  is the unrelaxed mechanical property,  $k_i$  is a weight factor and  $\tau_i$  is the relaxation time. This expression is used for the matrix  $\underline{K}$  of Equation (3).

The thermal strain is calculated using the following relation:

$$\varepsilon^{th}(x, y, z, t) = \int_0^t \alpha(x, y, z, T(\tau)) \frac{\partial T(x, y, z, \tau)}{\partial \tau} \partial \tau \quad (5)$$

where  $\alpha$  is the coefficient of thermal expansion.

The influence of fibre orientation on the generation of internal stresses is expressed in the variation of mechanical and thermal expansion properties as a function of the three spatial variables.

## 5) NUMERICAL MODEL - METHOD

Based on these governing equations, the stress distribution and deformation within the part after processing were calculated by the method of finite elements (FEM) using ABAQUS.

For the study of the influence of cooling rate, a purely thermoelastic analysis was also carried out for the purpose of comparison with

the thermoviscoelastic approach. For the study of the influence of the cooling profile, where both materials were modelled, only a thermoelastic approach was adopted, as APC2 is particularly difficult to treat thermoviscoelastically.

The numerical model is two-dimensional and the materials are considered as isotropic in the stress-deformation analysis. The tensile and shear moduli are linked through the relation:

$$G = \frac{E}{2(1 + \nu)} \quad (6)$$

where  $\nu$  is Poisson's ratio and can be calculated from this expression; for the thermoelastic case  $G$  and  $E$  are known from measurements, and for the thermoviscoelastic analysis, the unrelaxed shear and tensile moduli,  $G$  and  $E$ , are used.

For a 2D isotropic layer, where the index 2 refers to the thickness direction, a plane strain model is used. This assumption is acceptable as long as  $\sigma_{11} \gg \sigma_{22}$ , which is the case here, as the material is free to contract across the thickness, whereas appreciable stresses build up in the longitudinal direction because of the constraining effect of adjacent plies.

### 5.1 Influence of the cooling rate

The thickness of the layers in the  $[0_5, 90_{15}]$  PEI/GF laminate were found to be 0.8mm ( $0^\circ$ ) and 2.4mm ( $90^\circ$ ) by optical microscopy. The mesh used for the numerical analysis is shown in Figure 4. Only half of the length of the sample was modelled, AB being the axis of symmetry. The same mesh of four-node, isoparametric linear elements was used for the thermal and for the stress-deformation analyses. During the heat transfer analysis, the evolution of temperature for each cooling rate was applied as a boundary condition on both top and bottom faces.

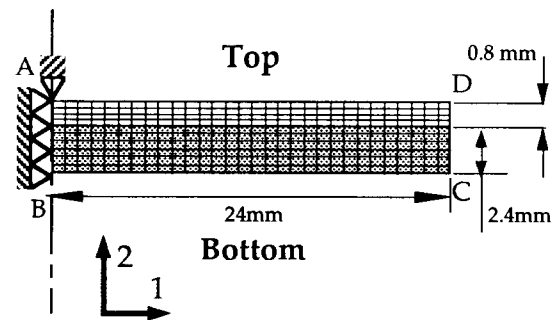


Figure 4: Mesh for PEI/GF  $[0_5, 90_{15}]$  laminate

As shown in Figure 4, symmetry boundary conditions were applied to nodes on the edge AB while node A was fully constrained. This corresponds to a beam free to deform during cooling.

Micromechanics were used to determine the thermal properties of the PEI/GF composite, based on the properties of each constituent [6]. Table 4 shows the values obtained.

**Table 4: Thermal properties**

	PEI/GF	APC2/AS4
Density ( $\text{kg}\cdot\text{m}^{-3}$ )	1878	1600
Specific heat ( $\text{J}\cdot\text{kg}^{-1}\cdot\text{K}$ )	2096	1700
Transverse conductivity ( $\text{W}\cdot\text{m}^{-1}\cdot\text{K}^{-1}$ )	0.364	0.7
Longitudinal conductivity ( $\text{W}\cdot\text{m}^{-1}\cdot\text{K}^{-1}$ )	0.61	5.9

For the thermoviscoelastic analysis, the relaxation behaviour was expressed by Equation (4), the values of the unrelaxed tensile modulus and of the relaxation times at 215°C being as listed in Table 5.

**Table 5: Parameters for Equation (4) for PEI/GF at 215°C**

	Transverse	Longitudinal
E (GPa)	8.87	45.1
$k_1$ (-)	0.1463	0.08
$k_2$ (-)	0.3592	0.19
$k_3$ (-)	0.4794	0.27
$\tau_1$ (s)	0.013	0.013
$\tau_2$ (s)	0.277	0.277
$\tau_3$ (s)	3	3

The relaxation time was expressed as a function of temperature by:

$$\tau_i(T) = \tau_i(T_g) 10^{a(T)} \quad (7)$$

where  $\tau_i(T_g)$  is the  $i$ th relaxation time at the glass transition temperature and  $a(T)$  the shift factor. From the relaxation times derived from measurements, the shift factor  $a(T)$  is:

$$a(T) = \log_{10} \left[ 1.33 \cdot 10^{33} \exp(-0.359T) \right] \quad (8)$$

## 5.2) Influence of the cooling profile

$[0_{20}]$  laminates of thickness 3.2mm (PEI/GF) and 2.8mm (APC2/AS4) were modelled. The mesh used for this analysis is shown in Figure 5; half of the length of the sample was modelled, AB being the axis of symmetry.

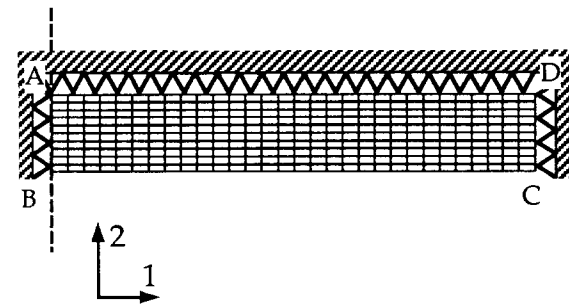


**Figure 5: Mesh for  $[0_{20}]$  laminates of PEI/GF and APC2**

The heat transfer and stress-deformation analyses were performed as in the previous section, with the temperature profiles as shown in Figure 3 as the boundary conditions.

The stress-deformation analysis was performed in two steps. Firstly, for the analysis of the cooling of the laminate inside the mould, the boundary conditions were defined as in Figure 5, where on AB and CD no longitudinal motion is allowed and on AD no motion in the thickness direction is allowed. The boundary condition on CD was set to avoid an edge effect, so the stresses vary only across the thickness. For the second step, demoulding of the part, the conditions on AD and CD were removed while node A was kept fully constrained.

## 6) NUMERICAL MODEL - RESULTS

### 6.1) Influence of cooling rate

The curvature obtained by both thermoelastic and thermoviscoelastic analyses is compared with the experimental curvature as a function of cooling rate in Figure 6. Figure 7 shows the residual stresses within the warped

part after demoulding, calculated as a function of cooling history.

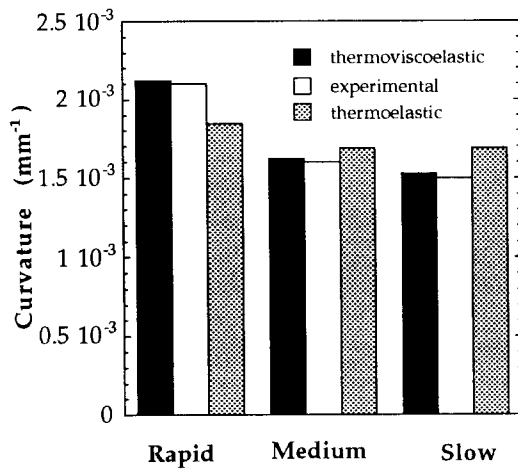


Figure 6: Calculated and experimental curvature of  $[0_5, 90_{15}]$  PEI/GF as a function of cooling rate

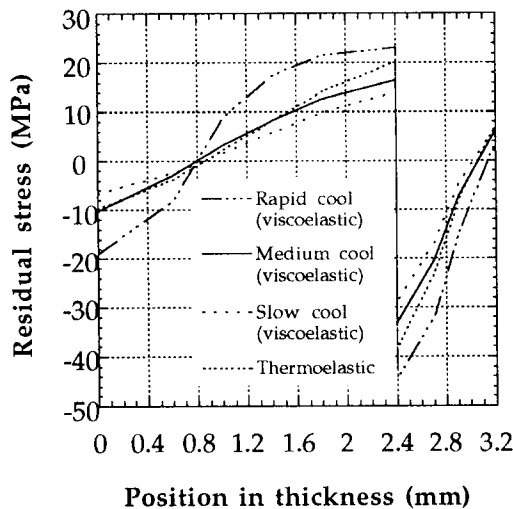


Figure 7: Calculated residual stresses in  $[0_5, 90_{15}]$  PEI/GF as a function of cooling rate

## 6.2) Influence of cooling profile

The curvature obtained by numerical analysis for PEI/GF is compared with the experimental curvature as a function of cooling profile in Figure 8.

According to other authors [1,7], the stress-deformation analysis of PEI/GF should begin once all the plies have cooled below the glass transition temperature. For APC2, the starting point of stress build-up is less obvious, and in the

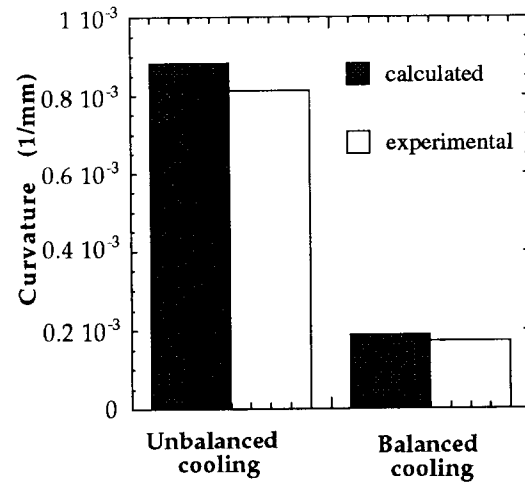


Figure 8: Calculated and experimental curvature of  $[0_{20}]$  PEI/GF as a function of cooling profile

literature several different opinions exist [1,8]. In this study, analysis of APC2 was begun once all plies had solidified. With the aid of a crystallisation kinetics model, the end of solidification was found to be around 285°C. In this way the contraction due to morphological effects is not taken into account.

The curvature obtained by FEM analysis for APC2 is compared with the experimentally observed curvature in Figure 9.

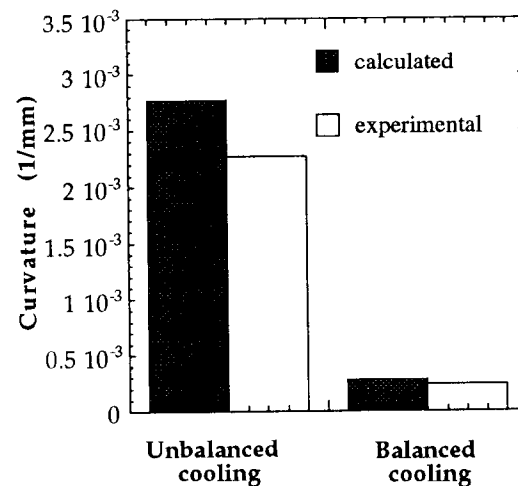


Figure 9: Calculated and experimental curvature of  $[0_{20}]$  APC2 as a function of cooling profile



## 7) DISCUSSION

### 7.1) Influence of the cooling rate

As is clearly shown in Figure 6, the amplitude of the warping increases with the cooling rate. As the cooling rate increases, the transition between viscous and elastic behaviour (marked by a sharp increase of the modulus) is shifted towards higher temperatures, and the time available for relaxation decreases. This phenomenon is represented schematically in Figure 10, where the transverse modulus is plotted as a function of temperature for different cooling rates. In the thermoelastic approach, the transition between viscous and elastic behaviour is independent of the cooling rate. As a consequence, the thermoelastic approach will not calculate correct values for the deformation and for the stress distribution. This phenomenon is clearly in evidence in Figures 6 and 7. At a high cooling rate the curvature is underestimated and at a low cooling rate the curvature is overestimated. Introducing viscoelastic relaxation into the calculations allows a better prediction of the experimental curvatures. It appears that too rapid a cooling rate must be avoided if stress relaxation is to occur.

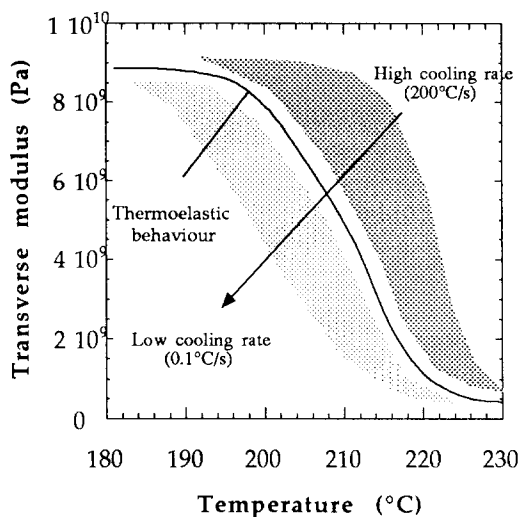


Figure 10: Influence of cooling rate on the evolution of the transverse modulus for PEI/GF

### 7.2) Influence of the cooling profile

In unbalanced cooling, the warping of the unidirectional laminate is caused by the difference in cooling rate acting on the external

surfaces of the part. If the bottom surface cools faster than the top, then the bottom surface will solidify first and will be able to contract freely with no stress build-up, since the remaining part of the laminate is still viscous. Thus the contraction of the bottom surface does not affect the shape of the part. However, when the top surface solidifies its contraction is hindered by the presence of a solid bottom surface. The laminate thus begins to bend as the upper section contracts. When cooling is balanced the two surfaces solidify at the same time and no bending is induced.

APC2/AS4 is more sensitive to unbalanced cooling than PEI/GF. This is related to the phase transitions of the material on cooling. The PEEK matrix undergoes two transitions, crystallisation and glass transition. After crystallisation, the material is still in the viscous state, but as it has developed a semi-crystalline structure, the laminate is stiff enough to sustain stresses. Moreover the coefficient of thermal expansion in the interval between the end of crystallisation and the glass transition is high. Thus large deformations occur in this interval. Such a phenomenon does not exist for PEI/GF as the matrix is amorphous.

The experimental and calculated curvatures are compared in Figures 8 and 9 for PEI/GF and APC2/AS4 respectively. The simulation overestimates the curvature for both materials and for both cooling profiles, to the order of 8% for PEI/GF and 14% for APC2/AS4. However, the influence of cooling profile on the curvature appeared clearly in both the experimental and calculated cases, and so the assumption that stress build-up begins when every ply of the laminate has solidified is justified.

## 8) CONCLUSIONS

This study showed that the cooling profile and the cooling rate are process parameters of major importance for the control of dimensional stability. Only the incorporation of the viscoelastic relaxation behaviour of the polymer matrix in the thermomechanical modelling of dimensional stability will lead to precise prediction of these effects.

## 9) ACKNOWLEDGEMENTS

The Swiss Federal Office for Education and Science (OFES) and the Commission for the Encouragement of Research and Science (CERS)

provided funding for this study. The work was carried out as part of the European Commission BRITE-EURAM programme, project number BE5092.

## 10) REFERENCES

- [1] G. Jeronimidis and A.T. Parkyn, "Residual stresses in carbon fibre-thermoplastic matrix laminates", *J. Composite Materials*, **22**, p401-415 (1988)
- [2] T.A. Bogetti and J.W. Gillespie, "Process-induced stress and deformation in thick-section thermoset composite laminates", *J. Composite Materials*, **26**, p626-660 (1992)
- [3] T.J. Chapman, J.W. Gillespie, R.B. Pipes, J.-A.E. Manson and J.C. Seferis, "Prediction of process-induced residual stresses in thermoplastic composites", *J. Composite Materials*, **24**, p616-643 (1990)
- [4] W.E. Lawrence, J.C. Seferis and J.W. Gillespie, "Material response of a semicrystalline thermoplastic polymer and composite in relation to process cooling history", *Polymer Composites*, **13** (2), p86-96 (1992)
- [5] I.M. Ward, "An Introduction to the Mechanical Properties of Solid Polymers", pub. John Wiley & Sons (1993)
- [6] R. Taylor, in "International Encyclopaedia of Composites", ed. S.M. Lee, VCH Publishers, **Vol. 5**, p530 (1991)
- [7] J.A. Nairn and P. Zoller, "Matrix solidification and the resulting residual thermal stresses in composites", *J. Materials Science*, **20**, p355-367 (1985)
- [8] M. Nardin, El.M. Asloun, F. Muller and J. Schultz, "Study of the carbon fibre-poly(ether-ether-ketone) (PEEK) interface, 3: influence and properties of interphases", *Polymers and Advanced Technologies*, **2**, p161-169 (1991)

# Design and manufacture of an accurate composite piece

M.Raymond, L.Martin, L.Lopez  
Centre de Physique des Particules de Marseille  
163, avenue de Luminy - case 907 - 13288 Marseille cedex 9 - France

F.Navarro, C.Esnault  
B+, Parc d'activités de Gémenos - 13420 Gémenos - France

## Abstract

In the 1995 upgrade of the micro-vertex detector of DELPHI, one of the mechanical components that support the particle detectors will be made of Carbon/Epoxy composite material.

The goal is to produce an accurate piece which is used to position the detectors with the high precision which is demanded.

The paper presents the most important aspects of the design and the manufacturing of the piece in order to comply with the specifications. The authors show the modelling and calculations done to optimize the fiber orientation and to estimate the thermo-elastic behaviour.

Then the main technological choices are explained, as well as the manufacturing process.

Finally, some measurements performed on the prototype are shown and compared with the results of the calculations.

## 1. Introduction

An upgrade of Delphi for LEP 200 has been decided in 1992. A part of this upgrade concerns the micro-vertex detector. It will be mounted in the Delphi's experiment at the beginning of 1995.

This paper deals with one of the mechanical pieces, made of carbon/epoxy composite material, which supports two layers of silicon detectors : the "Closer" layer and the "first Pixel" layer.

The most important technical specifications are the accuracy of detectors positioning and the stability of this positioning with respect to thermal expansion. A distortion lower than 10  $\mu\text{m}$  is demanded.

We will present the modelling and calculations as well as the manufacturing of the piece.

The study does not pretend to be an exploration of the behaviour of the materials which constitute the composite prototype. We want to show how we worked to develop and to produce this piece and how we tried to optimize it.

This study is the result of the combined knowledge of the Centre de Physique des Particules de Marseille (CPPM) on particle detectors, and the expertise of Bplus company specialized on composite materials.

## 2. Functional description

The different components of the micro-vertex detector are shown in Figure 1 which is representative of a quarter of the whole micro-vertex detector :

- A : aluminium end ring (or crown) supporting the Closer layer of silicon ladders,
- B : composite half-cylinder,
- C : aluminium half-crown supporting the first Pixel layer,
- D : Inner and Outer layers,
- E : Pixel detectors (and heat source),
- F : heat source of the closer detectors ladders.
- G : Very Forward Tracker.

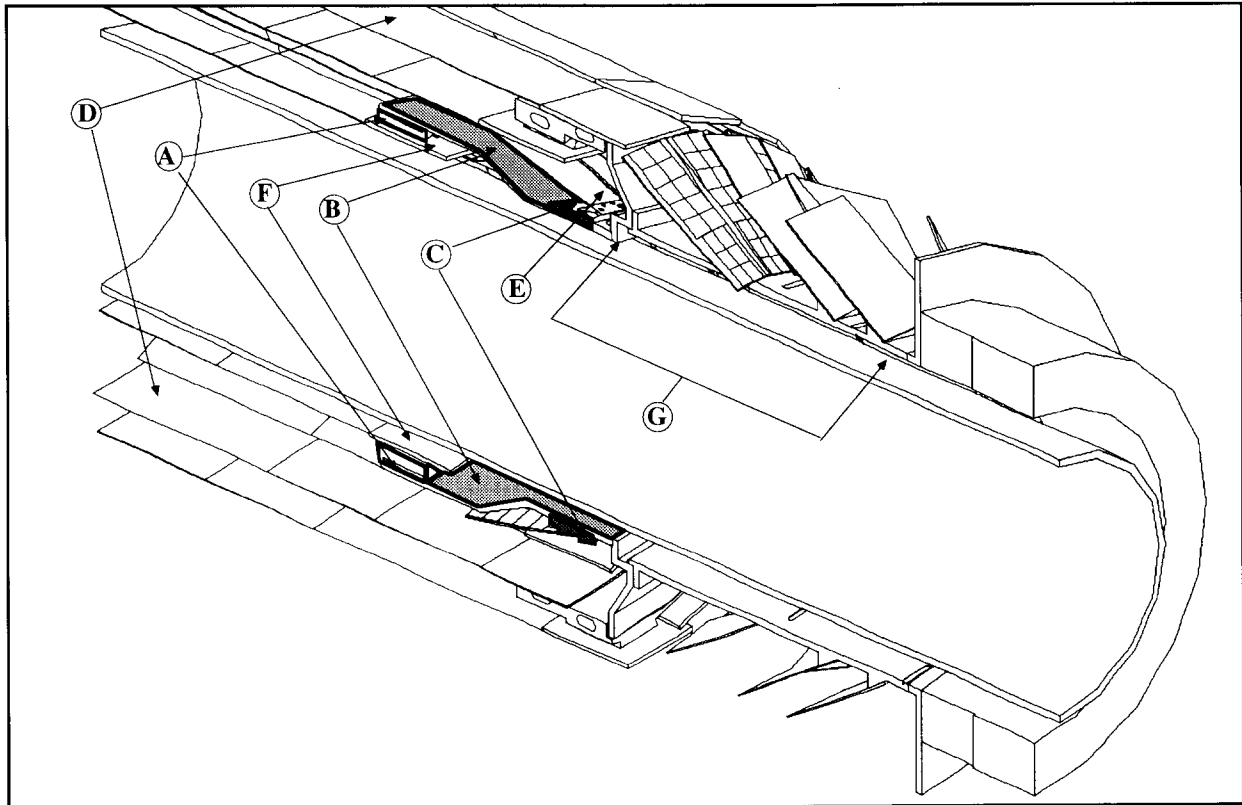


**Figure 1. General view of DELPHI's micro-vertex detector**

The length of the micro-vertex detector is 1033 mm, including electronics at each edges, its external diameter is 280 mm.

In this study, we will present the behaviour of the mechanical system  $\{A+B+C\}$ , which constitutes the part the closest to the beam-pipe. All this system is included in a  $\varnothing 160$  mm diameter cylinder, its length is 568 mm edge to edge.

The electronic circuits associated to the Closer layer (G) produce a thermal power evaluated at 17 Watts per half-crown.

The electronic components connected to the Pixel layer (E) produce a thermal power evaluated at 12 Watts per half crown. This heat is applied to the Aluminium crowns A and C. A cooling channel is glued on crowns A and C, it carries water at 20°C.

Then, a temperature gradient appears in the system  $\{A+B+C\}$ . This gradient is one of the most important parameters that produce a distortion of the mechanical structure.

The objective is to get a deformation smaller than 10  $\mu\text{m}$ .

In order to reduce this distortion it is necessary to study carefully the behaviour of the composite half-cylinder with respect to temperature.

However, all the directions of deformation have not a similar importance. Indeed, as the silicon detector ladders are fixed at each edges on an aluminium crown, any axial deformation would produce either a bending or a tension of the ladders (depending on the direction of the deformation). The radial deformation may produce a large or small distortion depending on whether the deformation is symmetrical or not.

So we will look separately at these two kinds of deformation.

### 3. Modelling and calculations

#### 3.1. Position of the problem

The purpose was to determine what is the best arrangement in layers inside the composite material to minimize thermo-mechanical deformations.

The characteristics of the final multilayer material depend strongly on :

- the characteristics of the carbon fibers,
- the characteristics of the epoxy resin,
- the orientation of each layer.

Because the structure is not strongly loaded, it is not necessary to choose a fiber with a high modulus of elasticity. Actually, this kind of fibers are less resistant to impact and we preferred to fix as the important criterion the aptitude for using the material and getting the shape, instead the mechanical characteristics of the carbon fibers. For this reason we decided to choose a Torayca T300 carbon fiber.

As the characteristics of fibers were fixed and the ones of the resin not preponderant, the main parameter was the fiber orientation of each layer.

The data used to do the calculations are shown in Table 1. They are derived from the supplier's table of properties, for a fiber ratio of volume of 60% .

**Table 1. Properties of unidirectional carbon/epoxy textile**

E (GPa)	$E_1 = 120$	$E_2 = 6$	$E_3 = 3$
G (GPa)	$G_{12} = 4.4$	$G_{23} = 2.2$	$G_{31} = 1.1$
Nu	$N_{12} = 0.34$	$N_{23} = 0.36$	$N_{31} = 0.34$
A ( $10^{-6}$ )	$A_1 = 0,3$	$A_2 = 36,5$	$A_3 = 36,5$
$\lambda$ (W/mK)	$\lambda_1 = 3$	$\lambda_2 = 0,6$	$\lambda_3 = 0,6$

1, 2, 3 are the principal direction of a layer.

1 : parallel to fiber

2 : perpendicular to fiber

3 : perpendicular to the layer

E : Young's modulus of elasticity

G : modulus of transverse elasticity

Nu : Poisson's ratio

A : coefficient of thermal expansion

$\lambda$  : coefficient of thermal conduction.

### 3.2. Modelling

All the computations have been done using a finite element method.

We used Mosaic/Systus from Framasoft company to calculate temperatures. Then the results are used as an external stress for the thermo-mechanical simulation.

As Mosaic/Systus cannot use a structural modelling of stratified materials, the thermal expansion calculations have been made by Bplus company using a specific software dedicated to composite material calculation which is a part of Samcef, from Samtech company.

To compare the two softwares, we did some thermal expansion calculations using Mosaic/Systus, considering the material as an anisotropic homogeneous medium.

To determine the mechanical characteristics of this equivalent material, from the characteristics of one layer, we used a specific software dedicated to plates, called Stratif, developed at Cern, by B. Nicquevert and F. Butin.

We built a tridimensional modelling to allow a better comparison of the results from the two softwares and we noticed that the use of a homogeneous material introduces some zeros as coupling coefficient in the flexibility matrix.

The most consistent results are obtained using Mosaic/Systus for temperature calculations only and then, Samcef for thermal expansion ones.

### 3.3. Simulation results

The purpose of this first approach was to determine the influence of the laminate on the distortion of the piece.

We assumed a thirty layers material (each being 0.1 mm thick) to allow more sensitivity in the material definition.

All the results are obtained with the same temperature distribution. The maximum calculated gradient is 2°C.

We first privileged the 0° fiber orientation (i.e. the axis direction) in the layer laminate because we were interested in reducing mostly the axial deformation to avoid bending of the Closer layer of silicon detectors .

Then we introduced some layers at  $\pm 45^\circ$  in order to reduce the transverse coefficient of thermal expansion.

Finally, we mixed different laminates depending on the area of the piece (see Figure 2). In every case the laminate is mirror-symmetrical.

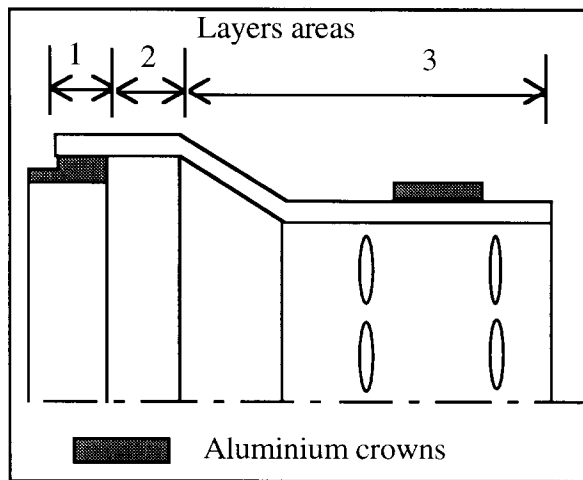


**Figure 2. Definition of the areas of the piece**

Table 2 summarizes the behaviour of the half-cylinder in different cases. One can see that when the same laminate is used in every area of the piece, the deformation decreases in the same way than the number of  $\pm 45^\circ$  layers. But the direction of the deformation (inward or outward) changes when there is no layer at  $45^\circ$ . Therefore, it is impossible to get a deformation smaller than  $5,7 \mu\text{m}$  using the same laminate everywhere.

A special design, where several areas of laminates have been defined on the piece (Figure 2), permits to decrease the deformation.

**Table 2. fiber orientation influence on deformation ( $\mu\text{m}$ )**

Areas	Layers	maximum deformation
1-2-3	$/0^\circ;30/$	6.0 / outward
1-2-3	$\pm 45;8/0^\circ;14/\pm 45;8$	7.9 / inward
1-2-3	$\pm 45;4/0^\circ;22/\pm 45;4$	6.9 / inward
1-2-3	$\pm 45;2/0^\circ;26/\pm 45;2$	5.7 / inward
1-2 3	$/0^\circ;30/$ $\pm 45;4/0^\circ;22/\pm 45;4$	5.4 / outward
1 2-3	$/0^\circ;30/$ $\pm 45;4/0^\circ;22/\pm 45;4$	3.4 / inward
1 2-3	$/0^\circ;30/$ $\pm 45;2/0^\circ;26/\pm 45;2$	3.4 / outward
1 2-3	$/0^\circ;30/$ $\pm 45;1/0^\circ;28/\pm 45;1$	5.7 / outward

*Nota bene* : the notation  $[\pm 45;2/0^\circ;26/\pm 45;2]$  means that the laminate is : one layer at  $+45^\circ$ , one layer at  $-45^\circ$ , twenty six layers at  $0^\circ$ , one layer at  $-45^\circ$ , one layer at  $+45^\circ$ .

Finally, the smallest deformation is obtained using the laminate  $/0^\circ;30/$  in area 1 and two or four layers at  $\pm 45^\circ$  in area 2 and 3.

### 3.4. Optimization

Taking the previous results as a basis, a new modelling has been made. In order to be as close to the real piece as possible, the number of layers has been decreased to ten with a thickness of 0.3 mm for each layer. Some glass fiber layers have been introduced between the aluminium crowns and the carbon/epoxy layers to avoid corrosion.

The main difficulty is that one layer is equivalent to 10% of the whole thickness while it was equivalent to 3% in the previous modelling. This difference of definition of the material makes the previous piled-up not so good.

An additional study has been done to find a better laminate. After several attempts, the solution which has been kept was to break the mirror-symmetry and to introduce one layer at  $-30^\circ$  and one layer at  $+30^\circ$  in front of the aluminium crown supporting the closer ladders of detectors. Then it was necessary to reduce the value of the coefficient of thermal expansion in crossgrain direction. This is the reason why we added two layers with an orientation of  $90^\circ$  in area 2 and 3.

The simulation has given a deformation smaller than  $2\mu\text{m}$  everywhere in the structure if we assume a temperature gradient of  $2^\circ\text{C}$ . Figure 3 summarizes the last laminate, chosen for the fabrication of the piece.

## 4. Fabrication

### 4.1. Materials

The materials used to manufacture the structure are :

- unidirectional carbon fiber G1057 (Brochier), its characteristics are :

weave : taffetas

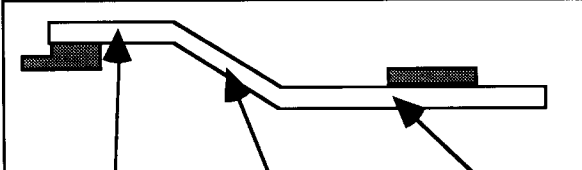
type of arm, warp : Torayca T300

weft : EC5 11Z40

weight distribution, warp : 99%

weft : 1%

nominal thickness : 0.3 mm



Angle	Fibers	Angle	Fibers	Angle	Fibers
0°	carbon	0°	carbon	0°-90°	glass
0°	carbon	-45°	carbon	-45°	carbon
0°	carbon	+45°	carbon	+45°	carbon
0°	carbon	0°	carbon	0°	carbon
0°	carbon	90°	carbon	90°	carbon
0°	carbon	90°	carbon	90°	carbon
-30°	carbon	0°	carbon	0°	carbon
+30°	carbon	+45°	carbon	+45°	carbon
0°	carbon	-45°	carbon	-45°	carbon
0°-90°	glass	0°	carbon	0°	carbon

**Figure 3. Last laminate chosen for fabrication**

- Epoxy resin STM (REA industrie), which polymerizes at room temperature
- glass fibre textile 1581TF (Excel-Génin) :  
weave : satin  
nominal thickness : 0.3 mm

Mechanical and thermal characteristics have been given in 3.1.

The choice of these materials are imposed by the following criteria :

- the accuracy of the final piece was not compatible with a polymerization at high temperature, because of the thermal expansion,
- most of the carbon/epoxy pre-pregs that were available polymerize at high temperature (more than 150°C). We then decided to use, on the one hand, an unidirectional carbon textile and on the other hand, a resin with a room temperature polymerization.
- glass fibre textile is used to insulate the carbon fibers from the aluminium and avoid corrosion of the fibers.

#### 4.2. Tools

Molding is made using a steel mold for the internal shape of the piece and a glass/epoxy mold for the external shape. The polymerization is done in a pressure digester under controlled conditions of temperature and pressure.

#### 4.3. Process

Carbon textiles are impregnated with epoxy resin. After a determined time, the pre-pregs are cut according to detailed drawings. Then, the different layers are piled up on the steel mold and the assembly is placed in the pressure digester.

The polymerization cycle consists of a 16 hours curing at 23°C and a post-cure at 60°C during 16 hours. The pressure inside the autoclave is 6.5 bars.

The shape of the piece is obtained after the holding time at 23°C.

The pressure is realised during the post-cure, the piece is free to expand but comes back to its original shape when the operation is finished.

The next step is the machining of the piece. The main difficulty is the dimensional tolerances on the two diameters that fit with aluminium half-crowns (A and C) supporting the detectors (see figure 4). In addition to the accuracy that is required during the operation, it is necessary to take into account the relaxation stress caused by the machining. This point will be developed later on.

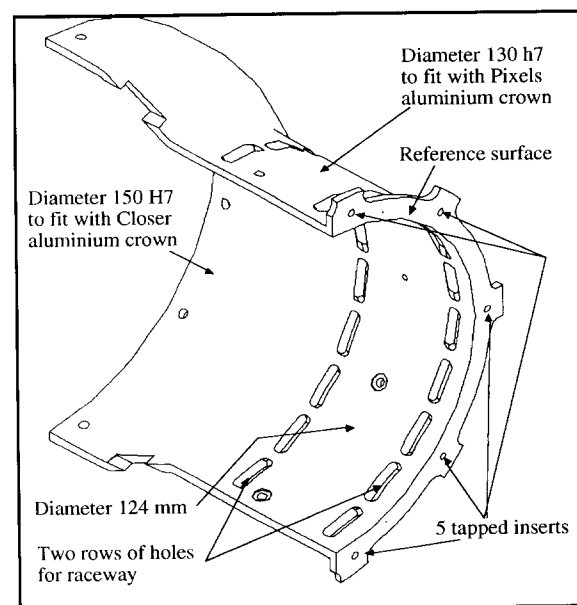


**Figure 4. Carbon/Epoxy piece**

Finally, controls are performed. The amount of fibers in the composite materials is measured by dissolution of the resin in an hydrous solution of sulfuric acid and

comparison of the weights before and after the dissolution.

The dimensions are measured using a tri-dimensional measuring machine.

#### 4.4. Study of the relaxation stress after machining

The aim is to determine the deformation of the structure caused by the machining so that it could be anticipated during molding.

A test piece has been made, according to the following process :

- molding,
- 1st dimensional measurement,
- turning of diameters and routing,
- 2nd dimensional measurement,
- machining of the two rows of holes for the raceway,
- 3rd dimensional measurement.

**Table 3 : Deformations caused by machining**

	Measurement		
	1st	2nd	3rd
Surface smoothness	0,01mm	0,01mm	0,01mm
Ø124 diameter	123,920	123,927	123,725
Ø130 diameter	---	129,968	129,755

Reading Table 3, we can see that there is no real evolution of the piece between the molding and the turning of the diameters.

On the contrary, we notice a decrease of about 0.2 mm of the diameters when the rows of holes are machined.

More, the measurements show a variation in diameter with respect to the distance from the reference surface (see figure 4).

Figures 5a and 5b illustrate this variation and the dimensions of the diameters before and after the machining of the holes.

These results are very important because they show that it is absolutely necessary to take into account the deformation after machining to be able to achieve the dimensional tolerance (40 µm on the diameters).

As the main deformation appears after the machining of the holes, we have decided that :

- the machining of the two rows of holes must be done before the turning of the diameters,
- the cylinders have to be oversized so that it is possible to get the right cylindricity everywhere during the turning,
- a special tool to hold in place the composite piece will be made to minimize the variation on diameter.

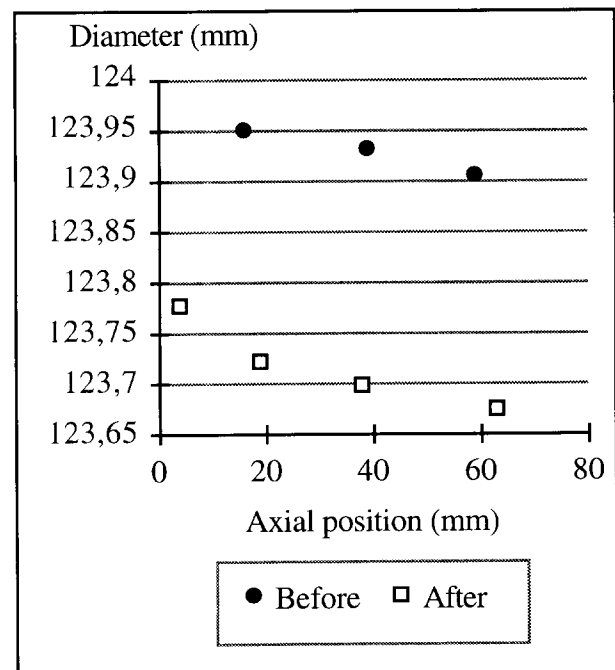


**Figure 5a. Ø124 mm diameter before and after holes machining**

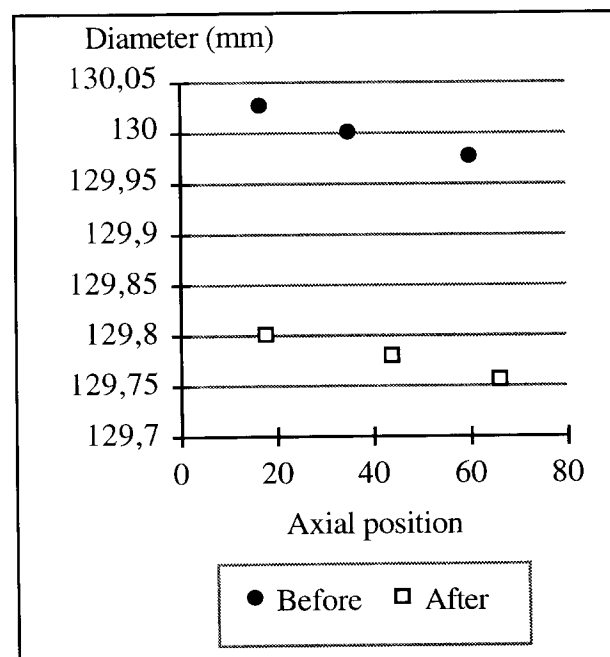


**Figure 5b. Ø130 mm diameter before and after holes machining**



## 5. Expansion tests

### 5.1. Testing stand

The dimensional measurements are performed in a temperature controlled environment, using an automatic tri-dimensional measuring machine. A sequence of operations is recorded so that the best repeatability is ensured.

The piece is positioned by five screws on the machine plate, using a special tool that prevents deformation at the five points of the piece. Two aluminium crowns are mounted on the composite piece and both crowns are equipped with thin flexible heaters that simulate the electronic components and provide heat to the structure.

Temperatures are measured with platinum RTD probes in several points to check the temperature distribution.

The dimensional measurements are performed on the composite material prototype, on the diameter where deformations are the largest : the one which fits to the Closer crown.

The reliability of the measurements has been checked doing 5 measurements at the same temperature but at different times. We can assume that the measurement repeatability is  $\pm 1 \mu\text{m}$ .

The measurement accuracy is estimated to  $\pm 2 \mu\text{m}$ .

The main consequence of this accuracy is that it is not possible to validate the calculations using only a  $2^\circ\text{C}$  temperature gradient : the estimated deformation would be too close to the measuring uncertainty. For this reason, we measured the piece distortion from room temperature ( $21,6^\circ\text{C}$ ) to  $30^\circ\text{C}$ .

### 5.2. Results of the tests

The measurement of the deformation is done in 5 points P1 to P5, located as shown in Figure 6. The deformation is measured in the YZ plan, can be written as :

$$d = \sqrt{(y - y_0)^2 + (z - z_0)^2}$$

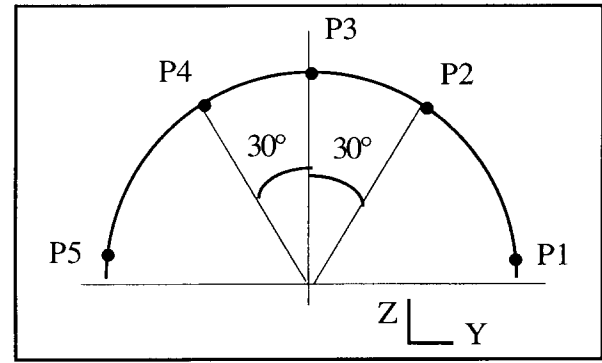


Figure 6. Points position for measuring

We can see (figure 7) that the deformation increases linearly with the temperature. The slopes of the curves are nearly identical for P2, P3 and P4.

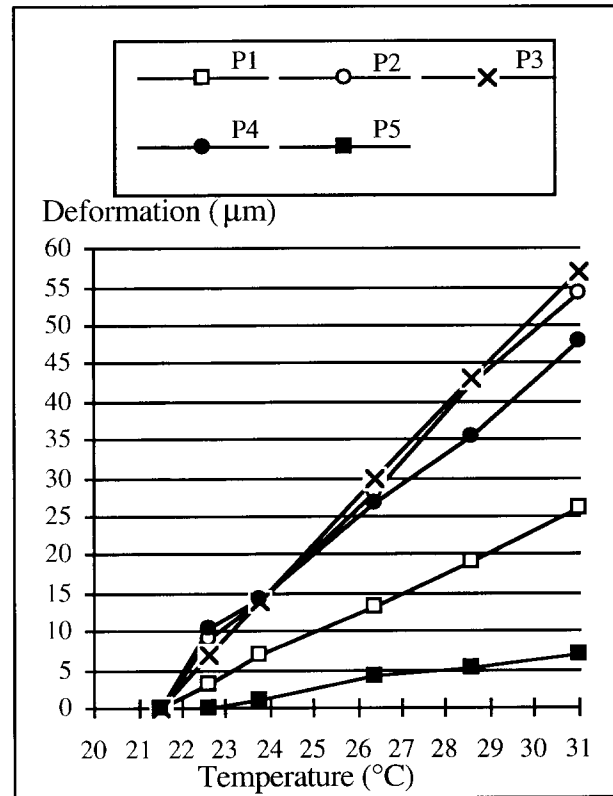


Figure 7. Structure deformation

P1 and P5 slopes are lower than the others.

The values of the slopes are :

0.8  $\mu\text{m}/^\circ\text{C}$  for P5,

2.7  $\mu\text{m}/^\circ\text{C}$  for P1,

5.5  $\mu\text{m}/^\circ\text{C}$  for P2, P3, and P4.

In order to explain the divergence between {P2,P3,P4} and {P1,P5}, it is important to notice that the measuring method is not fully representative of the prototype deformation at P1 and P5. Though, we can also explain that the radial deformation is smaller when the points are closer to the edges, without considering the measuring method.

Actually, on the one hand, the tangent plan in P1 to the composite half-cylinder is almost parallel to the XZ plan, which means that when the sensor of the measuring machine touches the half-cylinder at P1, it does not record any significant displacement along Z axis.

It is the same for P5.

In the same way, we do not exactly estimate the displacement of P3 along Y axis.

This is the reason why we cannot conclude definitely on the divergence between the slopes of P1 and P5. Actually, the deformation of the structure is probably unsymmetrical, but a displacement of the whole structure to the direction of Y+ may exist.

On the other hand, as the Ø150 mm diameter of the half-cylinder is deformed by the machining and the radius is larger at P1 and P5 than at P3, a stress field appears in the prototype when the composite half-cylinder fits the closer crown.

The stress is higher at the edges than at the center of the half-cylinder and it produces an antagonistic force that reduces the displacement of P1 and P5.

At the moment, the results are sufficient to estimate globally the deformation of the half-cylinder and to compare it to the previous results of calculation. We can notice that :

1- The measured deformation reaches 55  $\mu\text{m}$  while the calculated one would be less than 20  $\mu\text{m}$  (by linear extrapolation from the 2  $\mu\text{m}$  obtained with a temperature gradient of 2°C).

The divergence is not negligible of course, but some factors could influence it :

- an uncertainty of about 20%, at least, on the thermo-mechanical characteristics is realistic,
- for the manufacturing, the layers of composite material are cut and then piled up on the steel mold. It means that the continuity of the fibers is not ensured everywhere, which

is inevitable but cannot be taken into account by the theoretical modelling,

- the external stress field is not taken into account by the theoretical modelling.

2- The deformation along the Z axis is larger than the calculated one. The theoretical modelling has shown the edges of the half-cylinder as the more deformed, and P3 the point of the diameter which is the less deformed. This is an important divergence between the theoretical modelling and the experimental results.

3- The values of the deformation for P1 and P5, that we have recorded along the Y axis without taking into account the displacement along the Z axis, are compatible with the results of the calculation.

A schematic view of the radial deformation of the Ø150 mm diameter is shown in Figure 8.

Some tests have been performed in the axial direction too. Figure 9 shows the influence of temperature on the axial deformation for the theoretical modelling, the prototype and an aluminium half-cylinder which has the same shape than the composite prototype.

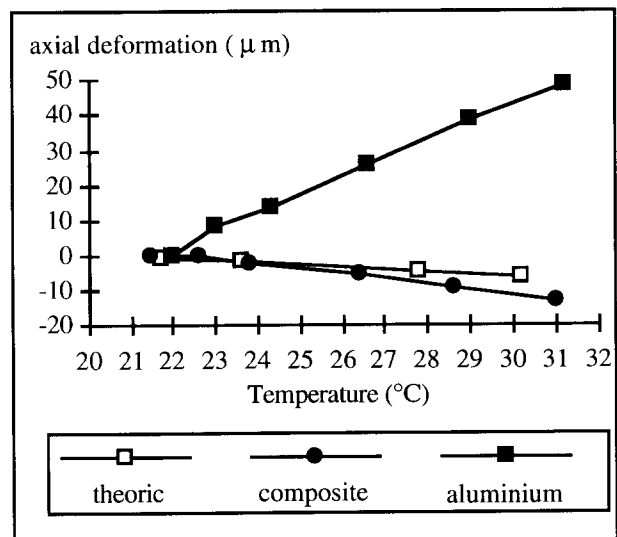


**Figure 9. Comparison of axial deformations**

We see that the behaviour of the structure is close to the theoretical one. The comparison of the composite structure with aluminium one confirms the important decrease of deformation in the axial direction caused by the use of composite material, with an adapted laminate (see paragraph 3).

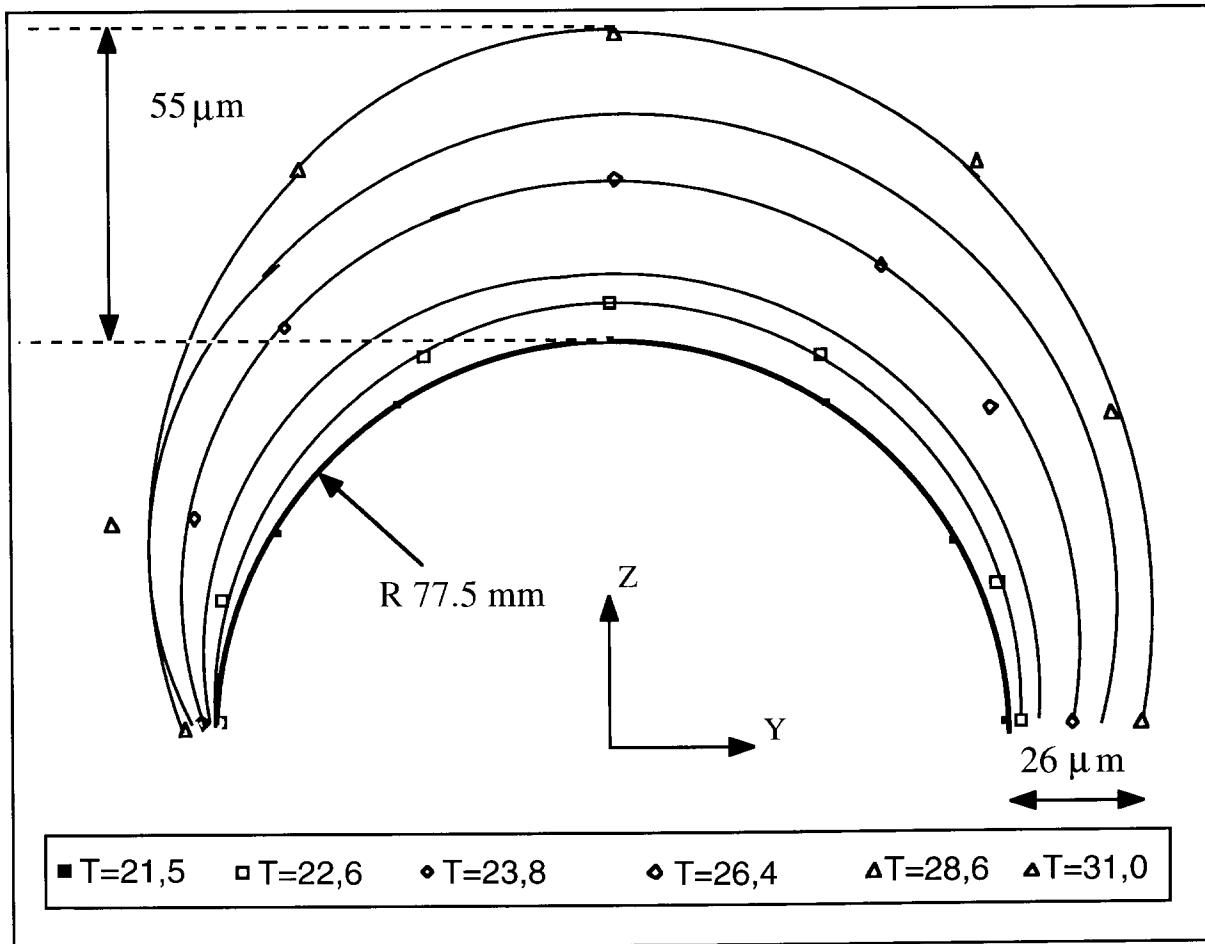


Figure 8. Schematic view of Ø150 mm diameter distortion

## 6. Conclusions

Taking as a basis the study we did, using finite element modelling, we have made a prototype of the carbon/epoxy half-cylinder and performed some preliminary tests on it.

The results show a satisfactory behaviour of the prototype in the axial direction. In the radial direction, the first tests we did show some divergences with the theoretical approach, and underline some difficult points.

Some factors, already presented in this paper, can explain these divergences. Though the aim of the theoretical modelling was to avoid the making of several prototypes using different laminates in order to determine the best of them to minimize deformation, it did not pretend to fit perfectly with the measured deformations.

The next step of this study will be to reduce the stress field in the structure when the composite half-cylinder fits to the crowns. An improvement of the measuring method will then make it possible to determine in realistic conditions the 3D deformations for each point of measurement.

# A HIGH DIMENSIONAL STABILITY STRUCTURES VERIFICATION FACILITY

I. Cabeza, G. Galipienso  
C.A.S.A. - SPACE DIVISION  
28022 Madrid - Spain

## Abstract

The growing demand in the European Space Market for structures of high dimensional stability raised the question for the need of high accuracy measurements which would enable to check the stability performances of such structures. The so-called Optical Measurement System (OMS) is a test facility devoted to verify high stability performances of structural components. The OMS, developed by C.A.S.A. and in operation since March 1993, is capable of measuring distortions, in the range of micrometers, of structural components when submitted to thermal disturbances or moisture desorption. The OMS is housed in a clean room and mainly constituted by a vacuum chamber in which a seismic isolated optical bench is installed. A set of configurable thermal shrouds provides the thermal environment to specimens. The distortion measurement is carried out by optical interferometry complemented with a dedicated image processing software to reach the most outstanding performance of the system: An axial distortion resolution of 0.03 micrometers.

## 1. Introduction

High accuracy optical instruments and detection experiments constitute an increasing demand for scientific observation, teledetection (civil and military) meteorology,... purposes. Both orbiting satellites and experimental laboratories at Earth need highly accurate alignment of optical and detection systems, so dimensional stability during operation is one of the main structural requirements.

The major problems to be solved are the design and manufacturing of stable structures under several disturbing causes; i.e. structures remaining dimensionally stable when submitted to temperature changes or gradients.

A high dimensional stability can be achieved by structural design making use of composites (carbon-epoxy, metal matrix or ceramics materials). Theoretically, the designs can provide solutions for

what the predictable distortions are so "small" that conventional methods are not able to measure.

With the objective of experimentally verify the stability performances of a manufactured structure, submicron resolution measurement methods are necessary.

Its experience in the development of high stability space components and structures, encouraged CASA to initiate the development of a test facility devoted to cover the emerging verification necessity.

Partially supported by National Funds, CASA has developed the Optical Measurement System, "OMS". The baseline of the system development was based upon a set of functional requirements suggested by the Technological Center of the European Space Agency (ESTEC).

Today, the OMS is fully operational (Figure 1).

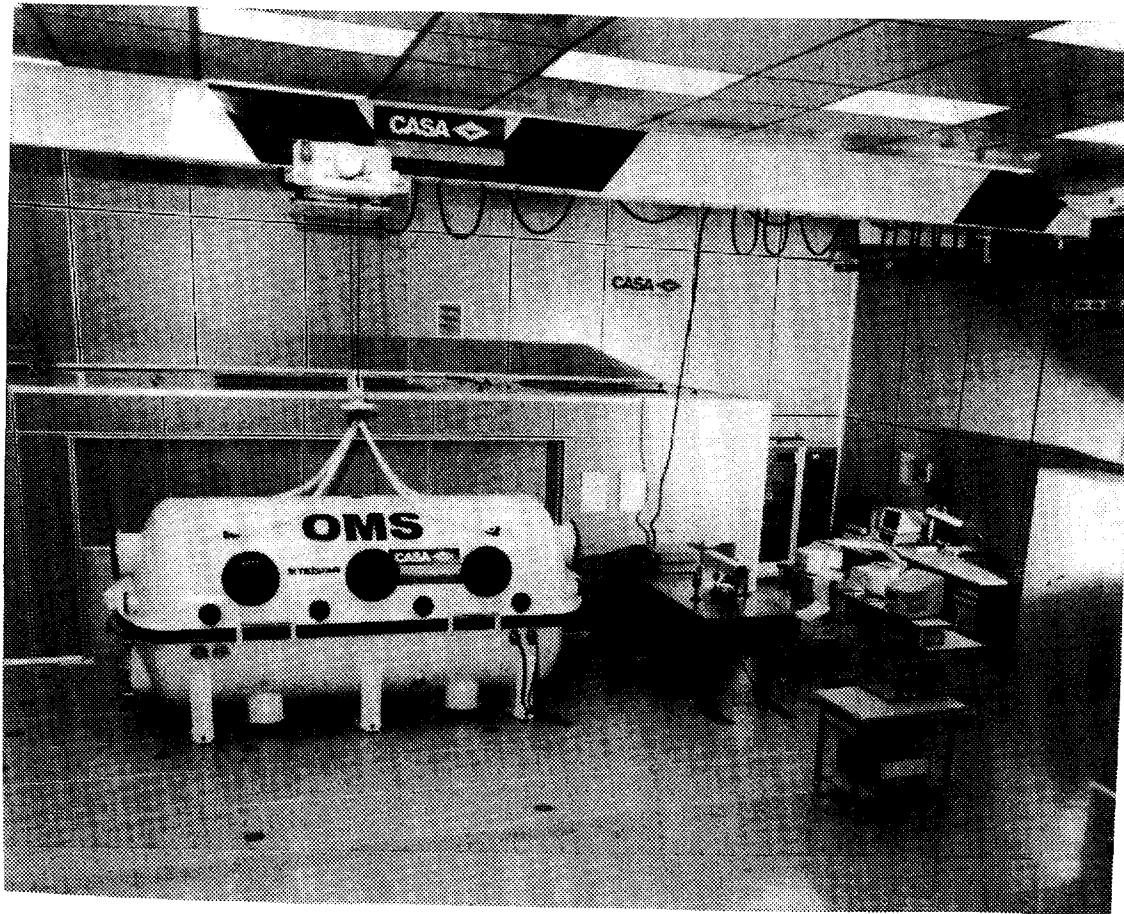


Figure 1. OMS Laboratory

## 2. OMS description

The OMS can be described as a Test Facility capable of:

- Reproducing a Thermal/Vacuum environment.
- Performing Optical measurements.
- Offering a seismic isolated working surface.
- Facilitating the execution of many different type of tests.

Although submicron distortions measurement has been the main goal of the development, the OMS has been conceived under the basis of modularity and versatility.

For a better understanding, the description of the facility is done by partial subsystems. A small effort of the reader is asked to keep in mind that all the OMS components are integrated to configure a system able to operate as a whole.

### 2.1. Vacuum and Thermal Subsystems

The vacuum enclosure of the system is constituted by a cylindrical vacuum chamber (1700 mm diameter, 3800 mm long). The pumping equipment is formed by a set of roots, rotary and diffusion pumps, to reach a pressure down to  $10^{-5}$  mbar.

To facilitate the tests set-up assembling, the vacuum chamber opens by its horizontal generatrix (see figure 2), dividing it into two parts.

The down part is fixed and locates all the connections to the rest of the system, as well as different aims feedthroughs.

From outside, the optical access to the interior of the vacuum chamber can be done by one of the windows distributed on the upper part (diameters 100 mm and 300 mm).

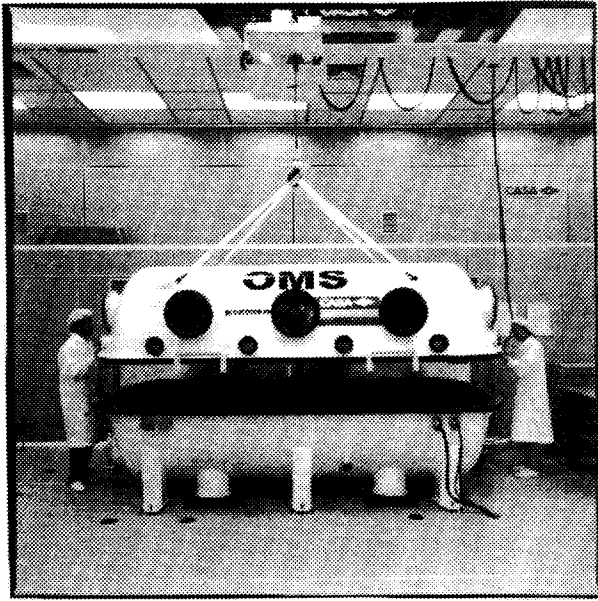


Figure 2. Vacuum Chamber

To provide a controlled thermal environment on the specimens, the thermal subsystem consists of a set of 10 semielliptical thermal shrouds. They are independent from the vacuum chamber (not fixed on it) and can be configured under tests demand.

Depending on the kind of test and on the shape and size of the specimen, the most adequate thermal controlled volume is assembled. Figures 3 and 4 show two different thermal shroud configurations. For the most complete configuration a thermal controlled volume of  $800 \times 700 \times 2500 \text{ mm}^3$  can be set.

The thermal shrouds are supported by the vacuum chamber. To avoid thermal changes of the vacuum chamber, thermal isolation devices are located all along the thermal paths.

The thermal control consists of four (4) independent thermal channels. Each channel can feed 1 or 2 thermal shrouds and it is commanded by a PID controller. The 4 degrees of freedom makes possible to simulate thermal gradients on the specimen. A temperature range from  $-55^\circ\text{C}$  till  $+100^\circ\text{C}$  with a spatial/time stability of  $\pm 0.5^\circ\text{C}$  can be achieved at the thermal shrouds. The maximum attainable, both cooling and heating, ramp-rate is  $3^\circ\text{C/min}$ .

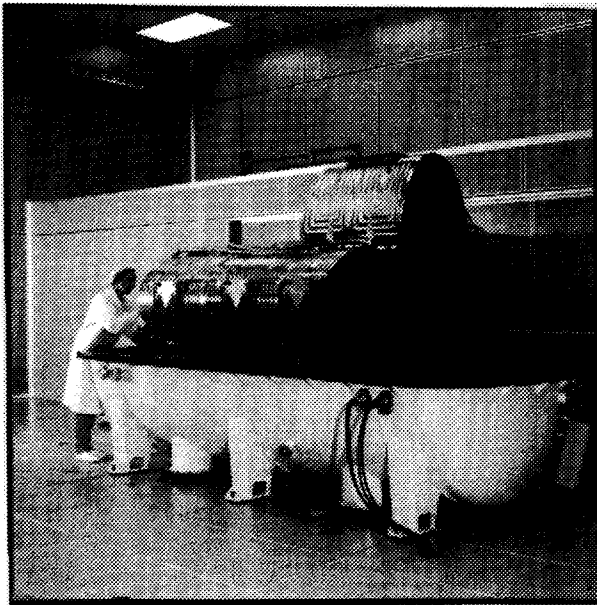


Figure 3. Longitudinal axis shroud configuration

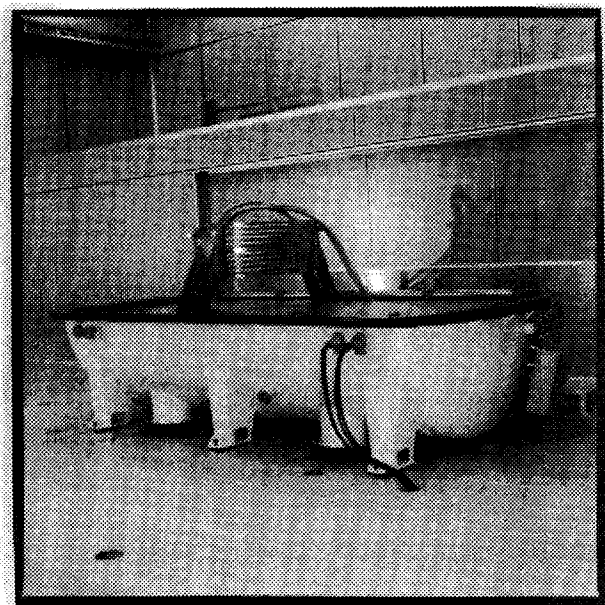


Figure 4. Vertical axis shroud configuration

## 2.2. Seismic Isolation

Inside the vacuum chamber an optical bench provides a seismic isolated working surface with dimension 1200 x 3000 mm<sup>2</sup>.

A 40 Tm seismic block supported by a spring-damping system constitutes the basis on which the optical bench is laying.

To be sure that perturbations do not reach the working surface, the optical bench has its proper damping system. The complete configuration has a frequency of  $\approx 1.5$  Hz.

To support auxiliar optics, another optical bench outside the vacuum chamber is also resting on the seismic block.

Moreover, a big effort has been done to avoid that perturbations coming from equipments of the proper system, reach the working surface.

The working surface offers a square pattern (25 x 25 mm) of M6 mounting holes, what clearly facilitates the tests set-up assembly.

## 2.3. Optomechanical Equipments

The OMS is a test facility capable of being used for many different type of tests and specimens. It is clear that each one will require specific devices and tools.

The OMS measures distortions making use of optical interferometry methods.

Particularly, Fizeau type interferometric cavities (one or more depending on test specification) are configured on specimens.

Up to a maximum of 20 interferometric cavities can be observed "simultaneously".

The optical set-up combines general purpose optomechanical equipments:

- A frequency stabilized He-Ne laser source (coherence length larger than 100 m).
- A spatial filter/collimator for the laser beam.
- Optical components (lenses, mirrors, beam-splitters).
- Standard mechanical supports for optical components.
- High quality optics ( $\lambda/20$ ) for interferometric cavities,

and specific devices depending on specimen characteristics:

- Mechanical interface mirror/specimen.
- Specimen supporting tools.

With the exception of the interferometric cavities, all the optical components are installed on an Optical Bench outside the vacuum chamber.

Inside the vacuum chamber the laser beam is transported by means of what it has been called Beam-Deflector.

The Beam-deflector is a vacuum compatible mechanism with 4 motion degrees (two translations and two rotations). When more than one interferometric cavity is configured, the beam-deflector can be programmed to "visit" successively all the installed interferometric cavities allowing the "simultaneous" distortion measurements.

Figure 5 shows an overview of the optical assembly.

Up to now, specific devices (mechanical interface mirror/specimen and specimen supporting tools) are available for:

- Flat samples.
- Sandwich panels (flat or with curvatures).
- Tubes and different sections longitudinal structures.

## 2.4. Image acquisition and Processing subsystem

Whereas the optomechanical equipments are encharged of producing an image containing the specimen distortion information, the Image Acquisition and Processing subsystem is devoted to extract such information.

The image is acquired by a CCD camera (512 x 512 pixels) and digitized by a MATROX card enabling its computer processing.

A specific dedicated software to process interferometric fringes images has been developed.

The software is able to extract the three fringe pattern parameters per image: Interfringe, Tilt and Fringes Displacement. It is based on FFT technics.

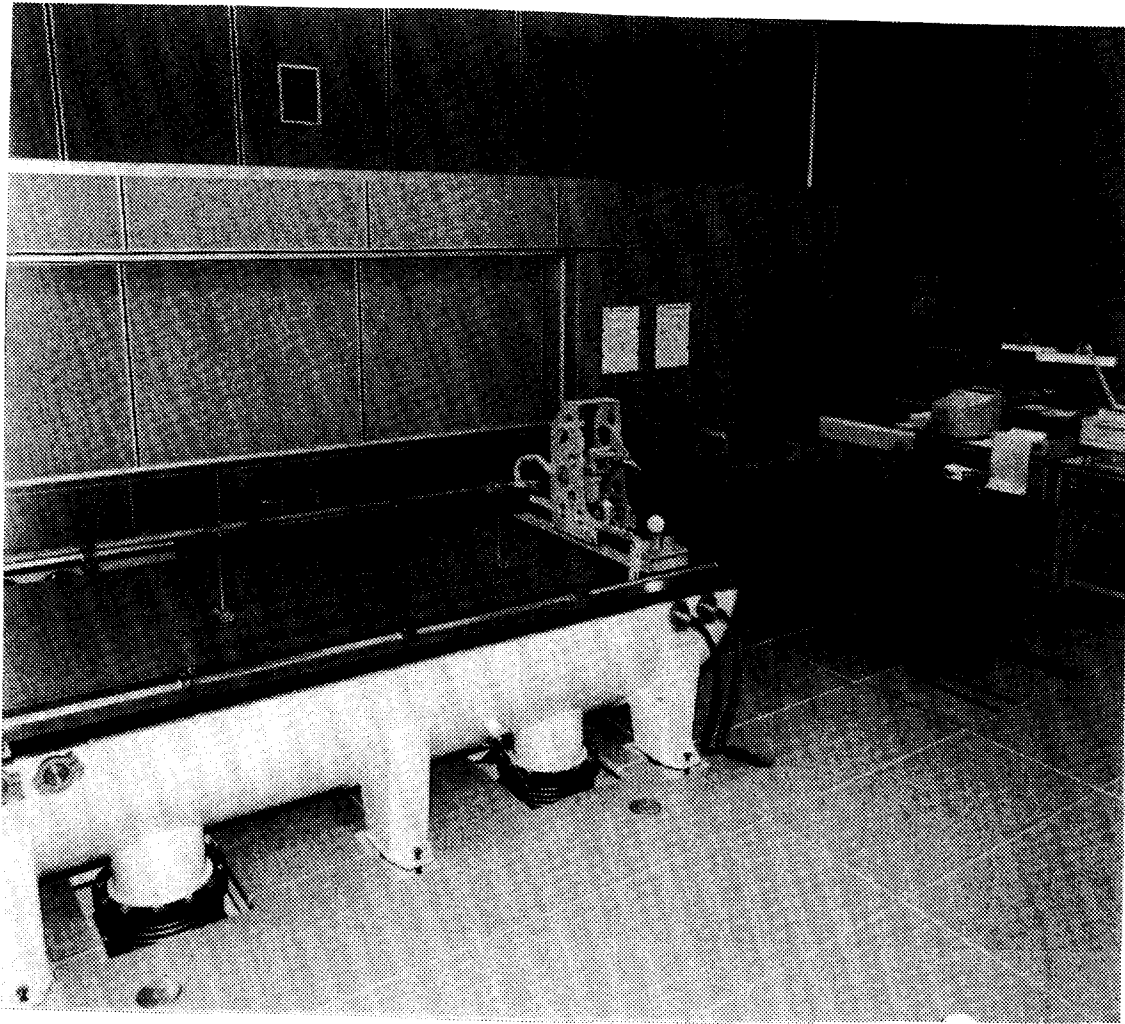


Figure 5. Overview of the Optical Assembly (an interferometric cavity is installed on a CFRP tube)

The error of which each parameter is affected is:

- Interfringe relative error  $< 10\%$
- Fringe displacement (phase) relative error  $< 10\%$
- Tilt error  $\pm 0.01$  rd

### 2.5. Data acquisition and Control subsystem

Several functions are commended to the Data Acquisition and Control Subsystem:

- To acquire all the relevant data (but images) produced during a test.
- To control all the active equipments during a test execution.
- To process the test results.
- To assist on specific and routine activities of the lab.

Inside the vacuum chamber a total of 330 temperature measurements are available by means of thermocouples T-type (up to 300) and PT-100 sensors (up to 30) connected to a data-logger.

Apart from temperature, other physical properties can also be measured, making use of the signal feedthroughs available at the vacuum chamber and the multipurpose data-acquisition cards with which the data-logger is equipped.

A Hewlett-Packard computer constitutes an IEEE-Network with 15 Nodal Points. All the "active" equipments of the OMS are connected to it. A specific software has been developed to easily program the tests execution sequence. When performing a test, the computer becomes in a real manager of the system.

Figure 6 shows the image processing and control computers.



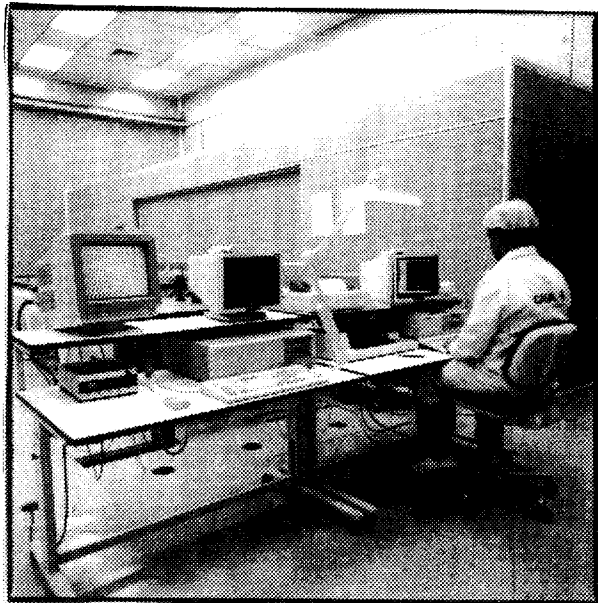


Figure 6. Data-acquisition control and image processing computers

### 2.6. Overall environment and services

The OMS is installed in a clean room (class 10000) with controlled temperature ( $20 \pm 2$  °C) and Relative Humidity ( $50 \pm 10\%$ ).

Laboratory dimensions are  $15 \times 15 \times 5$  m<sup>3</sup>. It has available all the resources needed for a correct and efficient functioning of the system.

## 3. OMS performances

Following the main performances of the Optical Measurement System are resumed:

- Available volume (thermal/vacuum environment):  $800 \times 700 \times 2500$  mm<sup>3</sup>
- Attainable vacuum:  $10^{-5}$  mbar
- Temperature range: -55, +110 °C
- Thermal gradient capability (4 independent thermal channels)
- Temperature signals: Up to 330
- Interferometric cavities: Up to 20
- Axial Distortion measurement resolution: Better than  $0.03$  μm
- Clean Area conditions: Class 10000

## 4. OMS capabilities

As it was said before, the development of the Optical Measurement System has been done under the basis of modularity and versatility.

Several originalities can be found when one has a look at the system:

- Modular shroud configuration and thermal control.
- Accessibility of the working surface: one can think of an Optical Laboratory with vacuum and thermal capabilities.
- Easy to operate and high degree of automation.
- Set-up versatility and multi-purpose.

The OMS has resulted in a Test Facility capable of:

- Reproducing a Thermal/Vacuum environment.
- Performing Optical measurements.
- Offering a seismic isolated working surface.
- Facilitating the execution of many different type of tests.

## 5. Acknowledgements

From here CASA wishes to make public acknowledgement to all those that have made the OMS possible.

CASA is specially grateful to:

- TELSTAR (Vacuum/Thermal Subsystems), VIBRACHOC (Seismic Block) and MICRO-CONTROL (Beam-Deflector) subcontractors by the effort done and interest shown.
- INI (National Industry Institute) and CDTI (Centre for Industrial Development and Technology) National Organisms that have contributed to support the development.
- ESTEC that encourage CASA to go ahead with the challenging project.

**PART VI**

**Index of Authors**

**List of Participants**

# Index of Authors

J.M. Andrés (CASA, Space Division, Spain) .....	39
F. Arévalo (CASA, Space Division, Spain) .....	39
D. Bashford (ERA Technology Ltd, Leatherhead, UK) .....	9
W. Benhamida (Lab. Modélisation et Mécanique des Structures, Univ. Paris VI, France) ..	133
A. Bonet (CASA, Space Division, Spain) .....	39
I. Cabeza (CASA, Space Division, Spain) .....	189
V. Dobulevitch (Meson, St Petersburg, Russia) .....	77
H. Dumontet (Lab. Modélisation et Mécanique Structures, Univ. Paris VI, France) .....	133
D. Eaton (ESA/ESTEC, Noordwijk, The Netherlands) .....	9
W. Eichberger (ISOVOLTA, Austria) .....	147
C. Esnault (B+, France) .....	179
J. Enz (DASA-Dornier GmbH, Germany) .....	69
A. Fallou (CPPM, CNRS, France) .....	59
V. Fedorov (Meson, St Petersburg, Russia) .....	77
G. Feofilov (St Petersburg State Univ., Russia) .....	77
P. Fialla (ISONOVA, Austria) .....	105
G. Galipienso (CASA, Space Division, Spain) .....	189
S. Gerasimov (Mendeleev Institute for Metrology, St Petersburg, Russia) .....	77
P. Giubellino (INFN, Italy) .....	77
O. Godisov (Meson, St Petersburg, Russia) .....	77
C. Grastataro (Los Alamos Nat. Lab., USA) .....	21
C. Hauviller (CERN) .....	vii, 3, 49
G. Helwig (DASA-Dornier GmbH, Germany) .....	33
S. Igolkin (Meson, St Petersburg, Russia) .....	77
S. Johnson (YLA Inc., USA) .....	115
P. Kim (Lab. Tech. Composites, EPF Lausanne, Switzerland) .....	123, 171
A. Lekhder (Lab. de Mécanique et des Matériaux, Fac. Sciences, Rabat, Maroc) .....	133
N. Levoy (Nuclear Metals Inc., USA) .....	89
G. Lippmann (DASA-Dornier GmbH, Germany) .....	69
L. Lopez (CPPM - CNRS, France) .....	179
J.A. Månson (Lab. Tech. Composites, EPF Lausanne, Switzerland) .....	123, 171
L. Martin (CPPM - CNRS, France) .....	179
F. Navarro (B+, France) .....	179
B. Nicquevert (CERN) .....	49
I. Novikov (Mendeleev Institute for Metrology, St Petersburg, Russia) .....	77
E. Ozores (CASA, Space Division, Spain) .....	39
G. Patz (YLA Inc., USA) .....	115
J.-F. Peltier (Aerospatiale Espace et Défense, France) .....	99
J. Pernon (Aerospatiale Espace et Défense, France) .....	99
E. Perrin (Univ. Genève, Switzerland) .....	59

R. Phillips (Lab. Tech. Composites, EPF Lausanne, Switzerland) .....	123, 171
A. Pradier (ESA/ESTEC, Noordwijk, The Netherlands) .....	9
M. Price (CERN) .....	49
M. Rabinovitch (ONERA, France) .....	97
K. Raftery (Nuclear Metals Inc., USA) .....	89
M. Raymond (CPPM - CNRS, France) .....	179
L. Riccati (INFN, Italy) .....	77
S. Robitaille (YLA Inc., USA) .....	115
H. Schönbacher (CERN) .....	139
J. Schukraft (CERN) .....	77
B. Smith (Los Alamos Nat. Lab., USA) .....	21
P. Sunderland (Lab. Tech. Composites, EPF Lausanne, Switzerland) .....	171
G. Tappern (Rutherford Appleton Lab., UK) .....	59
M. Tavlet (CERN) .....	139, 157
T. Thompson (Los Alamos Nat. Lab., USA) .....	21
S. Toll (Lab. Tech. Composites, EPF Lausanne, Switzerland) .....	123
H. Van der Burgt (ERTA-EPEC, Belgium) .....	157
L. Vitushkin (Mendeleev Institute for Metrology, St Petersburg, Russia) .....	77
R. White (Nuclear Metals Inc., USA) .....	89
M. Yudkin (Meson, St Petersburg, Russia) .....	77

# List of participants

Jan-Olof AIDAMPAA	SICOMP, Piteå, Switzerland
Fernando AREVALO	CASA, Space Div., Madrid, Spain
Geoff BARBER	Imperial College - Physics Dept., United Kingdom
David BASHFORD	ERA Technology Ltd, United Kingdom
Isabel CABEZA	CASA, Space Div., Madrid, Spain
Jeff CHERWINKA	Cornell Univ., United States
Nathalie CHIEUSSE	Aerospatiale, France
Allan CLARK	DPNC, Univ. Genève, Switzerland
Franco DAUDO	INFN, Torino, Italy
Richard DAVEY	Rutherford Appleton Lab., United Kingdom
Alexander DONAT	DESY - IfH, Zeuthen, Germany
Hélène DUMONTET	Lab. Modélisation et Mécanique, Paris, France
Walter EICHBERGER	Isovolta, Wien, Austria
Jurgen ENZ	Dornier GmbH, Germany
Aboud FALLOU	CPPM, Marseille, France
Claudio FANIN	INFN, Padova, Italy
Gregory FEOFILOV	St. Petersburg State University, Russia
Peter FIALLA	Isonova, Wien, Austria
Joachim FUSS	Univ. Dortmund, Germany
Andrea GADDI	INFN, Frascati, Italy
Gonzalo GALIPIENSO	CASA, Space Div., Madrid, Spain
Rikard GEBART	SICOMP, Piteå, Switzerland
Hubert GERWIG	CERN-PPE
Denis GIRARD	SAGEM, Paris, France
Giuseppe GIRAUDO	INFN, Torino, Italy
William GLESSING	CERN-PPE
Oleg GODISOV	Meson Sci., St Petersburg, Russia
Jan GODLEWSKI	Inst. Nucl. Physics, Krakow, Poland
Thierry GRENIER	B+ Développement, France
Hansjürg GYSIN	Sulzer Innotec A.G., Switzerland
Carl HABER	Lawrence Berkeley Laboratory, United States
Claude HAUVILLER	CERN
Reiner HELLER	DESY - IfH, Zeuthen, Germany
Gunter HELWIG	Dornier GmbH, Germany
Alain HERVE	CERN-PPE
Hans Jürgen HILKE	CERN-PPE
John HILL	University of Oxford, United Kingdom
Sergueï IGOLKINE	Meson Sci., St Petersburg, Russia
Patrick KIM	LTC, EPF Lausanne, Switzerland
Wolfgang KLEMP	CERN-PPE
Tadeusz KURTYKA	CERN-MT
Guy LABORIE	Institut des Sciences Nucléaires, Grenoble, France
Michel LEBEAU	CERN-PPE
Nicole LEVOY	NMI Inc., United States
Gerhard LIPPMANN	Dornier GmbH, Germany

Michel MATHIEU .....	CERN-MT
Pierre MEGRET .....	SAGEM, Paris, France
Jos METSELAAR .....	NIKHEF, Amsterdam, Netherlands
Derek MILLER .....	Imperial College - Physics Dept., United Kingdom
Stefano MOCCIA .....	INFN, Frascati, Italy
Jean-François MURAZ .....	Institut des Sciences Nucléaires, Grenoble, France
Bertrand NICQUEVERT .....	CERN
Johannes OBERLEHNER .....	Isonova, Wien, Austria
Morley O'NEILL .....	Carleton Univ., Ottawa, Canada
Antti ONNELA .....	CERN-PPE
Eduardo OZORES .....	CASA, Space Div., Madrid, Spain
Jean PERNON .....	Aerospatiale, France
Eric PERRIN .....	DPNC, Univ. Genève, Switzerland
Richard PHILLIPS .....	LTC, EPF Lausanne, Switzerland
Ronald PINTUS .....	CERN-PPE
Mike PRICE .....	CERN-PPE
Fabrizio RAFFAELLI .....	INFN, Pisa, Italy
Paul RATZMANN .....	Fermilab, United States
Michel RAYMOND .....	CPPM, Marseille, France
Danling REN .....	ETH Zürich, Switzerland
Susan ROBITAILLE .....	YLA Inc., United States
Helmut SCHMUECKER .....	Max-Planck Inst., München, Germany
Helmut SCHONBACHER .....	CERN-TIS
Arndt SCHULTZ von DRATZIG .....	I. Phys. Inst., Aachen, Germany
Henk SCHUYLENBURG .....	NIKHEF, Amsterdam, Netherlands
Paul SEILER .....	Angst + Pfister S.A., Switzerland
Rolf SIEDLING .....	I. Phys. Inst., Aachen, Germany
Paul SUNDERLAND .....	LTC, EPF Lausanne, Switzerland
Balazs SZELESS .....	CERN-AT
Geoff TAPPERN .....	Rutherford Appleton Lab., United Kingdom
Marc TAVLET .....	CERN-TIS
Timothy THOMPSON .....	Los Alamos Nat. Lab., United States
Thierry TROUSSEAU .....	Eskenazi S.A., Switzerland
Roger VALBUENA .....	CERN-MT
Luc VAN LANCKER .....	Inst. High Energies, Univ. Brussels, Belgium
Raymond VENESS .....	CERN-MT
Gert VIERTEL .....	ETH Zürich, Switzerland
Peter VOIROL .....	Stesalit A.G., Switzerland
Hanspeter VON GUNTEN .....	ETH Zürich, Switzerland
Silvia WALDMEIER .....	ETH Zürich, Switzerland
Werner WITZELING .....	CERN-PPE
Wonjae YU .....	LTC, EPF Lausanne, Switzerland



# List of participants

Jan-Olof AIDAMPAA	SICOMP, Piteå, Switzerland
Fernando AREVALO	CASA, Space Div., Madrid, Spain
Geoff BARBER	Imperial College - Physics Dept., United Kingdom
David BASHFORD	ERA Technology Ltd, United Kingdom
Isabel CABEZA	CASA, Space Div., Madrid, Spain
Jeff CHERWINKA	Cornell Univ., United States
Nathalie CHIEUSSE	Aerospatiale, France
Allan CLARK	DPNC, Univ. Genève, Switzerland
Franco DAUDO	INFN, Torino, Italy
Richard DAVEY	Rutherford Appleton Lab., United Kingdom
Alexander DONAT	DESY - IfH, Zeuthen, Germany
Hélène DUMONTET	Lab. Modélisation et Mécanique, Paris, France
Walter EICHBERGER	Isovolta, Wien, Austria
Jurgen ENZ	Dornier GmbH, Germany
Aboud FALLOU	CPPM, Marseille, France
Claudio FANIN	INFN, Padova, Italy
Gregory FEOFILOV	St. Petersburg State University, Russia
Peter FIALLA	Isonova, Wien, Austria
Joachim FUSS	Univ. Dortmund, Germany
Andrea GADDI	INFN, Frascati, Italy
Gonzalo GALIPIENSO	CASA, Space Div., Madrid, Spain
Rikard GEBART	SICOMP, Piteå, Switzerland
Hubert GERWIG	CERN-PPE
Denis GIRARD	SAGEM, Paris, France
Giuseppe GIRAUDO	INFN, Torino, Italy
William GLESSING	CERN-PPE
Oleg GODISOV	Meson Sci., St Petersburg, Russia
Jan GODLEWSKI	Inst. Nucl. Physics, Krakow, Poland
Thierry GRENIER	B+ Développement, France
Hansjürg GYSIN	Sulzer Innotec A.G., Switzerland
Carl HABER	Lawrence Berkeley Laboratory, United States
Claude HAUVILLER	CERN
Reiner HELLER	DESY - IfH, Zeuthen, Germany
Gunter HELWIG	Dornier GmbH, Germany
Alain HERVE	CERN-PPE
Hans Jürgen HILKE	CERN-PPE
John HILL	University of Oxford, United Kingdom
Sergueï IGOLKINE	Meson Sci., St Petersburg, Russia
Patrick KIM	LTC, EPF Lausanne, Switzerland
Wolfgang KLEMP	CERN-PPE
Tadeusz KURTYKA	CERN-MT
Guy LABORIE	Institut des Sciences Nucléaires, Grenoble, France
Michel LEBEAU	CERN-PPE
Nicole LEVOY	NMI Inc., United States
Gerhard LIPPMANN	Dornier GmbH, Germany



Michel MATHIEU .....	CERN-MT
Pierre MEGRET .....	SAGEM, Paris, France
Jos METSELAAR .....	NIKHEF, Amsterdam, Netherlands
Derek MILLER .....	Imperial College - Physics Dept., United Kingdom
Stefano MOCCIA .....	INFN, Frascati, Italy
Jean-François MURAZ .....	Institut des Sciences Nucléaires, Grenoble, France
Bertrand NICQUEVERT .....	CERN
Johannes OBERLEHNER .....	Isonova, Wien, Austria
Morley O'NEILL .....	Carleton Univ., Ottawa, Canada
Antti ONNELA .....	CERN-PPE
Eduardo OZORES .....	CASA, Space Div., Madrid, Spain
Jean PERNON .....	Aerospatiale, France
Eric PERRIN .....	DPNC, Univ. Genève, Switzerland
Richard PHILLIPS .....	LTC, EPF Lausanne, Switzerland
Ronald PINTUS .....	CERN-PPE
Mike PRICE .....	CERN-PPE
Fabrizio RAFFAELLI .....	INFN, Pisa, Italy
Paul RATZMANN .....	Fermilab, United States
Michel RAYMOND .....	CPPM, Marseille, France
Danling REN .....	ETH Zürich, Switzerland
Susan ROBITAILLE .....	YLA Inc., United States
Helmut SCHMUECKER .....	Max-Planck Inst., München, Germany
Helmut SCHONBACHER .....	CERN-TIS
Arndt SCHULTZ von DRATZIG .....	I. Phys. Inst., Aachen, Germany
Henk SCHUYLENBURG .....	NIKHEF, Amsterdam, Netherlands
Paul SEILER .....	Angst + Pfister S.A., Switzerland
Rolf SIEDLING .....	I. Phys. Inst., Aachen, Germany
Paul SUNDERLAND .....	LTC, EPF Lausanne, Switzerland
Balazs SZELESS .....	CERN-AT
Geoff TAPPERN .....	Rutherford Appleton Lab., United Kingdom
Marc TAVLET .....	CERN-TIS
Timothy THOMPSON .....	Los Alamos Nat. Lab., United States
Thierry TROUSSEAU .....	Eskenazi S.A., Switzerland
Roger VALBUENA .....	CERN-MT
Luc VAN LANCKER .....	Inst. High Energies, Univ. Brussels, Belgium
Raymond VENESS .....	CERN-MT
Gert VIERTEL .....	ETH Zürich, Switzerland
Peter VOIROL .....	Stesalit A.G., Switzerland
Hanspeter VON GUNTEN .....	ETH Zürich, Switzerland
Silvia WALDMEIER .....	ETH Zürich, Switzerland
Werner WITZELING .....	CERN-PPE
Wonjae YU .....	LTC, EPF Lausanne, Switzerland